Galaxy Transformations in the Last 5 Billion Years

by

Ting Lu

A thesis
presented to the University of Waterloo
in fulfillment of the
thesis requirement for the degree of
Doctor of Philosophy
in
Physics

Waterloo, Ontario, Canada, 2010

I hereby declare that I am the sole author of this thesis. This is a true copy of the thesis, including any required final revisions, as accepted by my examiners.

I understand that my thesis may be made electronically available to the public.

Abstract

It has become clear that the global star formation rate in the Universe has been decreasing since at least $z \sim 1$, and blue, star-forming galaxies are transformed into red, passive galaxies through one or more processes. The origin of this decline and transformation remains unclear. The role environment plays in all this is especially uncertain. Despite the observed domination of a passive population in the cores of clusters, in contrast to the more actively star-forming field population, whether or not, and how environment affects the properties of galaxies when they fall into clusters is an unsettled question. In this thesis, we look into these issues by examining both the passive and star-forming galaxies, from the cores out to the infall regions, in a large sample of clusters at $0.15 < z < 0.36$ we detected from the Canada-France-Hawaii Telescope Legacy Survey (CFHTLS).

We find that in the cores of clusters, the red-sequence galaxies are a mixture of two populations, indicated by the inflexion in their luminosity function. There is no strong evolution in the shape of the red-sequence between $z \sim 0.4$ and $z \sim 0.2$; however, from $z \sim 0.2$ to today, there is a rapid increase in the number of faint galaxies on the red-sequence relative to the bright ones, suggesting a rapid quenching of the faint galaxies in cluster cores within the last few billion years.

At $z \sim 0.2$, we find that, at all stellar mass explored ($9.0 < \log_{10}(M_*/\ \mathrm{M}_\odot) < 11.5$), the red fraction (star-forming fraction) has no dependence on the clustercentric distance at $3 \lesssim r \lesssim 7$ Mpc. However, within the inner 3 Mpc, there is a clear increase (decrease) in the red fraction (star-forming fraction). Also, for the lowest stellar mass galaxies, their red fraction has increased by a factor of 2 from $z \sim 0.3$ to $z \sim 0.2$ (over 1 Gyr), and yet we do not detect any difference between the star formation properties of the star-forming galaxies in clusters at all radii and that in the field. This suggests that for the low mass galaxies, it is likely that a mechanism that truncates star formation rapidly (within 1 Gyr) is at work. In the outskirts of the clusters, despite the low density contrast with the field, the red fraction is still higher than that in the field, suggesting that those galaxies have had their star formation quenched relative to the field population, supporting the pre-processing scenario.

Acknowledgements

I would like to thank my supervisor, Michael Balogh, for his guidance and patience over the course of the last five years. Michael has always been available for help, always made me feel welcomed, and just has a way of explaining things clearly. I really enjoyed working with him. I would also like to thank David Gilbank, whose presence, since he joined the team three years ago, has been a great benefit in many areas: from understanding the big picture all the way to carrying out technical details, not to mention getting me ready for my first solo observing run. I very much appreciate all his help and encouragement. I would also like to thank Mike Hudson, Brian McNamara and James Taylor for their numerous useful discussions, as well as thank Anthony Gonzalez and Mathew Scott for being on my committee. My thanks also go out to David Patton for getting me started on the path to Astronomy.

Thank you to Sean McGee for being good company and for the cheering (and teasing) along this journey. I would also like to thank various other people in the Astronomy group, especially Carolyn McCoey, Chad Greene, Clif Kirkpatrick, Farbod Kamiab, Robbie Henderson, Gopika Krishnan Sreenilayam, and Mina Rohanizadegan. I also thank Goat for the help on grammar issues. Thanks also goes to all my good friends outside the Astronomy circle, who have made life very interesting—you know who you are.

Further, I would like to express my gratitude for all the support from my parents all these years. I have also enjoyed the friendship from my friends back home. A special thanks goes to Xiaomei—thanks for being the best friend ever.

Contents

List of Tables **ix**

List of Figures **xii**

1 Introduction **1**

1.1 Background 1
1.2 Galaxy Formation 2
1.3 Modelling of Galaxy Formation 3
1.4 Global Evolution of Star Formation 6
1.5 Basic Properties of Clusters 7
1.6 Cluster Detection 7
1.7 Observations of Quenching in Clusters 9
1.8 Environmental Quenching 10
1.9 The Infall Regions 11
1.10 This Thesis 13

2 Red-sequence Luminosity Function **15**

2.1 Introduction 15
2.2 Data 16
2.2.1 The Survey 16
2.2.2 Photometry 17
2.2.3 Star-Galaxy Separation 18

2.3 Cluster Detection . . . 22
2.3.1 Model CMD . . . 22
2.3.2 Subsamples in each Colour Slice . . . 24
2.3.3 Significance Map and Detection . . . 26
2.3.4 Refinements to the Cluster Catalogue . . . 26
2.4 Cluster Properties . . . 30
2.4.1 Richness . . . 30
2.4.2 Mass Estimates . . . 33
2.4.3 Redshift Accuracy . . . 35
2.5 Local Comparison Sample . . . 37
2.6 Luminosity Function Construction . . . 37
2.7 Results . . . 41
2.7.1 Red-sequence Luminosity Functions . . . 41
2.7.2 Red-sequence Dwarf-to-Giant Ratio (DGR) . . . 47
2.8 Discussion . . . 51
2.8.1 Comparison with Literature . . . 51
2.8.2 The Relation between Red Galaxies and Passive Galaxies . . . 54
2.8.3 Possible Systematics . . . 55
2.9 Conclusions . . . 60

3 Star Formation Rate from Cluster Cores to Outskirts 62
3.1 Introduction . . . 62
3.2 Data . . . 63
3.2.1 Optical Data . . . 63
3.2.2 GALEX Data . . . 64
3.2.3 Cross-matching Catalogues . . . 67
3.3 Analysis . . . 71
3.3.1 Background Subtraction . . . 71
3.3.2 k-corrections . . . 72

3.3.3 Star Formation Rate . . . 75
3.3.4 Stellar Mass . . . 76
3.3.5 Field Sample . . . 76
3.4 Results . . . 76
3.4.1 Luminosity Function . . . 76
3.4.2 SSFR vs. Stellar Mass . . . 78
3.4.3 Star-forming Fraction . . . 82
3.4.4 Red Fraction . . . 82
3.5 Discussion . . . 85
3.5.1 Implication from the Red Fraction . . . 85
3.5.2 Model Star Formation Histories . . . 86
3.6 Conclusions . . . 88

4 Structures out to the Accretion Zone **89**
4.1 Introduction . . . 89
4.2 Imaging Data . . . 90
4.3 Photometrically Identified Structure . . . 91
4.4 Spectroscopy . . . 94
4.4.1 Observations . . . 94
4.4.2 Data Reduction . . . 94
4.5 Results . . . 96
4.5.1 Dynamics . . . 96
4.5.2 Colour Distribution . . . 100
4.5.3 Mass Estimate . . . 102
4.6 Discussion . . . 109
4.6.1 Dynamical State of the Main Cluster . . . 109
4.6.2 A possible filamentary connection . . . 113
4.7 Summary . . . 115
4.8 Future . . . 117

5 Conclusions and Future Work **119**

APPENDICES **122**

A **123**

A.1 Redshift Completeness, Success Rate and Efficiency 123

A.2 Redshift Uncertainty 123

A.3 Sample Spectra 127

Bibliography **147**

List of Tables

2.1 Total area covered by the Wide survey and area used in this work. 17

2.2 Model m^* and colour at m^* as a function of redshift. 24

2.3 Best-fit parameters of the LFs of our cluster sample constructed using method Red_4σ. Bracketed values are fixed from the lowest redshift bin. 47

List of Figures

1.1 Different between the distribution of luminous and dark matter 5

2.1 Central surface brightness and completeness vs. magnitude in g' and r' . . 19
2.2 $(g' - r')$ and $(r' - i')$ colour uncertainty vs. r' and i' magnitude 20
2.3 Half-light radius vs. magnitude for star/galaxy separation 21
2.4 Location of 4000Å break at different redshifts in CFHTLS filters 23
2.5 Model $(g' - r')$ vs. r' in CFHTLS filters 25
2.6 Evolutionary tracks of $(g' - r')$ vs $(r' - i')$ 27
2.7 Stacked CMDs in $(g' - r')$ vs. r' and $(r' - i')$ vs. i' 28
2.8 Correlation between N_{red,m^*+2} (r <0.5 Mpc) and the number of cluster members within r_{200} of MaxBCG clusters 31
2.9 CMD of Abell 0362 before background subtraction 32
2.10 Cumulative surface density of the clusters as a function of N_{red,m^*+2} 34
2.11 Angular correlation function of our clusters 36
2.12 Photometric redshift of our clusters vs. their spectroscopic redshift 38
2.13 Redshift distribution of clusters in our sample 39
2.14 Composite CMDs, and best-fit subtracted CMDs 42
2.15 Composite $r'-$band red-sequence LFs constructed with four methods . . . 43
2.16 Background-subtracted red-sequence LFs with k-correction and $(k + e)$-correction 46
2.17 $r'-$band red-sequence LFs at different redshifts, passively evolved to $z = 0.2$ 48
2.18 Red-sequence DGRs as a function of look-back time and redshift 50
2.19 Comparison of our red-sequence LFs with those in the literature 53

3.1 Current GALEX NUV coverage over the four CFHTLS wide fields 65
3.2 An example of the regions with residual elevated background in GALEX NUV images 66
3.3 The standard deviation of the magnitude differences of duplicate objects measured from overlapping regions in GALEX NUV images, as a function of NUV magnitude. 68
3.4 Number counts and completeness limit of our GI5 data 69
3.5 $u^* - r'$ vs $NUV - u*$ for cross-matching optical and NUV sources 70
3.6 Spatial distribution of galaxies in the field of view (r<7Mpc) of one example cluster 73
3.7 CMDs of the example cluster 74
3.8 NUV luminosity function of stacked clusters within the central 1 Mpc . . . 77
3.9 SSFR vs. stellar mass of our stacked clusters 79
3.10 Ensemble average SSFR vs. r 80
3.11 Distribution of the SSFR 81
3.12 Fraction of star-forming galaxies 83
3.13 Fraction of red galaxies 84
3.14 $(FUV - g')$ vs. $(u' - g')$ colour 87

4.1 The spatial distribution of galaxies around RX J1347-1145 93
4.2 Spatial distribution of the large-scale structure with the surface density contours of red galaxies overlaid 95
4.3 Redshift distribution of galaxies around RX J1347-1145 97
4.4 Rest frame velocity offset 99
4.5 CMD of galaxies in each targeted pointing 101
4.6 Deprojected mass profile for RX J1347-1145 103
4.7 Weak-lensing signal-to-noise map, with contours of surface density of red galaxies 106
4.8 Tangential distortion as a function of the distance from the cluster center . 107
4.9 The projected mass as a function of radius for RX J1347-1145. The solid hexagons are estimates from this work, and the other symbols are from the literature. See text for details. 108

4.10 Spatial distribution of galaxies in the centre of RX J1347-1145 111
4.11 Rest-frame velocity offset of galaxies around two simulated clusters 116
4.12 Spatial distribution of galaxies around RX J1347-1145 and Cl0024 118

A.1 Completeness of spectroscopic follow-up and success rate for red galaxies . 124
A.2 Completeness of spectroscopic follow-up and success rate for blue galaxies . 125
A.3 Distribution of the difference in redshift or rest-frame velocity for galaxies with repeated observations 126
A.4 Distribution of the difference in redshift and rest-frame velocity for common objects between our sample and the sample of Cohen & Kneib (2002) . . . 127
A.5 Example spectra 128

Chapter 1

Introduction

1.1 Background

Great progress has been made in the last century towards understanding the composition of our Universe and how it came to be the way it is today. The discovery (by Penzias and Wilson in 1965) of the cosmic microwave background (CMB) strongly supported the Big Bang Model, according to which the Universe started in a hot and dense state, and has been expanding and cooling ever since. This model naturally explains the largely isotropic microwave background we see today. Subsequent observations from the Cosmic Background Explorer (Mather et al., 1990; Smoot et al., 1991; Bennett et al., 1992) and the more recent Wilkinson Microwave Anisotropy Probe (Bennett et al., 2003; Komatsu et al., 2003, 2009; Larson et al., 2010), together with other measurements from, for example, supernovae (Knop et al., 2003), galaxy clustering (Cole et al., 2005), and gravitational lensing (Contaldi et al., 2003), all point to a cold dark matter model. In this model, we live in a flat Universe that is dominated by non-luminous components. About 72 per cent of the energy in today's Universe is in a form called dark-energy. It is the component that keeps the Universe expanding, but the nature of it remains unclear. The normal baryonic matter we can see only makes up about 5 per cent of today's Universe, and the matter we cannot see, the so called dark-matter, makes up the rest of the $\sim$23 per cent.

Even though we cannot see the dark matter directly, its influence on the luminous matter around it was detected a long time ago. For example, as early as the 1930s, Zwicky (1933) showed that the measured velocity dispersion of galaxies in a galaxy cluster (we will describe the properties of galaxy clusters in Section 1.5) requires more mass than that from the luminous matter alone. Further, in the 1970s, measurements of the rotational speed of stars in disk galaxies by, e.g. Rubin & Ford (1970); Rubin et al. (1978); Clemens (1985), showed that the rotation curve is flat at large radii. This is not the expected behavior if

luminous matter is the only source of mass, in which case the curve should fall off with increasing radius at large radii. Instead, more mass is needed to produce the constant rotation curve.

Although initially the Universe was largely homogeneous and isotropic, there were small scale fluctuations, with some regions being slightly overdense and others underdense. The overdense regions collapse under gravity, and keep attracting more matter with the growing gravitational potential. This process gives rise to the structure we see today.

The evolution of the dark matter is relatively straightforward because only gravity is at work. In comparison, the formation of the luminous matter–stars and galaxies–involves much more complicated physics. As dark matter halos collapse, the baryonic gas falling into the potential well gets shock heated to the virial temperature. If the gas can radiate away its energy quickly enough, it will condense and form galaxies. Under this general picture, there are still many aspects of the formation of galaxies that we do not understand, as we will see with the proceeding of this thesis. Below we discuss some important aspects of galaxy formation.

1.2 Galaxy Formation

It has been known that galaxies we see today have a wide range of properties in terms of, for example, morphology, colour, and star formation history. In terms of morphology (Hubble, 1936), some galaxies are dominated by a bulge component (usually referred to as early-type or elliptical galaxies), while others have both a bulge and a prominent disk components (late-type or spiral galaxies), and some are in between (S0 or lenticular). There seems to be a correlation, although with scatter (Bernardi et al., 2006), between morphology and colour and star formation, in the sense that bulge dominated galaxies tend to be redder with low star formation activity, while disk dominated galaxies tend to be bluer with more active star formation.

Many theories have been proposed to explain the evolution of the galaxies. In the very early days, a process of "monolithic collapse" was proposed by Eggen et al. (1962) to explain some of the observations of our own galaxy. In this scenario, a single large cloud of gas collapses and forms the bulk of the stars on a short time scale. However, this theory is unable to explain many other observations such as the retrograde orbits of some of the stars. Another scenario, which has become standard, is the bottom-up scenario, originally proposed by White & Rees (1978). In this framework, small structures form first, then merge to form larger structures. During the merger, the disk of galaxies can be destroyed and the end product will be an elliptical galaxy (Barnes & Hernquist, 1992; Mihos & Hernquist, 1996; Cretton et al., 2001).

It appears that the stellar population in elliptical galaxies is very uniform. This was first supported by the observations that early type galaxies exhibit a very tight correlation between colour and magnitude, with brighter ones being redder, as noticed in the early studies by Visvanathan & Sandage (1977); Sandage & Visvanathan (1978a,b). In a later study, Bower et al. (1992) showed that the bulk of the stars in elliptical galaxies is formed early, prior to $z \sim 2$. Note that this does not contradict the hierarchical formation scenario, in which more massive structures form later. In contrary, it fits in well with the picture that mergers of disk galaxies at high redshift result in elliptical galaxies and the stellar population evolves passively afterwards. Continuous star formation is prevented through some feedback processes, as discussed in Section 1.3.

Note that the slope of this tight correlation of early-type galaxies (usually referred to as the red-sequence) could be due to either metallicity or/and age, which is called the age-metallicity degeneracy (Worthey, 1994). The study by Kodama & Arimoto (1997) showed that the slope of the red-sequence has little evolution with redshift, which cannot be explained if age is the dominating factor, and thus concluded that metallicity dominates the sequence. Nonetheless, some age variations are also detected along the sequence (e.g. Trager et al., 2000; Smith et al., 2006; Allanson et al., 2009).

The tight red-sequence of early-type galaxies is the root of cluster detection techniques that utilise optical colours, as we will discuss in Section 1.6.

1.3 Modelling of Galaxy Formation

One powerful way of gaining understanding of the growth of large-scale structure and the evolution of galaxies with it is through modelling. Once the initial condition and cosmological parameters are set, the evolution of the dark matter can be modelled very well with N-body simulations, because the evolution is determined entirely by gravity. So far, the largest N-body simulation is the Millennium Simulation, carried out at the Max-Planck-Institute (Springel, 2005). It simulates the evolution of 10^{10} particles from $z = 127$ to $z = 0$ in a box with the size of $500h^{-1}$ Mpc. Within these dark matter halos, semi-analytic models (described below) can be implemented to model the formation of galaxies.

In comparison, modelling the formation and evolution of galaxies is far more complicated, due to the various complex physical processess involved that are not well understood, such as the efficiency of gas cooling (and thus the efficiency of star formation), and the recycling of the material from the previous generations of stars. Two main approaches have been used. One is direct numerical simulation, in which hydrodynamics equations that describe the gas dynamics are solved numerically (e.g. Katz et al., 1992; Evrard et al., 1994; Navarro & Steinmetz, 1997). However, this method is limited by the resolution

one can reach within finite computing time. The other approach is called "semi-analytic" modelling. In this approach, prescriptions with simplified assumptions of various physical processes involved in the star formation are pasted onto the dark matter simulations (e.g. White & Frenk, 1991; Kauffmann et al., 1993; Cole et al., 1994, 2000; Baugh et al., 2005; Croton et al., 2006; Bower et al., 2006; Benson & Bower, 2010).

One important development in the semi-analytical modelling is the implementation of the "feedback", which is required to explain the observed shape of the luminosity function (number of galaxies as a function of luminosity). The luminosity function of the luminous matter has a cut-off at the bright end, and has a slow increase at the faint end. This is different from the distribution of dark matter halos, in the sense that high and low mass halos are relatively under-occupied by galaxies (see Figure 1.1 for an illustration, taken from Benson et al. 2003). Since galaxies form when gas in the halo cools, this discrepancy means the efficiency of forming stars is suppressed in these high and low mass halos. So the question is: why? For the low mass systems, the inclusion of supernova feedback (Cole et al., 2000; Benson et al., 2003) and photoionization heating (Efstathiou, 1992) suppresses the cooling of the gas, and alleviates the problem at the faint end. However, these processes are too weak to prevent star formation in the more massive halos. Therefore, some stronger energy source is needed. One popular mechanisms is the active galactic nucleus (AGN) feedback, where the energy from the AGN reheats (or expels) the gas. This mechanism is evoked to explain the absence of big blue central galaxies in clusters, which would form if gas can keep cooling down to the centre. Semi-analytical models that implement the AGN feedback are able to reproduce the shape of the bright end of the luminosity function (Croton et al., 2006).

With these feedback processes included, semi-analytical models have been able to successfully reproduce many observed galaxy properties, such as the bimodality of the colour distribution. However, there are also observations that the models fail to reproduce. For example, models predict too many red galaxies in galaxy groups and clusters (more in Section 1.8), which indicates there is still a problem in our understanding of the quenching of star formation.

One important ingredient of the modelling of galaxy formation is the stellar population synthesis model. This was originally proposed by Tinsley & Gunn (1976). Assuming some initial mass function (the distribution of masses stars are born with), and star formation history, the stars are evolved according to theoretical and empirically calibrated evolutionary tracks. With this, the composite stellar population of galaxies can be constructed, and the spectral energy distribution of the galaxies can be extracted at any age (redshift). Convolving this with the response curves of different filters, the observed properties such as the colour and magnitude of galaxies can be obtained, at any redshift. The most uncertainty in the synthesis model lies in the treatment of the asymptotic giant branch (AGB) and post-AGB stars. Over the years, many stellar synthesis models have been developed

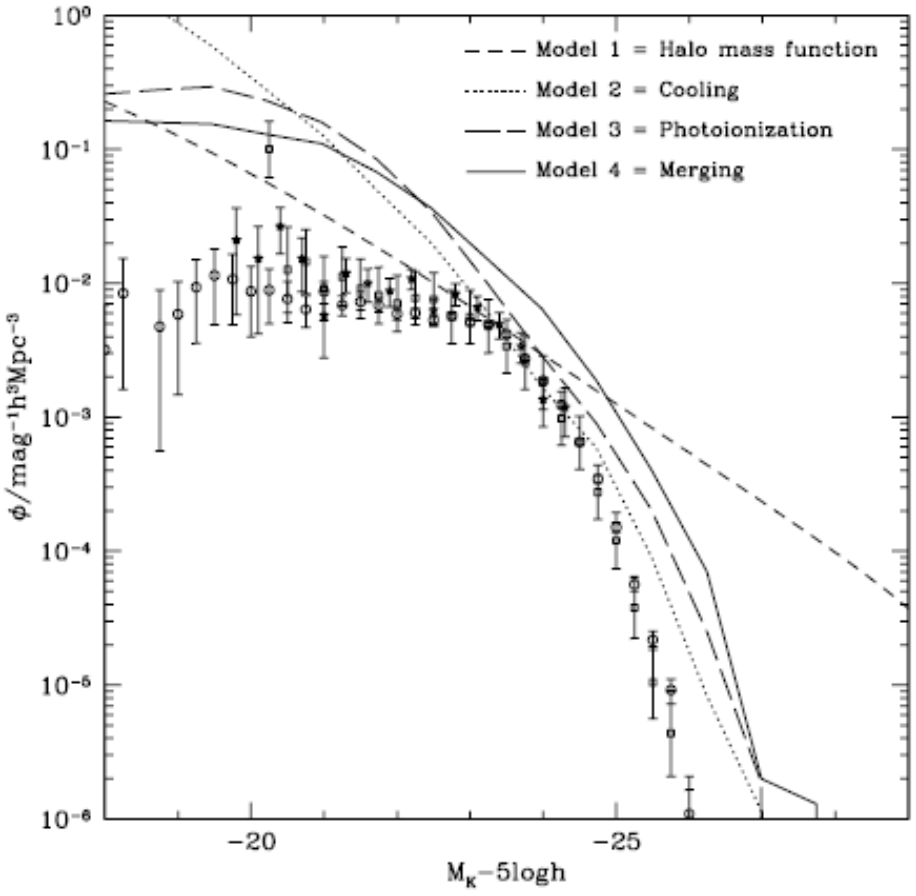

Figure 1.1: Fig. 1 from Benson et al. (2003), which shows the difference between the shape of the distribution of the luminous matter (different symbols), and that of the dark matter (short dashed straight line). The other lines represent models including various physical processes, as described in the legend, in an attempt to reconcile the shapes.

with various improvements (e.g. Bruzual A., 1983; Arimoto & Yoshii, 1986; Buzzoni, 1989; Bruzual A. & Charlot, 1993; Charlot & Longhetti, 2001; Bruzual & Charlot, 2003; Maraston, 2005; Vazdekis et al., 2010). In the study presented in Chapter 2, we use the model by Bruzual & Charlot (2003) to predict the colour of red-sequence galaxies at different redshifts.

1.4 Global Evolution of Star Formation

We have also learned a great deal about the evolution of the global star formation rate in the Universe. Early studies (e.g Lilly et al., 1996; Madau et al., 1996) have showed that the star formation rate density peaked at about $z \sim 1-2$, and has decreased by a factor of ~ 10 since then. This decrease spans all stellar mass ranges down to less than $10^9 M_{\odot}$ (Gilbank et al., 2010). Furthermore, it appears that the contribution to the star formation rate density is shifting from more massive galaxies to lower mass ones with decreasing redshift (e.g. Cowie et al., 1996; Cowie & Barger, 2008; Damen et al., 2009).

Considering just the actively star-forming galaxies, their star formation rate has been decreasing with redshift (Noeske et al., 2007), and this is accompanied by an increase in the number of passive galaxies (Pozzetti et al., 2009). The study by Bell et al. (2007) showed that, if the stars formed in blue galaxies since $z \sim 1$ were to stay in blue galaxies, their stellar mass today would be overproduced, which indicates a transformation of blue galaxies onto the red-sequence. This is consistent with the study by Bell et al. (2004), where it was shown that the stellar mass of the red-sequence galaxies has increased by a factor of ~ 2 since $z \sim 1$.

The origin of this global decline of star formation activity remains unclear. On one hand, it could be due to processes that are internal to galaxies, such as the consumption of gas, or the supernova and AGN feedback that prevent stars from forming. On the other hand, it could also be due to some mechanisms related to the hierarchical growth of structure. Among the various possible processes, the role environment (ranging from voids to superclusters) plays in quenching star formation is especially uncertain. The goal of this thesis is to gain more insight into this, by looking at galaxies in large samples of clusters and their surrounding structures. Note, although only a small fraction of the galaxies reside in the cores of galaxy clusters, evidence (see Section 1.7) has started to indicate that the influence of the environment starts before galaxies reach the very central regions, which means it could have a profound influence on the global star formation rate.

Since the focus of this thesis is on galaxy clusters, in the following sections, we first introduce the basic properties of galaxy clusters, and how they can be detected. Then we will discuss observational evidence of the quenching of the star formation in clusters. In

the last part of this introduction, we will describe the specific projects that are presented in this thesis.

1.5 Basic Properties of Clusters

There is a range of environments in which a galaxy may reside. The lowest density regions are the voids, where galaxies are relatively isolated. The intermediate environment is galaxy groups, which usually consist of a few to tens of large, gravitationally bound galaxies. Galaxy clusters represent the densest and largest virialised structure in the Universe, and they grow by accreting galaxies from the field (e.g. Lacey & Cole, 1993). Typical rich clusters consist of hundreds of massive galaxies, and the space between them is filled with hot, X-ray emitting gas ($T \sim 10^8 K$) (Mitchell et al., 1976). The total mass (mostly dark matter) function of different structures is continuous, but typically halos that have mass greater than about $10^{14} M_\odot$ are considered clusters. The mass can be estimated in several ways, such as through the velocity dispersion of its member galaxies, the caustic technique, weak lensing and X-ray analysis. Some details are discussed in Chapter 4.

The typical virial radius, within which galaxy orbits are in virial equilibrium (of course this does not apply to clusters that are not dynamically relaxed yet, e.g. in the process of merging), is about $\sim 1 - 2$ Mpc. The influence of a cluster can go far beyond the virial radius, out to $\sim$10 Mpc, where the density decreases to that similar to the field. As seen in simulations such as the Millennium Simulation, around clusters there are large-scale structures of filaments and sheets, and galaxies and groups of galaxies fall into clusters along these structures. Therefore, this accretion zone is of particular interest, as we will see below.

1.6 Cluster Detection

Because of the above described properties, there are several ways that clusters can be detected, at different wavelengths. We will discuss some of the most common ones briefly in this section.

In the early days, the first homogeneous cluster catalogue was constructed by Abell (1958), by visually examining the overdensity of galaxies on Palomar Observatory Sky Survey photographic plates. With the development of new devices and thus large digitized surveys, more advanced techniques have been developed. For example, Postman et al. (1996) developed a "matched-filter" method, which searches for clusters by filtering data with a model that describes the luminosity and spatial distribution of galaxies in a cluster. Subsequent studies have made various variations and improvements over the original

matched-filter method (e.g. Gilbank et al., 2004; Olsen et al., 2007; Grove et al., 2009; Milkeraitis et al., 2010).

More recently, the Red-sequence Cluster Survey (RCS) (Gladders & Yee, 2000; Yee et al., 2007), designed to search for galaxy clusters, was carried out on the Canada-France-Hawaii Telescope (CFHT). It covers ∼1000 square degrees of the sky, in three passbands. The idea behind this technique is that in the core of every rich cluster, there is a tight red-sequence in the colour and magnitude distribution of galaxies. Therefore, looking for a spatial overdensity of galaxies that are on the red-sequence effectively reduces the background contamination. Most of our studies presented in this thesis are based on a large sample of galaxy clusters we detected from the CFHT Legacy Survey (CFHTLS, more in Section 1.10) using a method based on this technique, with modifications.

Several cluster catalogues have been constructed, using different methods, out of the Sloan Digital Sky Survey (SDSS), a five-band imaging and spectroscopy survey (York et al., 2000). One of them is the C4 algorithm (Miller et al., 2005), which uses four colours, redshift, and position information to look for overdensities of galaxies. Another is the MaxBCG method (Koester et al., 2007). This method uses the fact that most rich clusters have a brightest cluster galaxy (BCG) sitting at the centre, and thus they evaluate the likelihood of a galaxy being a BCG through its colour and magnitude and its local density. Another commonly used group/cluster finder is call the Friends-of-Friends algorithm, which has been applied with different modifications by Weinmann et al. (2006a) and Yang et al. (2007).

The above mentioned optical surveys all require deep imaging. A noval technique that requires only shallow imaging was developed by Dalcanton (1996) and implemented in the Las Campanas Distant Cluster Survey (Gonzalez et al., 2001). The idea behind this technique is to look for excess of integrated light of cluster galaxies that are not individually detected.

In addition to these optical cluster detection techniques, the hot X-ray emitting gas in galaxy clusters provides another way of detecting them. Many clusters have been found this way from X-ray surveys carried out with the *ROSAT* satellite (Voges et al., 1999; Böhringer et al., 2000; Ebeling et al., 2001) and more recently with *XMM-Newton* and *Chandra* (Romer et al., 2001; Green et al., 2004; Pacaud et al., 2007). In fact, one of the clusters which we will study in detail in Chapter 4, is the most X-ray luminous cluster known, discovered by the *ROSAT* satellite.

Further, clusters can be detected through the Sunyaev-Zel'dovich (SZ) effect (Sunyaev & Zeldovich, 1972) , which refers to the distortion in the observed CMB spectrum due to the scatter of the CMB photons passing through the hot intracluster medium (Vanderlinde et al., 2010). Weak lensing, which measures the distortion of distant galaxies due to the concentration of mass of galaxy clusters is also a viable way of detecting clusters (Wittman

et al., 2001, 2006; Gavazzi & Soucail, 2007). At high redshift $z \gtrsim 2$, many radio galaxies reside in overdensity regions, and thus searching around radio galaxies is another way of detecting (proto)clusters (e.g. Miley & De Breuck, 2008).

Each detection technique has its own advantages and drawbacks. Optically selected clusters are prone to the projection effect, where two groups of galaxies projected along the line-of-sight would be considered as one rich cluster. These two scenarios would be hard to distinguish without follow-up spectroscopy. According to the estimate from the RCS cluster sample, contamination from projected systems is about 5 to 10 per cent over $0.4 < z < 1$ (Gilbank et al., 2008). In comparison, X-ray detection does not suffer as much from the projection effect. However, it is difficult to pick out X-ray underluminous clusters (either intrinsically or below the detection limit), and thus would bias the sample.

1.7 Observations of Quenching in Clusters

As discussed in Section 1.5, galaxy clusters represent the largest gravitationally bound structures and the densest environments in the Universe. In this section, we describe some of the observations related to clusters in the literature.

The early study by Dressler (1980) using 55 rich clusters ($z < 0.06$) found a correlation between the morphology of the galaxies and their local density, in the sense that there are more early type galaxies in high density regions (such as the core of galaxy clusters than that in low density regions. Since then, with the advent of large surveys such as SDSS (**?**), 2dF Galaxy Redshift Survey (Colless et al., 2001), and CFHTLS, it has been well established that in the core of today's galaxy clusters there are more galaxies with redder colours and lower average star formation rates, relative to the field (Gómez et al., 2003; Balogh et al., 2004a; Weinmann et al., 2006a; Haines et al., 2006).

A lot has been learned about the evolution of galaxy clusters over the years. In the 1970s, Butcher & Oemler (1978) found that two clusters at $z \sim 0.4$ have a higher fraction of galaxies with blue colours when compared to local clusters. This is now referred to as the Butcher-Oemler (BO) effect, and was soon confirmed with a larger sample in their subsequent study (Butcher & Oemler, 1984).

Since the discovery of the original BO effect, subsequent studies have found different flavors of the BO effect. For example, Couch & Sharples (1987) found that there are more galaxies with strong Balmer lines in their spectra (indicating truncation of star formation) at higher redshift. This is termed by Kodama & Bower (2001) as the spectroscopic BO effect.

In terms of the morphology, since the study by Dressler (1980), the morphology-density relation has been found to be in place out to $z \sim 0.5$ (Couch et al., 1994; Dressler et al.,

1997; Couch et al., 1998; Smail et al., 1997) and even to $z \sim 1$ (Smith et al., 2005). These studies also showed that in general the fraction of early-type galaxies decreases with redshift, which is referred to as the morphological BO effect by Kodama & Bower (2001).

The different forms of the BO effect are clearly related to each other, but its origin is still debated (see next section). Nonetheless, they indicate that star formation in clusters is decreasing with time. It is worth pointing out that this decrease is not a cluster specific phenomenon, because the global star formation rate is declining as well (as discussed in Section 1.4). However, a careful comparison by Kodama & Bower (2001) showed that, although the star formation activities in both clusters and the field are declining since $z \sim 1$, the decline in cluster cores is faster than that in the field.

It has become clear that a key parameter that decides the colour or star formation rate of a galaxy is its stellar mass. The study by Kauffmann et al. (2003) showed that galaxies with stellar mass above $3 \times 10^{10} M_{\odot}$ tend to be older, and those with lower stellar masses are younger. Therefore, it is important to point out that the lower star formation rate in clusters is not entirely due to the domination of massive galaxies in clusters (Baldry et al., 2006); as showed for example by Kimm et al. (2009), at a fixed stellar mass, there is still a higher fraction of passive galaxies in clusters relative to the field.

From studying the passive population alone, a lot can be learned about the quenching of star formation. There have been many studies on the build-up of the red-sequence galaxies (especially the faintest or lowest–mass galaxies) in the inner region of clusters in the literature. Yet, the results are controversial. Some studies found a significant deficit of faint red-sequence galaxies in high redshift clusters, relative to that in low redshift clusters. This favors a scenario in which low mass galaxies have their star formation shut off and move onto the red-sequence at $z \lesssim 1$ (De Lucia et al., 2007; Stott et al., 2007; Gilbank et al., 2008). Other studies found no evolution of the faint-end of the red-sequence since $z \sim 1.3$, implying the build-up was complete by $z \sim 1.3$ (Andreon, 2008; Crawford et al., 2009). This is the focus of one of the projects presented in this thesis.

As described before, in the hierarchical galaxy formation model, clusters grow by accreting galaxies from the field (e.g. Lacey & Cole, 1993). Therefore, the difference between the galaxy properties in the field and clusters indicates that there has to be some transformation. In the following section, we describe several popular mechanisms that have been proposed.

1.8 Environmental Quenching

As mentioned before, in galaxy clusters the space between galaxies is filled with hot X-ray emitting gas. Therefore, the cold gas in the disk of a galaxy can be stripped by the pressure

felt by the galaxy when travelling through the dense intracluster medium, thus shutting off star formation. This process is referred to as ram-pressure stripping as proposed by Gunn & Gott (1972). A more gradual process is starvation or strangulation (Larson et al., 1980). The study by Larson et al. (1980) showed that star formation is sustained by gas falling into a galaxy from a surrounding envelope. Therefore, if this loosely bound halo gas is stripped away, there is no fuel available for replenishment, and star formation will cease after the cold gas that is already in the disk is consumed. Other popular mechanisms include harassment (Moore et al., 1996) and tidal stripping (e.g. Fujita, 1998).

There has been lots of debate on the effectiveness of these different processes. The direct observation of the stripped HI region by e.g. Kenney et al. (2004) supports the ram-pressure scenario. However, this requires a very dense intracluster medium and high galaxy velocities, and thus is not likely to be effective outside the cores of clusters. Whether or not galaxies go through a star-bursting phase triggered by cluster specific mechanisms is also debated. Many groups have suggested that the cluster environment triggers a star-bursting phase and thus the gas is exhausted quickly this way (e.g. Barger et al., 1996; Poggianti et al., 1999). While other studies such as Balogh et al. (1999) and Morris et al. (1998) did not detect a larger number of galaxies with starburst relative to the field, and suggest the cluster environment is not particularly effective in inducing starbursts. Instead, the cessation of star formation is more likely to be a gradual process. Another possible scenario is that the burst happens earlier, within infalling groups (Tran et al., 2009).

Galaxy formation models (e.g. Bower et al., 2006) that assume the hot gas associated with the galaxies' parent dark matter halos is stripped immediately once they enter the group or cluster environment fail to reproduce certain observed properties, such as the fraction of red galaxies in groups and clusters (Weinmann et al., 2006a; Baldry et al., 2006). Revised models with reduced stripping efficiency that allow galaxies to retain some gas still fail to reproduce the observed colour distribution of cluster galaxies (e.g. Font et al., 2008). This indicates a fundamental problem in our understanding of the physics that happens in dense environments. Therefore, we need further observations to constrain model parameters.

1.9 The Infall Regions

It has become clear that the low star formation rate of cluster galaxies is not restricted to those in the cluster cores. Studies by e.g. Balogh et al. (1997, 1998); Lewis et al. (2002) showed that the star formation rate is suppressed relative to the field beyond ~ 2 virial radii. Also, various studies have found a low star formation rate and a high fraction of early type galaxies in groups (Jeltema et al., 2007; Wilman et al., 2008; McGee et al., 2008; Balogh et al., 2009) Those studies detect a change in the fraction of star-forming galaxies

as a function of distance from cluster centres, but the change in star formation rate of the star-forming galaxies themselves has not been detected. A recent study by Peng et al. (2010) showed, using the SDSS data, that the specific star formation rate of star-forming galaxies is the same in the lowest and highest density regions.

It has been proposed by several studies (e.g. Zabludoff & Mulchaey, 1998; Balogh et al., 2000; Gonzalez et al., 2005) that galaxies might be "pre-processed", meaning the quenching of star formation starts long before galaxies reach the core of clusters. Recently, Balogh & McGee (2010) used a sample of groups and clusters from the SDSS and found a very small intrinsic scatter in the fraction of passive galaxies. This cannot be explained if the quenching starts after galaxies are accreted onto the clusters. Instead, this requires that the quenching starts in halos that have mass less than $\sim 10^{13} M_{\odot}$.

Simulations have shown that clusters are surrounded by large-scale structures such as filaments and sheets, and galaxies are accreted mainly along these structures (Bond et al., 1996; Colberg et al., 1999). These accretion zones are where galaxies reside before they reach the cluster cores, and thus might be an attractive candidate for where the transformation of galaxies happens. However, studying the infall regions of clusters is very difficult. Because of the low density contrast with the foreground/background field, photometric study is only possible by stacking a very large number of clusters. For the same reason, the current spectroscopic studies on the infall regions are limited by sparse sampling and small sample size.

The Panoramic Imaging and Spectroscopy of Cluster Evolution with Subaru (PISCES) project, taking advantage of the wide-field of view of the Subaru Telescope (Iye et al., 2004), was designed to study distant clusters out to large radius from the cluster centres (Kodama et al., 2005). In an early study, Kodama et al. (2001) traced large-scale structures around a cluster at $z \sim 0.4$ out to > 5Mpc using photometric redshifts, and they found a sharp transition of colour in a local density that corresponds to subclumps along the filamentary structures. In a subsequent study, Tanaka et al. (2006) spectroscopically confirmed the large-scale structure around a high redshift cluster at $z \sim 0.8$, and showed that the composite spectra of galaxies in clumps in the outskirts and those in the field show strong Balmer absorption, indicating recent star formation activity.

Galaxy groups in the infall regions are particularly interesting. The recent study by McGee et al. (2009) suggests that a large fraction of galaxies that accrete onto clusters are in groups (but see Berrier et al., 2009). Therefore, as we will describe in the following section, in the project presented in Chapter 4 of this thesis, we will introduce a detailed study of two contrasting clusters, focusing on groups in the outskirt regions.

1.10 This Thesis

It is the goal of this thesis to look into some aspects of the transformation of galaxy properties with the growth of large-scale structure, over the last 5 billion years. We do this by examining the passive and star-forming galaxies in a large sample of clusters, and groups in the outskirt regions of two contrasting clusters. In this section, we first give more description on the data used in these projects, and then outline the structure of the thesis.

Most of our studies here are based on a large sample of clusters at $0.15 < z < 0.35$ we detected from the CFHTLS Wide Survey. The CFHTLS Wide Survey is an ideal choice of data for the science goals we are after here for several reasons: its depth allows us to probe low-mass galaxies; its photometry in u^*, g', r', i', z' filters allows using multi-colour information to reduce background (more on this in Chapter 2); its overlap with other surveys allows multi-wavelength studies; it covers a large area that provides large samples of clusters; and its high image quality will enable future morphology studies. In addition to the optical data, we obtained GALEX NUV coverage over the whole legacy fields. With these data, we will examine the properties of the star-forming galaxies in those clusters, and the number of star-forming galaxies relative to the passive ones as a function of radius.

In another project, we study in detail the structures around the most X-ray luminous cluster known, RX J1347-1145. We detected photometrically, using wide-field imaging data obtained with MegaCam, an elongated large-scale structure going through the cluster core, and followed it up with spectroscopic observations. This interesting structure leads to a future project, where we will spectroscopically identify groups in and outside the structure, and compare their properties with that in a cluster at a similar redshift but with no obvious surrounding large-scale structure. We will also compare those groups with isolated groups in the field, and thus put more constraints on the effect of environment on altering galaxy properties.

In Chapter 2, we present our study on the passive red-sequence galaxies from our CFHTLS cluster sample. This chapter is almost as it is published in the Monthly Notices of the Royal Astronomical Society. This is a multi-author paper, but the only part of the analysis that I did not lead was the calculation of the correlation-function.

In Chapter 3, we present the results on our examination of the actively star-forming population in clusters out to regions well beyond the virial radius. The content of this chapter is the main body of a paper in preparation.

In Chapter 4, we present a study of the dynamics and large-scale structure of RX J1347-1145, using spectroscopic data obtained on the Magellan Telescope, and photometric data on CFHT. The content in this chapter is mostly from a paper that is published in the Monthly Notices of the Royal Astronomical Society. The section regarding the gravitational lensing was the only part I did not lead.

We conclude, and outline some near future work in Chapter 5.

Chapter 2

Red-sequence Luminosity Function

2.1 Introduction

It has been established that the galaxy population today can be broadly divided into two categories: those that have red colours, consisting of mostly non-star-forming galaxies (the 'red-sequence'); and those with blue colours and active star formation (the 'blue cloud'). This colour bimodality can be modelled by a sum of two Gaussian distributions (Balogh et al., 2004a,b; Baldry et al., 2004), and it has been observed out to $z \sim 1$ (Bell et al., 2004). The red population exhibits a tight correlation between colour and magnitude, with brighter galaxies being redder. Due to the age-metallicity degeneracy (Worthey, 1994), the slope of this colour-magnitude relation (CMR) of the red population could be attributed to either an age or metallicity sequence. The study by Kodama & Arimoto (1997) concluded that metallicity variation dominates the slope, because of its relatively slow evolution. Nonetheless, some age variation along the red-sequence is also detected (e.g. Trager et al., 2000; Nelan et al., 2005; Smith et al., 2006; Allanson et al., 2009).

The origin of red-sequence galaxies is still an open question. Studies by Bell et al. (2004) and Faber et al. (2007) concluded that brighter red-sequence galaxies are built up through dry mergers since $z \sim 1$, based on observations that the $B-$band luminosity density of red-sequence galaxies remains constant since $z \sim 0.9$. With the dimming of galaxies, the luminosity density would be overproduced if the number density of red-sequence galaxies remained constant, as in the pure passive evolution scenario. However, other studies by, for example, Cimatti et al. (2006) and Scarlata et al. (2007), showed that the number density of the massive red galaxies remains constant and their luminosity function is consistent with passive evolution. It is the number density of less-massive galaxies that decreases rapidly with increasing redshift, and this can be explained by a gradual quenching of star formation in those galaxies. Therefore, no significant amount of dry mergers are required

to explain the formation of massive red-sequence galaxies. Which of the two proposed scenarios is more important is still not clear.

As to how the faint end of the red-sequence builds up, it is even less clear. Especially in galaxy clusters, different studies have yielded conflicting results. For example, observations by De Lucia et al. (2007), Stott et al. (2007) and Gilbank et al. (2008) found a significant deficit of faint red-sequence galaxies in high redshift clusters, compared to low redshift clusters. This supports a scenario where low mass galaxies have their star formation shut off and move onto the red-sequence recently ($z \lesssim 1$). However, Andreon (2008) and Crawford et al. (2009) found no evolution of the faint-end slope spanning $0 < z < 1.3$, which implies the build-up of the faint red-sequence galaxies was completed by $z \sim 1.3$.

Current galaxy formation models (e.g. Bower et al., 2006) produce too many red galaxies in clusters and groups that are not observed (Wolf et al., 2005; Weinmann et al., 2006a,b; Baldry et al., 2006), indicating a fundamental problem in our understanding of how star formation is quenched in dense environments. More precise observations are needed to resolve this problem.

In this work, we make use of optical imaging data from the Canada-France-Hawaii Telescope Legacy Survey (CFHTLS) data to construct a large sample of 127 clusters and study their red-sequence luminosity functions over the redshift range $0.17 \leq z \leq 0.36$. In §2.2 and §2.3 we describe the data, and the cluster detection algorithm. The properties of our cluster catalogue, and a local comparison sample are described in §2.4 and §2.5. We present our methods for measuring the red-sequence luminosity function and dwarf-to-giant ratio in §2.6, and the results in §2.7. In §2.8 we discuss the comparison with literature and possible systematics, and conclude in §2.9.

Throughout this work, we assume a cosmology with present day matter density parameter $\Omega_m = 0.3$, vacuum energy density parameter $\Omega_\Lambda = 0.7$, and Hubble constant H_o=70 km s^{-1} Mpc^{-1}. All magnitudes are in the AB system unless otherwise specified.

2.2 Data

2.2.1 The Survey

The CFHTLS is a joint Canadian and French imaging survey in u^*, g', r', i' and z' filters using MegaCam, with an approximately 1x1 square degree field of view. We use the "Wide" and "Deep" surveys in this work. The Wide survey covers a total area of 171 square degrees with a total exposure time of about 2500 seconds in g' band, 1000 seconds in r' band and 4300 seconds in i' band per pointing. The Deep survey contains four 1 square degree fields with exposure times ranging from 33 hours in u^* band to 132 hours in i' band.

	W1	W2	W3	W4
Total (sq. deg)	72	25	49	25
Used in this work (sq. deg)	42	20	41	16

Table 2.1: Total area covered by the Wide survey and area used in this work.

The survey started in 2003 and is now complete, but not all data have been processed and released yet. The data we used in this work are from data release T0004 (released internally July 3, 2007). We carry out our cluster detection using the Wide survey data over a total area of 119 square degrees (details summarized in Table 2.2.1), where the photometry in all three of the filters, g', r' and i', is available. We use data from one of the four Deep fields, D1, as auxiliary data to examine surface brightness selection effects (§2.2.2) and other possible systematics (§2.8.3).

2.2.2 Photometry

For our analysis, we are interested in measuring the colours and total magnitudes of galaxies. The photometric catalogue we use was produced by TERAPIX (Traitement Elementaire, Reduction et Analyse des PIXels de megacam). Magnitudes in the catalogue are measured using SExtractor (Bertin & Arnouts, 1996) within different apertures. We take *mag_auto*, where flux is measured within the Kron radius, as the total magnitude of galaxies.

We measure colours of galaxies using magnitudes within a fixed aperture of 4.7 arcsec in diameter. The seeing* of all images in this release is better than 1.3 arcsec, and the typical seeing of each pointing is $\sim$0.94 arcsec in g', $\sim$0.86 arcsec in r' and $\sim$0.81 arcsec in i'. For each pointing, the maximum difference in the seeing of the stacked, single-filter images between g', r' and i' band is less than 0.5 arcsec in the worst case − small compared with the radius of the aperture used to measure the colour. Therefore, we do not convolve the images in different filters to the same seeing. TERAPIX compared the photometry of objects in the overlap regions between the CFHTLS and the Sloan Digital Sky Survey (SDSS) (York et al., 2000), and found that the mean offset in g', r',and i' filters in each individual pointing ranges from ~ 0.01 to ~ 0.05 mag.

The galactic E(B-V) extinction calculated using the Schlegel et al. (1998) dust map is provided in the catalogue for each object. We use the A/E(B-V) values given in Schlegel et al. (1998) in SDSS (York et al., 2000) u, g, r, i, and z filters to calculate the extinction

*defined by TERAPIX as twice the median half-light radius of a selection of point sources on each CCD as measured by SExtractor.

correction and apply this to the observed magnitude. The median extinction in r' band is 0.072 mag in W1, 0.056 in W2, 0.032 in W3 and 0.217 in W4.

Depth and Photometric Uncertainty

To examine how surface brightness might affect the completeness of the sample, we plot the surface brightness for the brightest pixel, μ_{max} (which is a good proxy for the central surface brightness, measured using SExtractor), vs. magnitude for galaxies that are in the overlap region between D1 and W1, as shown in the left column in Figure 2.1. Blue points represent objects in D1 and red points W1. In g' band, at about $g' \sim 25$, W1 starts to become incomplete due to the surface brightness detection limit. To quantify this, we calculate the fraction of sources in D1 that are also detected in W1 as a function of magnitude. As shown in the right column of Figure 2.1, W1 is ~ 100 per cent complete at $g' = 25$, and $r' = 24$. Since the $(g' - r')$ colour of red galaxies at the highest redshift we focus on in this work is around 1.8 (Figure 2.5), we make a cut at $r' = 23.2$ to ensure completeness in the g' band.

To determine the uncertainty on the colour, we examine the difference in the colours measured from each pointing, for galaxies in the overlap regions between pointings.[‡] In Figure 2.2, we plot the standard deviation of $(g' - r')$ (left panel) and $(r' - i')$ (right panel) colour differences as a function of magnitude, and fit the logarithm of it by two straight lines. At the magnitude limit of $r' = 23.2$ of our catalogue, the uncertainty on the $(g' - r')$ colour is about 0.2 mag, which makes isolating red-sequence galaxies from the contamination of the blue cloud less reliable at fainter magnitudes (see §2.6).

2.2.3 Star-Galaxy Separation

TERAPIX classified objects in the magnitude range $17.5 < i' < 21.0$, using the stellar locus in the half-light radius vs. magnitude plot, in a series of 10 arcmin cells distributed over each MegaCam stack. All objects fainter than $i' = 21.0$ are considered galaxies. At magnitudes brighter than $i' = 17.5$, we keep objects that have SExtractor parameter $class\_star \leq 0.98$, but exclude those on the stellar locus, as galaxies. Objects in our final galaxy catalogue are plotted as small points in Figure 2.3, and stars are represented by circles. Only a subset of the data is plotted for clarity.

[‡]The residual mean offset in colour between two overlapping pointings is < 0.05 mag, and we correct for this residual offset before we stack all the overlap regions together to examine the distribution of the difference between colours measured from two overlapping pointings.

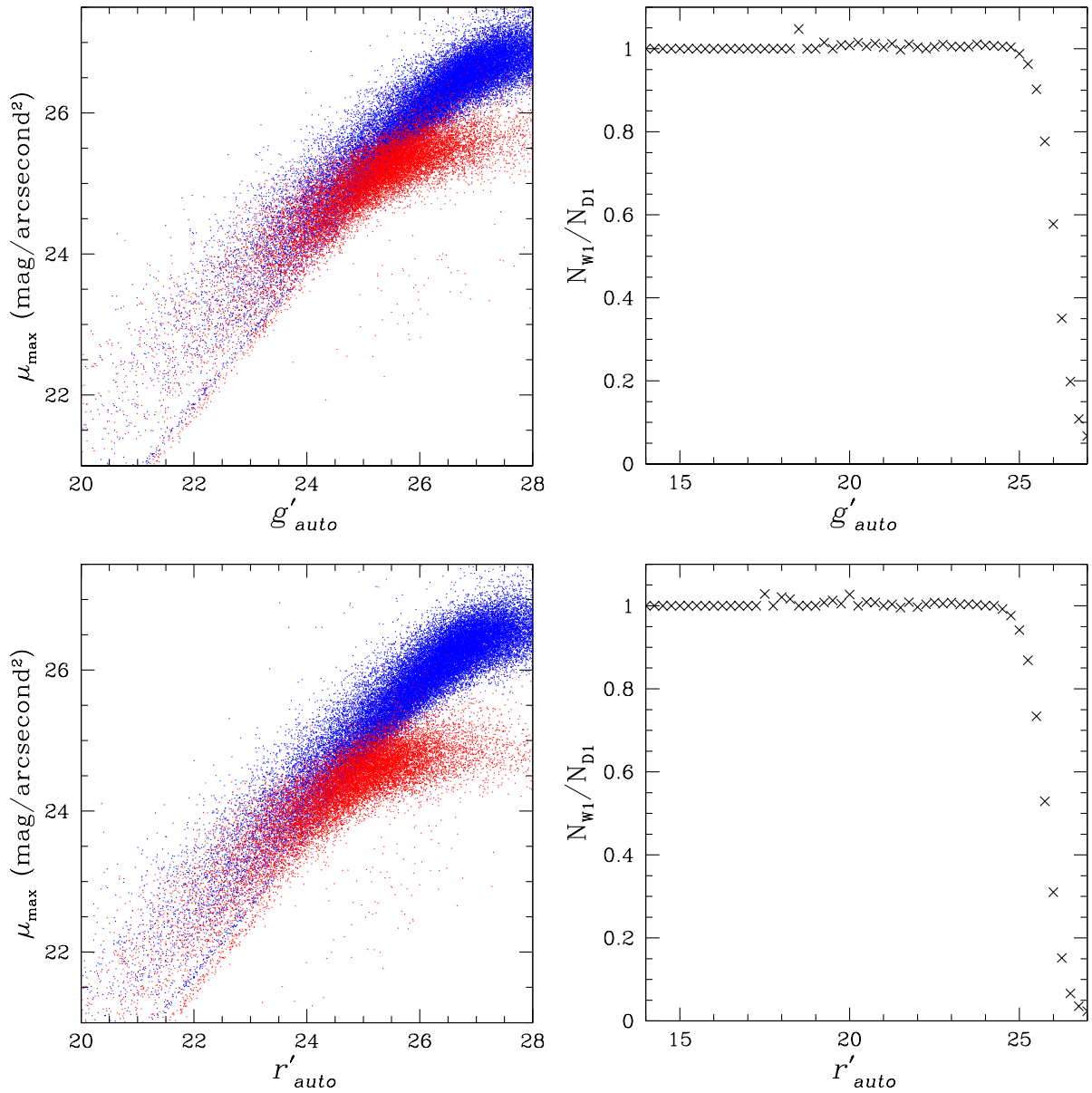

Figure 2.1: Left column: central surface brightness, μ_{max}, as a function of g' (top) and r' (bottom) magnitude. Red points are objects in W1 and blue points D1. Right column: fraction of sources in D1 that are also detected in W1, as a function of magnitude.

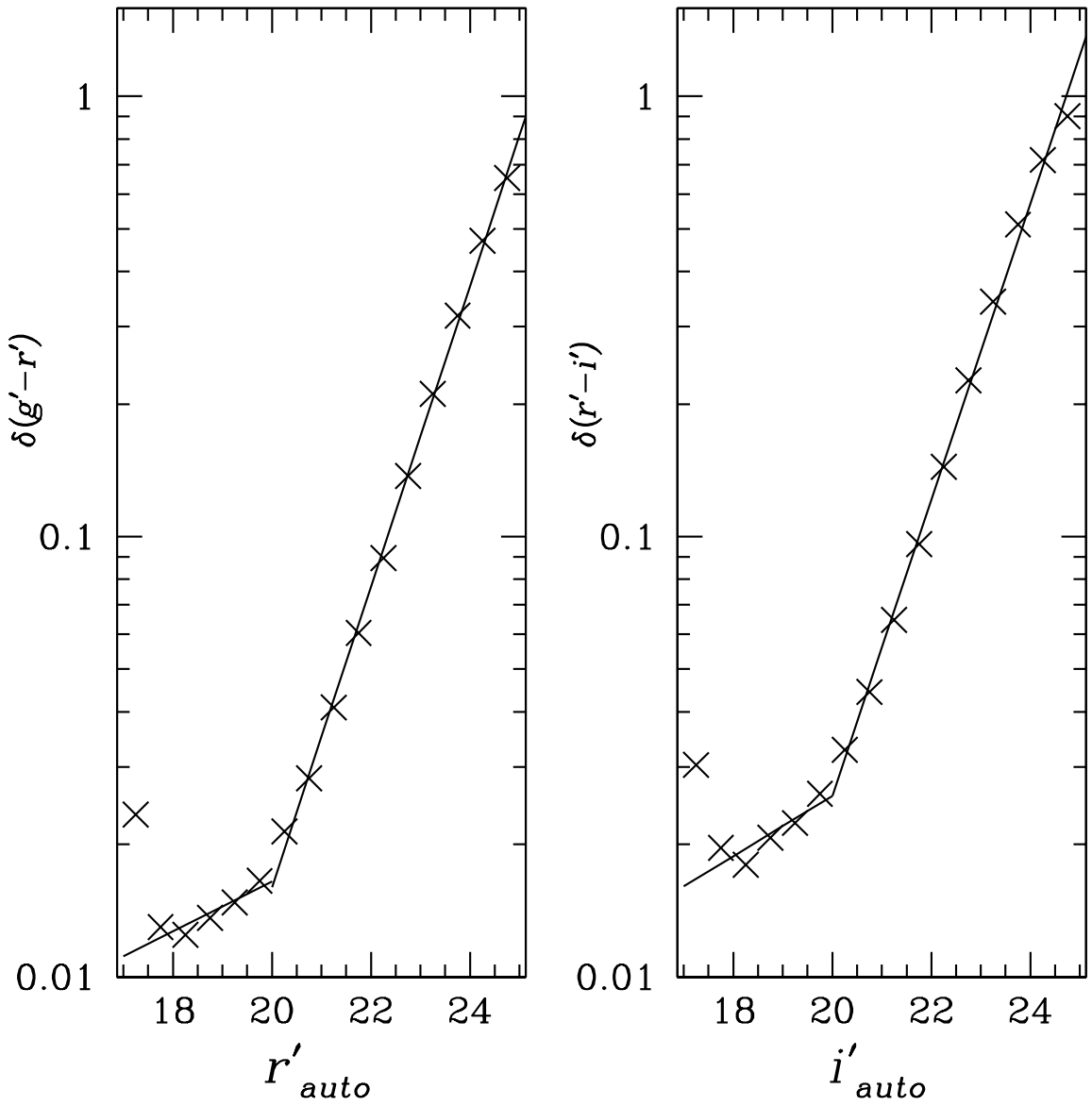

Figure 2.2: Left panel: the standard deviation of $(g' - r')$ colour differences in overlapping pointings as a function of r' magnitude, fitted by two straight lines on logarithmic scale. Right panel: the standard deviation of $(r' - i')$ colour differences as a function of i' magnitude.

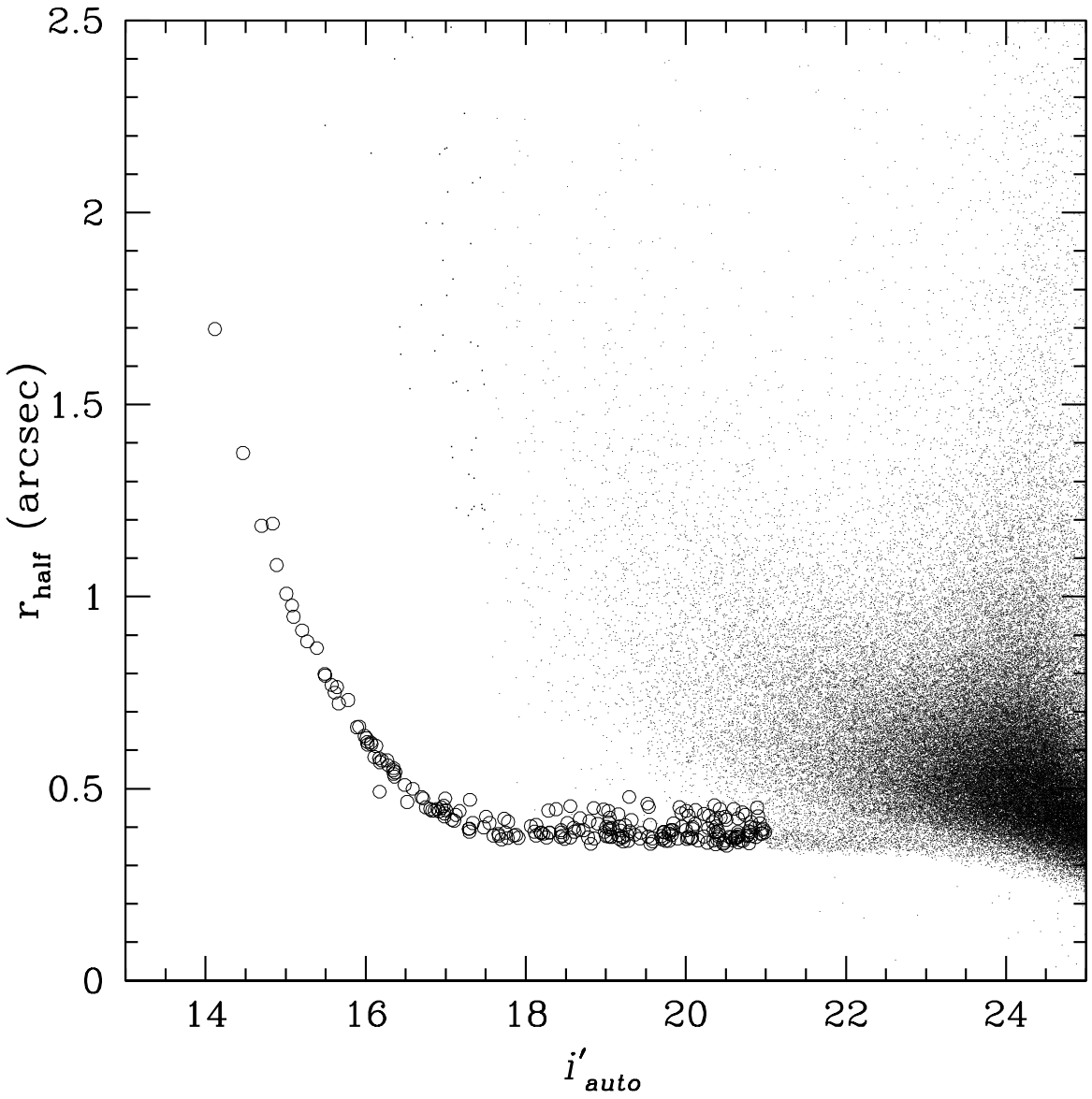

Figure 2.3: Half-light radius vs. magnitude. Points represent a subset of the galaxies that are in our final galaxy catalogue, and circles represent stars. See text for details on star-galaxy separation.

2.3 Cluster Detection

The cluster detection method we use is based on the spirit of the cluster-red-sequence (CRS) method (Gladders & Yee, 2000), but with some modifications. The foundation of the CRS technique is that in every cluster there is a population of red galaxies that forms a tight red-sequence in the colour-magnitude diagram (CMD), which can be used as an overdensity indicator. Four major steps are involved in the cluster detection: 1) model the CMD at different redshifts; 2) select a subsample of galaxies that belongs to each colour slice; 3) count galaxies around a grid of positions in the sky and estimate the background in the same way; 4) select overdensities as cluster candidates. Below, we describe each step in detail.

2.3.1 Model CMD

First we model the CMD for the red-sequence galaxies. Since we only need a model that produces the correct CMR over a small redshift range, and we will calibrate it empirically, a simple model is sufficient. We use a single burst model from Bruzual & Charlot (2003) with a Salpeter IMF and formation redshift of $z_f \sim 2$. We follow the passive evolution of galaxies with different metallicities, and calibrate the model by defining a magnitude-metallicity relation so that it reproduces the observed CMD of E+S0 galaxies in Coma (slope -0.0743, zero point 4.21, Bower et al. 1992). The resulting magnitude-metallicity relation is in good agreement with the result from a more complicated model by Kodama & Arimoto (1997).

Under the assumption that this magnitude-metallicity relation does not evolve with redshift, we can define for each metallicity a correlation between the model colour and magnitude for the passively-evolving galaxies at each redshift. We fit the resulting CMR with a straight line. To model m^* at different redshifts, we take the m^* at $z = 0$ estimated by Blanton et al. (2001) using SDSS data, transform it into CFHTLS filters, and evolve it using the same model with solar metallicity.

Figure 2.4 shows the CFHTLS filter transmission curves[†], and into which filters the 4000Å break (the most prominent feature in a red-sequence galaxy's spectrum) falls at different redshifts. When the 4000Å break is in the g' filter, the $(g' - r')$ colour is very sensitive to a small shift of the break position, and thus gives the best redshift resolution. When the break is approaching the boundary between g' and r' filters, the $(g' - r')$ colour becomes degenerate. Therefore, we limit our study in this work to $z < 0.36$.

[†]http://www3.cadc-ccda.hia-iha.nrc-cnrc.gc.ca/megapipe/docs/filters.html

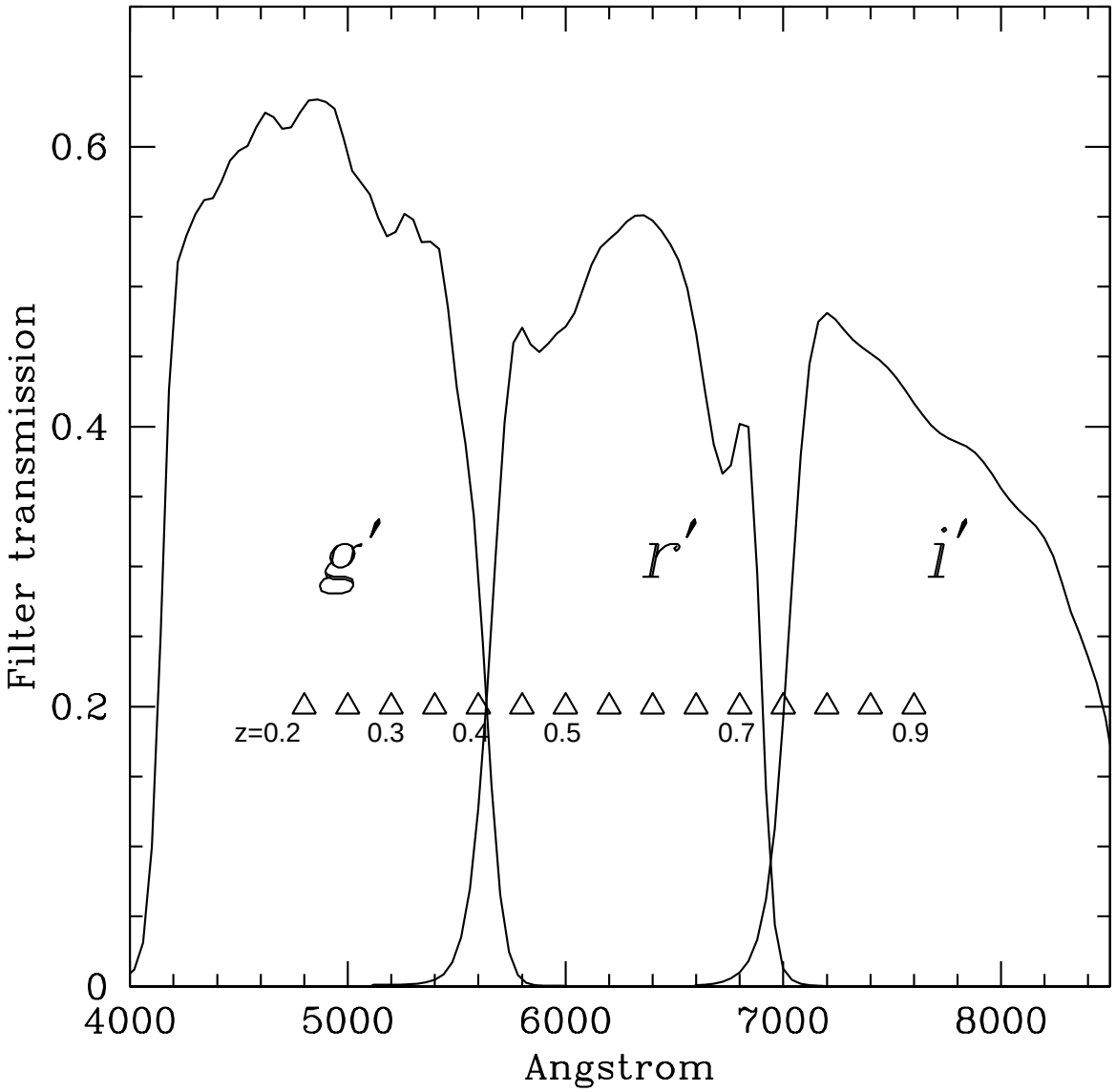

Figure 2.4: Position of the 4000Å break at different redshifts in CFHTLS filters. Solid curves are total filter transmissions (filter+mirror+optics+CCD), and triangles indicate the positions of the 4000Å break at different redshifts.

z	$m^*_{r'}$	$(g'-r')$ at $m^*_{r'}$
0.19	17.65	1.048
0.22	18.1	1.128
0.25	18.48	1.213
0.28	18.81	1.309
0.31	19.12	1.394
0.34	19.4	1.462
0.37	19.67	1.517

Table 2.2: Model m^* and colour at m^* as a function of redshift.

Figure 2.5 shows the modelled $(g'-r')$ vs. r' diagram as a function of redshift, with m^* indicated. The redshift interval between slices is 0.03. The m^* and colour at m^* are tabulated in Table 2.3.1, with a small, empirical correction applied to the redshifts as discussed in §2.4.3.

2.3.2 Subsamples in each Colour Slice

The next step is to construct a subsample of galaxies for each redshift based on the colours of the galaxies. At each redshift, we define a colour slice centred on the model CMR, with the half width determined by the intrinsic scatter in the colours of red-sequence galaxies, 0.075 (Gladders & Yee, 2000). The colour slices overlap with each other to avoid missing clusters on the edge of each colour slice. We then calculate, for each galaxy, the probability that it belongs to a specific colour slice, assuming that the probability distribution of the colour of each galaxy is Gaussian, with $\sigma = \triangle c$, dominated by the colour errors estimated from the overlapping regions as shown in Figure 2.2. For each colour slice, all galaxies with probabilities larger than 10 per cent are selected. A subset of the galaxies from W1 that are associated with the colour slice at $z = 0.25$ are shown as points in Figure 2.5. At the faint end, due to the larger colour uncertainties, galaxies belonging to that colour slice spread out of the boundary of the slice.

This colour-weighting step is the same as prescribed by Gladders & Yee (2000). In the original CRS technique, after the colour weighting, a magnitude weighting is applied to downweight the fainter galaxies because the contrast between cluster and the field is lower at faint magnitudes. We do not want to bias our detected clusters to a certain luminosity function shape, so we do not apply any magnitude-weighting here. However, to avoid high contamination from the field at the very faint magnitudes, we only use galaxies brighter than $m^* + 2$ for detection. For the purpose of our study here, we only need a sample of rich clusters without worrying about the completeness of poorer systems, which further

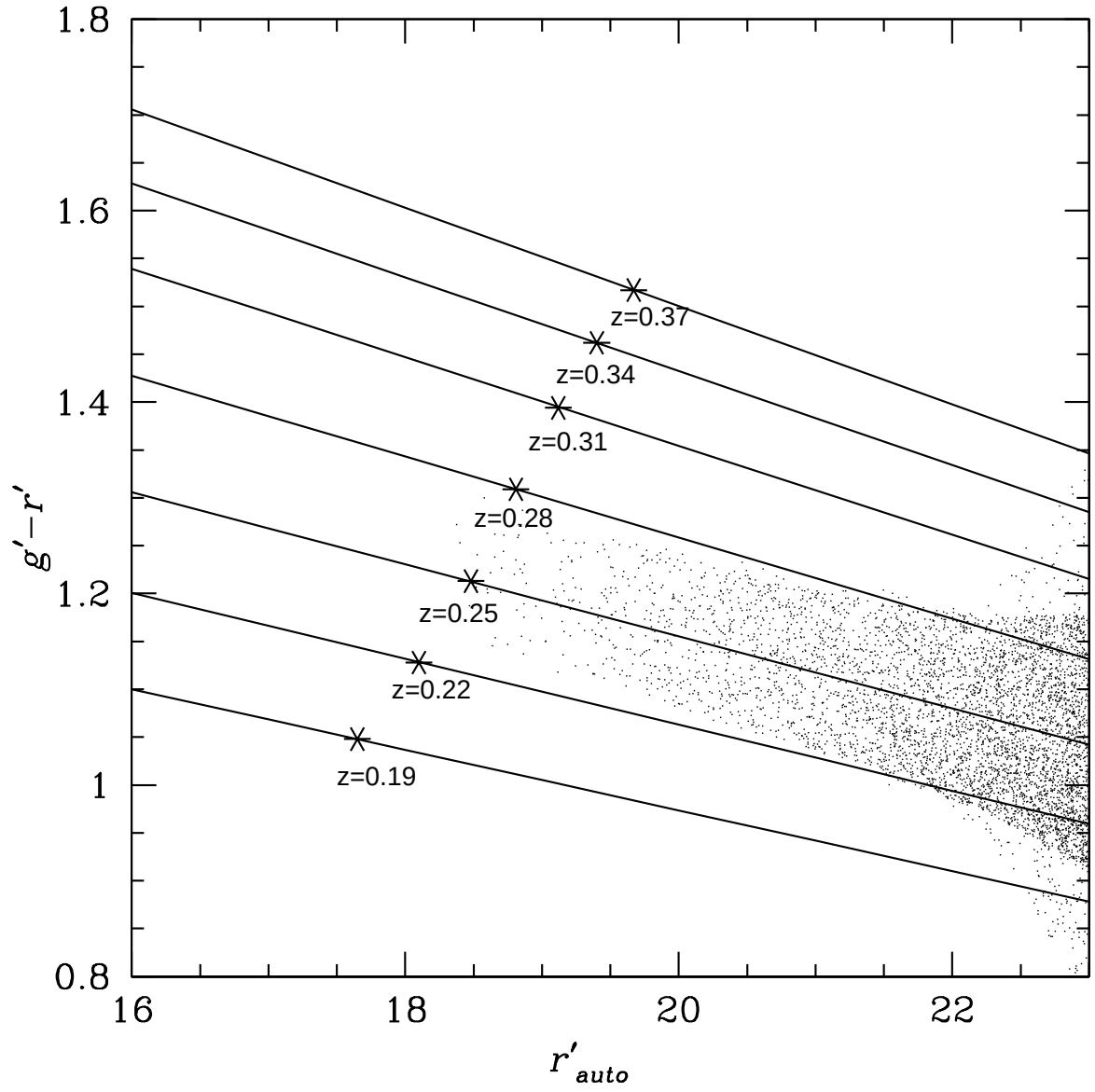

Figure 2.5: Model CMD in CFHTLS filters as a function of redshift with m^* indicated. The redshift interval is $\triangle z = 0.03$. The $z \sim 0$ relation is calibrated to Coma (Bower et al., 1992). The CMD is evolved passively, with a fixed magnitude-metallicity relation. Points represent a subset of galaxies from W1 that are associated with the colour slice at $z = 0.25$ (see §2.3.2).

justifies the modification we make here.

2.3.3 Significance Map and Detection

In each colour slice, we count the number of galaxies in the subsample within a circle of radius ~ 0.5 Mpc (the typical size of a cluster core) around a grid of positions in the sky. The grid size is about 0.1 Mpc. This gives the cluster+field count at each position. The field count is estimated in the same way, but from the average of 500 random positions in the sky. The difference between the total number count and the background count at each grid position divided by the rms deviation of the background distribution of the 500 random positions (comparable to Poisson uncertainty), σ_f, indicates the significance of the overdensity smoothed on a 0.5 Mpc scale at that position, i.e.

$$\sigma = \frac{N_{cluster+field} - N_{field}}{\sigma_f}. \tag{2.1}$$

FITS images of the significance maps for each colour slice are created. SExtractor is then run on those images to pick out peaks on the significance maps. We keep everything that has at least 1 pixel above 5σ as cluster candidates.

We now have a list of crude positions and significance of cluster candidates. If multiple peaks are detected within $\sim$1 Mpc from each other, either in the same colour slice or adjacent slices, only the one that has the highest significance will be kept. In the following sections, we refine the cluster catalogue, by using additional colour information, and improving the centring and redshift resolution.

2.3.4 Refinements to the Cluster Catalogue

High-z Contamination

For any cluster candidate we detected, higher-redshift blue galaxies projected along the line-of-sight may have the same $(g' - r')$ colour as the red-sequence members of that cluster. This is demonstrated in Figure 2.6, which shows the evolutionary tracks of $(g' - r')$ vs. $(r' - i')$ with redshift for three different populations produced by the model of Bruzual & Charlot (2003). Squares are a population that formed 10.3 Gyr ago and have constant star formation. Pentagons represents a 8 Gyr old single-burst model and triangles a 10.3 Gyr single-burst model. The lines are to guide the eyes. For the two old models, galaxies in the redshift range $0.4 < z < 0.9$ all have similar $(g' - r')$ colour. However, they have different $(r' - i')$ colours. Therefore, $(r' - i')$ colour can effectively eliminate high redshift galaxies from the red-sequence galaxies at a lower redshift. This is further demonstrated in

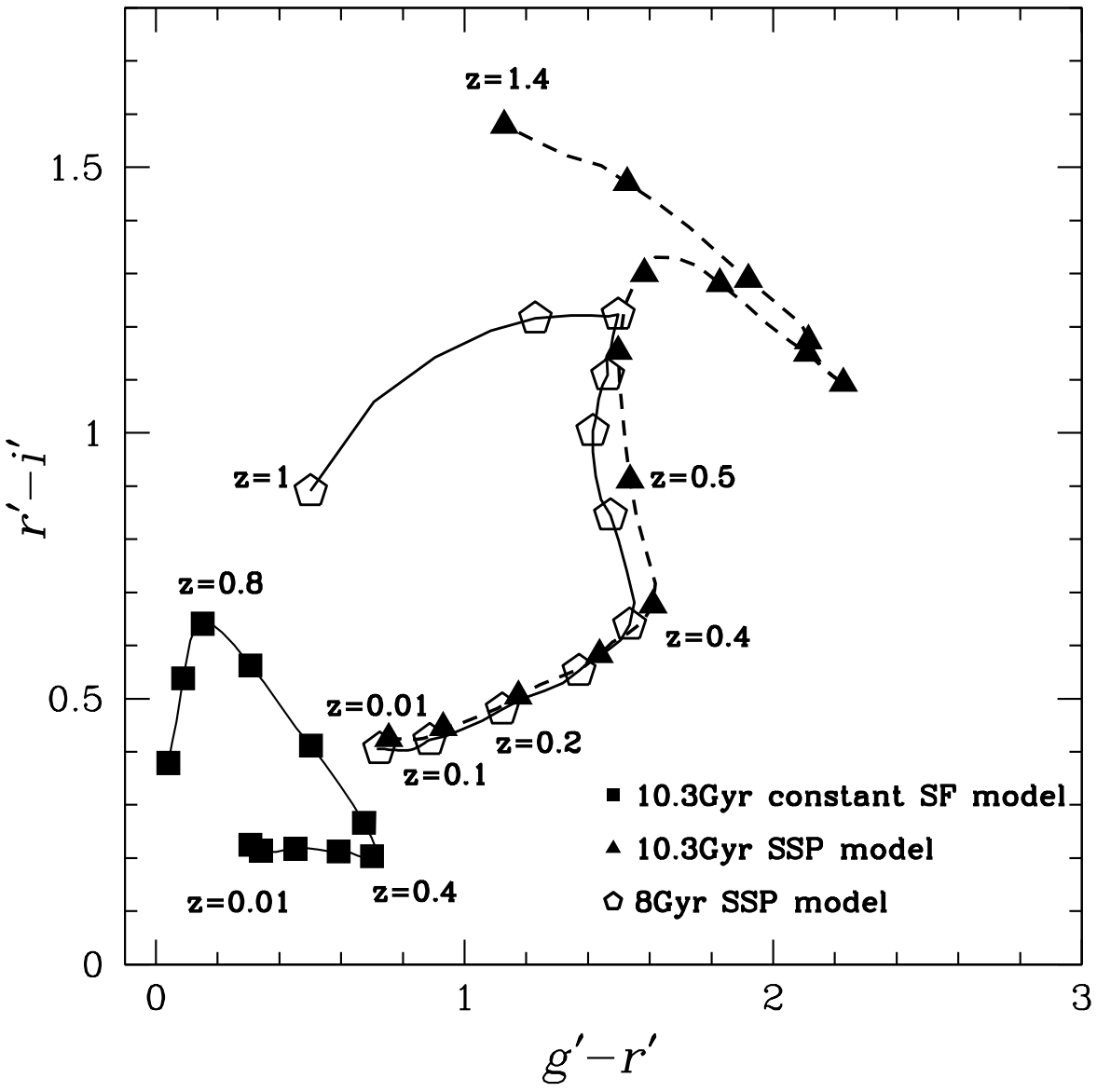

Figure 2.6: Evolutionary tracks of $(g' - r')$ vs $(r' - i')$ with redshift for three different populations produced by the model of Bruzual & Charlot (2003). Squares are a population that formed 10.3 Gyr ago and have constant star formation. Pentagons represents a 8 Gyr old single-burst model and triangles a 10.3 Gyr single-burst model. The lines are to guide the eyes.

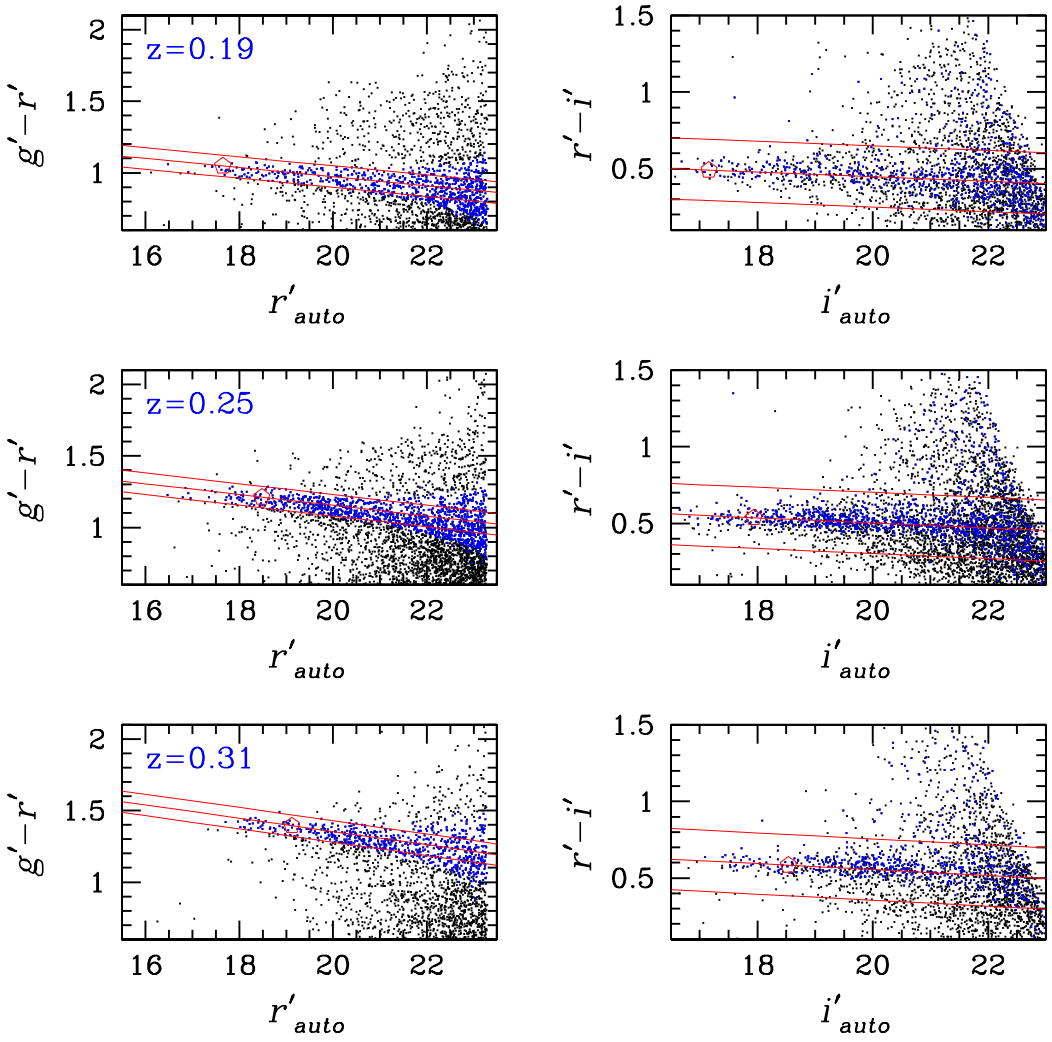

Figure 2.7: Stacked CMDs of galaxies within 0.5 Mpc around each cluster in $(g' - r')$ vs. r' (black points in the left column) and $(r' - i')$ vs. i' (black points in the right column) planes at three different redshifts. Pentagons indicate the position of m^*. Central solid lines in the $(g' - r')$ vs. r' plots indicate the model CMR and the upper and lower bounds indicate the width of the colour slice, ± 0.075 mag. On the $(r' - i')$ vs. i' plot, the central lines are the resulting CMR from the same model that produces the $(g' - r')$ vs. r' relation. The half width of the colour slice in $(r' - i')$ vs. i' is 0.2 mag as indicated by the upper and lower solid lines (see text for explanation). Blue points are galaxies that belong to the red-sequence in $(g' - r')$ vs. r'. As we can tell, many of them do not fall on the red-sequence in the $(r' - i')$ vs. i' plane, which shows the advantage of using two-colour information to select red galaxies.

Figure 2.7, which shows the stacked CMDs of galaxies within 0.5 Mpc around each cluster in $(g' - r')$ vs. r' (black points in the left column) and $(r' - i')$ vs. i' (black points in the right column) planes at three redshifts. Pentagons indicate the position of m^*. Central solid lines in the $(g' - r')$ vs. r' plots indicate the model CMR and the upper and lower bounds indicate the width of the colour slice, ± 0.075 mag. On the $(r' - i')$ vs. i' plot, the central lines are the resulting CMR from the same model that produces the $(g' - r')$ vs. r' relation. The half width of the colour slice in $(r' - i')$ vs. i' is 0.2 mag (justified below) as indicated by the upper and lower solid lines. Blue points are galaxies that belong to the colour slice in the $(g' - r')$ vs. r' plane. In the $(r' - i')$ vs. i' plane, most of those galaxies still fall on the red-sequence at low redshift, but as we go to higher redshift, many of them fall off the red-sequence even at bright magnitudes. Therefore, only galaxies that are on the red-sequence in both $(g' - r')$ vs. r' and $(r' - i')$ vs. i' planes are considered as potential red-sequence cluster members. Note we only use $(r' - i')$ colour to eliminate obvious background contamination; therefore we take a wide colour slice in $(r' - i')$ vs. i' so that we do not lose red-sequence galaxies due to the uncertainty on the $(r' - i')$ colour and any slight mismatches between the model $(g' - r')$ and $(r' - i')$ colour slices. This technique has been used in Andreon (2006).

Centres

As described above, the centre of each cluster is determined by the position at which the number of red-sequence galaxies within a radius of 0.5 Mpc selected using $(g' - r')$ vs. r' is maximised. We refine the determination of the centre in several ways. We divide the region within a radius of 0.5 Mpc around each cluster further into smaller grids of size ~ 0.06 Mpc and count galaxies that belong to the red-sequence in both $(g' - r')$ vs. r' and $(r' - i')$ vs. i' planes in a circle of radius ~ 0.1 Mpc. We also calculate the luminosity-weighted centre using galaxies that belong to the red-sequence in both $(g' - r')$ vs. r' and $(r' - i')$ vs. i' planes in a circle of radius ~ 0.5 Mpc around each cluster. We compare the centres obtained in both ways with the position of the brightest cluster galaxy in each cluster. For some rich, symmetric systems, the three centres agree with each other well. In the calculations later in the Chapter, we use the luminosity-weighted centre.

Redshift

As described in §2.3.1 (Figure 2.5), the redshift interval between adjacent colour slices is 0.03. To refine the redshift estimate of each cluster candidate, we insert two more colour slices between two existing adjacent ones. To determine, for each cluster, which redshift the model CMD fits the observed red-sequence the best, two criteria are used: 1) we count the number of red-sequence galaxies within a circle of 0.5 Mpc in radius around the

luminosity-weighted centre of that cluster; 2) we calculate the deviation of the colours from the model CMR for all red-sequence galaxies that are brighter than $m^* + 2$. We do this for each cluster in several adjacent colour slices and determine which one gives the highest number count and least deviation in colour. If these two criteria give the same optimal colour slice, then the redshift of that colour slice is assigned to the cluster. If these two select two different optimal colour slices, the one that gives the least deviation is chosen only if at least five galaxies are used in the fit and the deviation is significantly smaller than that from the slice that gives the highest count. We check how well this works by stacking all clusters at the same redshift and plotting the observed $(g' - r')$ vs. r' relation against the model.

Finally, we interpolate the CMD in the $(r' - i')$ vs. i' plane for the corresponding new redshift. A new centre is calculated for each cluster using the galaxies that fall on the red-sequence defined by the finely-interpolated colour slices in both the $(g' - r')$ vs. r' and $(r' - i')$ vs. i' plane. The significance of each cluster is re-estimated around the new centre.

2.4 Cluster Properties

2.4.1 Richness

Since we used the number of red-sequence galaxies brighter than m^*+2, and within only 0.5 Mpc from the cluster centre, in the cluster detection to reduce the noise, throughout this Chapter we use this number, denoted as N_{red,m^*+2}, to indicate the richness of the clusters in our sample. However, the typical extent of a cluster, r_{200} (the radius within which the mean density is 200 times the critical density), is larger than 0.5 Mpc; therefore, to get some idea of how our N_{red,m^*+2} corresponds to the more commonly used richness indicator, N_{200} (the number of cluster members within r_{200}), we plot N_{red,m^*+2} vs. N_{200} for the ten clusters that are both in our sample and the MaxBCG catalogue (Koester et al., 2007) at this redshift range in Figure 2.8. Based on the relation $r_{200} = 0.26 N_{200}^{0.42}$Mpc (Johnston et al., 2007; Hansen et al., 2009), the r_{200} for clusters that are in the lower left corner of Figure 2.8 is about 0.8 Mpc; thus, their N_{red,m^*+2} as measured within 0.5 Mpc is only slightly lower than N_{200}. As one goes to richer clusters, the difference between N_{red,m^*+2} and N_{200} becomes larger. Nonetheless, we can approximately scale N_{red,m^*+2} to N_{200} using Figure 2.8.

The richest cluster in our catalogue has a N_{red,m^*+2} of 46, a known Abell cluster (Abell0362) with Richness Class 1 and $z = 0.1843$ (Cruddace et al., 2002). Its CMD is shown in Figure 2.9. Solid lines indicate the colour slice it belongs to with the star indicating the position of m^*, and crosses are galaxies within a radius of 0.5 Mpc from the centre (before background subtraction).

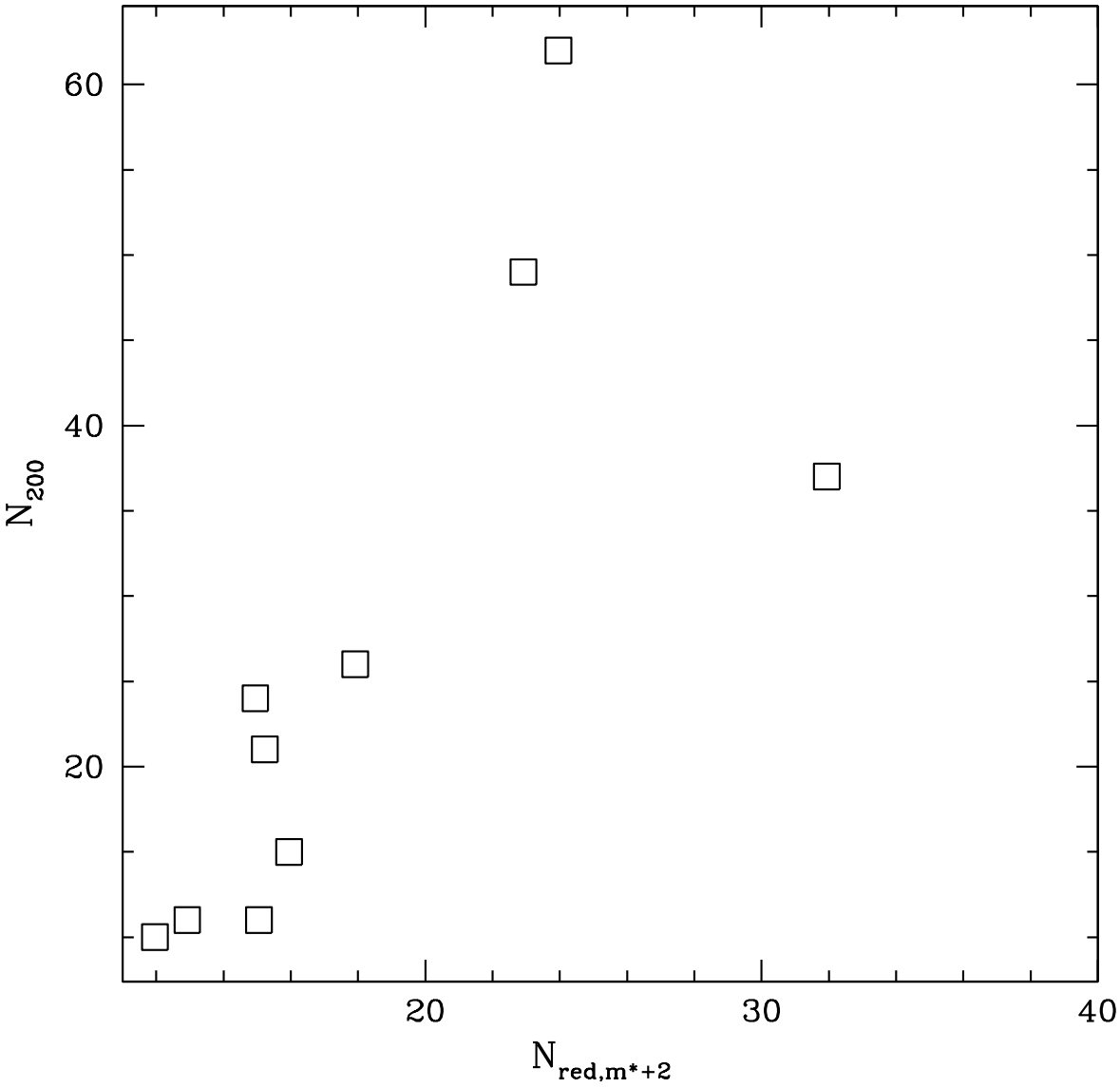

Figure 2.8: Correlation between our N_{red,m^*+2} measured within 0.5 Mpc and the number of cluster members within r_{200} from the MaxBCG sample (Koester et al., 2007).

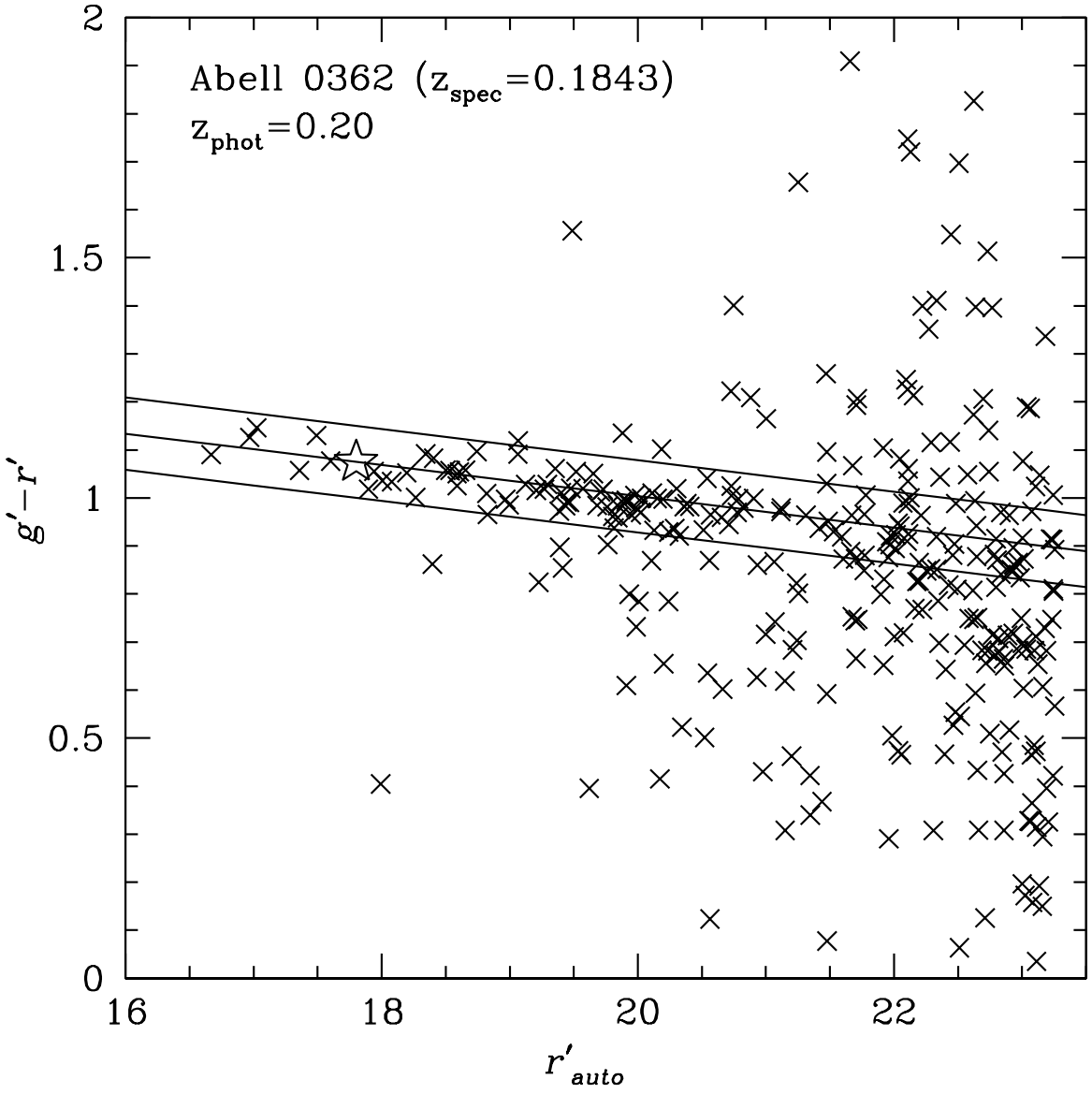

Figure 2.9: The CMD of the richest cluster in our catalogue (Abell 0362 Cruddace et al. 2002) before background subtraction. Solid lines indicate the colour slice it belongs to with the star indicating the position of m^*, and crosses are galaxies within a radius of 0.5 Mpc from the centre.

2.4.2 Mass Estimates

To get some idea of how massive the clusters in our sample are, we compare the surface density of the clusters in our catalogue with that from the Hubble Volume light cone. Based on the MS (spheres) cluster catalogue (Evrard et al., 2002), there are 1.26 clusters per square degree with mass greater than $1.4 \times 10^{14} M_{\odot}$ in the redshift range of $0.17 \leq z \leq 0.36$, and this surface density corresponds to that of the clusters with $N_{red,m^*+2} \geq 12$ in our catalogue (as can be seen in Figure 2.10).

We have calculated the projected correlation function, $\omega(\theta)$, of the clusters in each of the four wide fields separately, following the method of Landy & Szalay (1993). We select all clusters in our sample with $0.17 \leq z \leq 0.36$, and a richness $N_{red,m^*+2} > 10$, which leaves us with 74, 31, 57 and 32 clusters in the fields W1 through W4, respectively. This richness limit is slightly poorer than that adopted for most of the analysis in this Chapter in order to have sufficient statistics for the following analysis. This means our results in the Chapter actually correspond to systems slightly *more* massive than the limits given here.

The correlation function is shown in Figure 2.11. The random point distribution we use for comparison does not account for the intrinsic size of our detection filter; this means we will not measure the correlation function accurately on angular sizes of about $\theta \leq 0.1$ degree. We therefore fit the data with a power law function $\omega(\theta) = A_{\omega}\theta^{1-\gamma}$ over the range $0.2^o < \theta < 2^o$. We do not have enough data to measure both the amplitude and slope, so we fix $\gamma = 2.15$ as measured locally for clusters (Gonzalez et al., 2002). We find the best fit amplitude A_{ω} by maximizing the likelihood function as given in Gonzalez et al. (2002), and take the 95 per cent confidence limits to be the value where the relative likelihood is 0.1. These values are given in each panel in Figure 2.11. There is considerable variation from field to field, to be expected since the areas are still fairly small. The two fields with the most data, W1 and W3, actually represent the least- and most-clustered data, respectively, though we note that only the W3 data actually puts useful constraints on the clustering amplitude.

Deprojecting the angular correlation function using the Limber equation and assuming our standard cosmology, and including a Gaussian fit to the observed $N(z)$ distribution (see Figure 2.13), we find that the amplitude corresponds to a physical correlation length of $r_{\circ} \sim 41$ Mpc for W3, and 23.8 Mpc in the least-clustered field, W1. This range of correlation lengths in turn corresponds to a space density of $n_c = (0.2-4.6) \times 10^{-6}$ (Mpc)$^{-3}$ (e.g. Colberg et al., 2000). We use the Millennium simulation ($\Omega_m = 0.25$, $\Omega_{\Lambda} = 0.75$, $h = 0.73$, $\sigma_8 = 0.9$) (Springel et al., 2005) output at $z \sim 0.3$, and find that this space density corresponds to clusters with mass $M \geq 1.0 \times 10^{14} M_{\odot}$ (W1) and $M \geq 4.1 \times 10^{14} M_{\odot}$ (W3). Note that a lower value of σ_8 than used in the simulation is preferred by the latest WMAP measurement (Dunkley et al., 2009); in this case, the corresponding mass limit of

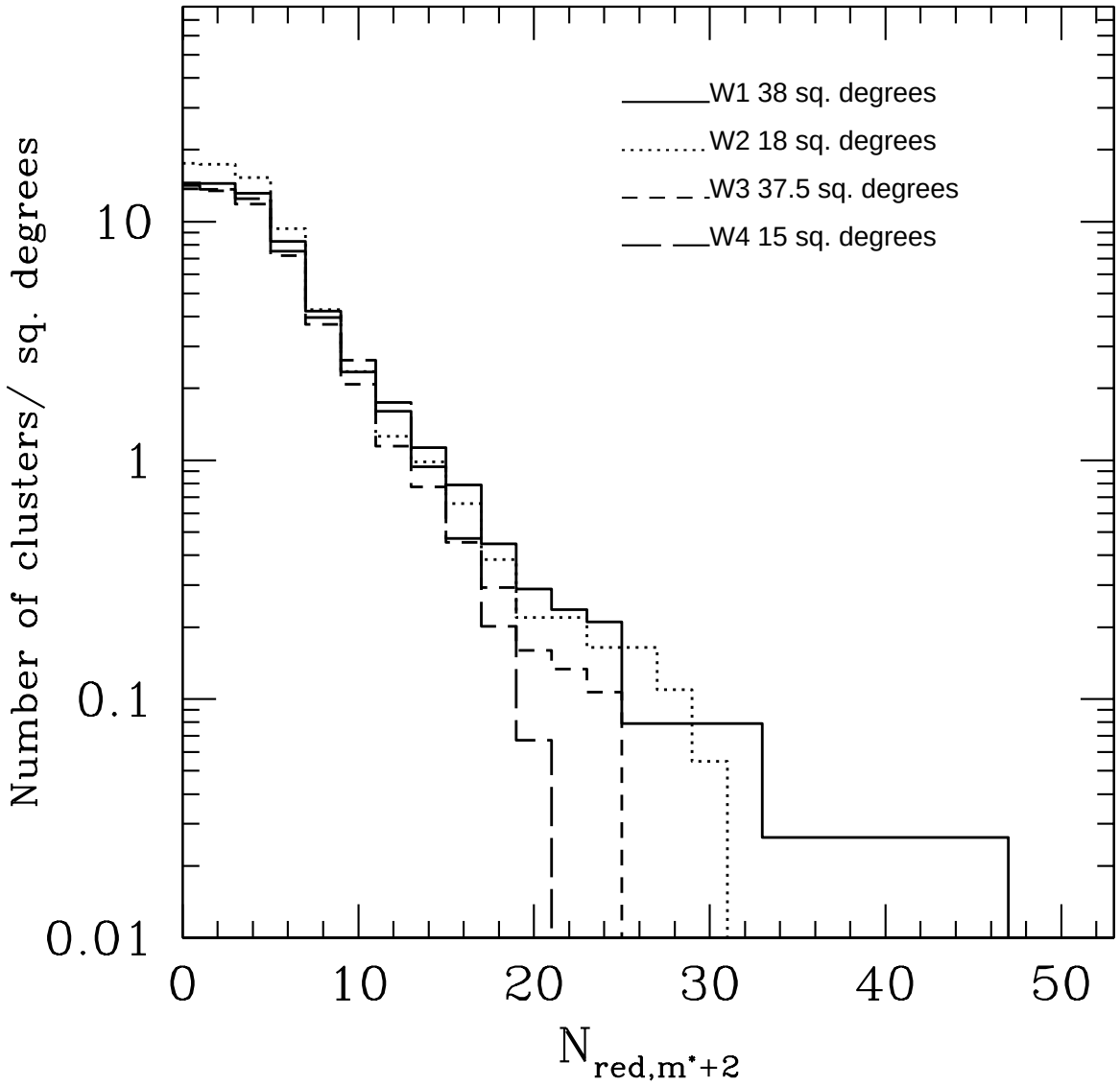

Figure 2.10: Cumulative surface density of the clusters we detected as a function of N_{red,m^*+2} in the redshift range $0.17 \leq z \leq 0.36$, in all four wide fields. Each line style represents one of the four wide fields.

our sample would be slightly lower.

As an alternative to deprojecting the angular correlation function, we also compare our correlation function directly with that of the Hubble volume simulation ($\Omega_m = 0.3$, $\Omega_\Lambda = 0.7$, $h = 0.7$, $\sigma_8 = 0.9$) (Evrard et al., 2002), by selecting clusters in the full-sky light cone, within a similar redshift range as the data and in discrete bins of total mass. We then compute the correlation function in the same way as for the data; the results are shown in Figure 2.11 as triangles ($M > 8.0 \times 10^{13} M_\odot$), crosses ($M > 3.0 \times 10^{14} M_\odot$) and squares ($M > 5.0 \times 10^{14} M_\odot$). In all fields except W1, the comparison with the data suggests our sample with $N_{red,m^*+2} \geq 10$ is limited at about $M \geq 2 \times 10^{14} M_\odot$, consistent with the deprojection analysis above.

The CFHTLS W1 field also overlaps with the XMM-LSS field and we recovered, in the redshift range we are interested in, all 9 X-ray confirmed clusters in the XMM-LSS archive (Pacaud et al., 2007). These clusters are all low-richness clusters in our sample. Their X-ray temperatures range from 1 keV to 3 keV. From the observed mass-temperature relation of galaxy clusters (e.g. Evrard et al., 1996; Shimizu et al., 2003), the mass of a cluster with a X-ray temperature of ~ 2 keV is $\sim 1 \times 10^{14} M_\odot$. This again indicates that the clusters in our sample have masses of $M > 1 \times 10^{14} M_\odot$.

Throughout this Chapter, unless otherwise specified, the analysis is carried out using the subset of 127 clusters that satisfy $N_{red,m^*+2} \geq 12$. We emphasize that such a richness-selected sample does not correspond exactly to a mass-selected one, and thus a mass limit cannot be precisely defined. Nonetheless the analyses above show that our results are applicable to fairly massive clusters, with $M > 1 \times 10^{14} M_\odot$; the sample is not dominated by low-mass groups.

2.4.3 Redshift Accuracy

The redshifts we initially assign to our clusters are based on the photometric data. In this section, we assess how good our photometric redshifts are.

As mentioned in §2.4.1, there are ten common clusters in our catalogue and the MaxBCG catalogue (Koester et al., 2007). For those clusters, we compare the spectroscopic redshifts of those BCGs with the photometric redshifts we assigned to those clusters. This comparison indicates that our photometric redshift is systematically lower, by a constant amount of 0.0435. Therefore, we apply this constant shift to the estimated photometric redshifts from our initial model. (Recalibration in this way is a standard part of the CRS method, Gladders & Yee 2000.) All redshifts quoted here have been adjusted in this way. Squares in Figure 2.12 show the comparison between the adjusted z_{phot} and the z_{spec} of MaxBCG clusters.

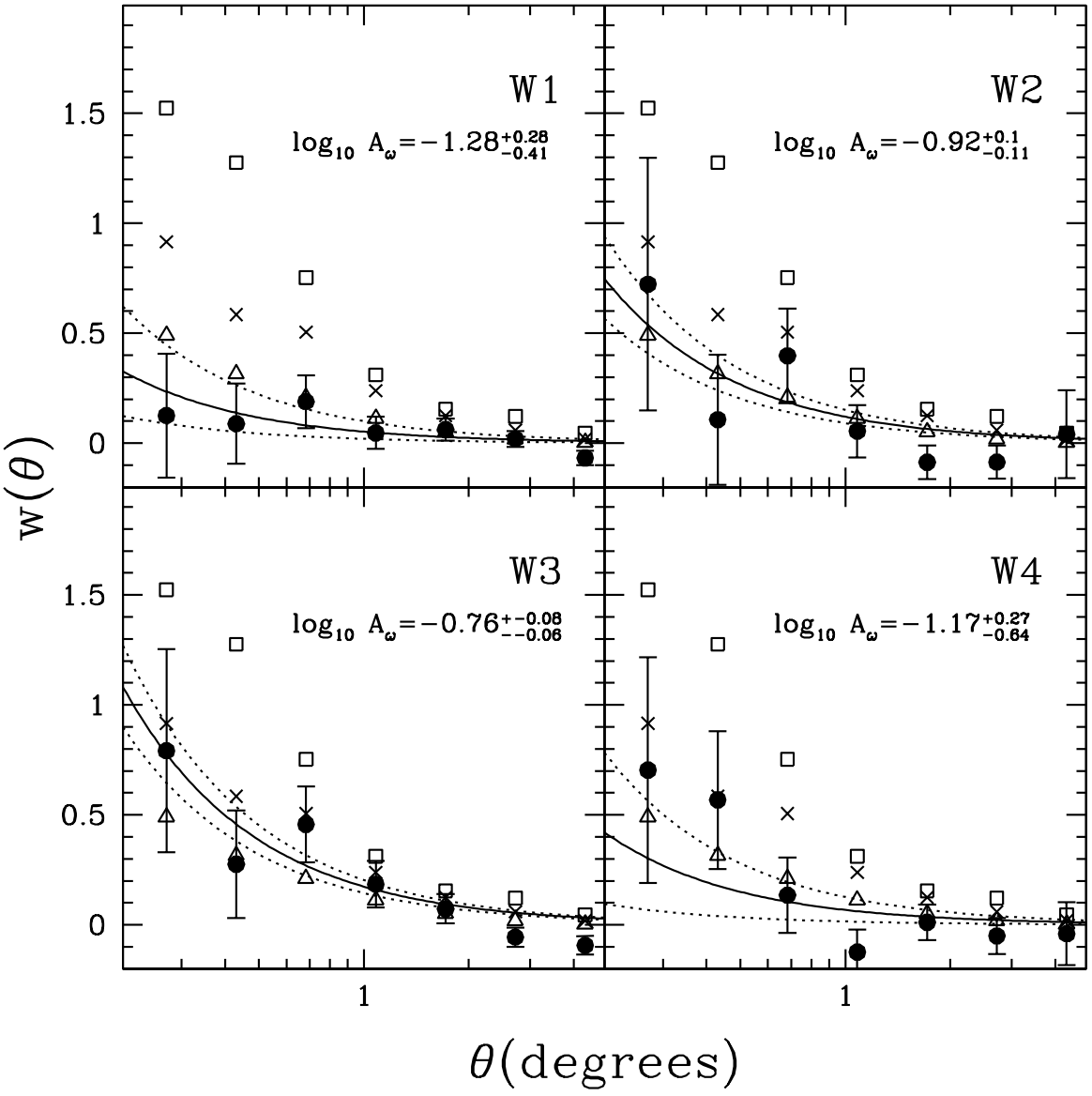

Figure 2.11: For each of the four CFHTLS survey fields, we show the angular correlation function for clusters with $N_{red,m^*+2} > 10$, as the solid points with Poisson error bars. The solid line is the best fit power law $\omega(\theta) = A_\omega \theta^{1-\gamma}$, with $\gamma = 2.15$ fixed. The dotted lines show the 95 per cent confidence limits. The triangles, crosses and open squares are theoretical angular correlation functions for clusters with $M = 8.0 \times 10^{13} M_\odot$, $M = 3 \times 10^{14} M_\odot$, and $M = 5 \times 10^{14} M_\odot$, respectively. These were computed from the Hubble volume simulation over a similar redshift range as the data.

We also compare the adjusted photometric redshifts of the X-ray confirmed clusters (§2.4.2) in our catalogue with their spectroscopic redshifts, shown as crosses in Figure 2.12. The two agree with each other well, providing an independent verification of our correction. The rms of the difference between the z_{photz} and z_{spec} (including both the MaxBCG and X-ray samples) is ∼0.014, with very little bias.

Figure 2.13 shows the distribution of clusters as a function of the adjusted z_{phot} in our sample, split into two subsamples based on N_{red,m^*+2}. The solid histogram represents the distribution of the subsample of clusters with $N_{red,m^*+2} \geq 20$, and the dotted histogram represents those with $12 \leq N_{red,m^*+2} < 20$. The distribution is smooth with redshift, peaking at around $z \sim 0.3$.

2.5 Local Comparison Sample

It is useful to extend our redshift baseline by examining a sample of local clusters, using our methods consistently. Therefore, we make use of the low-redshift galaxy group catalogue by Yang et al. (2007, hereafter Yang07), selected using a Friends-of-Friends algorithm from the SDSS spectroscopic data (York et al., 2000). We calculate N_{red,m^*+2} for these groups/clusters the same way as for our own cluster sample, except that the red-sequence galaxies are selected in $(u-r)$ colour to bracket the 4000Å break, because of the lower redshift of the sample. We select a subset of clusters that have $N_{red,m^*+2} \geq 12$, the same richness cut of our cluster sample. In order to carry out the calculations (e.g. background subtraction) exactly the same way as for our own sample, we only choose clusters that are in a contiguous region of the survey, and this limits the number of clusters in our local comparison sample to 22, at $0.08 < z < 0.09$.

In addition, we repeat the same measurement for the rich $z = 0.023$ cluster, Coma, using the same SDSS data, with the red-sequence galaxies selected using $(u-g)$ colour to bracket the 4000Å break at its redshift. Note Coma has a $N_{red,m^*+2} \sim 30$ and $N_{200} \sim 100$ (see §2.4.1), and therefore is ~ 4 times richer than the typical clusters in our sample and the Yang07 sample.

2.6 Luminosity Function Construction

In this Chapter, we focus on the $r'-$band red-sequence luminosity function (LF) in the core regions of clusters over the redshift range of $0.17 \leq z \leq 0.36$. We choose the r' band because it has the deepest photometry, and it is a red band which is less sensitive to recent star formation than bluer bands. We divide our cluster sample into three redshift bins and stack all clusters in each bin to obtain a composite red-sequence LF, to reduce the

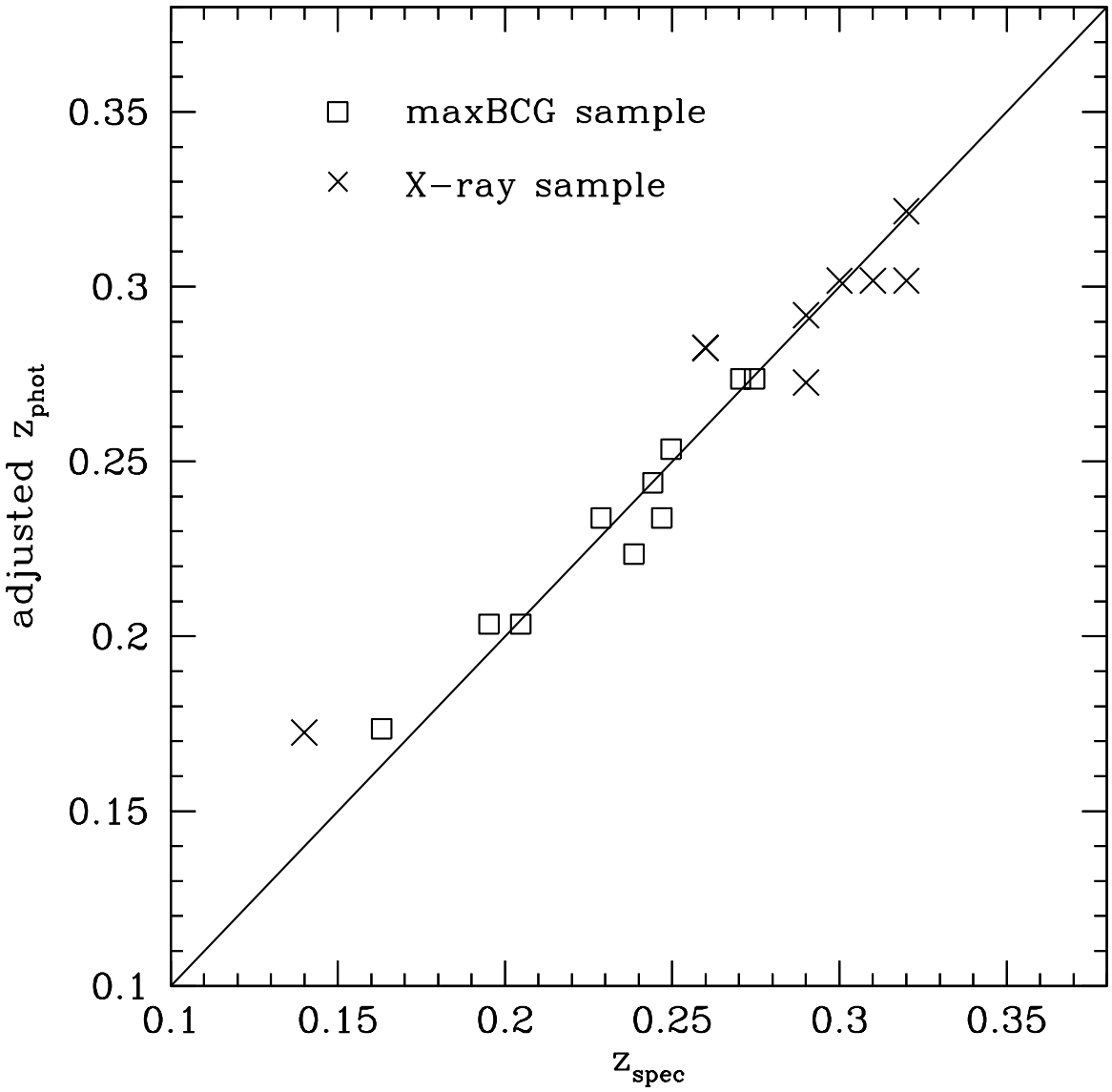

Figure 2.12: Comparison of our estimated photometric redshift with the spectroscopic redshift from the MaxBCG (Koester et al., 2007) and X-ray sample (Pacaud et al., 2007). Squares are our z_{phot} vs. z_{spec} from maxBCG sample, with z_{phot} corrected by a constant shift of 0.0435. Crosses are our corrected z_{phot} vs. the z_{spec} of the X-ray confirmed clusters from XMM-LSS in W1 field. The two agree with each other well, providing an independent verification of our correction.

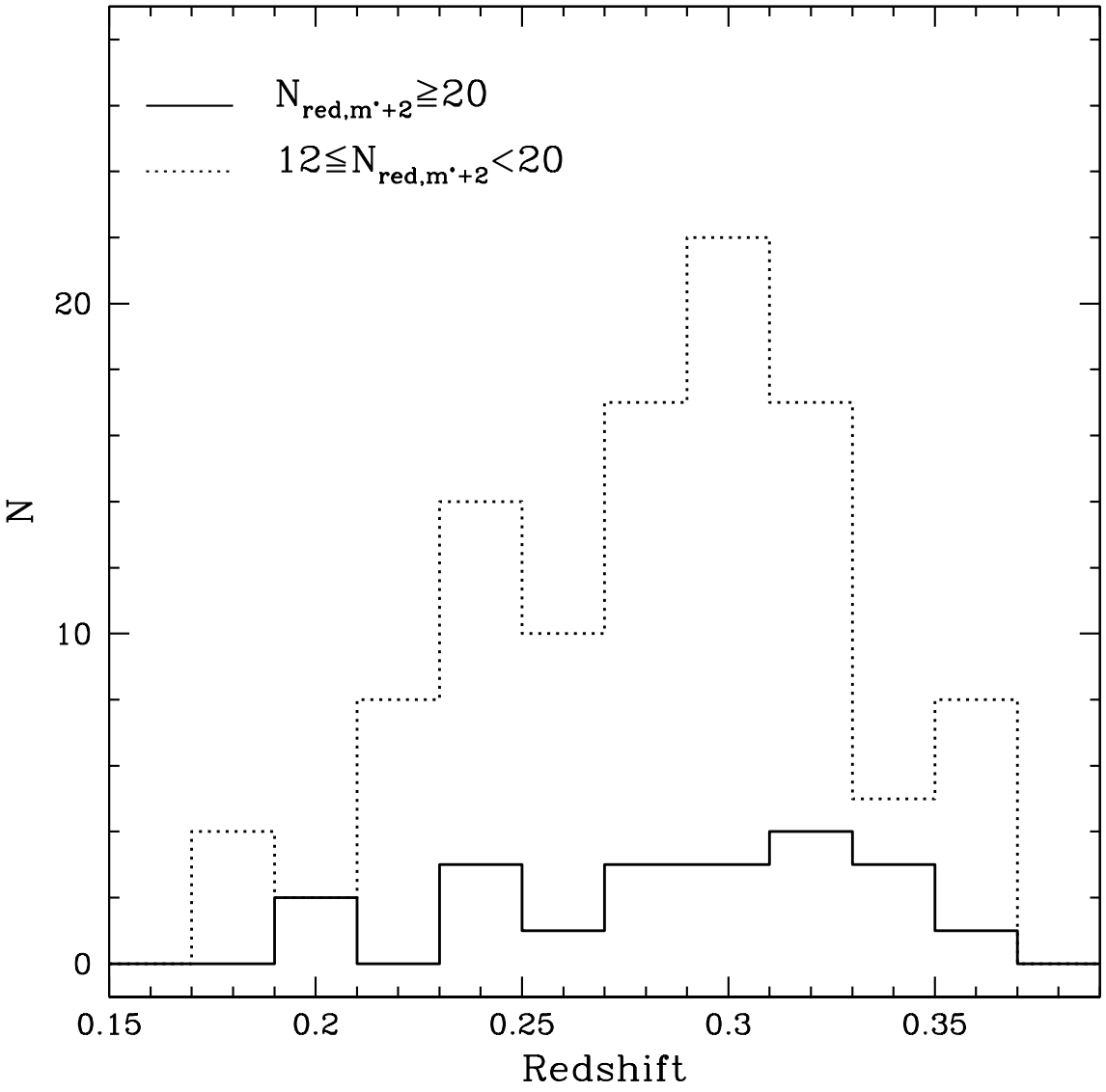

Figure 2.13: Redshift distribution of clusters in our sample, split into two subsamples based on N_{red,m^*+2}. The solid histogram represents the distribution of the subsample of clusters with $N_{red,m^*+2} \geq 20$, and the dotted histogram represents those with $12 \leq N_{red,m^*+2} < 20$. The distribution is smooth with redshift, peaking at around $z \sim 0.3$.

noise due to the uncertainty in cluster membership determination and cluster-to-cluster variation. The width of the redshift bin is chosen in a way that the number of clusters in each bin is roughly the same, to give similar statistics.

k-corrections or $(k+e)$ corrections are applied when necessary. The corrections are calculated using the same old, single-burst Bruzual & Charlot (2003) model used to define the CMR, and are magnitude dependent. The k-correction is about $0.2-0.5$ mag at $z<0.27$ (the two lower redshift bins), and about $0.5-0.7$ mag at $z\sim0.36$ (the highest redshift bin). The $(k+e)$ correction is less than ~0.2 mag at $z<0.36$.

We construct a composite CMD in each redshift bin to define the red-sequence. For clusters in each colour slice we calculate the position of every galaxy in the CMD relative to m^* in that colour slice, and shift those that fall onto the red-sequence defined by the wide $(r'-i')$ colour slice (to eliminate obvious foreground and background contamination) to the central redshift in both colour and magnitude. The first column in Figure 2.14 shows the composite CMDs of galaxies that are within a radius of 0.5 Mpc from cluster centres at three different redshifts. The dotted lines indicate ±0.2 mag from the modelled $(g'-r')$ vs. r' relation. To more accurately define the red-sequence, we fit a new $(g'-r')$ vs. r' relation using galaxies brighter than m^*+2 (m^* is indicated by the pentagon) that are within ±0.2 mag from the model $(g'-r')$ colour (as indicated by the blue points). We divide those galaxies into magnitude bins of 0.5 mag, calculate the median of the colour distribution in each magnitude bin, and fit the medians as a function of magnitude to a straight line, indicated by the central solid lines. To examine the fit more closely, we subtract the fitted $(g'-r')$ vs. r' relation and plot the relative position of each galaxy to the fitted CMR, which is shown in the second column in Figure 2.14, with the histograms in the third column showing the distribution of the residuals (down to m^*+2). The resulting CMD is centred at zero colour-difference relative to the fit by construction. To calculate the width, σ, of the colour distribution around the fitted $(g'-r')$ vs. r' relation, we mirror galaxies that are redder than the fitted CMR to avoid contamination from the blue cloud, and apply 3σ clipping. This σ is calculated from galaxies that are brighter than m^*+2, and is not magnitude dependent. The upper and lower solid lines in each panel are the 2σ bounds of the colour distribution of galaxies brighter than m^*+2.

Isolating red-sequence galaxies is non-trivial; both intrinsic scatter and photometric uncertainties can make it difficult to cleanly separate the red-sequence and blue galaxies. This is particularly a problem at faint magnitudes, where photometric errors are large, and the blue cloud dominates the population. Here we select red-sequence galaxies in several different ways and show how they affect the results. The four methods we use are :
1) Red_4σ, where red-sequence galaxies are defined as those that are redder, but not more than 4σ, than the best-fit CMR. The total is twice this number.
2) Red_all, a slight variation of method Red_4σ, where red-sequence galaxies are defined as all those that are on the red side of the best-fit CMR. Again, the total is twice this number.

Method Red_4σ and Red_all are motivated by Barkhouse et al. (2007) and Gilbank et al. (2008) (but in their work the red-sequence galaxies are not mirrored at the bright end).
3) P10_2σ, where red-sequence galaxies are defined as those that have > 10 per cent probability belonging to the colour slice defined by the best-fit CMR with a width of $\pm 2\sigma$ as indicated by the solid lines in Figure 2.14. This method is consistent with how the subsample in each colour slice is selected (§2.3.2) prescribed by Gladders & Yee 2000. Note each galaxy that satisfies this criterion is counted as one galaxy, not weighted by this probability.
4) NP_2σ, where red-sequence galaxies are defined as those that are completely contained within $\pm 2\sigma$ from the best-fit CMR.

To correct for the background contamination, the same strategy is applied to a sample of galaxies at 500 random positions within the four CFHTLS wide fields, for each finely-interpolated colour slice. They are shifted to each central redshift bin in the same way as for the cluster+field sample, and the average number count is used when subtracting the field contribution. The error bars are estimated assuming that the noise follows Poisson statistics, including the background subtraction. Note that the Poisson error on the background is negligibly small, because of the large number of random fields. We do not include the variance of the background field distribution in the error estimate, because here we are primarily interested in the average properties of a large ensemble of clusters, not the cluster-to-cluster variation.

2.7 Results

2.7.1 Red-sequence Luminosity Functions

Our sample

Figure 2.15 shows the $r'-$band red-sequence LFs of all clusters with $N_{red,m^*+2} \geq 12$ in the range of projected radius $0 \leq r < 0.5$ Mpc, k-corrected to rest frame, calculated using the four methods described in §2.6. The depth of the CFHTLS data enables us to reach $M_{r'} \sim -17$ at $z \sim 0.2$, a limit that has never been probed before at this redshift for such a large sample of clusters.

In all panels in Figure 2.15, the dotted histograms are the cluster+field counts, the dashed histograms are background counts, and the solid histograms with error bars are the background-subtracted LFs. The number count in each magnitude bin is normalized by the number of clusters contributing to that bin. The number of clusters in each redshift

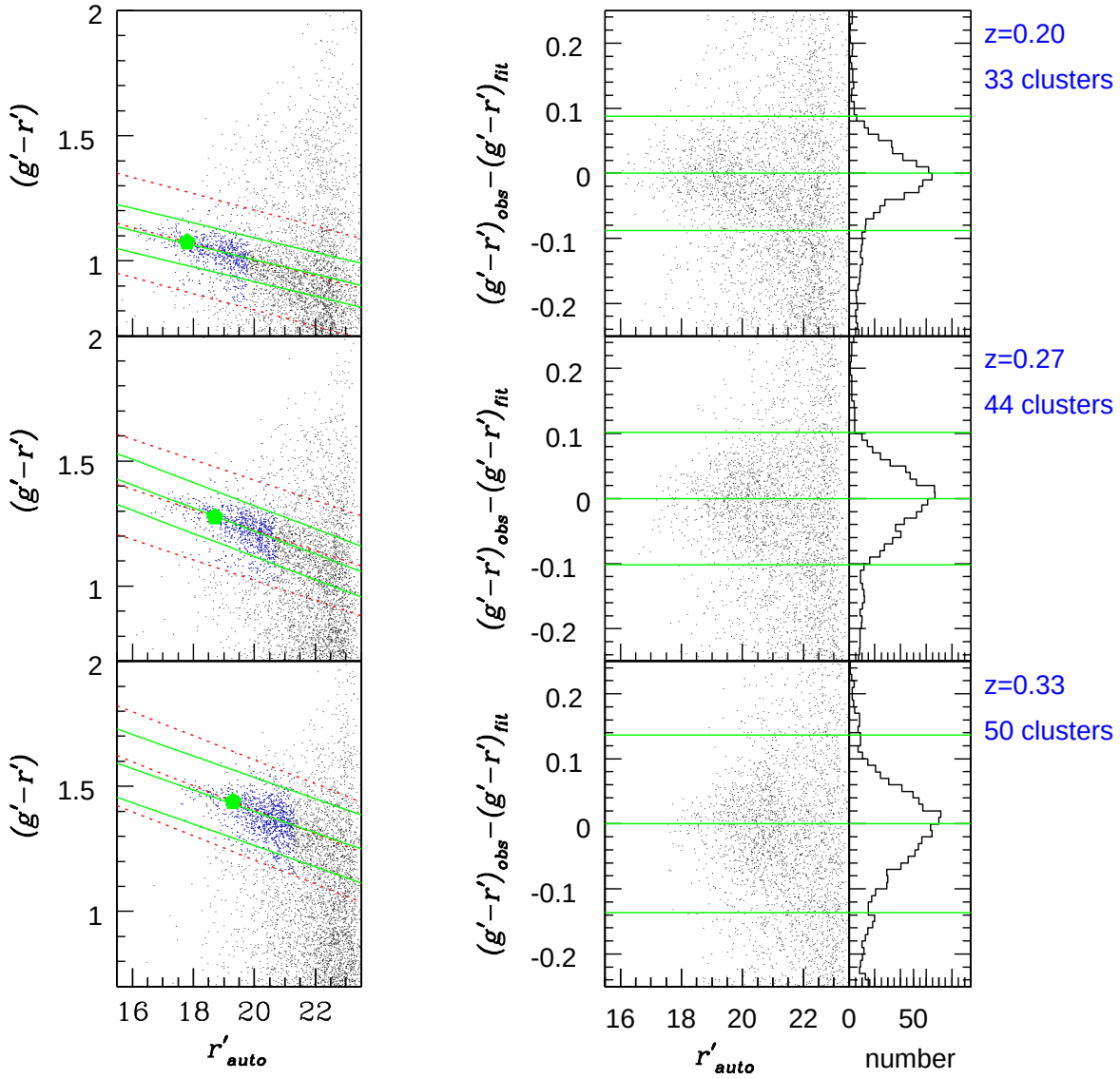

Figure 2.14: Left panel: Composite CMDs of galaxies that are within a radius of 0.5 Mpc from the cluster centre at three different redshifts. The dotted lines indicate ± 0.2 mag from the modelled $(g' - r')$ vs. r' relation. Central solid lines are the new best-fit CMR, based on galaxies that are brighter than $m^* + 2$ (m^* is indicated by the pentagon), shown as the blue points. The upper and lower solid lines are the 2σ bounds. Right panel: in the left column is the CMD with the best-fit CMR subtracted, and in the right column the histograms show the distribution of galaxies relative to the fitted CMR down to $m^* + 2$. The upper and lower solid lines in each panel are the 2σ bounds. See text for details.

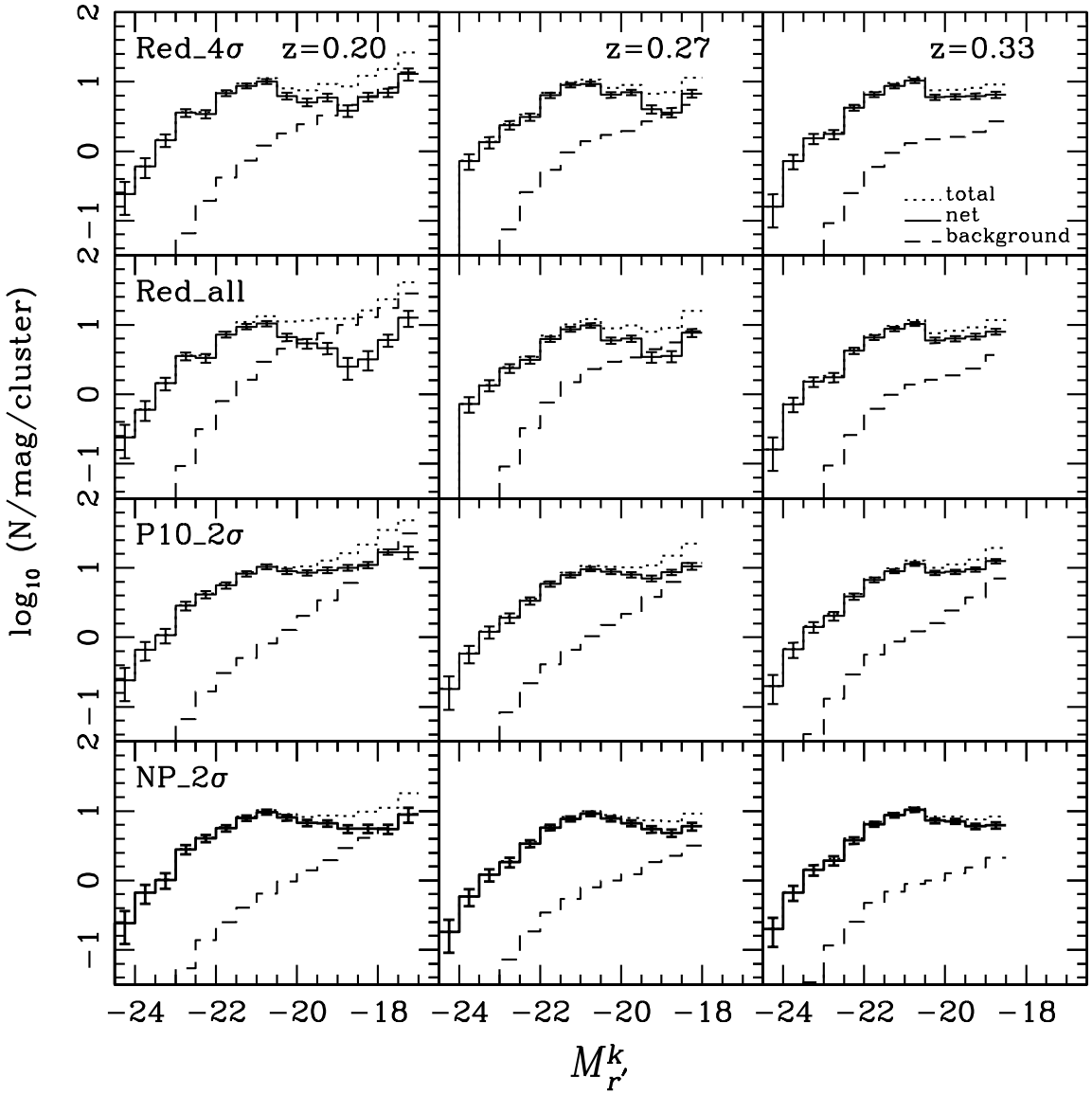

Figure 2.15: Composite $r'-$band red-sequence LFs of clusters with $N_{red,m^*+2} \geq 12$ in the projected radius range of $0 \leq r < 0.5$ Mpc, calculated using the four methods described in the text, shown in four rows respectively. The top row, Red_4σ, is our preferred method, as it minimizes the contamination from the blue cloud, and background galaxies. Magnitudes are k-corrected to rest frame. The dotted histograms are the cluster+field counts, the dashed histograms are background counts and the solid histograms with error bars are the background-subtracted LFs. See text for discussions on each method.

bin is 33, 44 and 50 from low to high redshift, and all clusters contribute fully to all but the faintest magnitude bin due to the completeness limit.

At bright magnitudes, all four methods give consistent results, so it does not matter whether one uses only galaxies on the redder side of the CMR or not. However it makes a difference at faint magnitudes. In Figure 2.15, comparing the net counts from the four methods at magnitudes fainter than $M^k_{r'} = -20.5$ (2 magnitudes fainter than M^*), P10_2σ gives the highest count. This is an overestimate because, at faint magnitudes, the error on the colour is larger; galaxies that are just outside the colour slice can still have a probability of > 10 per cent belonging to the colour slice. Note that the LFs are background-subtracted; therefore this higher net count in method P10_2σ at faint magnitudes is not due to field contamination, but due to the contribution from the cluster blue cloud. Method NP_2σ suffers from the same problem as P10_2σ over the magnitude range $-20.5 < M^k_{r'} < -18.5$, as can be seen from the net count shown in the bottom row. However, at the very faintest magnitudes, NP_2σ gives the lowest net count among the four methods. This is because, in this case, the width of the fixed colour slice is not wide enough compared to the error on the colour at this faint magnitude; thus it underestimates the number of red-sequence galaxies, due to the preferential scattering of the red-sequence galaxies out of the colour slice. This problem cannot be alleviated by using a wider colour slice because then it would significantly overestimate the number of red-sequence galaxies at slightly brighter magnitudes given the above reasoning about method P10_2σ.

On the other hand, method Red_4σ and its slight variation, Red_all, mirror only galaxies on the redder side of the CMR, and thus do not include contributions from the cluster blue cloud that occupy regions blueward of the CMD (especially at faint magnitudes). Moreover, since method Red_all takes account of all galaxies redder than the best-fit CMR, it does not underestimate the number of red-sequence galaxies regardless of the photometric errors. In method Red_4σ, a cut of 4σ redder than the best-fit CMR is applied to eliminate high redshift galaxies with colours much redder than the best-fit CMR. This cut corresponds to $\sim 0.17 - 0.27$ mag from our lowest redshift bin to the highest, which is comparable to or greater than the 1σ error on the colour even at the very faintest magnitude (~ 0.2 mag at $r' \sim 23$, see Figure 2.2); therefore, this cut is broad enough to not significantly underestimate the number of red-sequence galaxies scattered off the CMR due to photometric errors. Comparing the results from these two methods (first and second row in Figure 2.15), we see that the net counts are consistent (solid histograms), but the background (dashed histograms) in method Red_4σ is significantly reduced compared to that in method Red_all; therefore, we conclude that Red_4σ is the best, and in the rest of the Chapter, we will use this method for all the analysis.

The most outstanding feature of our red-sequence LF at $z \sim 0.2$ is a significant and broad dip starting at $M_{r'} \sim -20.5$. The number of red-sequence galaxies reaches its maximum at $M_{r'} \sim -20.5$, and then decreases to 40 per cent of the maximum value

at $M_{r'} \sim -18.5$, and comes back up at magnitudes fainter than that. At this redshift, $M_{r'} \sim -18.5$ corresponds to $r' \sim 22$, where the error on the colour and total magnitude is still small (see Figure 2.2); thus this inflexion is robust. This feature is also present at $z \sim 0.27$. It is hard to discern at $z \sim 0.33$ due to the magnitude limit of the data and the fact that the error on the colour is getting large at the very faintest magnitudes. The dip in the LF probably suggests that the LF is made up of a mixture of two populations of red-sequence galaxies, possibly giant/regular elliptical and dwarf ellipticals (dEs): as can be seen in figure 1 of Binggeli et al. (1988), the LF of E and S0 galaxies peak at bright magnitudes and drop off at the faint end where the LF of dEs starts to increase. The disappearance of dEs over the magnitude range seen in our LF could mean that those dwarf galaxies on this mass scale are either disrupted (by, for example, tidal forces) or they merge into more massive galaxies.

Although the existence of dips in the red-sequence/early-type LFs has been established in many studies (e.g. Popesso et al., 2006; Barkhouse et al., 2007; Mercurio et al., 2006; Secker & Harris, 1996), the depth of the dip and the faint-end slope of the LFs are still not well constrained, varying significantly in different studies. We examine this issure more closely in §2.8.1.

In most cases, instead of fitting a single Schechter function, double Schechter functions: one for the bright end and one for the faint end; or Gaussian (bright end) + Schechter (faint end) functions are used to try to accurately represent the shape of the LFs with dips. In our two lowest redshift bins, we find that double Schechter functions do not provide a good fit to the LF (without removing the brightest cluster galaxies). Instead, a Gaussian + Schechter function fit describes the shapes of our LFs better. For the highest redshift bin, due to the limit of the data, it is hard to tell whether the inflexion exists; therefore a single Schechter function provides an acceptable fit as well. In the lowest redshift bin, all six parameters in the Gaussian + Schechter function are free; but in the two high redshift bins, the data are not adequate to constrain the faint end and therefore we fix the M^* and α at the best-fit values from the lowest redshift bin. Note we do not explore the degeneracy among the parameters as that is not our purpose here; we only seek a set of parameters that accurately reflect the shape of our LFs. The best-fit parameters of our LFs obtained using method Red_4σ are listed in Table 2.7.1 and the fits are plotted as solid curves over the k-corrected and background-subtracted LFs (histograms) in the top panel in Figure 2.16. Within the uncertainty, the fit to the LF in the lowest redshift bin can also fairly represent the LFs in the two higher redshift bins. Note the fits are for k-corrected LFs, but given the low redshift probed here, the evolutionary correction is small; thus this implies no strong evolution in this redshift range.

In the bottom panel of Figure 2.16, we plot our $(k+e)$-corrected LFs. Solid histograms represent the LF in each redshift bin, and the one from the lowest redshift is overplotted as dotted histogram in the two high redshift bins. There does not seem to be a strong evolution

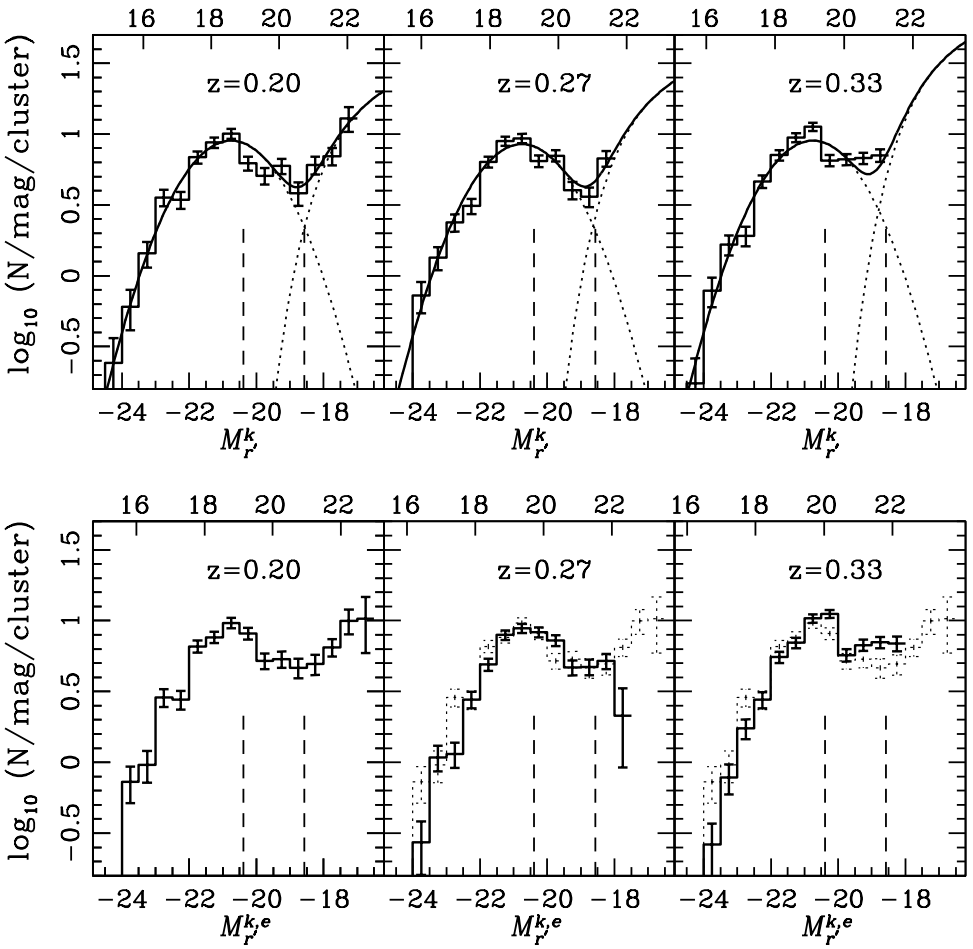

Figure 2.16: Top panel: k-corrected, background-subtracted red-sequence LFs (histograms) obtained using method Red_4σ in three redshift bins with the best-fit Gaussian + Schechter functions overplotted as solid curves (dotted curves show the two components separately). For the lowest redshift bin, all 6 parameters in the fit are free; for the two higher redshift bins, the M^* and α are fixed at the best-fit values from the lowest redshift bin. k-corrected rest-frame absolute magnitude and apparent magnitude are labelled on the bottom and top axes, respectively. The two vertical dashed lines indicate the division between dwarf and giant as in De Lucia et al. (2007). Bottom panel: LFs with $(k+e)$-correction applied. Solid histograms represent $(k+e)$-corrected LF at each redshift. The one in the lowest redshift bin is plotted for reference on top of that in the two higher redshift bins as dotted histograms. Top and bottom axes label the apparent magnitude and $(k+e)$-corrected rest-frame absolute magnitude, respectively. Again, the vertical dashed lines indicate the division between dwarf and giant.

	Gaussian			Schechter		
z	$< M_{r'} >$	σ	ϕ_{gau}	$M^*_{r'}$	α	ϕ
0.20	-20.75	1.3	9.0	-17.75	-1.15	22.5
0.27	-20.75	1.3	8.5	(-17.75)	(-1.15)	26.5
0.33	-20.75	1.3	9.0	(-17.75)	(-1.15)	50.0

Table 2.3: Best-fit parameters of the LFs of our cluster sample constructed using method Red_4σ. Bracketed values are fixed from the lowest redshift bin.

above that of passive evolution. In each panel, the two vertical dashed lines indicate the division between dwarf and giant as in De Lucia et al. (2007). Galaxies brighter than the magnitude indicated by the line on the left are considered giants; and galaxies between the two lines are defined as dwarfs (the dwarf-to-giant ratio, DGR, will be discussed later on).

Low-redshift comparison

As seen in the above section, there does not seem to be a strong evolution of the red-sequence LFs within our sample at $0.2 \lesssim z \lesssim 0.4$. In this section, we compare the LFs of our sample with that of the Yang07 sample and the intensely studied local rich cluster, Coma. In Figure 2.17, the solid histogram is the red-sequence LF of our sample at $z \sim 0.2$, with the brightest cluster galaxies removed (for easier comparison with the literature later). Solid points and triangles are the red-sequence LFs of the Yang07 sample ($z \sim 0.085$, §2.5) and Coma ($z = 0.023$), respectively, calculated using our method Red_4σ, and passively evolved to $z = 0.2$. To compare the shapes of these LFs, in Figure 2.17 they are all normalised to give the same total number count down to $M_{r'} = -20.5$. Since these LFs are constructed using the same method, and the filter combinations used at these redshifts bracket the 4000Å break in a similar way, the differences in their faint ends are not likely due to method differences, but genuine, suggesting a steepening of the faint end with decreasing redshift (but note that Coma is ~ 4 times richer than the typical clusters in our and the Yang07 samples, and we will discuss this in §2.8.3).

2.7.2 Red-sequence Dwarf-to-Giant Ratio (DGR)

The DGR is the ratio of the number of faint galaxies to bright ones, and thus is commonly used as a simple indicator of the shape of the LF. Since red-sequence galaxies represent the population that have had their star formation shut off, the evolution of red-sequence DGR traces the history of the quenching of the star formation.

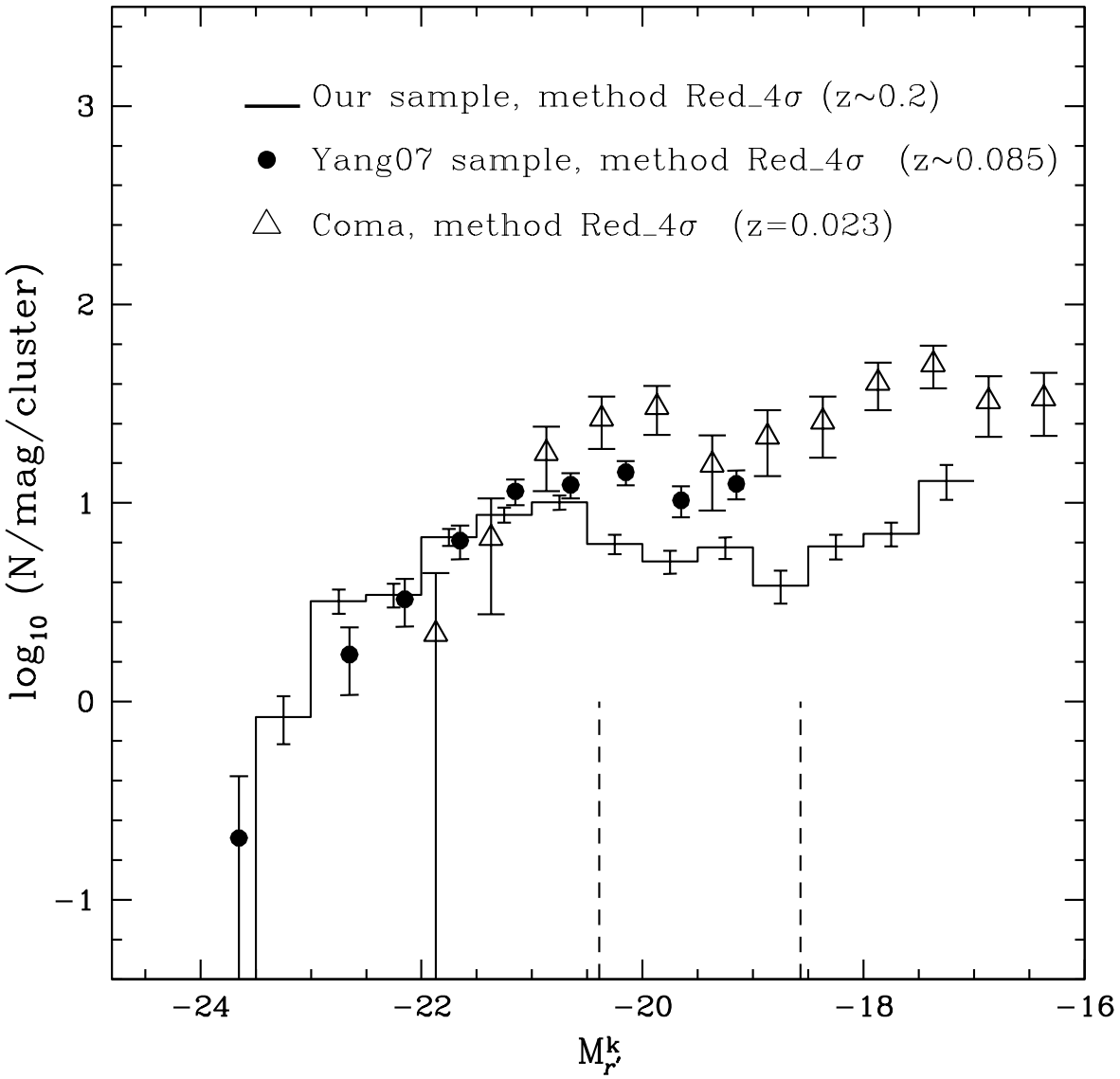

Figure 2.17: $r'-$band red-sequence LFs at different redshifts, passively evolved to $z = 0.2$. Magnitudes are k-corrected to rest-frame at $z = 0$. The solid histogram is the red-sequence LF of our sample at $z \sim 0.2$, with the brightest cluster galaxies excluded. Solid points and triangles are the red-sequence LF of the Yang07 sample ($z \sim 0.085$, §2.5) and Coma ($z = 0.023$), respectively. All LFs are calculated using our method Red_4σ, and normalized to give the same cumulative number count down to $M^k_{r'} = -20.5$. The two vertical dashed lines show the approximate division between dwarf and giant as in De Lucia et al. (2007). See text for details.

DGR of Our Cluster Sample

To make it easier to compare with previous works, here we $k + e$ correct the apparent magnitude to rest frame at $z = 0$, and adopt the definition of dwarf and giant used by De Lucia et al. (2007), i.e. galaxies brighter than -20 in rest-frame V in the Vega system are considered as giant and those between -20 and -18.2 are defined as dwarf. We convert the definition of dwarf and giant in V to our rest-frame r' magnitude using the $(V - r')$ colour produced by the same old, single-burst model described in §2.3.1. The triangles in Figure 2.18 are the red-sequence DGRs of our cluster sample with $N_{red,m^*+2} \geq 12$, in the radius range $0 \leq r < 0.5$ Mpc, calculated using method Red_4σ. The bottom and top axis labels show the look-back time and redshift respectively. The small error bars on our data points are estimated assuming Poisson statistics, without including the variance of the background field distribution, because what we are after is the average behaviour of the large sample. To get an idea of how large the error bar would be on the DGR of a single cluster, we calculate the uncertainty on the DGRs for a few individual clusters that have DGRs similar to the ensemble average, taking into account the noise on the mean background and the variance of the distribution of the 500 random fields. The typical uncertainties are plotted as dotted error bars on the triangles in Figure 2.18. We also find a wide cluster-to-cluster variation, and 8 out of 127 of our clusters have $DGR > 2$. We will explore this further in the following discussion section.

Evolution with Redshift

To explore the redshift evolution of the red-sequence DGR, we also calculate the DGR for the local comparison sample and Coma (§2.5), shown as the square and solid pentagon in Figure 2.18. The DGRs we have calculated consistently at different redshifts show no strong evolution in the redshift range $0.2 \lesssim z \lesssim 0.4$, but a rapid increase from $z \sim 0.2$ to $z \sim 0$. Assuming that the bright end of the LF has not evolved significantly, our results imply that the number of dwarf galaxies has increased by a factor of ~ 3 over the last 2.5 Gyr. This rapid evolution since $z \sim 0.2$ is not inconsistent with the predictions from either single burst simple stellar population (SSP) or quenched models by Smith et al. (2009) through the measurement of the age of faint red galaxies in Coma using line indices (see their figure 15), although our results agree more with their prediction for the outskirt regions instead of the core regions. Despite the rapid increase in the number of dwarf galaxies, they do not contribute significantly to the growth of the stellar mass on the red-sequence, *per cluster*. Using the stellar mass-to-light ratios from the same simple model we used to construct the CMD, an increase in the DGR from ~ 0.8 to ~ 2.5 corresponds to a ~ 15 per cent increase in the stellar mass on the red-sequence, *per cluster*.

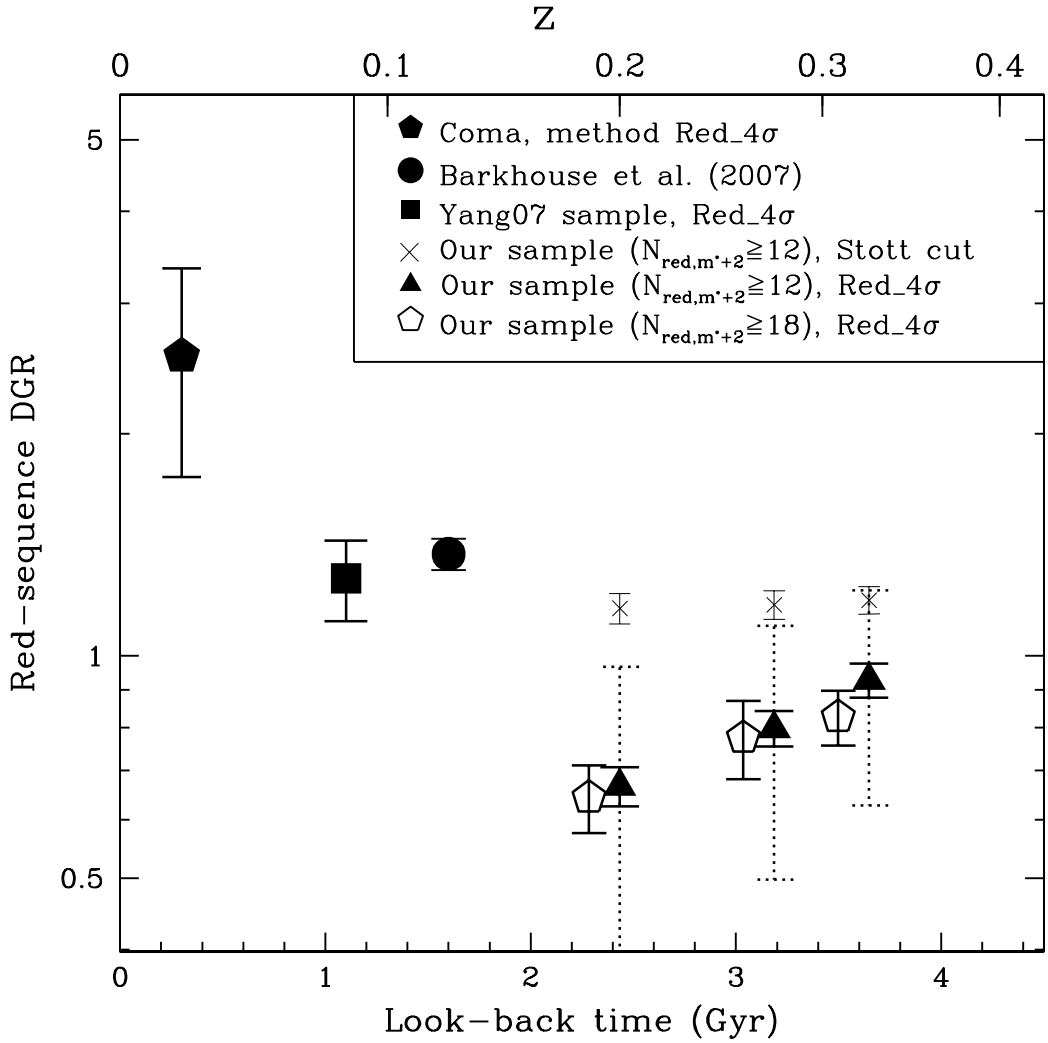

Figure 2.18: Red-sequence DGRs as a function of look-back time and redshift. Triangles are the DGRs of our cluster sample with $N_{red,m^*+2} \geq 12$, in the radius range of $0 \leq r < 0.5$ Mpc, calculated using method Red_4σ. The solid error bars indicate uncertainties on the sample average DGRs, while dotted error bars represent typical errors on the DGR of a single cluster whose DGR is similar to the ensemble average. Open pentagons are the DGRs of a rich subset of our cluster sample with $N_{red,m^*+2} \geq 18$ (discussed in §2.8.3), plotted with slight offset in redshift for clarity. The solid square and pentagon are the red-sequence DGR of the Yang07 sample and Coma, calculated using method Red_4σ. The filled circle is from Barkhouse et al. (2007). Crosses are the DGR of our sample, calculated using the Stott et al. (2007) colour cut. See text for more discussion.

2.8 Discussion

2.8.1 Comparison with Literature

Studies on cluster red-sequence LF in the literature have used quite different colour cuts to select red-sequence galaxies. In this section, we compare our red-sequence LFs and DGRs with that in the literature. Given the redshift evolution shown above, we split the comparison into two redshifts. The LFs in the literature are transformed into our r' filter and passively evolved to $z = 0.2$, using the same SSP Bruzual & Charlot (2003) model described in §2.3.1. Magnitudes are converted to the cosmology used in this work, if different.

In the work by Barkhouse et al. (2007), the red-sequence galaxies are selected in a way that is very similar to our method Red_4σ (see §2.6); therefore it is directly comparable to our measurement of the Yang07 sample (Figure 2.17) given the similar redshift. In the left panel of Figure 2.19, the solid histogram is the red-sequence LF of a sample of Abell clusters that are X-ray detected in the EINSTEIN X-ray images (Jones & Forman, 1999) used in Barkhouse et al. (2007), measured within the same physical radius (< 0.5 Mpc) as in this work (Barkhouse, priv. comm.). The filled circles represent the LF we measured for the Yang07 sample. The two LFs agree fairly well with each other in general. Note the LFs are normalized to give the same cumulative number count down to $M_{r'} = -20.5$ (around $m^* + 2$); if a slightly fainter magnitude cut is used, given the relatively large uncertainties at the bright end, the two LFs would then have an even better agreement at the faint magnitudes. A simple way to circumvent the issue of the relative normalization is to calculate the DGR. The DGR calculated from the LF of the sample from Barkhouse et al. (2007) is shown as the filled circle in Figure 2.18, and it is consistent with that from the Yang07 sample (the square). At a similar redshift, Stott et al. (2007) studied 10 X-ray-luminous ($L_X > 5 \times 10^{44}\ ergs\ s^{-1}$) clusters at $\bar{z} = 0.13$ from the Las Campanas/AAT Rich Cluster Survey (LARCS; Pimbblet et al. 2001, 2006), and their LF is shown as the open circles in Figure 2.19. It has a steeper faint end than that from both Barkhouse et al. (2007) and the Yang07 sample. We attribute this difference to the way red-sequence galaxies are selected: in the work by Stott et al. (2007), red-sequence galaxies are considered as those within a fixed colour cut around the CMR ($|\triangle(B-R)| < 0.4$ mag). This cut is very wide, and therefore would include contamination from the blue cluster members, overestimating the number of faint red-sequence galaxies. Other works at a similar redshift include, for example, Tanaka et al. (2005) and Hansen et al. (2009). We do not compare our LFs with that in those works here because, in Tanaka et al. (2005) the cluster environment is defined using local density, and thus is not clear within what physical radius the measurement is made. And in the work by Hansen et al. (2009) the cluster sample spans over a redshift range ($0.1 < z < 0.3$) within which we see evolution in this work; therefore it is not directly

comparable.

In the right panel of Figure 2.19, the solid histogram is the LF of our sample at $z \sim 0.2$, calculated using method Red_4σ, with the brightest cluster galaxies included for easy comparison with the study from Smail et al. (1998). Circles and triangles are red-sequence LFs of a sample of 10 X-ray clusters from ROSAT All Sky Survey at $z = 0.22 - 0.28$ from Smail et al. (1998). Circles represent red galaxies selected using $(U - B)$ colour with a width from $0.28 - 0.43$ mag as a function of magnitude, and triangles are selected using $(B - I)$ colour with a width from $0.18 - 0.33$ mag. The filter combination of $(B - I)$ is similar to $(g' - r')$, and the relatively narrow colour slice with varying width as a function of magnitude makes it more similar to our method P10_2σ. The LF selected using $(U - B)$ has a better agreement with our LF from method Red_4σ, which could be due to the fact that at $z \sim 0.2$ the $(U - B)$ colour is more sensitive to recent star formation than $(B - I)$, and therefore the population that is red in $(U - B)$ is less contaminated by the cluster blue cloud. As a result, the DGR from this LF would be located close to that of our sample at $z \sim 0.2$ if plotted in Figure 2.18. To show how a wide colour cut affects the LF and DGR of our sample, we calculate the LF of our sample using the colour cut of Stott et al. (2007). We transform the difference in $(B - R)$ into $(g' - r')$ making use of the colour difference between E and Sab galaxies in $(B - R)$ and in $(g' - r')$ at $z = 0.2$ from Fukugita et al. (1995). The resulting LF for the sample at $z \sim 0.2$ is shown as the dotted histogram in the right panel of Figure 2.19, and the DGRs are shown as crosses in Figure 2.18. Comparing with our LF calculated using method Red_4σ, it produces significantly more faint red-sequence galaxies, and as a result gives a higher DGR. This shows that the faint end is sensitive to the selection method; therefore when looking for evolution with the redshift, it is important to make sure all methods are consistent.

The DGR of Coma we calculated (2.5 ± 0.8) is comparable to that in other studies in the literature that used statistical background subtraction (e.g. De Lucia et al., 2007; Stott et al., 2007; Andreon, 2008). Also, a complete spectroscopic study on Coma by Marzke (priv. comm.) obtained a red-sequence DGR of ~ 2.1, which confirms the results from statistical studies.

The red-sequence DGRs from the studies in the literature are compiled in the work by Gilbank & Balogh (2008) (see their figure 1). In the redshift range $0.1 \lesssim z \lesssim 0.4$, our measurements of the DGRs are systematically lower than those in the literature (but note most of those studies do not directly overlap with this redshift range). Given that the available studies in the literature for the compilation all used different selection criteria for red-sequence galaxies, and we have shown that the faint end and thus the DGR is sensitive to the selection method, we suggest the discrepancy is mostly due to how red-sequence galaxies are selected.

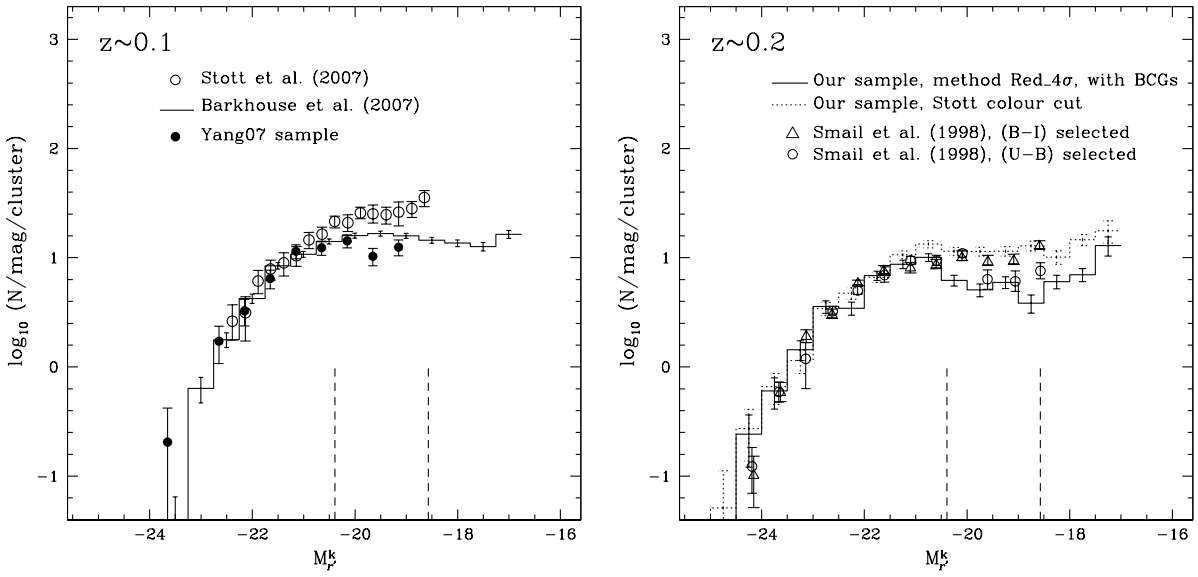

Figure 2.19: Comparison of our red-sequence LFs with those in the literature. Left panel: the solid histogram, filled circles, and open circles represent the red-sequence LFs of the Yang07 sample, Barkhouse et al. (2007) and Stott et al. (2007), all passively evolved to $z = 0.2$. Right panel: the solid histogram is the LF of our sample at $z \sim 0.2$, calculated using method Red_4σ, with the brightest cluster galaxies included for easy comparison with the study from Smail et al. (1998). Circles and triangles are red-sequence LFs from Smail et al. (1998), with red-sequence galaxies selected using $(U - B)$, and $(B - I)$ colour respectively. The dotted histogram is the LF of our sample derived using the colour cut adopted by Stott et al. (2007). Again, Magnitudes are k-corrected to rest-frame at $z = 0$. The two vertical dashed lines show the approximate division between dwarf and giant as in De Lucia et al. (2007). See text for discussion.

2.8.2 The Relation between Red Galaxies and Passive Galaxies

Our purpose of studying red-sequence galaxies is to understand how their star formation is shut off as they move from the blue cloud; therefore we want to select a population that is as close to a truely quiescent population as possible.

The population selected using colour that brackets the 4000Å break probably is very close to a population that is truely dead, however it can be contaminated by dusty star-forming galaxies (e.g. Wolf et al., 2009). Since FIR ($24\mu m$) emission is sensitive to dusty star formation, it can be used to estimate the contamination from the dusty star-forming galaxies with red colours, and to select passive populations. The CFHTLS W1 field overlaps with the *Spitzer* Wide-area Infrared Extragalactic Survey (SWIRE) XMM-LSS field, but the depth of the 24 μm data is not enough to estimate the contamination of the dusty star-forming galaxies down to low enough SFR at the redshifts probed in this work. According to the work by Wolf et al. (2009), in the core of clusters, the contamination of dusty star-forming galaxies with SFR down to 0.14 $M_{\odot}$ yr^{-1} is $\sim$ 20 per cent, dominating at $M_* > 10^{10} M_{\odot}$, and $<$ 10 per cent at $M_* < 10^{10} M_{\odot}$. However, the contamination rate is likely to be lower because in that work not enough information is available to eliminate the contribution from AGNs. Therefore, we believe our LF is an accurate representation of the truly inactive population.

Other than colour, galaxies can be categorized according to their morphology as well. Traditionally, elliptical and lenticular galaxies are termed early-type galaxies, while spiral galaxies are considered late-type galaxies. Also, emission-line strength can be used to broadly divide galaxies into emission-line (star-forming) or non-emission-line (non-star-forming) galaxies. These methods may not select exactly the same population. The morphological selection does not always trace star formation: although elliptical galaxies are generally considered as non-star-forming, observations have indicated that a fraction of elliptical galaxies do show recent star formation (e.g. Kaviraj et al., 2007); thus they would be included in a morphologically selected sample. On the other hand, there could be spiral galaxies that do not have star formation, as indicated by the partially independent transformation in morphology and star formation rate in cluster environments (e.g. Kodama et al., 2004); thus these spiral galaxies would be missed. Therefore, we compare the passive population selected using these different methods.

Godwin & Peach (1977) constructed the LFs of Coma for different morphological types using the magnitude measured from photographic plates. Based on the numbers read off their figure 4, the DGR of the elliptical+lenticular galaxies is ~ 2.2. This is consistent with the DGR of the red-sequence galaxies in Coma selected using colour (this work, 2.5 ± 0.8; Marzke (priv. comm.); De Lucia et al., 2007; Stott et al., 2007; Andreon, 2008).

Christlein & Zabludoff (2003) constructed $R-$band LF for six Abell clusters at $0.013 \leq z \leq 0.067$, and split them into emission-line and non-emission-line samples, based on

their [OII] strength. The DGR we calculate from their LF of the non-emission-line cluster galaxies (2.0 ± 0.2), is between that of the Yang07 sample and Coma, consistent with the trend seen in Figure 2.18 (although note the criterion of EW[OII]<5Å used to select non-emission-line galaxies in their work still allows a moderate level of star formation). These comparsions suggest that at low redshift, colour, morphology or emission-line selects mostly the same passive population. This is consistent with the studies by for example, Schweizer & Seitzer (1992); Strateva et al. (2001) and Hogg et al. (2002).

2.8.3 Possible Systematics

Local vs. Global Background

We have used a global background subtraction to construct the LFs described in §2.7.1. However, since there are associated large-scale structures around clusters, the background around clusters might be different from the random field. Therefore, we test this effect by constructing the LFs for our sample using global background subtraction. Instead of taking 500 random fields, for each cluster we take the galaxy count in an annulus of radius 10 Mpc around the cluster centre, with an area equivalent to the $r < 0.5$ Mpc core, as the background. The resulting LFs are consistent with those shown in Figure 2.15. Thus, we conclude that the use of a global background does not bias our results.

Even if our background is underestimated due to the presence of large-scale structure, this will not have a significant effect on the red-sequence DGR. As can be seen from Figure 2.15, using method Red_4σ the background is negligible except at low redshift and at magnitudes fainter than those used to define the dwarf population.

Note that the LFs we derived, and those in the literature with which we compared, are of the projected galaxy distribution. Thus, they include galaxies from $r > 0.5$ Mpc. This may lead to a faint end slope which is somewhat steeper than that of the genuine core population, but would not significantly affect the DGR measurement (e.g. Barkhouse et al., 2007).

Systematic Uncertainties in Photometry

In this section, we examine any systematic uncertainties in photometry. We make use of the data in D1 to examine whether the shallower faint end of our LFs is due to incompleteness, or biased photometry. Two clusters in our sample are in both W1 and D1. We construct the LF based on the data from D1 and compare it with that constructed using data from W1. The two LFs are consistent within the uncertainty, although the error bars are rather large, given the small number of clusters. Thus, the lack of low-luminosity galaxies at

$0.2 \lesssim z \lesssim 0.4$ we find is not due to insufficient depth or biased photometry. This is not unexpected, as we have shown we are 100 per cent complete, with small errors at the relevant magnitude, based on comparison with the same D1 field.

As an external check, we extract from the SDSS archive a subset of galaxies in a 2x2 square degree region that overlaps with the CFHTLS W1 field, and compare the total magnitude (mag_auto for CFHTLS, and mag_model for SDSS) of the common galaxies. After transforming the CFHTLS magnitude to SDSS magnitude using the formula provided on the Terapix website[†], the median of the distribution of the magnitude difference in g', r' and i' filters are all less than ~ 0.05 mag, and with no obvious trend with magnitude.

Therefore, the uncertainties in the CFHTLS photometry is not a major source of error.

Redshift Accuracy

As described in §2.4.3, the redshifts we assign to our clusters are accurate to the ~ 0.01 level. If the estimated redshift of a cluster is slightly higher or lower than what it actually is, the absolute magnitudes of galaxies in that cluster converted from apparent magnitudes will be brighter or fainter than what they should be, and the intrinsic shape of the LF will be distorted. Here we examine how big this effect is using the Schechter function fit from Barkhouse et al. (2007). We simulate a sample of 100 clusters at $z = 0.2$, each of them with the same intrinsic LF as the Schechter function fit from Barkhouse et al. (2007). We use a Monte Carlo method, randomly assigning a redshift to each cluster in the range of $z = 0.2 \pm 0.01$. This is equivalent to randomly shifting the LF horizontally toward brighter or fainter magnitudes by 0.29 mag. We then take the average of the 100 shifted LFs as the stacked LF for this sample. The stacked LF only makes $\sim$1.3 per cent difference to the bright end (brighter than $M_{r'} = -21$) of the undistorted LF, and $\sim$0.1 per cent to the faint end. Therefore, this does not affect our results. Note, this uncertainty of $\triangle z \sim 0.01$ is comparable to the redshift interval between two adjacent colour slices; thus the effect of projection (§2.8.3) is of comparable uncertainty.

Aperture Effect

As mentioned in §2.2.2, the colour is measured within a fixed aperture of diameter 4.7 arcsec. To examine how colour gradients of galaxies affect our results, we measure the colour in a smaller aperture, of diameter 3 arcsec, and compare the colours measured in the two different apertures. The distribution of the colour difference of the red-sequence galaxies in the two apertures is symmetric in general. The scattering of the distribution

[†] http://terapix.iap.fr/rubrique.php?id_rubrique=241

is smaller than or comparable to the uncertainty on the colour determined using the overlapping pointings (see Figure 2.2). At the bright end, the median of the colour in the larger aperture is ~ 0.03 mag bluer (smaller than the width of the colour slice). For the LFs constructed using methods P10_2σ and NP_2σ, the number of red-sequence galaxies might be slightly underestimated due to this scattering. However, for methods Red_4σ and Red_all, the results are not affected as long as the scattering is symmetric.

Richness Dependence

Since we detect clusters using only galaxies brighter than m^*+2, which is around the magnitude that separates giant from dwarf galaxies, it is possible that our sample is biased towards systems with more giants. To test this, we examine whether clusters with fewer giants have higher DGRs. We calculate the DGRs for a subset of very rich clusters with $N_{red,m^*+2} \geq 18$ (plotted as open pentagons in Figure 2.18, with slight offset in redshift for clarity), and for a set of clusters that are not rich enough to be included in our final catalogue ($7 \leq N_{red,m^*+2} \leq 10$), using our best method Red_4σ. We do not find strong dependence of the DGR on the richness of the clusters. Therefore, our results are not biased due to the detection method. Note the richness of our clusters is measured within a radius of 0.5 Mpc from cluster centres, and all analysis are carried out for the same region. To check if this biases our results, we calculate the DGR using a slightly larger radius (r <1 Mpc), and find that the change of DGR is within $\sim 1\sigma$ of the values shown by the triangles in Figure 2.18; thus it does not change our conclusions either.

For clusters with $N_{red,m^*+2} \geq 12$, we do not detect obvious correlation between the individual DGR and N_{red,m^*+2}. For the richest cluster in our sample, Abell0362 at $z \sim 0.2$ (§2.4.1), its red-sequence DGR is $\sim 0.7 \pm 0.2$, similar to the sample average DGR. The deficit of dwarf galaxies ($20.5 < r' < 22.3$) is clearly visible on its CMD in Figure 2.9. For the four clusters in our sample that have comparable richness as Coma, their average DGR is 0.9 ± 0.1, similar to the sample average as well. We also constructed the composite red-sequence LF for the four X-ray confirmed clusters that have $N_{red,m^*+2} \geq 12$ (but they are all poor clusters with kT$\sim$ 2 keV), and it is consistent with the LF of the whole sample, within the uncertainties.

Note although Coma is ~ 4 times richer than the typical clusters in our sample and the Yang07 sample, the lack of strong richness dependence of the red-sequence DGR seen in our sample suggests that the rapid evolution between $z \sim 0.2$ and $z \sim 0$ we see in Figure 2.18 is probably a genuine redshift evolution. However, this is based on the assumption that the lack of richness dependence still holds at $z \sim 0$, and that Coma is a typical cluster at this redshift, that can be fairly compared with our ensemble averages. We will use a larger low redshift comparison sample to explore this issue in the future work.

Note, at higher redshifts, $z \sim 0.5$, the study by Gilbank et al. (2008), using a statistical sample of red-sequence selected clusters (similar to that presented in this work), found that the red-sequence DGR is higher for richer systems than that for poorer systems. This is contrary to the findings of De Lucia et al. (2007), who used ~ 10 optically selected clusters at $z \sim 0.4 - 0.8$. The richness cuts used in Gilbank et al. (2008) are $B_{gc} > 800$ for the richer subsample (the richness parameter, B_{gc}, is described in Yee & López-Cruz 1999), and $300 < B_{gc} < 500$ for the poorer subsample. De Lucia et al. (2007) calculated the dynamical masses (rather than richnesses) via velocity dispersions for individual clusters. The criterion they used to separate "richer" (higher velocity dispersion) and "poorer" (lower velocity dispersion) clusters was the velocity dispersion being higher or lower than 600 km s^{-1} (which is approximately $B_{gc} \sim 600$, Gilbank et al. 2008). The division used in both studies roughly corresponds to $N_{red,m^*+2} \sim 12$ in our cluster sample, since the virial mass of a cluster with $\sigma = 600$ km s^{-1} and $r_{200} \sim 1$ Mpc is $\sim 1 \times 10^{14} M_{\odot}$. Thus the richness/mass-dependence of the red-sequence DGR at $z \gtrsim 0.4$ is still an open question.

Projection Effect

If two clusters are close enough in redshift space (within neighbouring colour slices), and are projected along the line-of-sight, their red-sequences would not be distinguished. As a consequence of this projection effect, the number count of galaxies per cluster would be overestimated, and the shape of the LFs would be slightly smoothed (although this latter effect is small, see §2.8.3). Another consequence is that it might reduce any trend of the DGR with richness, since a rich system that consists of two projected poorer systems would give a DGR that is similar to the poorer systems.

According to, for example, Gilbank et al. (2008), for clusters in the Red-Sequence Cluster Survey (Gladders & Yee, 2005) over the redshift range $0.4 < z < 1$, the contamination rate from projected systems is $\sim 5 - 10$ per cent. Since the method we use to detect our clusters is based on the CRS method, we expect the contamination rate to be similar. In the future work, we will use the full CFHTLS data to explore this more thoroughly.

Slope of the CMR

Since our method Red_4σ mirrors galaxies on the redder side of the best-fit CMR to avoid contamination from the cluster blue cloud, it is important that the best-fit CMR goes through the centre of the red-sequence. Because of the heavy contamination from the blue cloud at faint magnitudes, the fit to the CMR is carried out at brighter magnitudes down to $m^* + 2$, and extrapolated to fainter magnitudes. To test the effect of the fitted slope on the DGR, we fix the colour of the best-fit CMR at m^*, vary the slope by $\pm \sim 20$ per cent,

and recalculate the red-sequence DGR using method Red_4σ. The variation of the DGR due to this slope change is about 20 per cent, and thus does not change our conclusions.

The extrapolation of CMR from bright magnitudes to fainter ones implicitly assumes that the slope is independent of magnitude. This is reasonable for a truely passive population that is already dead, which is what we are after here. For galaxies that are in the transition of moving from the blue cloud onto the faint end of the red-sequence, we would expect the colour of the red-sequence galaxies to be bluer towards fainter magnitudes; therefore a constant slope over the whole magnitude range would underestimate this population in transition. Which method to use depends on which population one is after.

Filter Transformation

Since the division between dwarf and giant galaxy is defined in the $z = 0$ rest-frame V band in the Vega system (De Lucia et al., 2007), we now examine the effect of the uncertainty in passband transformation on the red-sequence DGR.

As mentioned in §2.3.1, we use a simple single-burst model, calibrated with the data of Coma, to produce the red-sequence CMD. The $(V - r')$ colour we use to transform the definition of dwarf and giant in V to r' is produced by the same model. The uncertainty associated with this transformation could come from a few sources: for example, the magnitude-metallicity relation fitted to reproduce the CMR of Coma, which, if slightly different, would produce a different colour for a given magnitude; the uncertainties on the photometry of the Coma data (Bower et al., 1992) could also introduce an error on the $(V - r')$ colour. However, given that the spectral energy distribution of the old galaxy population is well known, and over the redshift range studied in this work the observed r' band is similar to the rest-frame V band, we expect the uncertainty on $(V - r')$ to be small, at a level of < 0.1 mag.

We now examine how an uncertainty of ± 0.1 mag on the division between dwarf and giant in r' would affect our results. To maximize the effect, we make the dividing point between dwarf and giant 0.1 mag brighter, and the faint limit of dwarf 0.1 mag fainter. The resulting DGRs for our cluster sample calculated exactly the same way as in §2.7.2 are 0.8 ± 0.05 at $z \sim 0.2$; 1.0 ± 0.05 at $z \sim 0.27$, and 1.1 ± 0.06 at $z \sim 0.33$. Note this demonstrates the maximum effect by taking an extreme case (two offsets of 0.1 mag in directions chosen to maximise changes in DGR); the real impact on the results due to the filter transformation is smaller than this.

None of the systematics discussed in this section significantly affects our results. Thus, the lack of evolution at $0.2 \lesssim z \lesssim 0.4$, and the stronger evolution since $z \sim 0.2$ seen is robust.

2.9 Conclusions

In this work we detected and compiled a large sample of 127 clusters over the redshift range of $0.17 \leq z \leq 0.36$ from the CFHTLS data using a method similar to the CRS method (Gladders & Yee, 2000), and constructed the $r'-$band red-sequence LFs within a projected radius of $r < 0.5$ Mpc from cluster centres. The depth of the CFHTLS data enables us to go deeper at these redshifts for a larger sample than previous studies. Our main results are as follows:

• We have presented a thorough study of the effect of colour selections on the red-sequence LF, and showed that the faint end of the LF is very sensitive to how red-sequence galaxies are selected. We find that one optimal way to minimise the blue cloud contamination is to consider only galaxies redder (but no redder than 4σ) than the CMR, and then double the number count; with a second colour cut to further reduce the background.

• The red-sequence LFs of our sample have a significant inflexion centred at $M_{r'} \sim -18.5$ (especially at $z \sim 0.2$), and thus cannot be described by a single Schechter function, suggesting a mixture of two populations.

• By comparing the red-sequence LFs of our sample with that of low redshift samples constructed from SDSS, calculated consistently using our best method, we showed there is a steepening of the faint end with decreasing redshift since $z \sim 0.2$, but no strong evolution between $z \sim 0.2$ and $z \sim 0.4$.

• As a result of the evolution of the LFs, the red-sequence DGRs we measured show no significant changes over $0.2 \lesssim z \lesssim 0.4$, but an increase of a factor of ~ 3 from $z \sim 0.2$ to $z \sim 0$ (over the last 2.5 Gyr). Also, we do not see a strong dependence of the DGR on the richness of the clusters within our own sample.

• We thoroughly checked possible systematics, and showed none of them significantly affects our results, and thus our results are robust.

One of the interesting results is the lack of evolution of the red-sequence DGR over $0.2 \lesssim z \lesssim 0.4$, and the increase since $z \sim 0.2$. This suggests a rapid build-up of the cluster red-sequence in terms of the *number* of dwarf galaxies over the last 2.5 Gyr (the corresponding *stellar mass* on the red-sequence has only increased by 15 per cent). Taking the time delay assumed in Smith et al. (2009) for galaxies to move onto the red-sequence (1 Gyr for the single burst SSP models, and 0.5 Gyr for the quenched models), our results imply a significant fraction of faint red galaxies have been quenched within the last ~ 3 Gyr.

At higher redshifts than probed in this work, the evolution of the faint end of the red-sequence is still controversial, see for example Stott et al. (2007), De Lucia et al. (2007), and Andreon (2008). Given the different colour selections employed in those studies, and the sensitivity of the faint end to the selection method we have demonstrated, in a subsequent

work, we will extend our current study and measure the red-sequence LFs consistently out to higher redshifts. With the release of new data from CFHTLS, we will have a larger cluster sample, and thus better statistics.

Chapter 3

Star Formation Rate from Cluster Cores to Outskirts

3.1 Introduction

A lot has been learned about the star formation history of our Universe since early studies showed that the global star formation rate has declined by about a factor of 10 since $z \sim 1$ (e.g Lilly et al., 1996; Madau et al., 1996). With decreasing redshift, the star formation rate of the star-forming galaxies has been decreasing (Noeske et al., 2007), with an increase in the number of passive galaxies (Pozzetti et al., 2009). The study by Bell et al. (2007) showed that a transformation from blue galaxies to red ones is needed, so that the stellar mass of today's blue galaxies is not overproduced.

The origin of this decline of the star formation rate and transformation remains unclear. Among all possible reasons, the role that environment plays is especially uncertain. It has been known that in dense regions such as the cores of galaxy clusters, the population is dominated by galaxies with red colours and low average star formation rates (Gómez et al., 2003; Balogh et al., 2004a; Weinmann et al., 2006a; Haines et al., 2006; Kimm et al., 2009). Since, under the hierarchical paradigm, galaxy clusters grow by accreting galaxies that are generally star-forming, a transformation must have happened to quench the star formation. However, how and where this happens remains elusive.

Studies have shown that the suppression of star formation is not restricted to cluster cores. For example, Balogh et al. (1997, 1998) and Lewis et al. (2002) detected a lower fraction of star-forming galaxies relative to the field beyond ~ 2 virial radii. However, despite the low star-forming fraction in clusters, the change of star formation rate within the star-forming population itself has eluded detection. A recent study by Peng et al. (2010) showed, using the SDSS data, that the specific star formation rate of star-forming

galaxies is the same in the lowest and highest density regions. Some recent studies have suggested that the quenching of star formation might have started well before galaxies reach cluster cores, and in halos with mass below $\sim 10^{13}$ $M_{\odot}$ (Balogh & McGee, 2010).

An interesting place to look for the transformations is the outskirt regions of clusters. Simulations have shown that clusters are surrounded by large-scale structures such as filaments and sheets, and galaxies are accreted mainly along these structures (Bond et al., 1996; Colberg et al., 1999). These accretion zones are where galaxies reside before they reach the cluster cores, and thus might be an attractive candidate for where the transformation of galaxies happens. However, due to the low density contrast with the foreground/background field, studying the infall regions of clusters is very difficult and thus progress has been slow.

In this Chapter, we use a large sample of clusters we detected from the Canada-France-Hawaii Telescope Legacy Survey (CFHTLS), to study the star formation properties of member galaxies using our GALEX UV data, from the cluster core out to the outskirt region. We examine these properties as a function of stellar mass, as it has become clear that stellar mass is one of the key parameters that determines the properties of galaxies (Kauffmann et al., 2003). In Section 3.2, we describe the data sets, and the cross-matching of the optical and UV catalogues. The background subtraction and stellar mass estimate are described in Section 3.3. Results and discussion are presented in Sections 3.4 and 3.5. We conclude in Section 3.6.

We assume a cosmology with present day matter density parameter $\Omega_m = 0.3$, vacuum energy density parameter $\Omega_\Lambda = 0.7$, and Hubble constant H_o=70 km s^{-1} Mpc^{-1} throughout. All magnitudes are in the AB system unless otherwise specified.

3.2 Data

The data we used in this study are from the CFHTLS Wide optical survey and the GALEX NUV survey. We describe them separately below.

3.2.1 Optical Data

The cluster sample we used in this study is detected from the wide survey of CFHTLS, which is a joint Canadian and French imaging survey in u^*, g', r', i' and z' filters using, the wide-field imager MegaCam. The survey is now complete, covering a total of 171 square degrees, composed of single pointings each with a field of view of 1x1 square degree. The data sets and our cluster detection are described in detail in Chapter 2, and thus here we only point out a few improvements. One of the improvements is that we used the

stellar locus of stars from SDSS to calibrate the colour offset of each individual CFHTLS pointing (see Gilbank et al. 2010 for details). After this calibration, the dispersion of the colour of all pointings is about 0.01 magnitude. This reduces the scatter in colour when we stack a large number of clusters together. Further, we excluded regions around bright stars, which would lead to photometry with larger uncertainty and an underestimate of the galaxy number density. This second effect has the most impact when we study the properties of galaxies far from cluster centres, where the density is low. In this work, we focus on clusters that are between $0.15 < z < 0.35$. For more information on the properties of our cluster sample, see Chapter 2.

3.2.2 GALEX Data

In Cycle 5 of the GALEX Guest Investigator Programme, we proposed extended GALEX NUV coverage over the whole CFHTLS wide fields (GI5-28), to the same depth as the Medium Imaging Survey ($\sim$1500s). The data collection is only partially complete, currently covering approximately 80 square degrees of the sky. In addition, we include existing archival data over the CFHTLS wide fields with exposure time greater than 1500s. For multiple observations taken at the same position, the one with deeper exposure is used. Figure 3.1 shows all the data we have in hand that are used in this work.

We make use of the photometry provided in the NUV catalogue measured using SExtractor (Bertin & Arnouts, 1996) by the standard GALEX pipeline (Morrissey et al., 2007). The standard pipeline uses a sophisticated method to correctly estimate the background in low-count regions. However, in some regions, there is residual elevated background, likely due to reflection from bright stars. An example is shown in Figure 3.2. These elevated backgrounds cause problems in both object detection and photometry measurements. Therefore, we mask out these regions when doing the analysis. The total area masked out is about 0.3 square degrees, which is insignificant compared to the whole coverage; however it can become more important when considering individual clusters.

The field of view of GALEX is circular, with a radius of $\sim$0.6 degree. To avoid the slightly degraded astrometry and photometry near the edge of the each pointing, we only include objects within a radius of 0.58 degree from the field centre, and we readjust the field centre since the default centre given in the image header is occasionally slightly off. As there are duplicate objects in the overlaps among adjacent pointings, we use a search radius of 5 arcsec to match duplicate detections, and keep the one that is closest to the centre of the pointing it comes from.

We use MAG_AUTO as the total magnitude. We correct for Galactic extinction using the relation between extinction and the reddening determined by Wyder et al. (2007), where the reddening E(B-V) is calculated using the Schlegel et al. (1998) dust map. Since the PSF

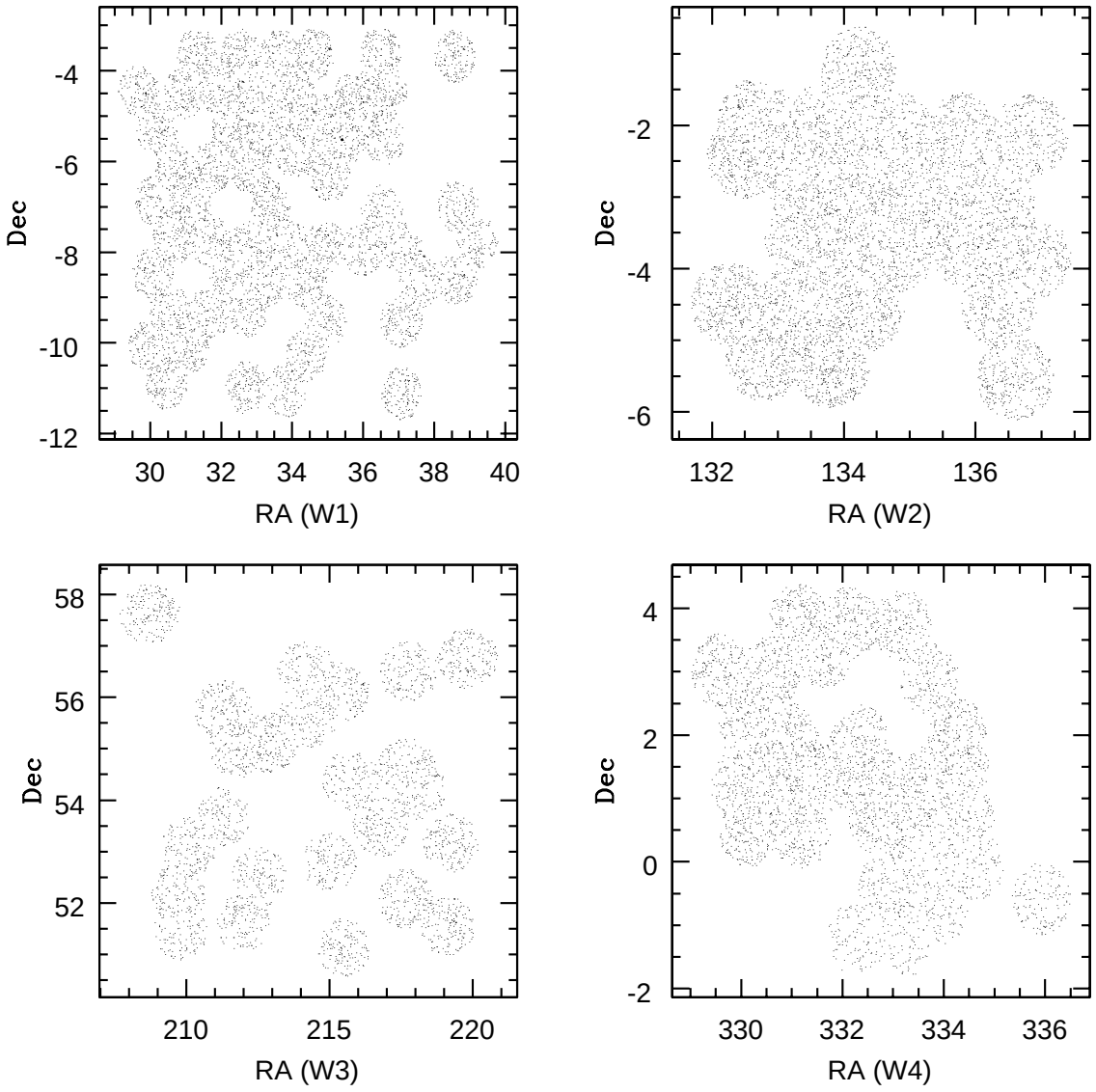

Figure 3.1: The current GALEX NUV coverage over the four CFHTLS wide fields, including both our GI data and archival data.

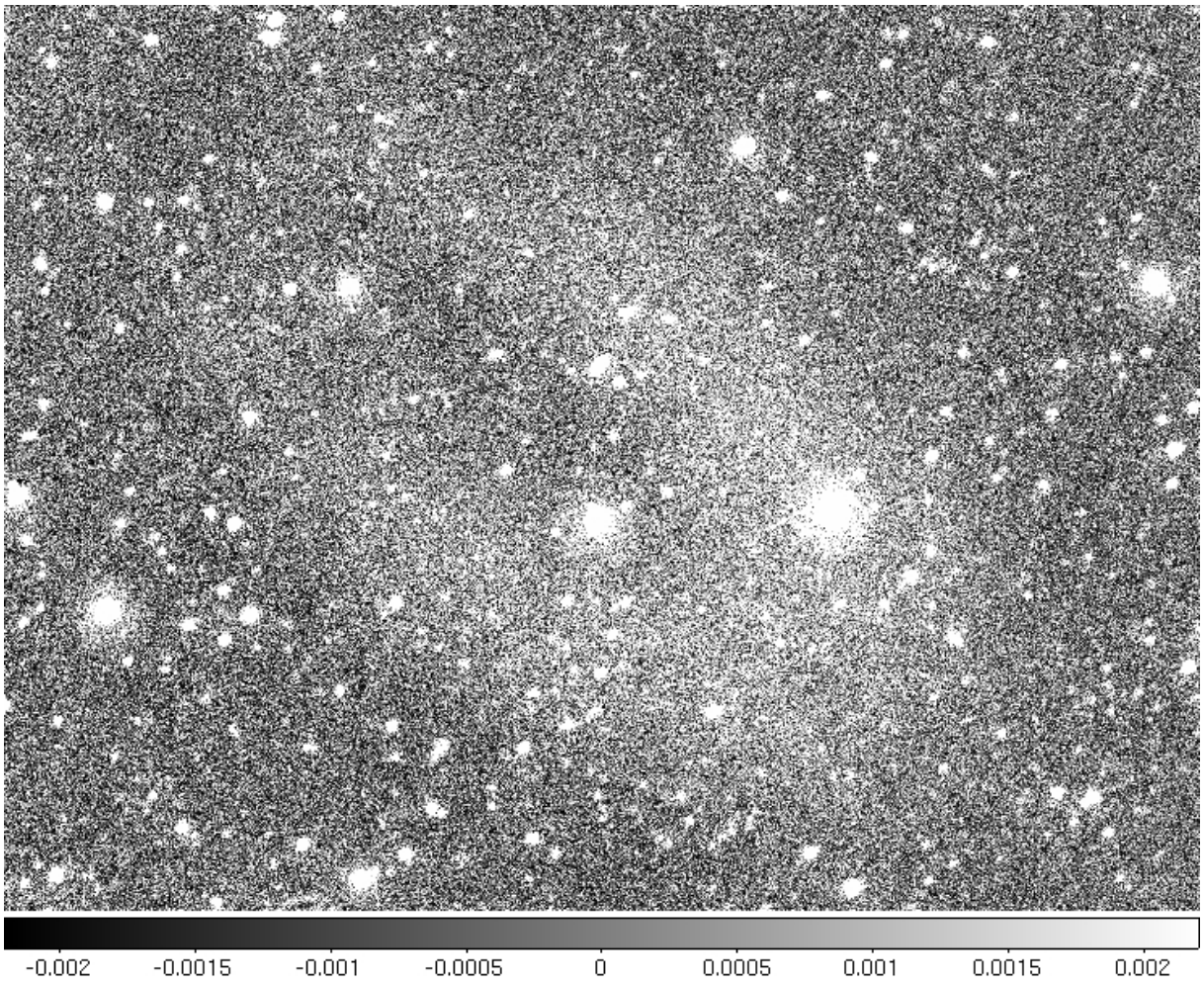

Figure 3.2: An example of the regions with residual elevated background in GALEX NUV images, which causes problems for both object detection and photometry measurement. The size of this region is about 0.15 x 0.15 square degree. The unit on the colourbar is counts per second per pixel.

of GALEX data is very different from that of the CFHTLS data, when measuring NUV-optical colours we use MAG_AUTO in both catalogues, instead of aperture magnitudes as for the optical-optical colour measurements. We estimate the NUV magnitude uncertainty using duplicate detections from overlapping pointings, and this is shown in Figure 3.3 as a function of magnitude. In the left panel of Figure 3.4, we show the number counts as a function of magnitude, normalized to per tile, from our GI5 data (red dotted histogram) and the deeper XMMLSS data (black solid line). In the right panel, we plot the ratio of the number counts from GI5 data to that from XMMLSS, which shows that the ~ 80 per cent completeness of our GI5 data is about NUV=23 mag. Therefore, for our analysis here, we only consider objects brighter than this limit.

3.2.3 Cross-matching Catalogues

Since the CFHTLS data are much deeper than our GALEX data, essentially all NUV detected sources should have a match in the optical catalogue, except for extremely blue, optically faint galaxies. Therefore, for each NUV source, we search the optical catalogue (without any magnitude cut) for matches within a radius of 4 arcsec. In ~ 40 per cent of cases, there are multiple optical matches for one NUV source. To deal with this, we do the matching in two rounds. In the first round, we do a one-to-one match, taking the closest optical source within 2 arcsec as the real match. We take this matched catalogue as the calibration catalogue. In the second round, for each NUV source, we keep all optical sources within 4 arcsec (a conservative threshold to include all possible matches), and still take the closest one as the real match if the next closest one is at least 1 arcsec away from the closest. In about 35 per cent of the multiple matches, there is at least one other possible match within 1 arcsec of the closest match. In these cases, we determine which one is more likely to be the real match using the process described below.

In Figure 3.5, we plot the $u^* - r'$ vs. $NUV - u^*$ colour of matched objects from the calibration catalogue (small dots) in the magnitude range $22.5 < NUV < 23$. This shows that, at a certain magnitude, there is a limited range of colour a galaxy is likely to have. Therefore, for each NUV source with multiple possible optical matches, we go to the calibration catalogue, and calculate the density around the location of each possible match in this $u^* - r'$ vs. $NUV - u^*$ space, in the range $NUV \pm 0.25$ mag around the magnitude of the NUV source. We take the one that has the highest density as the real match. One example is shown in Figure 3.5. The four squares are four possible optical matches to a NUV source with NUV=22.5, numbered in the order of distance from the NUV source, with 1 being the closest. The one that is the closest match in this case is less likely to be the real match than the second closest match.

We restrict the final matched catalogue to objects that are optically flagged as galaxies that are in the non-masked region (both around bright stars, see Section 3.2.1, and around

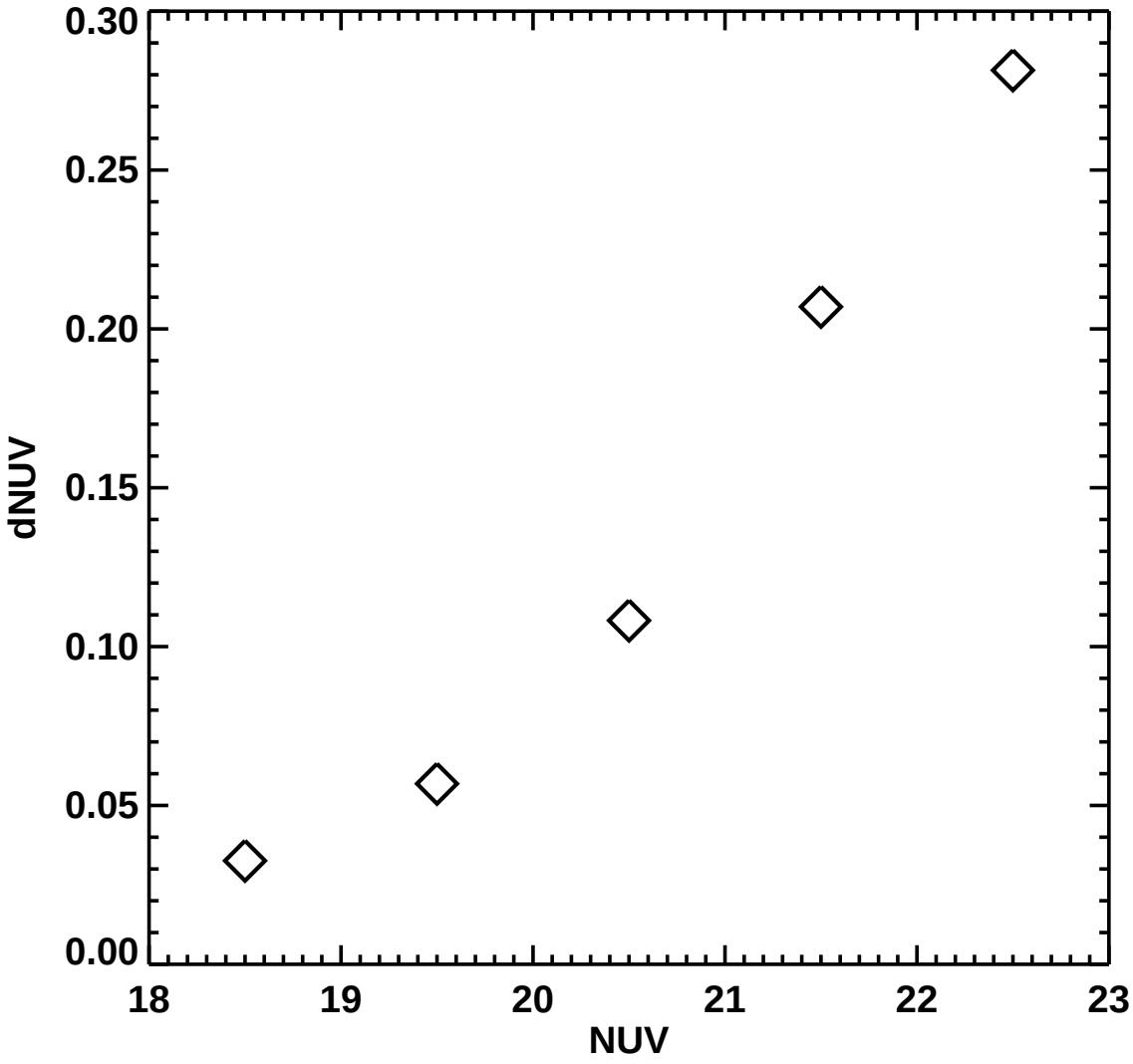

Figure 3.3: The standard deviation of the magnitude differences of duplicate objects measured from overlapping regions in GALEX NUV images, as a function of NUV magnitude.

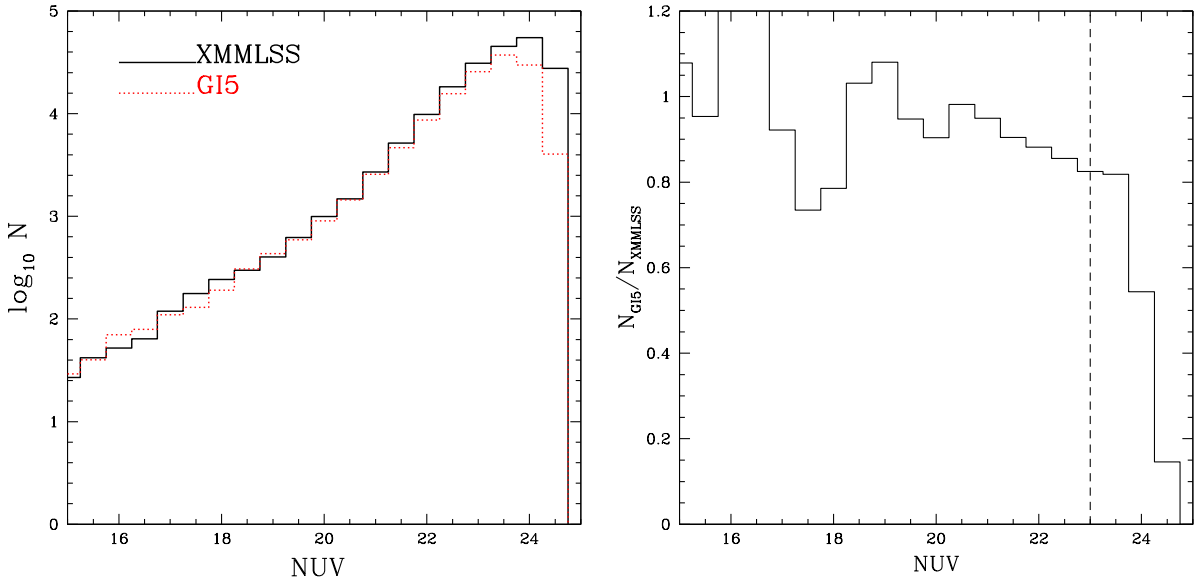

Figure 3.4: Left panel: number counts as a function of magnitude (normalized to per tile) from our GI5 data (red dotted histogram) and the deeper XMMLSS data (black solid line). Right panel: completeness of our GI5 data as a function of magnitude. In this work, we limit our sample to those brighter than NUV=23 mag, which is the $\sim$ 80 per cent completeness limit.

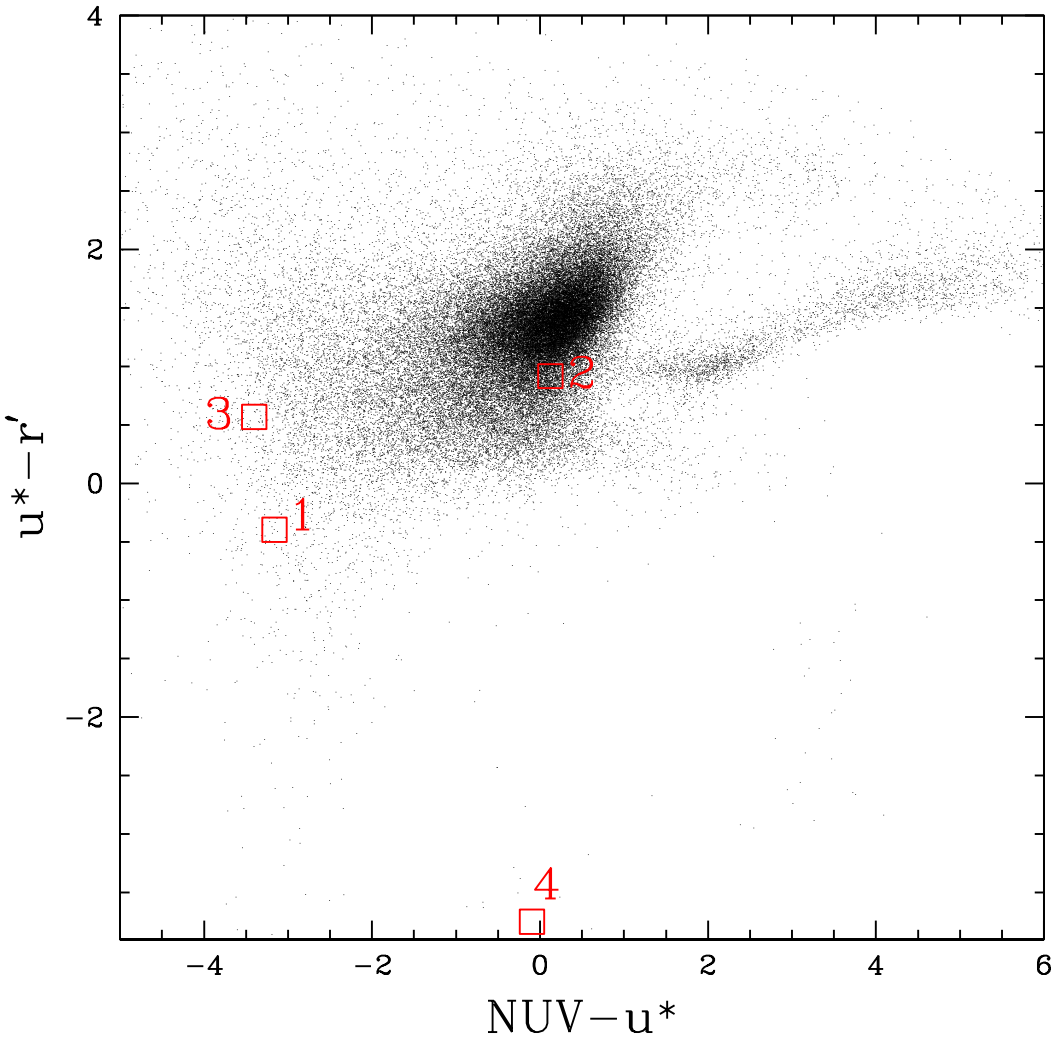

Figure 3.5: Small dots are matched objects from the calibration catalogue in the magnitude range $22.5 < NUV < 23$. This calibration catalogue contains one-to-one matches of optical and NUV sources whose spatial separation is less than 2 arcsec, all of which are very likely to be real matches. There is an obvious concentration of the dots in a specific region in this colour-colour space, indicating the colours the real matches are mostly likely to have. The thin locus (from $NUV - u^*$ of 1 to 6) separated from the bulk of the points are occupied by stars. The four squares are four possible optical matches within 4 arcsec from a NUV source with NUV=22.5, numbered in the order of distance from the NUV source, with 1 being the closest one. It shows that the one that is the closest match in this case is less likely to be the real match than the second closest match, because it is located in a less dense region.

the regions with elevated background in the GALEX data), with SExtractor flag less or equal than 3 in all filters (u^*, g', r', i', z' and NUV).

3.3 Analysis

3.3.1 Background Subtraction

To study the properties of galaxies in clusters, it is important to separate them from the foreground/background galaxies that are projected along the line-of-sight to the clusters of interest. We do not have spectroscopy for our large cluster sample to determine the membership of each galaxy. However, we can still study their average properties, by stacking clusters at similar redshifts and using a statistical background subtraction. Note that a photometric redshift catalogue of the CFHTLS wide survey has recently been released (Ilbert et al., 2006; Coupon et al., 2009). However, the dispersion of the redshift distribution of cluster members is narrower than the typical uncertainty of the photometric redshift. Therefore, in our case, especially when we examine the outskirt region of clusters where the contrast with the field is low, selecting cluster members using solely photometric redshift is not very reliable. However, before the statistical subtraction, using photometric redshift to exclude galaxies at redshifts much higher and lower than that of the clusters can efficiently reduce the noise. The results presented here are derived using photometric redshifts to preselect potential cluster members. We have checked that without using photometric redshifts, our results do not change except that the error bars are larger.

The statistical subtraction method we used here is somewhat different from that used in the literature, and we describe it in detail below. As with any other statistical background subtraction method, the goal is to determine the excess of galaxies in (for example), a certain magnitude or colour range that belong to a cluster, relative to the field population that is projected along the line-of-sight to the cluster of interest. In our case, we have photometry in six passbands, and therefore we do the subtraction in multi-colour space simultaneously. Because broad band colours roughly trace the shape of the spectrum, the use of multiple colours allows us to effectively remove galaxies that do not have the right spectral shape at a given redshift. This will be important when we turn to models to convert observed quantities to physical ones.

The data coverage is not 100 per cent for each cluster, due to gaps between tiles and masked-out regions with bad object detection or photometry. Therefore, we first calculate, for each cluster, within a certain radius that we are interested in, what fraction of the area is covered by valid data, using a high-resolution random catalogue. We then weight each galaxy within this radius by this fraction, and by the number of clusters in the stack so that the number attached to each galaxy represents the number per cluster.

To construct the field sample, we do exactly the same thing as the cluster sample, but replace the centre of each cluster with a random position generated from the same patch (W1,2,3,4) from which the cluster was detected*. This way, for each cluster in the stack, there is a corresponding field sample with the same systematics such as the imaging depth or overall number density (which could vary from patch to patch due to different Galactic extinction and cosmic variance).

With the two sets of samples in hand, one with cluster + field counts, and one with just field counts, we now do the subtraction in the following way. For each galaxy from the field sample, we search for the nearest neighbor in the NUV magnitude and $(NUV - u^*)$, $(u^* - g')$, $(g' - r')$, $(r' - i')$, $(i' - z')$ colour space. We then subtract the weight of this field galaxy from that of its nearest neighbor in the cluster image. Since each galaxy has a different weight, this may result in a negative number. In this case, we set the number attached to this nearest neighbor to zero and subtract the "negative excess" from the next-nearest neighbor, and so on until the number becomes positive. In the end, we have a subset of galaxies from the cluster sample that all have a positive number attached to them. These galaxies should essentially all be cluster members, because galaxies that have similar spectral shape as the field (foreground/background) galaxies are effectively removed by doing the subtraction in multi-colour space. The advantage of this method is that the galaxies that are left can then be treated individually as cluster members.

We perform the last two steps, constructing the field sample and subtracting it from the cluster sample, 100 times, and average the results over the 100 realizations. The error bars on the results presented here are the standard deviation of the 100 realizations.

As an example, in Figure 3.6 we show the result of one realization of the background subtraction of one of the clusters in our sample. Small cyan circles represent all potential cluster members in the field of view before the subtraction, selected from their photometric redshifts. Solid red dots are galaxies that are left after the subtraction, with UV detected galaxies indicated by the blue dots. The large black circle shows a radius of 5Mpc from the cluster centre. The colour-magnitude diagrams of this cluster, in four radial bins, are shown in Figure 3.7. The symbols are the same as in Figure 3.6, with the additional small black dots indicating field galaxies. The red-sequence is clearly visible in the core of the cluster.

3.3.2 k-corrections

The k-corrections are computed using KCORRECT v4_1_4 (Blanton & Roweis, 2007). We are able to use this because, as discussed above, after the background subtraction what we are left with are essentially cluster members, whose redshift is determined from the

*For the field sample, we mask out any known clusters, out to $r = 3$ Mpc

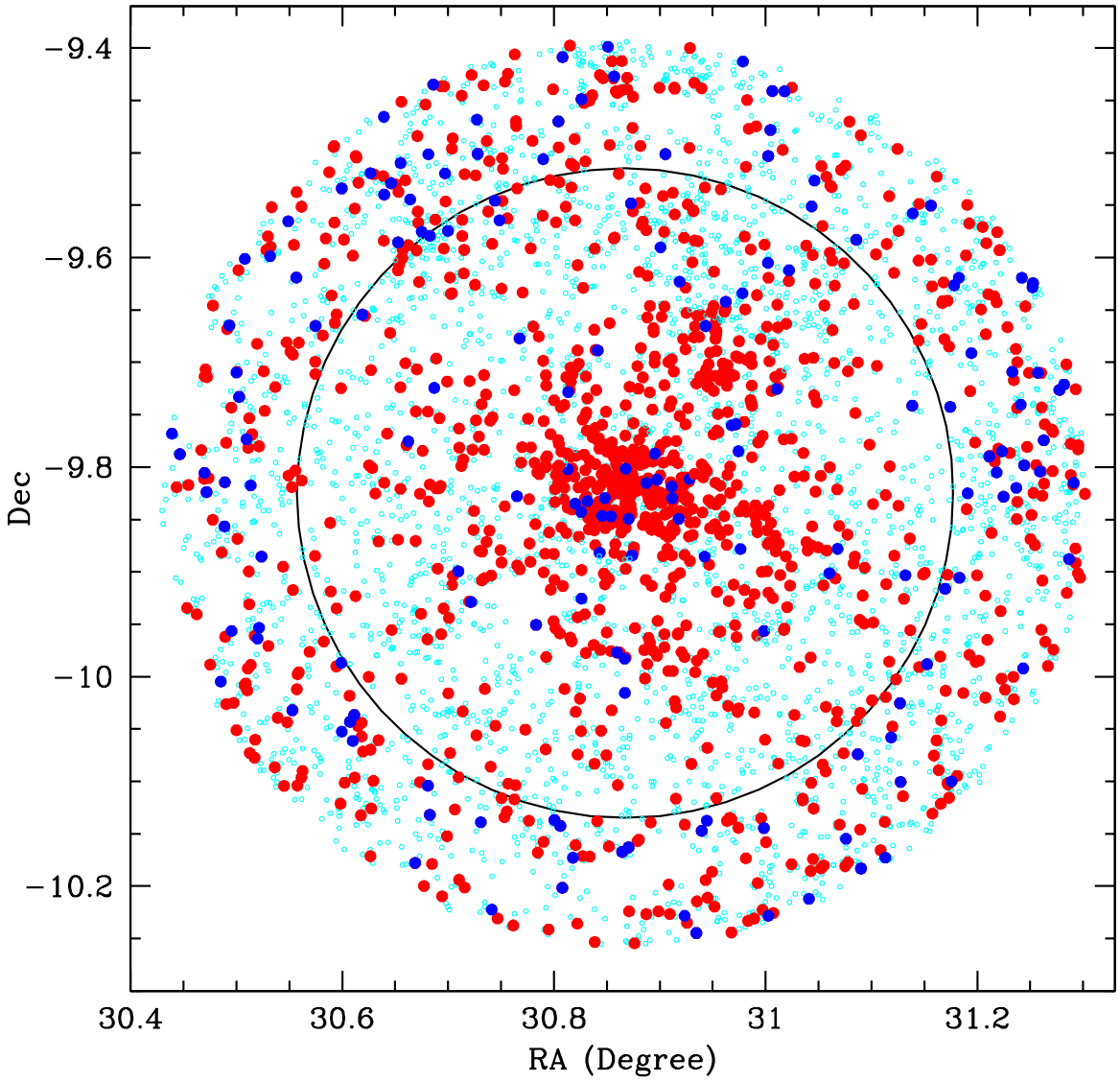

Figure 3.6: The spatial distribution of galaxies in the field of view (r<7Mpc) of one example cluster. Small cyan circles are all potential cluster members, as determined from their photometric redshifts. Solid red dots are galaxies that are left after the background subtraction, with NUV detected sources indicated in blue. The big black circle shows the 5 Mpc radius.

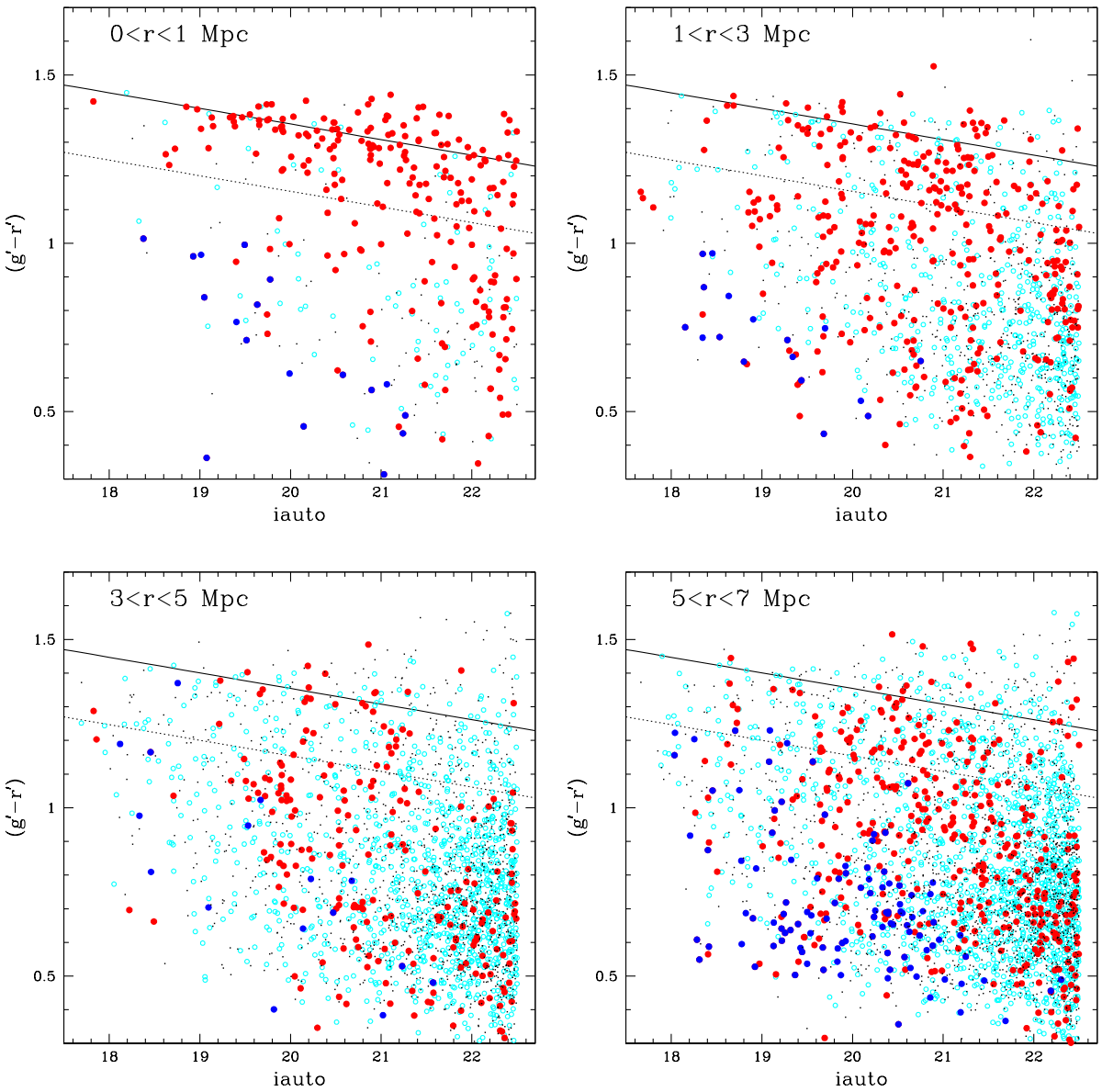

Figure 3.7: The colour-magnitude diagrams of the example cluster shown in Figure 3.6 is shown, in four radial bins. The symbols are the same as in Figure 3.6, with the additional small black dots indicating field galaxies.

red-sequence galaxies of the clusters as described in detail in Chapter 2. Because at the redshift of our cluster sample, the observed NUV magnitude probes the FUV wavelength, we reconstruct the rest-frame FUV magnitude from our six passband photometry using the public code of Blanton & Roweis (2007). The typical correction is about 0.6 mag.

3.3.3 Star Formation Rate

The UV luminosity we observe cannot be directly converted to a star formation rate because of the existence of dust around star-forming regions. The dust will absorb the UV emission and re-emit it at a longer wavelength. Therefore, it is important to correct for the effect of dust absorption, before we can infer the star formation rate from the UV luminosity.

The total IR to UV luminosity ratio (L_{TIR}/L_{UV}) is a reliable estimator of the dust extinction in star-forming galaxies (e.g. Buat, 1992). We do not have IR information for our cluster sample. However, it has been shown that there is a correlation between L_{TIR}/L_{UV} and the slope of the UV continuum (e.g. Meurer et al., 1999; Cortese et al., 2006). We use this to estimate L_{TIR}/L_{UV}, and eventually the dust extinction.

If fit by a power law, the UV continuum can be described as $f(\lambda) \propto \lambda^{\beta}$, where f is in unit of $ergs\ s^{-1}\ cm^{-2}\ \lambda^{-1}$ (Calzetti et al., 1994). Therefore, the slope β can be estimated as $\beta = (\lg f_2 - \lg f_1) \,/\, (\lg\lambda_2 - \lg\lambda_1)$. In the redshift range of our cluster sample, the rest-frame wavelength range used to measure the UV slope, 1250Å$< \lambda <$ 2600Å, is shifted to the bandpasses of NUV and u^*. Therefore, in our case, we reconstruct the rest-frame FUV and NUV from our observed multi-band photometry again using the code of Blanton & Roweis (2007). Converting the AB magnitude to flux using $m(AB) = -2.5\lg f_\nu - 48.6 = -2.5\lg(f_\lambda\lambda^2/c) - 48.6$, where f_ν is in unit of ergs s^{-1} cm^{-2} Hz^{-1}, we have:
$\beta = -0.4\,(m_{u^*} - m_{NUV}) \,/\, (\lg\lambda_2 - \lg\lambda_1) - 2 = 2.2(m_{FUV} - m_{NUV}) - 2$, where m_{FUV} and m_{NUV} are in the rest-frame.

It has been pointed out that the relation between the UV slope and L_{TIR}/L_{UV} is different for star-bursting galaxies and normal star-forming galaxies (Bell, 2002; Kong et al., 2004; Cortese et al., 2006). Since most of the galaxies we are after here are normal star-forming galaxies, we adopt the relation derived by Cortese et al. (2006)(eq. 5) for normal star-forming galaxies, which is:

$$\lg(L_{TIR}/L_{FUV}) = (0.7 \pm 0.06)\beta + (1.3 \pm 0.06). \tag{3.1}$$

In the study by Cortese et al. (2008), the relation between L_{TIR}/L_{FUV} and dust extinction A(FUV) is derived using SED fitting for galaxies with different ages. Therefore, for galaxies off the red-sequence (defined as those with $(g' - r')$ and $(r' - i')$ colour bluer by 0.2 magnitude than the red-sequence), we adopt the relation for young star-forming

galaxies (their $\tau > 7$ model), and for galaxies on the red-sequence we adopt the one for an older population (their $\tau \sim 5.4$ model) (see their table 1).

The dust-corrected magnitude is turned into a luminosity, and the star formation rate is then estimated using the Kennicutt (1998) relation:

$$SFR(M_\odot \text{ yr}^{-1}) = 1.4 \times 10^{-28} L_\nu(\text{ergs s}^{-1} \text{ Hz}^{-1}). \quad (3.2)$$

Note that, for our sample we do not have enough information to identify AGN; however, only a small fraction of galaxies in clusters are AGN hosts (e.g. Martini et al., 2002; Miller et al., 2003), and thus does not strongly affect our results.

3.3.4 Stellar Mass

It has become clear that the properties of galaxies are largely dependent on their stellar mass (e.g. Kauffmann et al., 2003). We estimate stellar mass using the i-band mass-to-light ratio, as a function of SDSS $(g - r)$ colour, from Bell et al. (2003). We project our k-corrected rest-frame $(g' - r')$ colour measured in CFHTLS filters onto the SDSS system, using the code of Blanton & Roweis (2007).

3.3.5 Field Sample

In Section 3.3.1, we described our background subtraction process, in which for each cluster sample we construct a corresponding field sample. When we stack clusters together, we also stack the corresponding field samples together, restricting to galaxies that span the redshift ranges covered by the clusters in the stack, as determined from the photometric redshift. We take this as the comparison field sample to our cluster sample.

3.4 Results

3.4.1 Luminosity Function

Before we start examining the star formation properties of our clusters, we first present the NUV luminosity function, constructed using two background subtraction methods. In Section 3.3.1, we described our background subtraction method in NUV magnitude and five colours simultaneously, which allows us to treat galaxies that are left as individual cluster members. To check that our method of removing the nearest neighbor in multi-colour space preserves the NUV magnitude distribution, we compare the luminosity

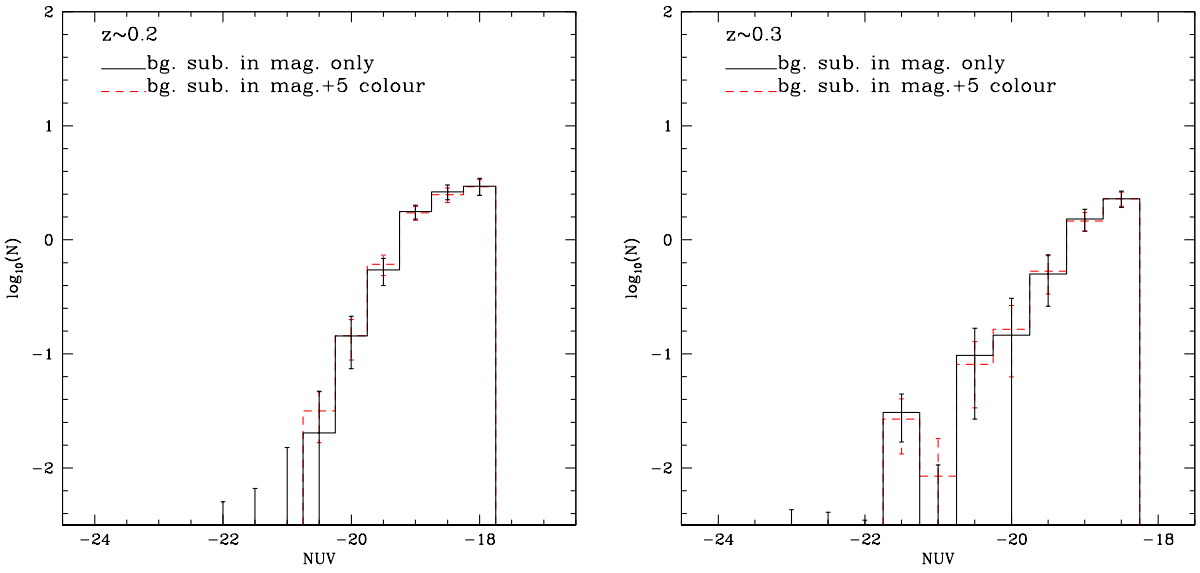

Figure 3.8: NUV luminosity function of stacked clusters within the central 1 Mpc in two redshift bins, constructed using two subtraction methods. The solid lines represent that constructed using a more traditional method; and the dashed lines represent that constructed using our method. In the more traditional method, we simply subtract the number of galaxies in a certain NUV magnitude bin in the field sample from that in the cluster+field sample. In our more sophisticated method, the subtraction is carried out in NUV magnitude and five colours simultaneously, which allows us to treat galaxies that are left as individual cluster members. The fact that these two agree very well with each other confirms that our multi-colour background subtraction method does preserve the NUV magnitude distribution.

function constructed from members left from this method with that constructed using a more traditional background subtraction method. In this more traditional method, we simply subtract the number of galaxies in a certain NUV magnitude bin in the field sample from that in the cluster+field sample (the same field and cluster+field samples as described in Section 3.3.1). In Figure 3.8, the solid lines represent the NUV luminosity functions of the stacked clusters within the central 1 Mpc, at two redshifts, constructed using the more traditional method; the dashed lines represent that constructed using our more sophisticated method. Those two agree very well with each other, confirming that our multi-colour background subtraction method does preserve the NUV magnitude distribution. Note these luminosity functions are not k-corrected, because we can only apply k-correction to "members" that are left from our multi-colour subtraction method.

3.4.2 SSFR vs. Stellar Mass

It has been found that star-forming galaxies form a tight sequence in the specific star formation rate (SSFR) vs. stellar mass (M_*) plane (Noeske et al., 2007; Salim et al., 2007), where SSFR is defined as SFR/M_*. In Figure 3.9, we show one realization of the SSFR vs. stellar mass of our stacked clusters at two redshifts, in the top and bottom panels respectively. The black dots are blue cluster galaxies, while red dots represent those that are on the red-sequence. The green dots are field galaxies. In the left and right panels, we present the relation in two regions with the most contrasting density: the core ($0 < r < 1$Mpc) and the outskirts ($5 < r < 7$Mpc). Note that the depth of our NUV data corresponds to a SFR detection limit of 0.3 $M_\odot$ yr^{-1} at $z \sim 0.2$ and 0.7 $M_\odot$ yr^{-1} at $z \sim 0.3$. Therefore, the slope of the SSFR vs. M_* of our sample is mostly driven by the detection limit, not reflecting the true slope. For this reason, we do not attempt to fit the relation of our sample. Nonetheless, comparing the left panels with the right ones, it seems that the relation in the cluster cores and the outskirts are both consistent with that in the field, showing no dependence on the environment. This is consistent with the findings of Peng et al. (2010), who found no difference of this relation in the lowest and highest density regions in the SDSS data. The recent study by McGee et al. (2010) also found that there is no significant difference between the star-forming galaxies in groups and the field.

The ensemble average SSFR (total SFR/total stellar mass) of our clusters is shown in Figure 3.10, at different clustercentric radii, split into three stellar mass bins. Squares, crosses, triangles represent the $9.0 < \log_{10}(M_*/\ M_\odot) < 9.7$, $9.7 < \log_{10}(M_*/\ M_\odot) < 10.5$, and $10.5 < \log_{10}(M_*/\ M_\odot) < 11.5$ mass bins respectively. It is clear that the average SFR of the star-forming galaxies (SFR> 0.7 $M_\odot$ yr^{-1}) is roughly constant from the cluster core out to the outskirt region. It is interesting to compare this with the field values, which are indicated by the solid, dotted, and dashed lines for the three stellar masses respectively.

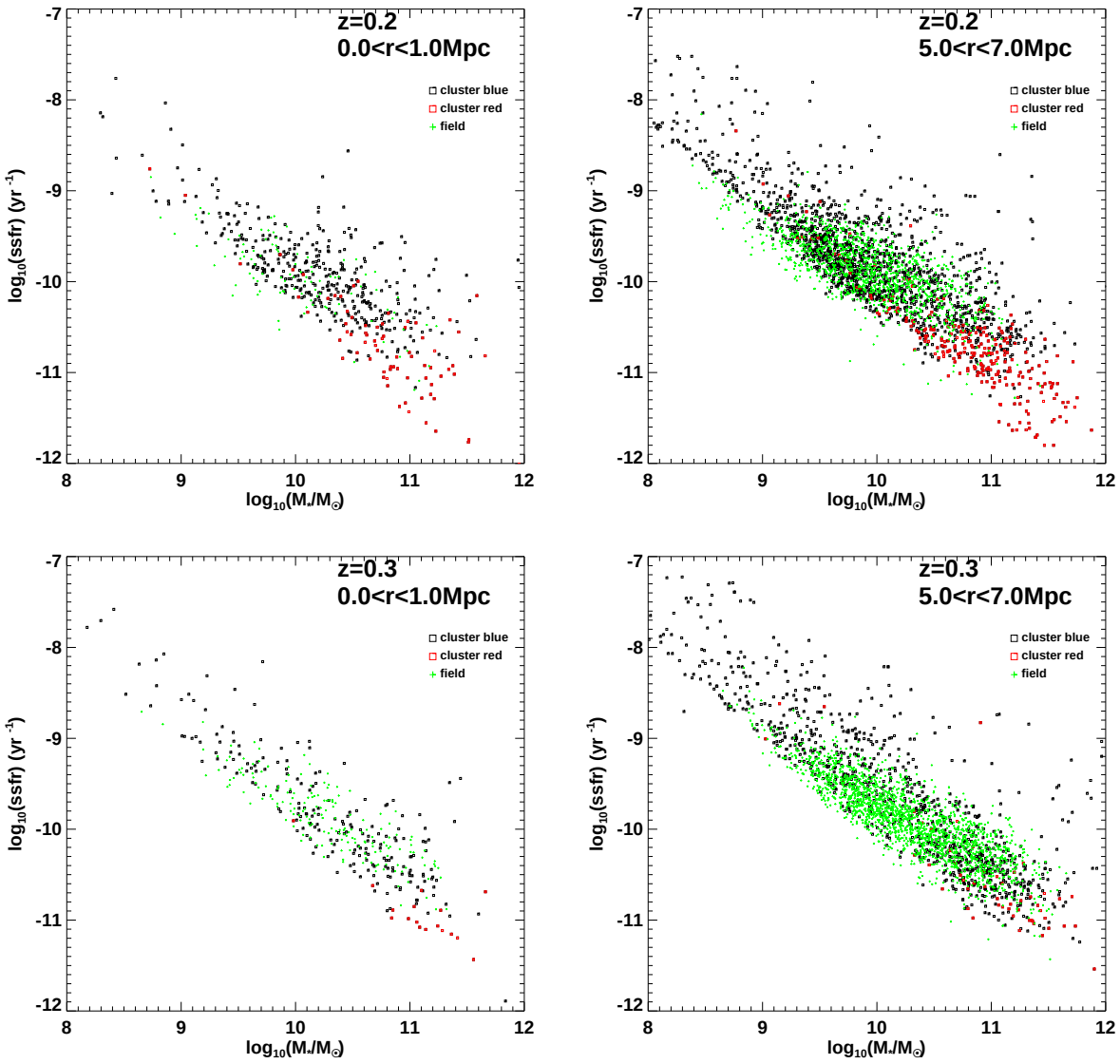

Figure 3.9: One realization of the SSFR vs. stellar mass relation of our stacked clusters at two redshifts (top and bottom panels). The black dots are blue cluster galaxies, and the red dots represent those that are on the red-sequence. The green dots are field galaxies. The relations in two regions with the most contrasting density, the core ($0 < r < 1$Mpc) and the outskirt ($5 < r < 7$Mpc), are shown in the left and right panels respectively.

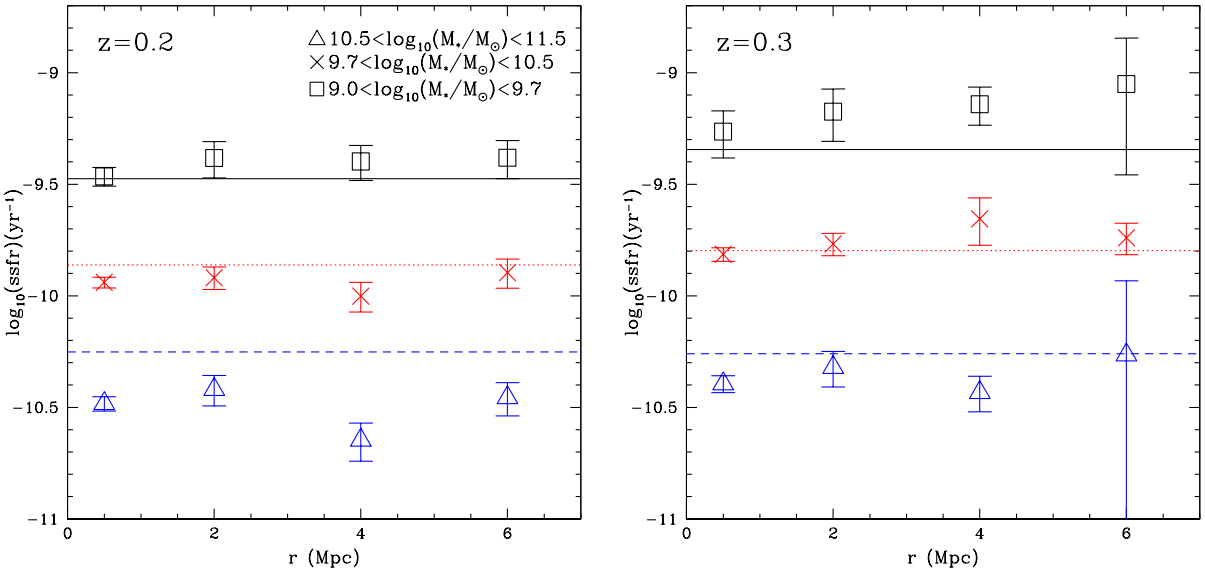

Figure 3.10: The ensemble average SSFR (total SFR/total stellar mass) of our clusters, at different clustercentric radii, split into three stellar mass bins. Squares, crosses and triangles represent the $9.0 < \log_{10}(M_*/\ \mathrm{M}_\odot) < 9.7$, $9.7 < \log_{10}(M_*/\ \mathrm{M}_\odot) < 10.5$, and $10.5 < \log_{10}(M_*/\ \mathrm{M}_\odot) < 11.5$ mass bins, respectively. The corresponding field values are indicated by the solid, dotted, and dashed lines respectively. It is clear that the average SFR of the star-forming galaxies (SFR$> 0.7\ \mathrm{M}_\odot\ \mathrm{yr}^{-1}$) is roughly constant from the cluster core out to the outskirt regions.

There does not appear to be a significant difference between the average SSFR in clusters and in the field, except for the highest stellar mass bin at $z \sim 0.2$, where the values in clusters are lower than that in the field. Note that the clustercentric distance plotted in Figure 3.10 (also in Figures 3.12 and 3.13 as we will see below) is not scaled to r_{200}. However, for most clusters in our sample, their r_{200} is from ~ 0.8 Mpc to $\sim$1.7 Mpc, which is mostly within the first radial bin, and thus does not change our conclusions.

We now further examine this by looking at the distribution of the SSFR (instead of just the average) in each stellar mass bin. In Figure 3.11, the circles, solid, dotted and dashed histograms represent respectively the distribution (normalized by the total stellar mass) of the SSFR at four clustercentric radii, for galaxies with $9.0 < \log_{10}(M_*/\ \mathrm{M}_\odot) < 9.7$ (left panel) and $10.5 < \log_{10}(M_*/\ \mathrm{M}_\odot) < 11.5$ (right panel). The triangles show the field distribution. For the lower stellar mass bin, within the error bars, we do not detect a significant change in the distribution from cluster core out to the infall region, and they seem to be consistent with that in the field as well. For the higher stellar mass bin, there is no significant change in the distribution at different clustercentric radii. However, when

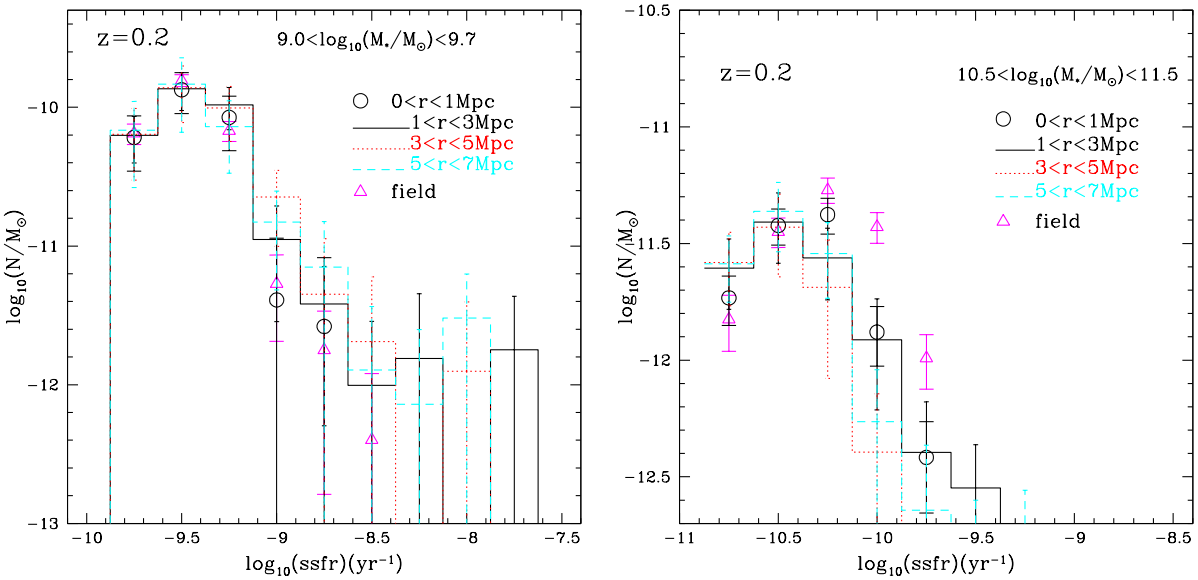

Figure 3.11: The distribution of the SSFR at different radii, for two fixed stellar masses (left and right panels). The circles, solid, dotted and dashed histograms represent respectively the distribution (normalized by the total stellar mass) of the SSFR at four clustercentric radii, and triangles show the field distribution. For the lower stellar mass bin, within the error bars, we do not detect a significant change in the distribution from the cluster core out to the infall region, and they seem to be consistent with that in the field as well. For the higher stellar mass bin, there is no significant change in the distribution at different clustercentric radii. However, when compared to the field distribution, it seems that in clusters there are fewer galaxies with SSFR above $10^{-10.2}$ yr^{-1} relative to those below, indicating a decline in the SFR of high stellar mass galaxies in clusters. This is also reflected in the lower average SSFR in clusters at that stellar mass compared to that in the field, as shown in Figure 3.10.

compared to the field distribution, it seems that in clusters there are fewer galaxies with SSFR above $10^{-10.2}$ yr^{-1} relative to those below, indicating a decline in the SFR of high stellar mass galaxies in clusters. This is also reflected in the lower average SSFR in clusters at that stellar mass compared to that in the field, as shown in Figure 3.10. This is visible in Figure 3.9 as a deficit of high stellar mass and low SSFR field galaxies.

3.4.3 Star-forming Fraction

We now examine the fraction of star-forming galaxies out of the whole population as a function of environment. To obtain the total number of galaxies, we follow the same procedure as for the optical-UV matched catalogue, except that we now include galaxies that are not NUV detected. In Figure 3.12, the fraction of star-forming galaxies with SFR above our detection limit is plotted as a function of clustercentric radius in three stellar mass bins, for the lower (left panel) and higher redshift samples (right panel). The most interesting thing is that, at $z \sim 0.2$, there is an abrupt change in the fraction of star-forming galaxies with SFR> 0.3 M$_\odot$ yr^{-1} between $0 < r < 1$Mpc and $1 < r < 3$Mpc, and beyond ~ 3 Mpc there is no further dependence on the clustercentric radius. For the $z \sim 0.3$ sample, there does not appear to be a significant change from the core out to the outskirts. However, note that the lowest SFR we can probe at that redshift is rather high (0.7 M$_\odot$ yr^{-1}); this prevents us from seeing any changes that might be associated with the population whose SFR is below this limit. Again, the star-forming fractions in the field are indicated by lines, and they are much higher than those in the clusters. It is interesting to note that, in the field at $z \sim 0.2$, the star-forming fraction is highest in the intermediate stellar mass range for both SFR> 0.3 M$_\odot$ yr^{-1} and SFR> 0.7 M$_\odot$ yr^{-1} (not plotted here), while at $z \sim 0.3$ the star-forming fraction is the highest in high stellar mass galaxies.

Note our detection limit in terms of SFR is too high for us to determine the fraction of truly passive galaxies using their SFR. Therefore, in the next section, we resort to the colour information to examine the passive population.

3.4.4 Red Fraction

We consider galaxies that are no bluer than 0.2 magnitude below the red-sequence in both $(g' - r')$ and $(r' - i')$ colour as red galaxies. The fraction of red galaxies as a function of distance from cluster centres is plotted in Figure 3.13, for the two samples at $z \sim 0.2$ (left panel) and $z \sim 0.3$ (right panel), again split into three stellar mass bins. The red fraction increases with stellar mass. At fixed stellar mass, it is quite clear that at both redshifts, the change of the red fraction happens within ~ 3Mpc from the cluster centres, with no further changes beyond ~ 3 Mpc. The change within the inner region is most obvious for

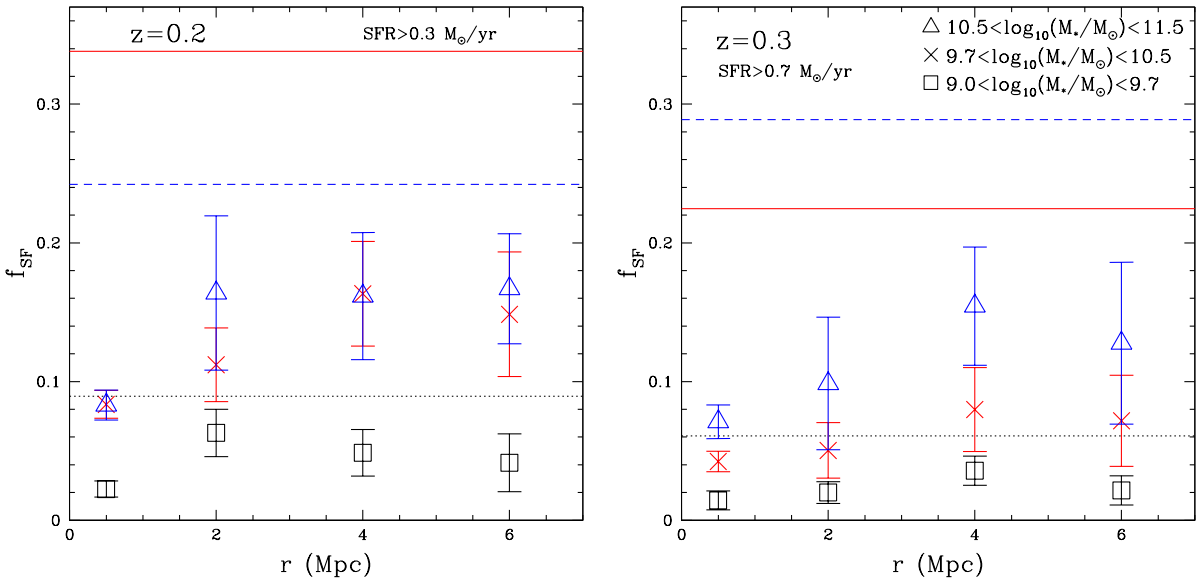

Figure 3.12: The fraction of star-forming galaxies with SFR above our detection limits, as a function of clustercentric radius in three stellar mass bins. Triangles, crosses, and squares represent three stellar mass bins, and the corresponding field values are indicated by blue dashed, red solid, and black dotted lines. The lower and higher redshift samples are shown in the left and right panels respectively.

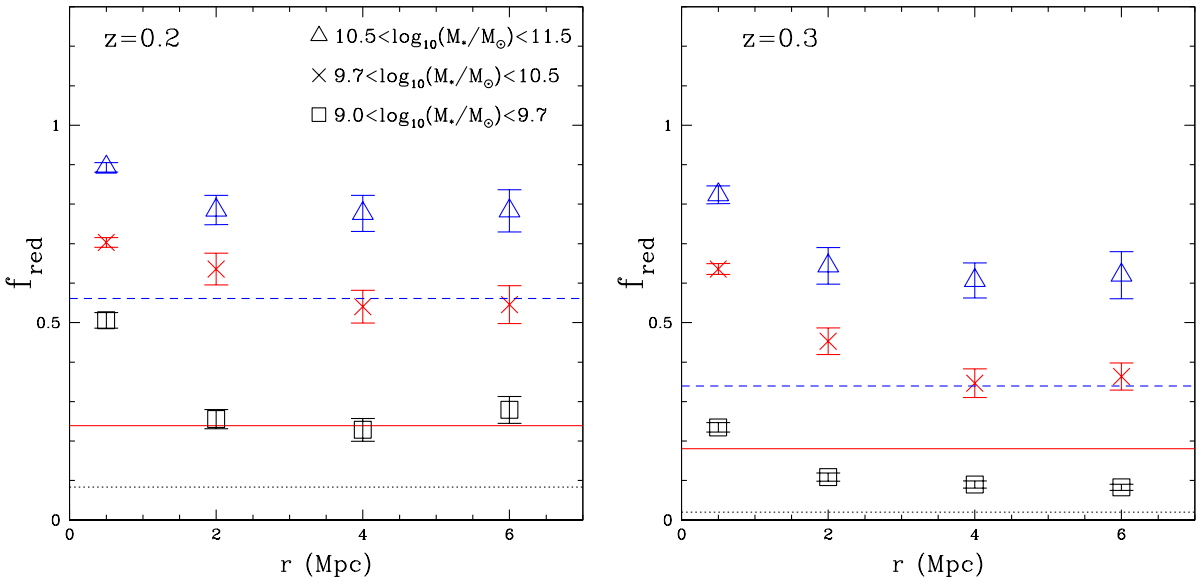

Figure 3.13: The fraction of red galaxies as a function of distance from cluster centres, for the two samples at $z \sim 0.2$ (left panel) and $z \sim 0.3$ (right panel), again split into three stellar mass bins. Symbols represent cluster values, while lines represent field values for the corresponding stellar mass. The red fraction increases with stellar mass. At fixed stellar mass, the change of the red fraction happens within $\sim$ 3Mpc from the cluster centres, with no further changes beyond $\sim$ 3 Mpc.

the lowest stellar mass galaxies, in the sense that their red fraction increase by a factor of ~ 2.

It is interesting also to compare this with the field values. The dashed, solid, and dotted lines represent the red fraction in the field for the three stellar mass bins. Not surprisingly, in the densest region, cluster cores ($r < 1$ Mpc), the red fraction is higher than that in the field. The more interesting thing is that even at the outermost region ($r \sim 7$ Mpc) where the density is in very low contrast with the field, the red fraction is still much higher than that in the field. We discuss the implication of this result in combination with the other results presented above in the next Section.

3.5 Discussion

3.5.1 Implication from the Red Fraction

A lot can be learned about the quenching of the star formation from the red fraction. In Sections 3.4.3 and 3.4.4, we found an increase in the fraction of red galaxies within the inner $\sim$ 3Mpc of the clusters compared to outer regions, and this fraction has increased by a factor of 2 for the lowest stellar mass galaxies from $z \sim 0.3$ to $z \sim 0.2$ (over 1 Gyr). However, we did not detect any changes in the star formation rate within the star-forming population at different clustercentric distance. One possible interpretation of this is that, within the core, the truncation of star formation happens rapidly within 1 Gyr, preventing the detection of the population in the process of having their star formation shut off, allowing only the resulting increase of passive galaxies to be seen. One good candidate in this case would be ram-pressure stripping, which truncates the star formation on short time scale and requires high density ICM that is present in the core of clusters.

In the outskirts ($\sim$ 7Mpc), despite the low density contrast with the field, we found that the red fraction is already higher than that in the field. This indicates that those galaxies that just arrived at the cluster environment already have their star formation quenched, supporting a "pre-processing" scenario suggested by several studies (e.g. Zabludoff & Mulchaey, 1998; Balogh et al., 2000; Balogh & McGee, 2010).

One thing that cannot be inferred clearly from our results here is whether or not the pre-processed galaxies in the outskirts are further processed by the cluster environment. Because we are using a background subtraction method to determine cluster memberships, in the outskirts, the excess we detected is possibly associated with denser regions (groups of galaxies) relative to the mean density at that large radius. This is a scenario supported by McGee et al. (2009), who suggests that a large fraction of galaxies that accrete onto clusters are in groups (but see Berrier et al. (2009)). If that is the case, a comparison with

the red fraction of the isolated groups in the field would tell us whether those groups in the outskirts are different from those in the field. With our current data that only allow the study of stacked clusters using a statistical background subtraction, it is hard to identify individual real groups in the outskirt regions; therefore, we defer a closer examination of groups in the outskirt regions to another project, where we use spectroscopic data to study two contrasting clusters (See Chapter 4).

3.5.2 Model Star Formation Histories

To gain more insight into the star formation history of the cluster galaxies examined here, we qualitatively compare the observed $(FUV - g')$ vs. $(u' - g')$ colours with model tracks. We use Bruzual & Charlot (2003) models to predict the evolution of galaxies with different star formation histories. In Figure 3.14, we show one realization of the observed $(FUV - g')$ vs. $(u' - g')$ colour of galaxies within 3Mpc from cluster centres in our $z \sim 0.2$ sample, in the stellar mass range of $9.7 < \log_{10}(M_*/\ \mathrm{M}_\odot) < 10.5$. Black squares represent blue galaxies and red diamonds represent red ones. The black dotted line shows the model track of a population whose star formation has been declining exponentially with a characteristic time scale of $\tau = 5$ Gyr (with a dust extinction of $\tau_\nu = 1$). Starting with this model, we truncate its star formation 3 Gyrs and 7 Gyrs later, and the subsequent colour evolution is shown by the grey solid and green long-dashed lines. If we add a burst onto the exponentially declining model at 5 Gyrs and then truncate the star formation, the evolution is indicated by the blue short-dashed (with burst strength of 10 per cent) and red dot-dashed (with burst strength of 1 per cent) lines. It seems the red galaxies detected in UV follow the exponentially decaying model well, but the blue galaxies seem to require some additional quenching. Note that it is not our purpose here to explore all parameter space; therefore these models are not unique, but they do provide a consistent explanation for the difference between the red and blue galaxies with UV detections. It is worth noting, at the lower left end of the burst models (blue short-dashed and red dot-dashed lines), where the burst is happening, we do not see any galaxies. This may not be too surprising because, given the short time scale of the burst, it would still be hard to detect many galaxies in that phase even if it is relatively common. The regions occupied by the field galaxies (not plotted here for clarity) do not appear to be significantly different from that of the cluster galaxies. This could be explained if a large fraction of the galaxies in our field sample are in groups, and they are having their star formation quenched as in the "pre-processing" scenario.

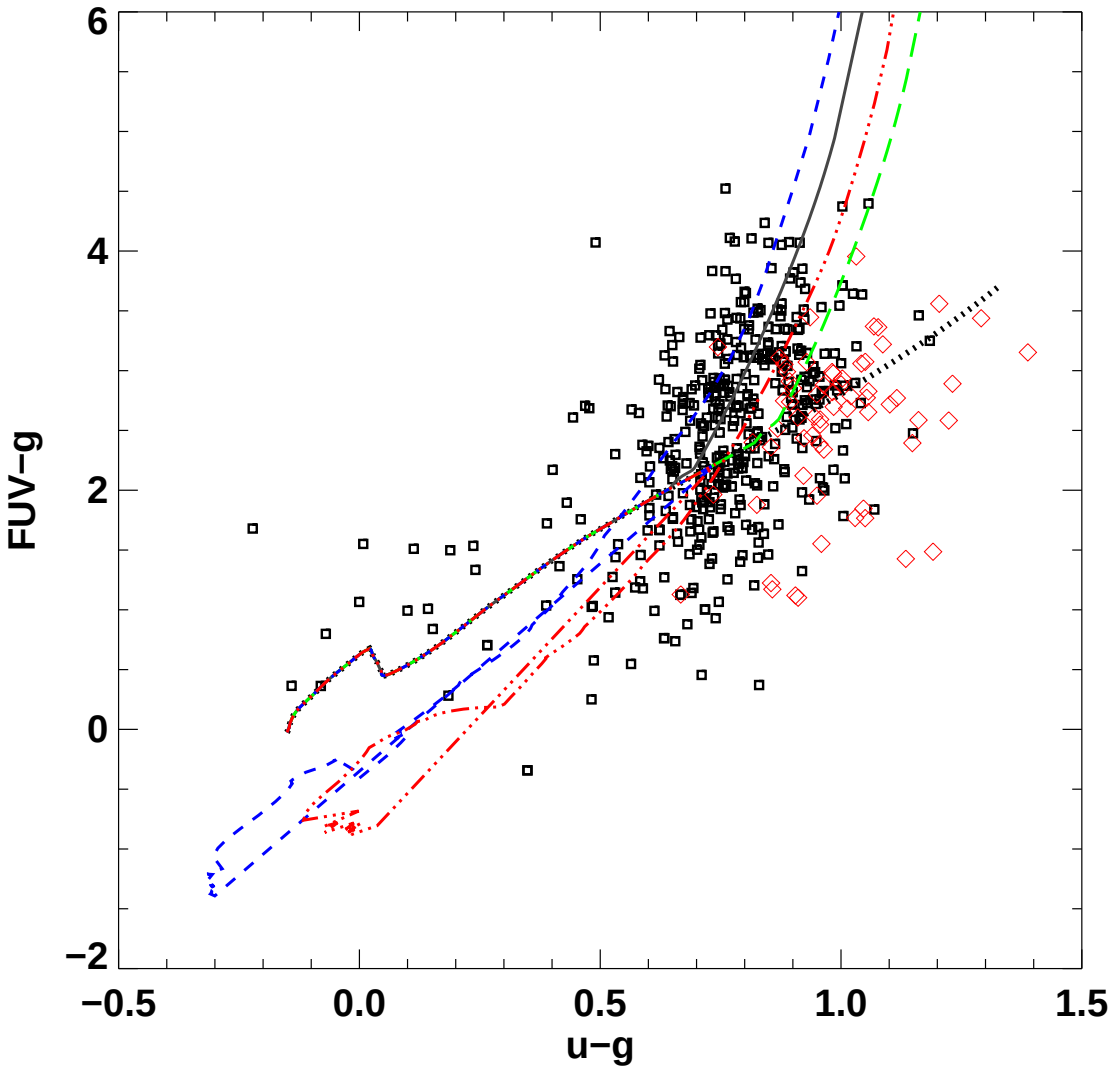

Figure 3.14: One realization of the observed $(FUV - g')$ vs. $(u' - g')$ colour of galaxies with $9.7 < \log_{10}(M_*/\ \mathrm{M}_\odot) < 10.5$, within 3Mpc from cluster centres of our $z \sim 0.2$ sample. Black squares represent blue galaxies and red diamonds represent red ones. The black dotted line shows the model track of a population whose star formation has been declining exponentially with a characteristic time scale of $\tau = 5$ Gyr (with a dust extinction of $\tau_\nu = 1$). The grey solid and green long-dashed lines show the evolution of the same exponentially declining population, but truncated 3 Gyrs and 7 Gyrs later. If a burst is added onto the exponentially declining model at 5 Gyrs right before the truncation of the star formation, the subsequent evolution is indicated by the blue short-dashed (with burst strength of 10 per cent) and red dot-dashed (with burst strength of 1 per cent) lines.

3.6 Conclusions

In this work, we examined the star formation properties of a large sample of galaxy clusters at $0.15 < z < 0.35$, from their cores out to ~ 7 Mpc, using the CFHTLS optical data and GALEX UV data. Our main findings are summarized below.

(i) We found that the average SSFR of galaxies with SFR above 0.7 $M_\odot$ yr^{-1} shows no dependence on the distance from the cluster centre, for all three stellar mass ranges examined here. Further, the SSFR distribution is similar to that in the field, with the exception of the high mass galaxies ($10.5 < \log_{10}(M_*/\ M_\odot) < 11.5$) at $z \sim 0.2$. A further examination of the distribution of the SSFR at this stellar mass showed that the number of galaxies with higher SSFR relative to those with lower SSFR is lower in clusters than in the field.

(ii) At $z \sim 0.2$, we found that the fraction of star-forming galaxies with SFR> 0.3 $M_\odot yr^{-1}$ at all stellar masses shows a clear decrease from $1 < r < 3$ Mpc to $0 < r < 1$ Mpc, but that there is no trend beyond $r = 3$ Mpc. At $z \sim 0.3$, we detected no change in the fraction of galaxies with SFR> 0.7 $M_\odot$ yr^{-1} (our detection limit) at all radii.

(iii) We found that the fraction of galaxies with red colours is constant from ~ 3 Mpc out to ~ 7 Mpc; however, within 3 Mpc, there is an abrupt increase in this fraction towards the cluster core. This is present at both redshifts, at all stellar masses examined here, but more so for the low stellar mass galaxies ($10.5 < \log_{10}(M_*/\ M_\odot) < 11.5$). Further, the red fraction of the low mass galaxies has increased by a factor of 2 from $z \sim 0.3$ to $z \sim 0.2$. Also, we found that even in the outskirts of the clusters, the red fraction is still higher than that in the field.

Our results suggest that, in cluster cores, it is possible that the star formation of the lowest stellar mass galaxies is truncated rapidly over the time of 1 Gyr. Further, galaxies in the outskirts seem to have had their star formation quenched relative to the field population, supporting the pre-processing scenario in which galaxies are quenched in groups before they fall into clusters. However, further investigation with spectroscopic data focusing on groups in the outskirt is required to determine if further quenching is happening in the outskirt relative to isolated groups.

Chapter 4

Structures out to the Accretion Zone

4.1 Introduction

How galaxy properties are affected by the environment they reside in remains one of the unsolved puzzles of galaxy formation. The galaxy population in clusters has been observed to have different properties from that in the field (e.g. Balogh et al., 2004a; Weinmann et al., 2006b; McGee et al., 2008), suggesting that this growth of large scale structure is accompanied by a transformation in galaxy properties. However, it is still an open question as to exactly what mechanisms are responsible for this difference (e.g. Balogh et al., 1999; Tanaka et al., 2006).

Clues might come from the outskirt regions of clusters, because that is where field and groups of galaxies are accreting onto clusters, especially along filamentary structures that are seen in simulations (e.g. Bond et al., 1996; Colberg et al., 1999). Groups in the outskirts are particularly interesting: a recent study by McGee et al. (2009), using a semi-analytic model, shows that a large fraction of galaxies that accrete onto clusters are in groups (but see Berrier et al. 2009), and they might have been pre-processed in the group environment before they fall into clusters (Balogh et al., 2000; Fujita, 2004; Li et al., 2009; Balogh & McGee, 2010). However, these groups are likely to be different from isolated groups in the field, due to their earlier formation time (Maulbetsch et al., 2007) and the tidal fields from the large-scale structure around clusters (Gnedin, 2003). Therefore, closer examination of groups and filamentary structures in the outskirts of clusters, and a comparison with isolated groups in the field, may provide important clues to how the cluster environment affects the properties of galaxies.

As we have shown in Chapter 3, the fraction of galaxies with red colour in the outskirts of clusters is already higher than that in the field, supporting the pre-processing scenario. However, there we were not able to determine if those galaxies are further processed due

to the large-scale structures around clusters. The issue there is, we studied a large sample of clusters (full spectroscopic coverage is impractical), using a statistical background subtraction method. This makes it hard to identify individual structures in the outskirts, such as groups, filaments, and relatively isolated galaxies. In this chapter, we turn to look at in detail the substructures around the most X-ray luminous cluster known, RX J1347-1145.

RX J1347-1145 is the most X-ray luminous cluster in the ROSAT All-Sky Survey (RASS, Schindler et al., 1995), with an X-ray temperature of about 10 keV (Schindler et al., 1997) at z=0.45. It has been the subject of intense study, through spectroscopic (Cohen & Kneib, 2002), X-ray (Schindler et al., 1997; Allen et al., 2002, 2008; Ettori et al., 2004; Gitti & Schindler, 2004; Gitti et al., 2007; Bradač et al., 2008; Ota et al., 2008; Miranda et al., 2008), lensing (Fischer & Tyson, 1997; Sahu et al., 1998; Kling et al., 2005; Bradač et al., 2005, 2008; Halkola et al., 2008; Miranda et al., 2008; Broadhurst et al., 2008), and Sunyaev-Zel'dovich (SZ) effect (Pointecouteau et al., 2001; Komatsu et al., 2001; Kitayama et al., 2004; Mason et al., 2009) analyses. However, most of the previous studies are on the inner regions. Here we focus on the large-scale structure extending out to $\sim$ 10 Mpc. The richness of this cluster allows us to trace its substructures using the same red-sequence technique described in previous chapters, but on much smaller scales. By looking at the distribution of red galaxies, an interesting structure presents itself immediately (as we will describe shortly below). We then carried out a spectroscopic follow-up on this structure, and study the dynamics of the structure.

In Section 4.2, we first describe our imaging data, and then show the structures traced by red galaxies in Section 4.3. In Section 4.4, we describe our spectroscopic follow-up on the interesting large-scale structure found in Section 4.3. In §4.5, we present the photometric and spectroscopic analysis on this structure, and the detection of another massive cluster, RXJ1347-SW, $\sim$ 7 Mpc from the cluster centre. We also present mass estimates of the two clusters through dynamical methods and weak lensing analysis. In §4.6 we compare our mass estimates of the main cluster with those in the literature, and discuss the possible filamentary connection between the main cluster and RXJ1347-SW using simulations. Our findings are summarized in §4.7.

Throughout, we assume a cosmology with present day matter density parameter Ω_m = 0.3, vacuum energy density parameter Ω_Λ = 0.7, and Hubble constant H_o=70 km s^{-1} Mpc^{-1}. All magnitudes are in the AB system.

4.2 Imaging Data

Deep g', r' , i', z' band images over a 1 square degree field were obtained using Megaprime on the CFHT in semester 05A (proposals 05AC10 and 05AC12), with total exposure times of 4200 s in g', 7200 s in r', 1600 s in i', and 3150 s in z'. The z' band data will not

be mentioned further, because they are not relevant for the work presented here. In each filter, images from single exposures are co-added using SWARP v2.16.0 (Bertin et al., 2002) and photometry is performed using SExtractor v2.4.4 (Bertin & Arnouts, 1996), with the camera run zero point. The latter quantity is provided by Elixir, and is extracted from the Landoldt field observed under photometric conditions every night. Since our science data were not taken under photometric conditions, a zero point offset calculated from a short exposure taken under photometric conditions is applied. The typical seeing is $\sim 0.8''$, $\sim 0.7''$ and $\sim 1''$ in g', r' and i' band respectively. Colours are measured using magnitudes within a fixed aperture of diameter 4.7 arcsec, which is much larger than the seeing difference in different filters. The magnitude measured within the Kron radius (*mag_auto*) is considered as the total magnitude for each object. Although crowding and blending of objects affects the photometry for about ten percent of the galaxies in our sample, we have checked that none of the results presented here are sensitive to this.

Star-galaxy separation is based on the stellar locus defined by the half-light radius as a function of total magnitude, in combination with the SExtractor parameter, *class_star*. Objects with $class\_star \leq 0.98$ in the g' band, and not on the stellar locus, are considered galaxies. The completeness limit for galaxies is $\sim$0.8 mag brighter than the 5σ limit for point sources (Yee, 1991); therefore, the completeness limit for galaxies in our catalog in the three bands that are relevant in this work is estimated to be $g' \sim 25$ mag, $r' \sim 25$ mag, and $i' \sim 23.2$ mag.

4.3 Photometrically Identified Structure

In this section, we describe the large-scale structure traced by the red-sequence galaxies. Only galaxies with $i' \leq 22$ mag are used, which ensures that for objects of interest here ($(g'-i') < 3$) our sample is complete in each band, and the colour measurement is reliable. At the redshift of this cluster ($z = 0.45$), the $(g' - i')$ colour brackets the 4000Å break; therefore we use this colour to identify red-sequence galaxies around this cluster, using a method based on the Red-sequence Cluster Survey technique (e.g. Gladders & Yee, 2000; Lu et al., 2009). We define the red-sequence at the redshift of the cluster using known cluster members from Cohen & Kneib (2002) that have $(g' - i')$ colour measurement in our catalogue. Given the small slope and the scatter of the colour, we choose to use a red-sequence that has zero slope with a half width of 0.15 mag. Assuming the probability distribution of the colour of each galaxy is Gaussian, with σ being the error on the colour measured from SExtractor, we can calculate the probability of each galaxy belonging to the colour slice (for details see Gladders & Yee 2000). The fact that the colour error from SExtractor is likely to be underestimated is not important here, because the width of the colour slice used is much wider than the colour uncertainties. We consider galaxies with at

least 10 per cent probability as red-sequence galaxies. In Figure 4.1, we show the spatial distribution of galaxies around RX J1347-1145. The black dots represent all galaxies (with obvious higher redshift galaxies excluded) in the field of view ($\sim$ 7 Mpc x7 Mpc), and small open red circles represent red-sequence galaxies.

One immediate interesting thing to notice is that there is an obvious elongated large-scale structure, going through the core of the cluster, running in the direction of NE-SW. It would be of great interest to know whether the proximity to this elongated structure has any effect on the properties of galaxies. To confirm and have a closer look at this large-scale structure, we carried out spectroscopic follow-up on the Magellan Telescope, targeting four positions along this structure. which we will describe in Section 4.4.

Before we go into our spectroscopic observation and analysis, we examine closer the photometric properties of this structure.

Using the background number counts measured from the Canada-France-Hawaii Telescope Legacy Survey (CFHTLS) Wide field 1, we can calculate the overdensity of red-sequence galaxies. We define the significance of the overdensity as the background-subtracted number of red-sequence galaxies divided by the *r.m.s.* of the background distribution. The contours of the significance map, smoothed over a region of radius $\sim$ 0.5 Mpc with a top hat function, are plotted in Figure 4.2, starting from 2σ, with an interval of 1σ.

The most significant peak ($\sim 25\sigma$) is the main cluster (the pointing "Centre"). The number of red-sequence galaxies (background subtracted) within 0.5 Mpc from the cluster centre, brighter than $m^* + 2$ ($i' = 22$ mag), denoted N_{red,m^*+2}, is $\sim 46 \pm 7$, where the uncertainty is estimated using Poisson statistics. Converting N_{red,m^*+2} to N_{200} according to figure 8 in Lu et al. (2009), and using the scaling relation between N_{200} and M_{200} (Johnston et al., 2007; Hansen et al., 2009), we estimate the mass of the main cluster from its richness to be $M_{200} \sim 1.4^{+0.4}_{-0.3} \times 10^{15} M_{\odot}$; although we note the conversion from N_{red,m^*+2} to N_{200} for such a high richness system is extrapolated from lower richness systems.

There is another prominent peak with a significance of $\sim 10\sigma$, about 7 Mpc (projected) away from the main cluster (pointing "SW"). The N_{red,m^*+2} for this system is $\sim 22 \pm 5$, which corresponds to $M_{200} = (3.3^{+1.3}_{-1.6}) \times 10^{14} M_{\odot}$. This suggests this system is a cluster in its own right, and we will refer it as RXJ1347-SW.

The significance contours also reveal several clumps of overdensities in the infall region around the main cluster, and an elongated large-scale structure running from NE to SW, along a line connecting the main cluster and RXJ1347-SW. Four positions along this line are targeted for our spectroscopic follow-up with the Magellan telescope as described in §4.4.1.

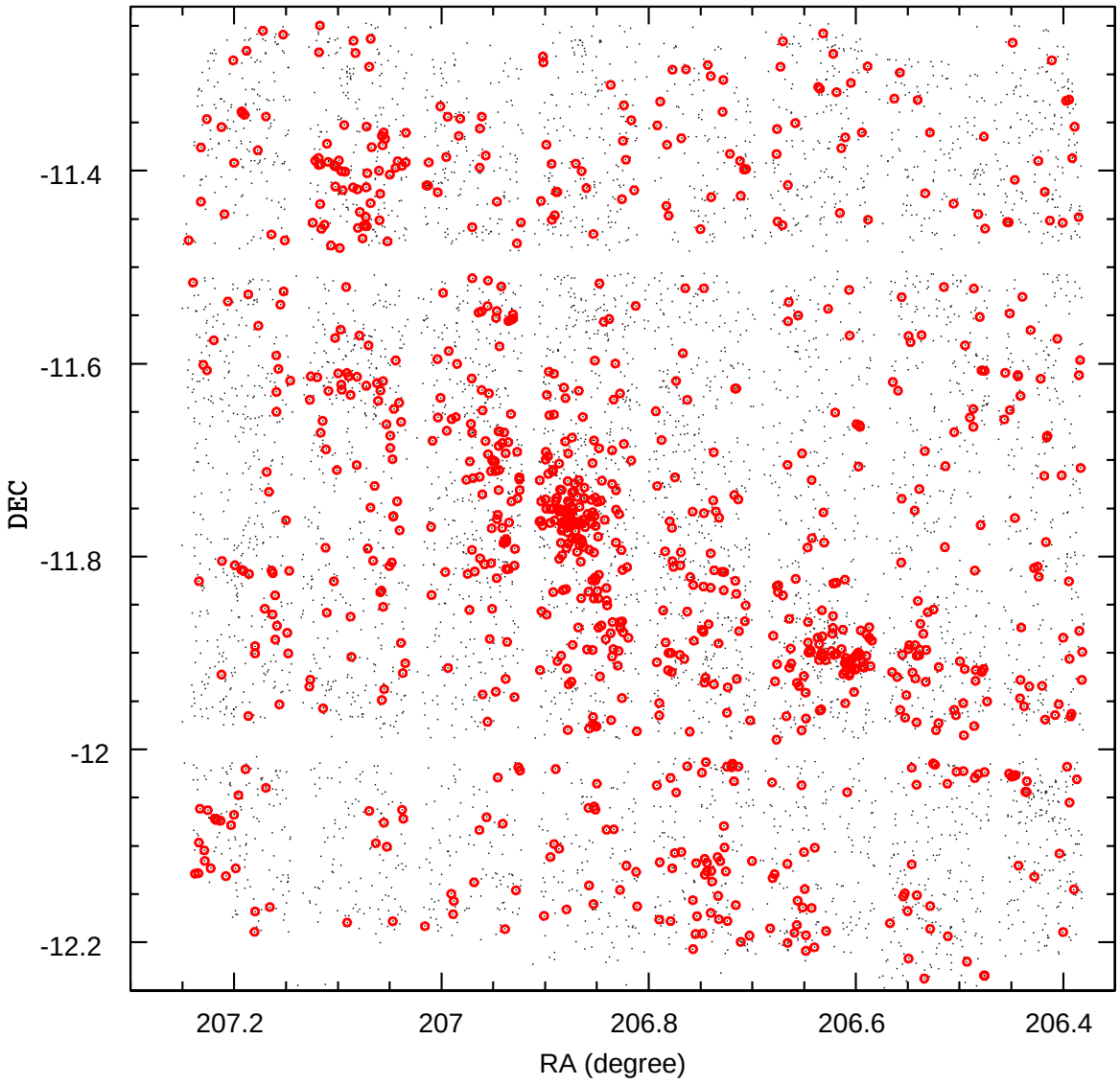

Figure 4.1: The spatial distribution of galaxies around RX J1347-1145 is shown, where the black dots represent all galaxies (with obvious higher redshift galaxies excluded) in the field of view, and small open red circles represent red-sequence galaxies.

4.4 Spectroscopy

4.4.1 Observations

In this section, we describe our spectroscopic observation at the four pointings (shown in Figure 4.2) that are chosen based on the large-scale structure traced by red-sequence galaxies.

To make the survey more efficient, we use the combination of $(g'-r')$ and $(r'-i')$ colour information to eliminate obvious higher redshift galaxies (see figure 6 in Lu et al. 2009 for more details). Again, we select galaxies with $i' \leq 22$ mag (see Section 4.3). We make sure our targets are not colour biased; as can be seen in Appendix A.1, the completeness in each pointing for the red and blue populations separately is similar, at ~ 50 per cent.

Spectra were obtained using the Low Dispersion Survey Spectrograph 3 (LDSS3) on the 6.5 meter Clay Telescope over the nights from 2008 April 28th to May 1st. The pointing positions are indicated in Figure 4.2, each with a FOV of 8.3 arcmin in diameter (corresponding to r=1.4 Mpc at the redshift of the cluster). The VR filter and Medium Red grism were used, which covers the wavelength range 5000Å to 7200Å. At the redshift of the cluster, the important spectral features CaH, CaK, G-band, Hδ and [OII] fall into this wavelength range. Each pointing was observed with two masks, with an average of ~ 60 objects and 3x20 mins exposure, per mask, with slit width 1.2 arcsec, providing a spectral resolution of ~ 14Å.

4.4.2 Data Reduction

The 2d raw spectra were first reduced using the COSMOS2 software package, then 1d spectra were extracted and redshifts were determined using a modified version of *zspec* kindly provided by Renbin Yan (Cooper et al., 2009). In *zspec*, spectra are first compared with eigen-templates and the ten best-fitted redshifts are provided. We then visually examine the spectra and determine the best redshift. Usually the first or second choice provided is a good fit. Occasionally when none of the ten choices is a good match, we manually cross-correlate the spectral features and find the best-fit redshift. We consider redshifts determined from at least three supporting spectral features as secure. Two example spectra, near the magnitude limit of our survey, are shown in Appendix A.3.

For the 473 objects targeted, we obtained 400 secure redshifts, which are used in the analysis here. Further details on the success rate, and the efficiency of our survey are presented in Appendix A.1. From the objects that have duplicate observations, the uncertainty on the redshift is estimated to be ~ 113 km s^{-1} in the rest frame (see Appendix A.2). We also compare the redshift of the common objects in our catalogue with that from

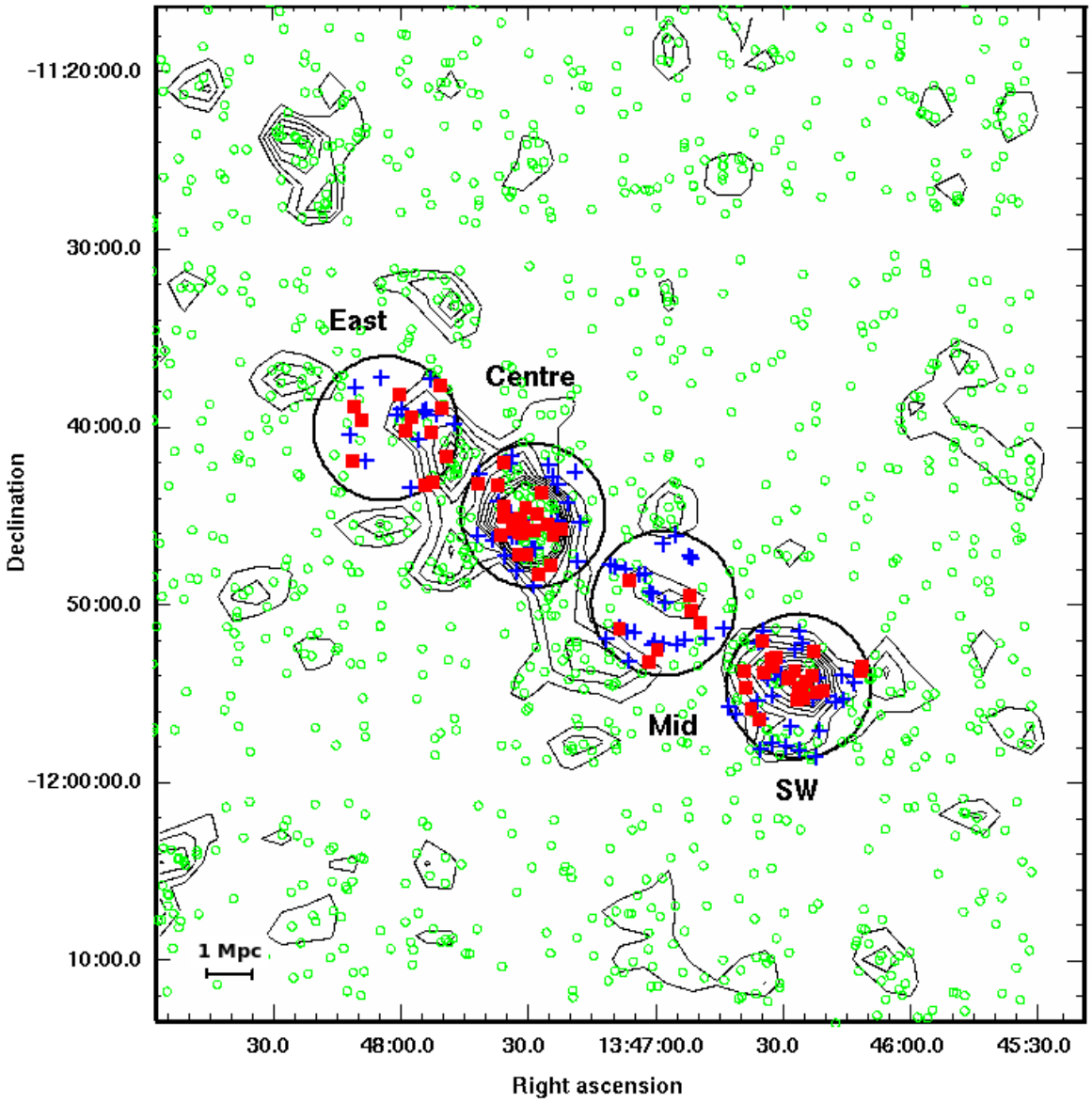

Figure 4.2: The spatial distribution of the large-scale structure with the surface density contours of red galaxies overlaid. The density contours start at 2σ from the mean and increase with an interval of 1σ. The small circles indicate all galaxies with red colours, the squares and crosses are respectively confirmed red and blue galaxies that are associated with the large-scale structure. The four large circles indicate the pointing positions with spectroscopic follow-up.

Cohen & Kneib (2002), and find no systematic difference between these measurements (Appendix A.2); therefore, in the following analysis, we add the extra 34 redshifts from Cohen & Kneib (2002) to our sample when applicable.

4.5 Results

4.5.1 Dynamics

In this section, we present the dynamical analysis of the above described photometrically identified structure, based on the redshifts obtained.

Redshift Distribution and Velocity Dispersion

In Figure 4.3, the full redshift distribution of all galaxies is shown as the dotted open histogram. There are two main peaks in the full distribution: one corresponds to the centre of the main cluster, and the other corresponds to RXJ1347-SW. We analyze these two clusters in detail first in this section, and examine the dynamics of the large-scale structure in the next section.

The redshift distribution of galaxies within $\sim$ 1.4 Mpc from the main cluster centre is shown as the shaded histogram. The distribution is smooth in general; there is an indication of two separate peaks, but the distribution is still consistent with being drawn from the single Gaussian overplotted on the shaded histogram in Figure 4.3. In particular, a χ^2 test shows that a subsample drawn from this single Gaussian distribution would have a χ^2 value as large as we observed about 80 per cent of the time. The mean redshift we measure is 0.4513 ± 0.0006, consistent with the previous measurement by Cohen & Kneib (2002). The dispersion we measure, using the bi-weight method of Beers et al. (1990), with 3σ clipping applied, is 0.0056 ± 0.0005, which corresponds to a rest-frame velocity dispersion of 1163 ± 97 km s^{-1}. The errors are estimated using Jackknife resampling (Wall & Jenkins, 2003). From now on, we refer to galaxies that are within 3 times the dispersion as members of the main cluster. The velocity dispersion we measure is higher than that of Cohen & Kneib (2002) (we discuss this more in §4.6.1).

Despite the consistency with a single Gaussian there is an indication of two separate velocity peaks in the distribution. A χ^2 test shows that, at the $\sim$30 per cent level, the distribution is consistent with a combination of two Gaussian functions: one with $\bar{z_1} = 0.4495$ and rest-frame velocity dispersion $\sigma_1 = 620$ km/s, and the other with $\bar{z_2} = 0.4552$ and $\sigma_2 = 535$ km/s. In that case, the centre of the cluster would be composed of two separate components with much smaller masses, and a relative velocity of ~ 1000 km s^{-1};

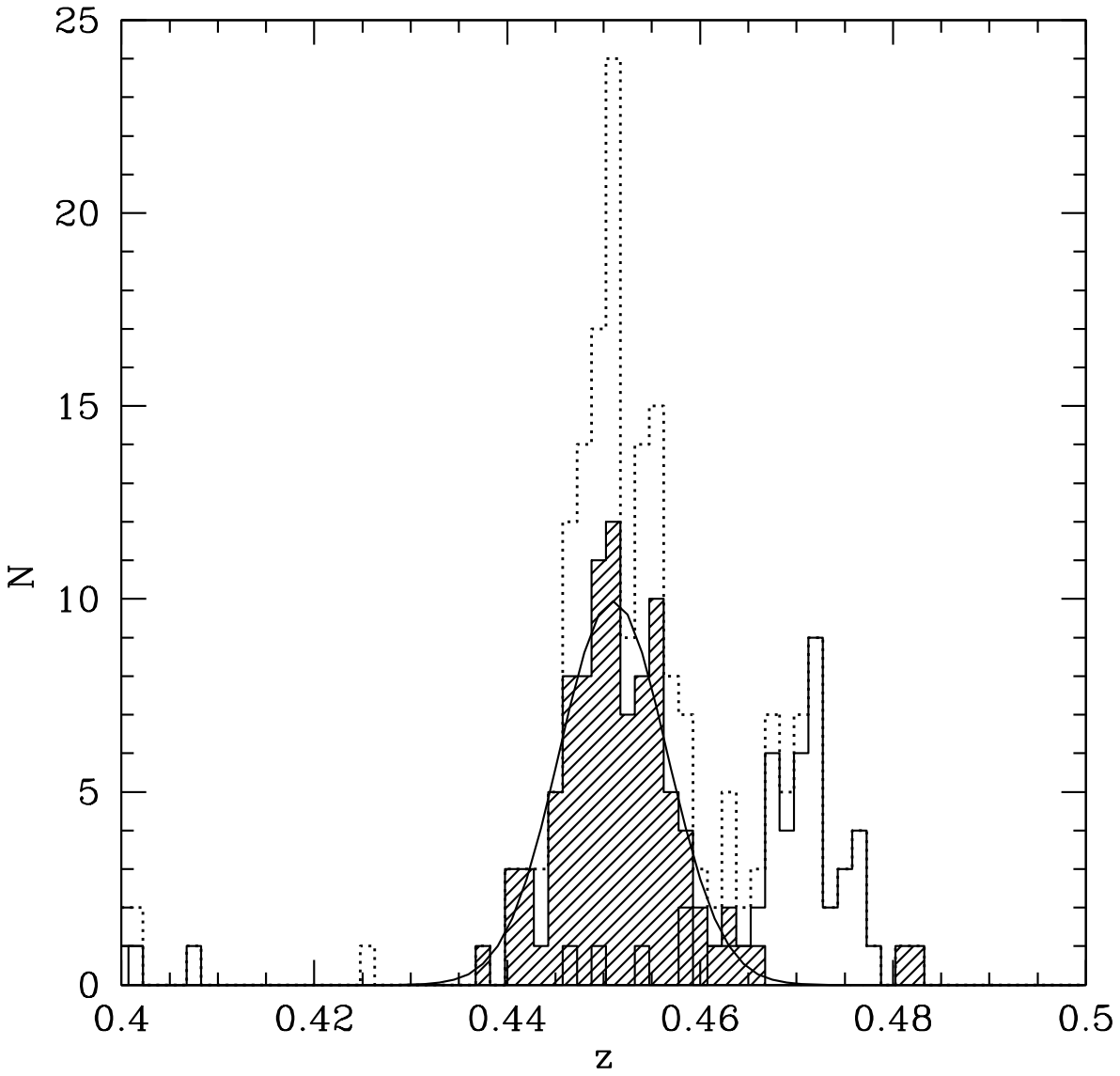

Figure 4.3: The galaxy redshift distribution from the full area is shown as the dotted, open histogram. The shaded histogram shows the distribution of galaxies in the centre of the main cluster ($r \lesssim 1.4$ Mpc), Gaussian function that is statistically consistent with this distribution, overlaid. The redshift distribution of galaxies within $r \lesssim 1.4$ Mpc around RXJ1347-SW is shown as the solid open histogram.

considerably larger than the < 100km/s difference between the two BCGs ($z_1 = 0.4515$ and $z_2 = 0.4511$). Although statistically this model is not favoured over the single-population model, we cannot rule out the possibility that there are two distinct dynamical components. We revisit this further in § 4.6.1 when we consider both the spatial and velocity distribution of galaxies.

The redshift distribution of RXJ1347-SW (pointing "SW") is shown as the open solid histogram in Figure 4.3. It is not significantly different from a Gaussian distribution, with a mean redshift of 0.4708 ± 0.0006, and dispersion of 0.0038 ± 0.0005, or 780 ± 100 km s^{-1}.

Phase Space Distribution

We examine the dynamics of the large-scale structure by converting the redshift of each galaxy to a rest-frame velocity relative to the central redshift of the main cluster. In Figure 4.4 we show the velocity offset as a function of position projected along the line connecting the main cluster and RXJ1347-SW. Galaxies in the inner region of the cluster mainly occupy regions spanning from -2000 km s^{-1} to 2000 km s^{-1}, symmetrically, while RXJ1347-SW is at ~ 4000 km s^{-1} from the main cluster. Note that in velocity space, the region occupied by members of massive clusters resembles a trumpet shape, as expected in a spherical infall model (e.g. van Haarlem & van de Weygaert, 1993). The dashed curves in Figure 4.4 indicate the boundary of the caustics for these two systems, derived analytically from equation (7) in Diaferio (1999) assuming the two systems follow a NFW profile (Navarro et al., 1997) (note this analytical curve is not used in the derivation of the mass using the caustic technique that will be discussed in §4.5.3). In pointing "East", on the other side of the main cluster away from RXJ1347-SW, there are almost no galaxies in the regions labelled "A" and "B" in Figure 4.4 around the cluster above the caustic curve. In comparison, there are ~ 8 galaxies occupying the region between the main cluster and RXJ1347-SW, labelled "C". Given that our redshift completeness is about 50 per cent, we expect there are approximately twice as many $i' < 22$ galaxies (~ 16) within that region in total. Note this is not a sampling bias, because the pointing "East" and "Mid" are located symmetrically on two sides of the main cluster. Also, the uncertainties on the redshift determination, or the position of the caustic curve, would not change the fact that there is an excess of galaxies between the main cluster and RXJ1347-SW. In §4.6.2 we will use simulations to investigate whether these galaxies are physically residing in regions between the main cluster and RXJ1347-SW, and thus suggest a possible structure connecting the two systems.

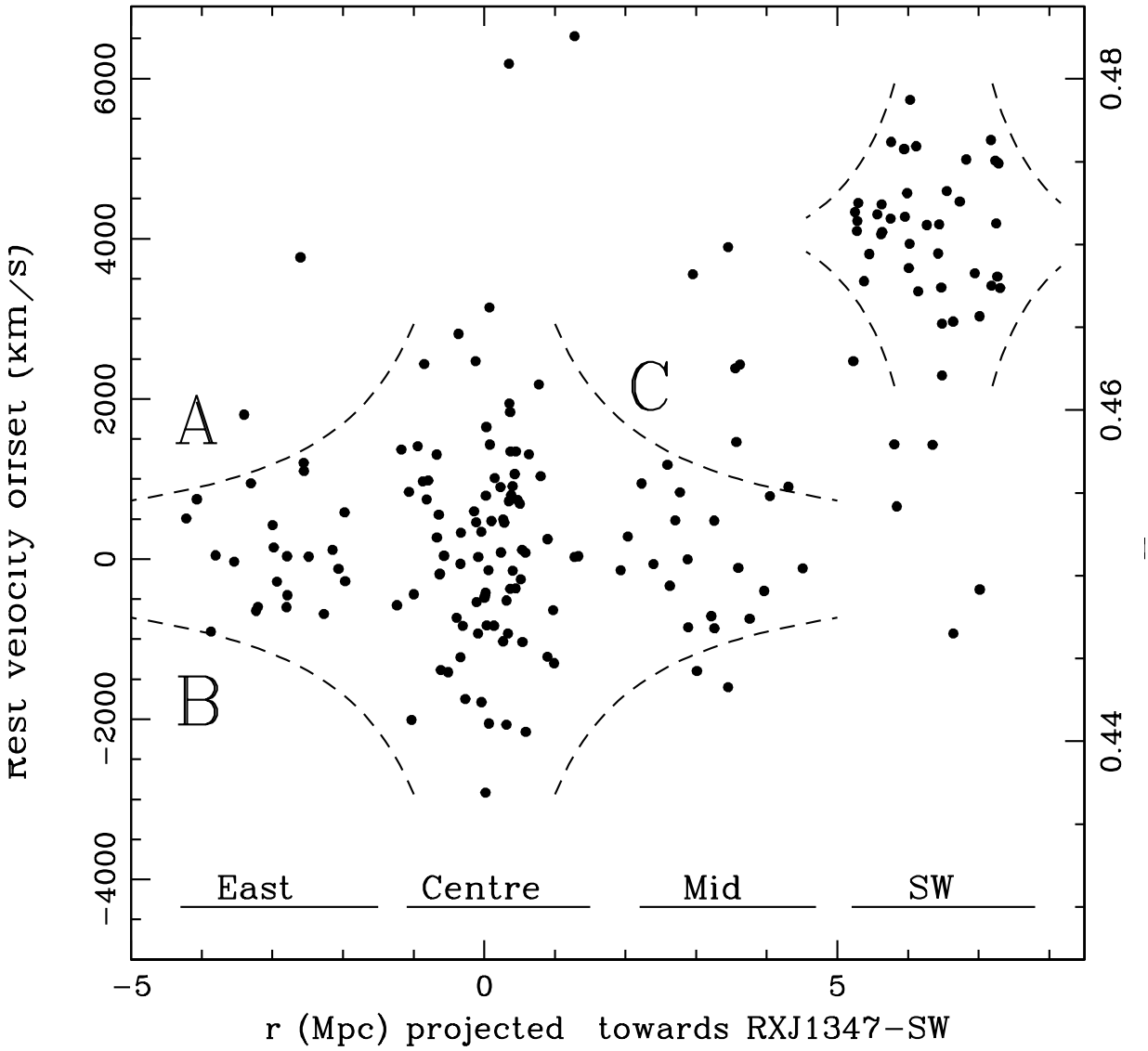

Figure 4.4: The rest frame velocity offset as a function of distance relative to the cluster centre projected along the line towards RXJ1347-SW. The dashed curves indicate the boundary of the caustics. See text for details.

4.5.2 Colour Distribution

As described in §4.3, we trace the large-scale structure around this cluster using red-sequence galaxies. We consider galaxies in the redshift range $\bar{z}_{cl} - 3\sigma_{cl} < z < \bar{z}_{sw} + 3\sigma_{sw}$ as associated with the structure, where $\bar{z}_{cl}$ and σ_{cl} are the mean and dispersion of the redshift distribution of the main cluster, and $\bar{z}_{sw}$ and σ_{sw} are the same for RXJ1347-SW. In Figure 4.2, solid squares and crosses represent red and blue galaxies that are spectroscopically confirmed to be associated with the structure, respectively.

The study by Butcher & Oemler (1984) revealed a higher fraction of blue galaxies in high redshift clusters compared to local ones (the Butcher-Oemler effect), indicating on-going star formation in high redshift clusters. Since then there have been many studies on the dependence of this effect on the environment, and cluster properties such as the X-ray temperature (e.g. Urquhart et al., 2010; Wake et al., 2005). RX J1347-1145 is the most X-ray luminous cluster known, and has an elongated large-scale structure; therefore it is interesting to explore the colour distribution of the galaxies in this structure. The colour-magnitude diagram of galaxies in the four pointings along the structure is shown in Figure 4.5. Open circles are all galaxies in the field of view, crosses are galaxies with secure redshift obtained, and filled circles are members associated with the structure.

We calculate the blue fraction of the main cluster using the Butcher & Oemler (1984) criterion, i.e. galaxies 0.2 mag bluer than the colour-magnitude relation (CMR) in rest-frame (B-V). We transform rest-frame $\triangle(B-V) = 0.2$ into our observed $\triangle(g'-i')$ using the colour difference between E and Sab galaxies from Fukugita et al. (1995), as indicated by the dashed lines in Figure 4.5. The number of blue cluster members is calculated by dividing the number of spectroscopically confirmed blue galaxies by the completeness of the spectroscopy for the blue population. The number of red cluster members is calculated in the same way, and the total number of members is then the sum of that of the blue and red galaxies. The blue fraction of RX J1347-1145 within the central 1.4 Mpc ($\sim 0.8 r_{200}$), down to $i' = 21$ (corresponding to $M_V \sim -20$) is $20^{+9}_{-8}\%$. The uncertainty is estimated using the weighted binomial statistics Gehrels (1986). Note although RX J1347-1145 is the most X-ray luminous cluster in the RASS, its blue fraction in the central region is similar to that of other less luminous clusters (Ellingson et al., 2001), consistent with the lack of X-ray luminosity dependence found by Wake et al. (2005). The blue fraction of the cluster RXJ1347-SW ($36^{+13}_{-12}\%$) is, within the uncertainty, consistent with that of the main cluster.

From the contours in Figure 4.2, the region between the main cluster and RXJ1347-SW shows an overdensity of red-sequence galaxies. Our spectroscopy also reveals a large population of blue galaxies, and it is interesting to note that they form two trails running in the same direction as the elongation of the large-scale structure. The large blue population associated with an overdensity of red galaxies is particularly interesting. It suggests that targeting regions with overdensities of red-sequence galaxies for spectroscopic follow-up is a

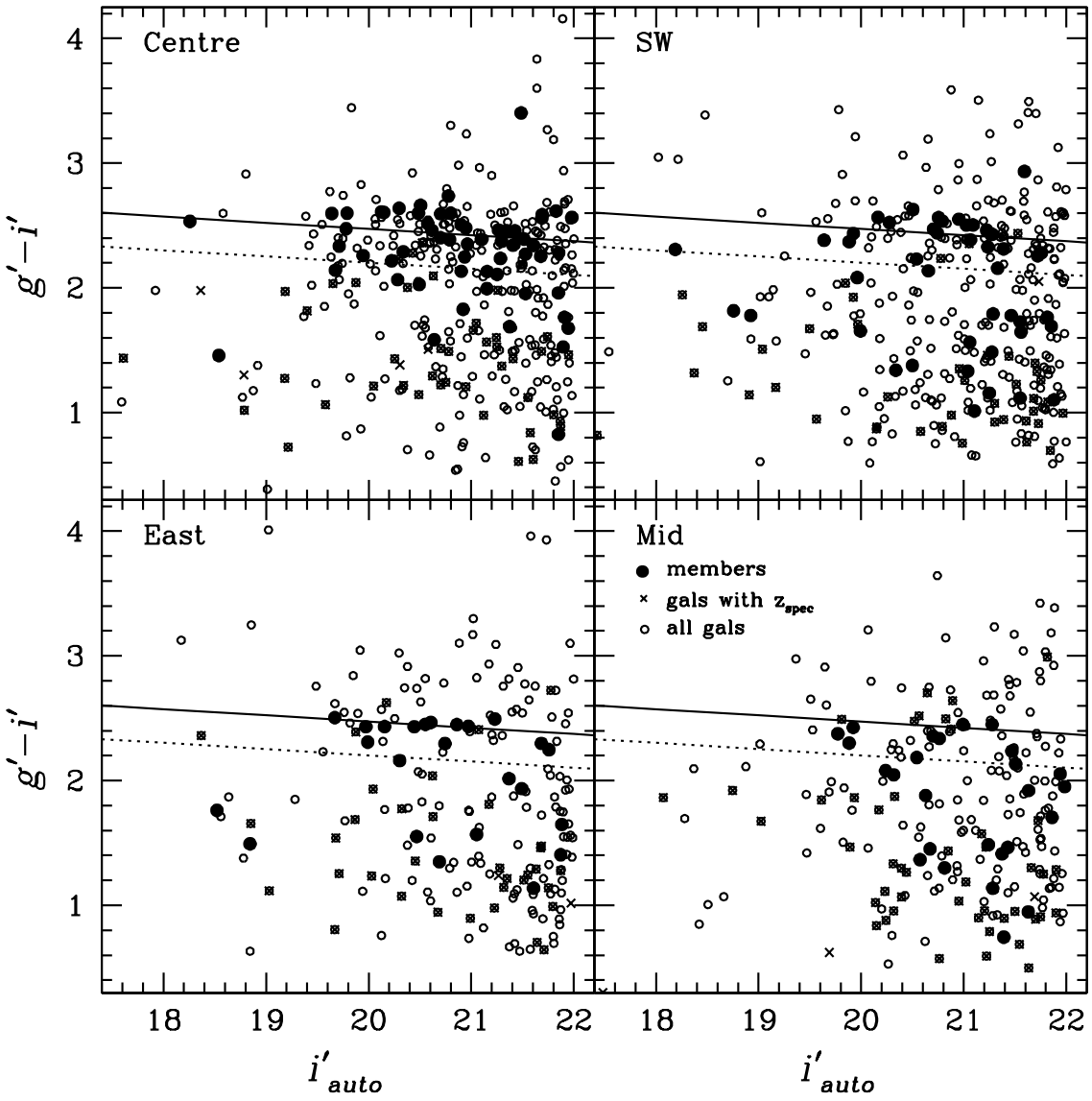

Figure 4.5: The colour-magnitude diagram of galaxies is shown for each of the four pointings we targeted, along the elongated structure. Open circles are all galaxies in the field of view, crosses are galaxies with secure redshifts, and filled circles are members associated with the structure. Solid lines are fitted red-sequences, and dashed lines separate blue galaxies from the red-sequence (see text for detail).

strategy that allows the efficient selection of cluster members, while still tracing interesting structures with active star formation. A more thorough analysis of the stellar populations in the large-scale structure will be done when the rest of the data are obtained.

4.5.3 Mass Estimate

In this section, we estimate the mass of the main cluster and RXJ1347-SW using different methods. We defer a comparison with the literature, and the discussion of the dynamical implication, to §4.6.1.

Dynamical Estimates

For a given density profile and velocity anisotropy, the velocity dispersion can be used to infer the virial mass. Under the assumption of a singular isothermal density profile and a velocity anisotropy that satisfies $\sigma = v_c/\sqrt{2}$ (Łokas & Mamon, 2001), the virial mass can be expressed as $M_v = 2\sigma_1^2 r_v/G$. Applying this to the measured velocity dispersion (§4.5.1) yields a $M_{200} = \sqrt{2}\sigma_1^3/\left[5H(z)G\right] = 1.16^{+0.32}_{-0.27} \times 10^{15} M_\odot$, with $r_{200} = \sqrt{2}\sigma/\left[10H(z)\right] = 1.85$ Mpc. This mass estimate agrees well with that inferred from the richness of the cluster, as described in §4.3.

Under the same assumptions, the mass of RXJ1347-SW is estimated to be $M_{200} = 3.4^{+1.4}_{-1.1} \times 10^{14} M_\odot$, with $r_{200} = 1.22$ Mpc. This M_{200} is also in good agreement with that inferred from the richness, and confirms that the cluster RXJ1347-SW we detected photometrically using the red-sequence galaxies is indeed a massive cluster. There has not been any report on the existence of this cluster in the literature.

Another method to estimate the mass through dynamical analysis is the caustic technique, under the assumption that clusters form through hierarchical accretion (Diaferio & Geller, 1997; Diaferio, 1999). The advantage of this technique is that it does not depend on the assumption of dynamical equilibrium, and it can probe the mass out to large radii where the virial theorem does not apply any more.

As described in §4.5.1 (Figure 4.4), cluster members occupy a region in velocity space with a trumpet shape delineated by caustics that separate them from the Hubble flow. Assuming spherical symmetry, the mass of the cluster can be estimated as:

$$M(< r) = \frac{1}{2G} \int_o^r \mathcal{A}^2(r) dr, \tag{4.1}$$

where $\mathcal{A}$ is the amplitude of the caustic. The prescription for implementing the caustic method is described in detail in Diaferio (1999). Here we only summarize the key steps.

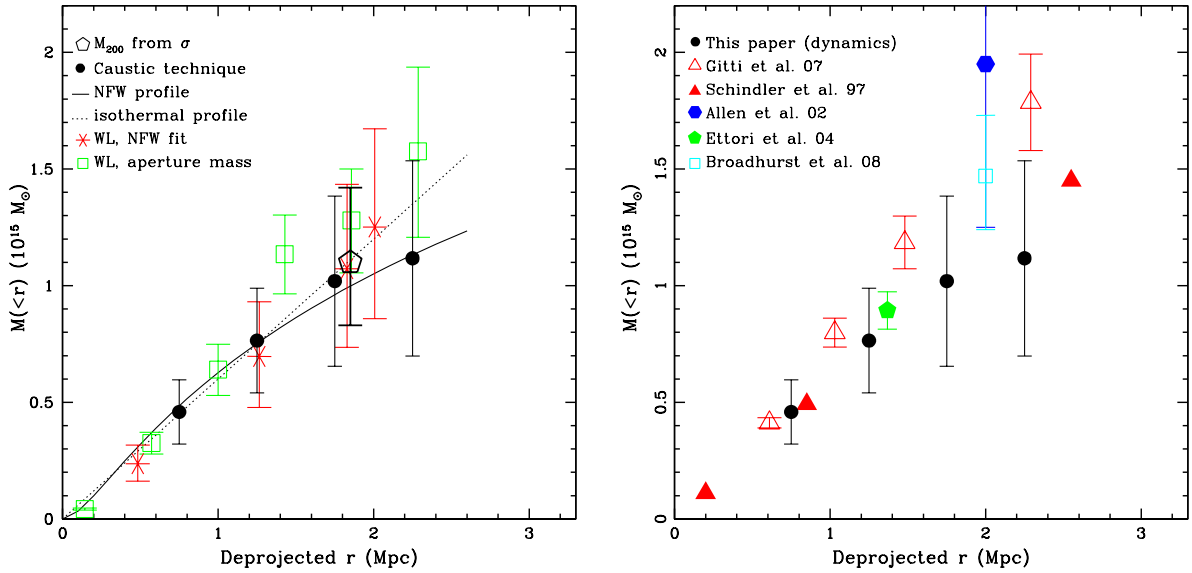

Figure 4.6: The deprojected mass profile for RX J1347-1145. Left panel: the black points represent the mass profile inferred from the caustic method. The solid, and dotted curves show the fitted NFW and isothermal profile respectively. The stars and open squares are our weak lensing analysis. Right panel: the black points are the same as in the left panel. The other symbols are mass estimates from the literature.

Since the location of the caustics is where clusters are separated from the Hubble flow, it is indicated by a significant drop of the density of cluster members in velocity space. Therefore, one first calculates the density as a function of velocity at different radii, using an adaptive kernel method (Silverman, 1986). In order to use the spherical smoothing window, the window size in velocity and distance, h_v and h_r, has to be rescaled (see Diaferio, 1999, for details). For our data, we choose $q = h_v/h_r = 6$, and a spherical smoothing window size of $\sim$ 700 km/s*. In the central region of clusters, the escape velocity (essentially the location of the caustics) is twice the velocity dispersion, which is valid under the assumption that the central region of the cluster is virialized. Therefore, in practice, the threshold density where the significant drop occurs (and thus determines the amplitude of the caustics) is chosen so that the above condition is satisfied.

The deprojected mass profile of the main cluster estimated using this technique is shown as solid dots in both panels of Figure 4.6. The errors are estimated using Jackknife re-sampling (Wall & Jenkins, 2003). At $r_{200} = 1.85$ Mpc the enclosed mass is $\sim 1 \times 10^{15} M_{\odot}$.

*Within the range of reasonable choices of parameters, the change of the resulting mass profile is within the resulting error bars.

This is in excellent agreement with that inferred from the velocity dispersion; however, this is largely true by construction, since the density threshold is chosen such that the two techniques agree within the virialized region of the cluster. The caustic-based measurements have the most value at larger radii, where the assumption of virial equilibrium is unlikely to hold. Note beyond $r \sim 2$ Mpc, we only have sparse sampling in two pointings, and the velocity distribution of galaxies in these pointings is not likely representative of that of the whole population at that radius, due to the presence of elongated large-scale structure. We fit the mass profile to a NFW (Navarro et al., 1997) and isothermal profile, shown as the solid and dotted curves respectively in the left panel of Figure 4.6[†]. Because of the large uncertainties on the mass profile due to limited data, the two profiles cannot be distinguished.

Weak Lensing Analysis

We use the deep CFHT r' imaging data to study the cluster mass distribution using weak gravitational lensing. Unlike dynamical methods, the weak lensing signal provides a direct measurement of the *projected* mass, irrespective of the dynamical state of the cluster. Furthermore, the observed signal can be used to "map" the distribution of dark matter (e.g. Kaiser & Squires, 1993).

Our cluster weak lensing analysis follows in detail the steps described in Hoekstra (2007). In order to relate the lensing signal to a physical mass requires knowledge of the redshift distribution of the sources. The wavelength coverage and limited depth of the observations prevent us from deriving accurate photometric redshifts for the individual sources. Instead we use the results from Ilbert et al. (2006) who determined photometric redshifts for galaxies in the CFHTLS deep fields.

To determine the lensing signal, we measure the shapes of galaxies with $22 < r' < 25$. We use such a relatively faint cut because of the high redshift of the cluster. The galaxy shapes are corrected using the method presented in Kaiser et al. (1995), with modifications described in Hoekstra et al. (1998). The weak lensing signal is sensitive to all structure along the line-of-sight and, as shown in Hoekstra (2001, 2003), this distant (uncorrelated) large-scale structure introduces additional noise to the mass estimate. This 'cosmic shear' noise is included in the errors listed below. We note that the noise due to the intrinsic ellipticities of the sources dominates because of the relatively high cluster redshift.

The weak lensing reconstruction of the projected surface density with a smoothing scale of $123.3''$ is presented in Figure 4.7[‡] out to ~ 10 Mpc. To indicate more clearly which

[†]The fitted NFW profile is used in the analytic derivation of the caustic curves shown in Figure 4.4 and discussed in §4.5.1.

[‡]The map presented in this Figure was constructed using source galaxies with $23 < r' < 25.5$

structures are significant, we show the signal-to-noise ratio, rather than the signal itself, as the grey scale (see the left panel in Figure 4.10 for a more detailed view). The main cluster and RXJ1347-SW are clearly detected, at $\sim 8\sigma$ and $\sim 4\sigma$ levels respectively. No other significant structures are evident in this map. The contours of the overdensity of the red-sequence galaxies, the same as in Figure 4.2, are overplotted on top of the mass map. For the main cluster and RXJ1347-SW, the mass concentrations coincide with the overdensities of red-sequence galaxies.

The smoothing of the mass map limits its use to determine the cluster mass. Instead, we compute the mean tangential distortions as a function of distance from the cluster center. The resulting measurements for the main cluster and RXJ1347-SW are shown in Figure 4.8. We estimate the cluster masses from these shear measurements using two different methods. The first, and most commonly used, is to assume a density profile and determine the best fit parameters to the observed tangential distortion. For comparison with the dynamical results, we first fit a singular isothermal sphere model (SIS) to the observations between 500 kpc and 2 Mpc, which yields a velocity dispersion of $\sigma = 1282 \pm 124$ km/s, in excellent agreement with the results based on the redshifts of the cluster galaxies. Thanks to the wide-field lensing data, we can also apply the same method to RXJ1347-SW (centred at $13^{\rm h}46^{\rm s}27.2^{\rm s}$, $-11^\circ 54' 20.2''$), for which we obtain a velocity dispersion of $\sigma = 927 \pm 165$ km/s, also in good agreement with the value inferred from the redshifts of the cluster members.

Although the SIS allows for an easy comparison to the observed velocity dispersion, a more physically motivated function is the NFW (Navarro et al., 1997) profile, which has been inferred from numerical simulations. We assume the mass-concentration relation from Duffy et al. (2008) and fit the NFW model to the data within 500 kpc and 2Mpc. With these assumptions, we find a best-fit value for the virial mass of $M_{\rm vir} = 1.89^{+0.59}_{-0.55} \times 10^{15} M_\odot$. The best fit NFW model within different apertures are indicated by stars in the left panel of Figure 4.6. For RXJ1347-SW we obtain $M_{\rm vir} = 6.4^{+3.9}_{-3.3} \times 10^{14} M_\odot$.

To compare to the results from the cluster galaxy dynamics, we also compute the corresponding masses within $r_{200}^{\rm dyn} = 1.85$ Mpc. For this choice of radius we obtain $M_{200} = 1.47^{+0.46}_{-0.43} \times 10^{15} M_\odot$ for the main cluster. This result is in excellent agreement with the value inferred from dynamics. For RXJ1347-SW we obtain $M_{200} = 4.8^{+2.9}_{-2.5} \times 10^{14} M_\odot$ for $r_{200}^{\rm dyn} = 1.22$ Mpc.

Since weak lensing signals are sensitive to the total mass projected along the line-of-sight; it is interesting to consider a non-parametric estimate for the projected mass within an aperture (e.g. Clowe et al. 1998; Fahlman et al. 1994; see Hoekstra (2007) for our implementation). The resulting *projected* masses as a function of radius are presented in Figure 4.9 as solid hexagons. Figure 4.9 also shows other estimates from the literature, which will be discussed in detail in §4.6.1.

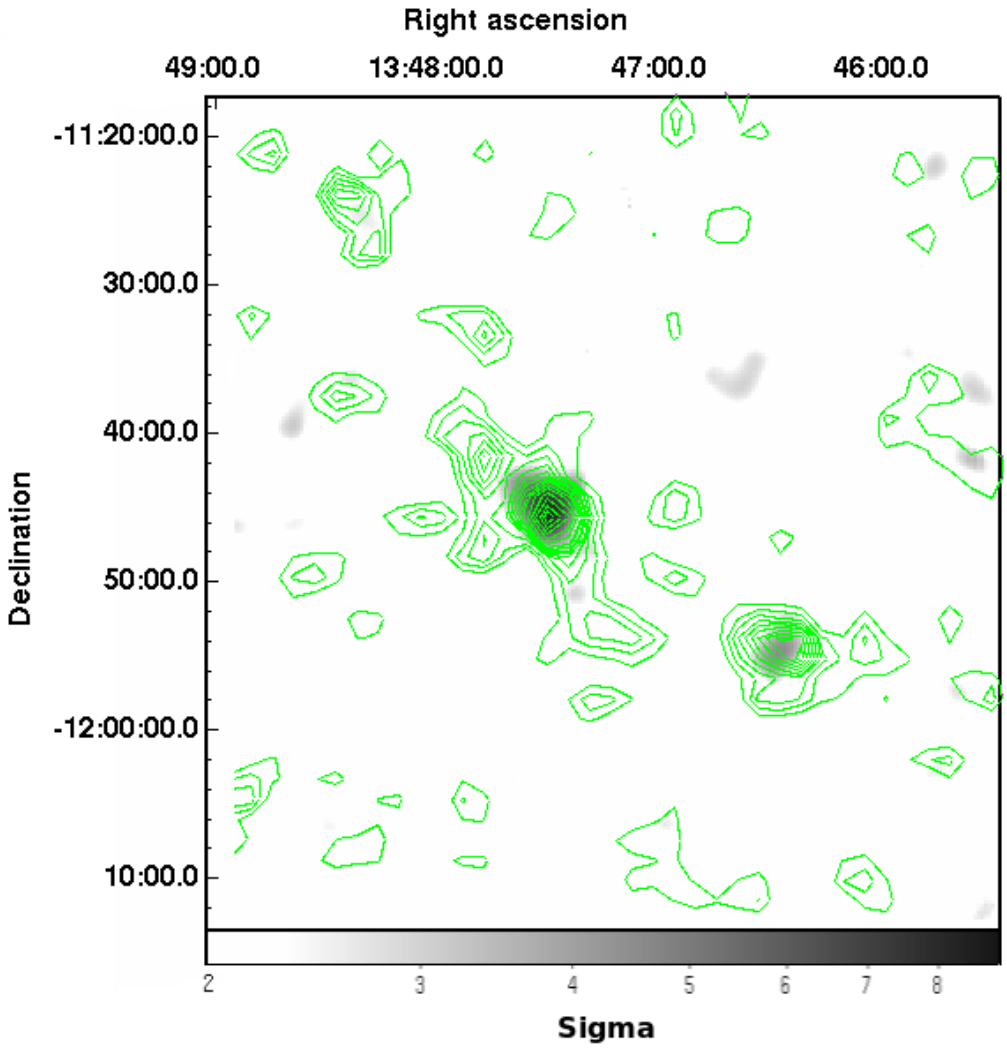

Figure 4.7: The grey scale shows the weak-lensing signal-to-noise map, out to ~ 10 Mpc from the main cluster centre. Contours of the red galaxy surface density (as in Figure 4.2) are overlaid, starting from 2σ with an interval of 1σ. The two prominent peaks are the main cluster and RXJ1347-SW; their mass concentrations coincide with the overdensities of the red-sequence galaxies.

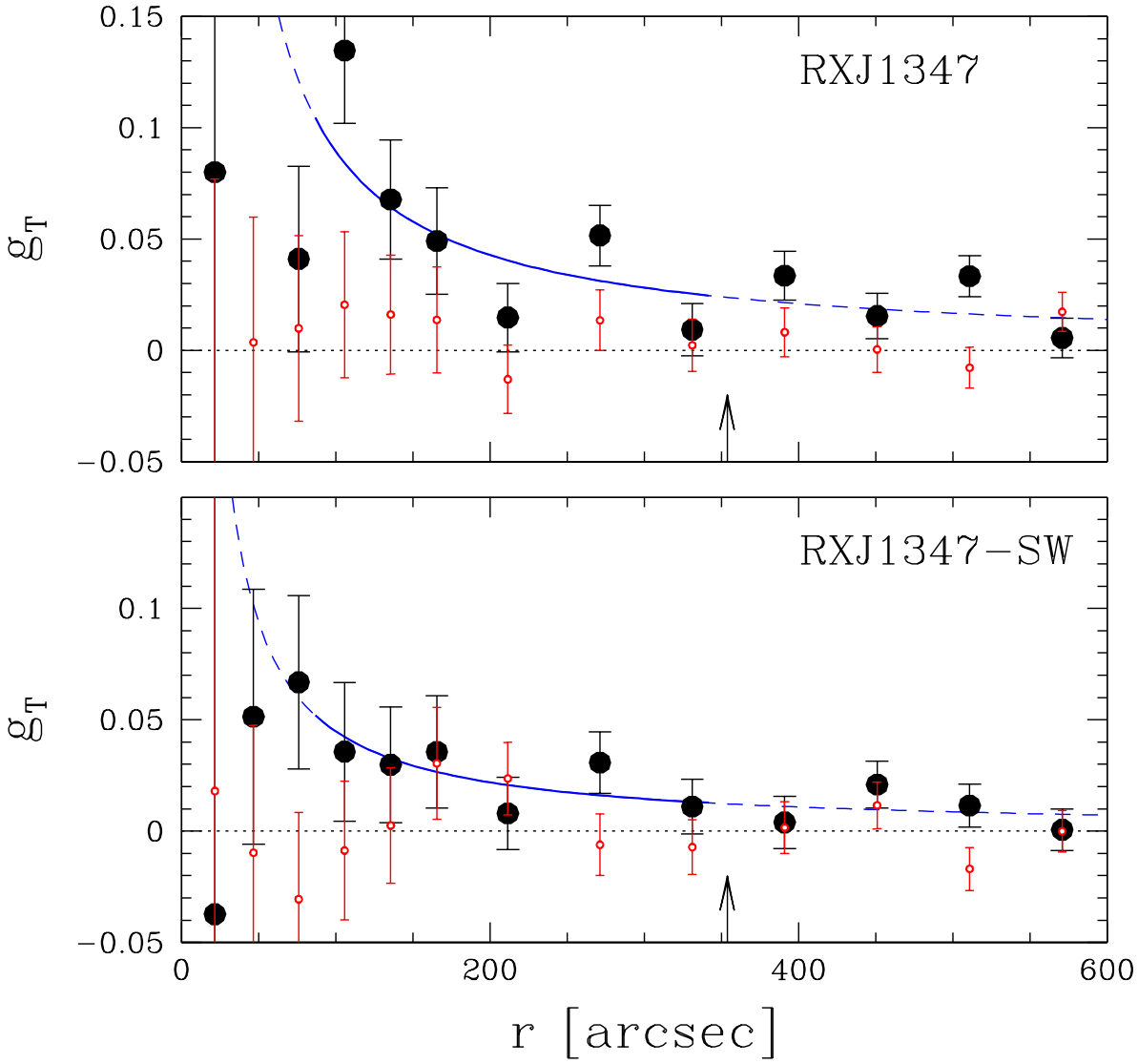

Figure 4.8: Tangential distortion as a function of the distance from the cluster center for the main cluster (top panel) and RXJ1347-SW (bottom panel). In both cases we detect a significant lensing signal out to large radii (the arrows indicate 2 Mpc). The open points correspond to the signal that is measured when the sources are rotated by 45 degrees, which provides a measure of the level of systematics. The points are consistent with zero. The blue dashed line shows the best fit SIS model, where the solid blue part indicates the region to which the model was fit. The errorbars indicate the statistical error in the measurement, due to the intrinsic ellipticities of the sources (see Hoekstra et al. 2000 for details).

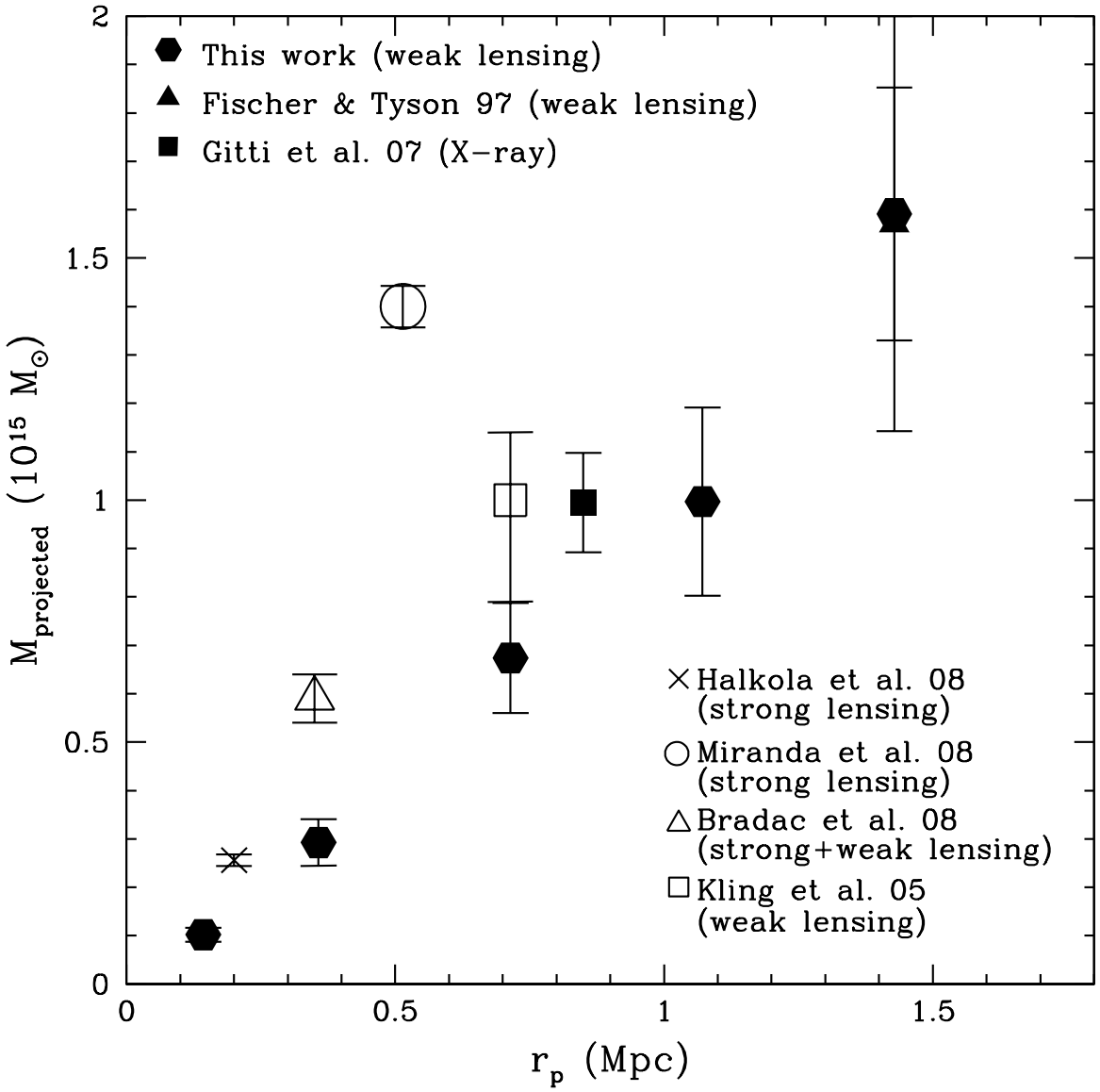

Figure 4.9: The projected mass as a function of radius for RX J1347-1145. The solid hexagons are estimates from this work, and the other symbols are from the literature. See text for details.

As discussed in Hoekstra (2007) and Mahdavi et al. (2008) one can assume spherical symmetry to deproject the resulting masses. We assume an NFW profile to extrapolate along the line-of-sight, but note that the results at large radii do not depend strongly on this assumption. The resulting deprojected masses are shown as open squares in the left panel of Figure 4.6. They are consistent with our dynamical mass estimate using the velocity caustics, within the uncertainties.

Within an aperture of $r_{200}^{\rm dyn} = 1.85$ Mpc, we find a deprojected mass for the main cluster of $M_{200} = 1.25 \pm 0.19 \times 10^{15} M_{\odot}$, again in excellent agreement with the dynamical measurements. Similarly we find a mass of $M_{200} = 5.6 \pm 1.6 \times 10^{14} M_{\odot}$ for RXJ1347-SW using $r_{200}^{\rm dyn} = 1.22$ Mpc, which is somewhat larger than the dynamical mass.

4.6 Discussion

4.6.1 Dynamical State of the Main Cluster

The mass estimate and the dynamical state of this cluster have been the focus of many previous studies. In this section, we first compare the mass estimated using different methods in this work and in the literature, and then discuss the dynamical state of the cluster.

Comparison of Mass Estimates

The mass of RX J1347-1145 has been estimated using different techniques. Other than through the dynamics and weak lensing signals as described in §4.5.3, X-ray data have also been used to infer the mass.

In a recent study by Gitti et al. (2007), they estimate the mass by finding a NFW mass profile (Navarro et al., 1997) that reproduces the observed X-ray temperature profile. The resulting integrated mass at different radii are plotted as open triangles in the right panel of Figure 4.6. This is consistent with our estimates from both the dynamics and the weak lensing analysis (§4.5.3).

Similarly, the study by Allen et al. (2002) estimated the virial mass by fitting a NFW profile to their Chandra observations, and their M_{200} is plotted as the solid hexagon in the right panel of Figure 4.6. Other mass estimates using X-ray data by Schindler et al. (1997) and Ettori et al. (2004) are plotted in the right panel of Figure 4.6 as well. All these estimates at different radii are consistent within their error bars.

As discussed in §4.5.3, the projected mass is a more direct measurement than the *deprojected* mass from the weak lensing analysis, since it is the total projected mass along

the line-of-sight that gives rise to the weak lensing signals; therefore, it is more direct to compare the measured projected mass from different studies.

In Figure 4.9, the projected mass enclosed within a certain radius estimated from strong, weak, and combined lensing analyses in the literature are plotted, along with our weak lensing estimate (see legends). Our weak lensing mass estimate (solid hexagons) is consistent with that of Fischer & Tyson (1997) (the solid triangle), and these two estimates are themselves in agreement with the X-ray analysis of Gitti et al. (2007) (the solid square).

The weak lensing mass estimate by Kling et al. (2005) is slightly higher ($\sim 2\sigma$). This discrepancy is likely due to differences in the assumed source redshift distribution; Kling et al. (2005) base their estimate on $r < 24.5$ spectroscopy over the small area of the Hubble Deep Field, while we use the photometric redshift distribution from the CFHTLS Deep survey. Given our good agreement with both X-ray and dynamical mass estimates, it seems likely that their analysis underestimates the mean source redshift, and thus overestimates the cluster mass.

In comparison, the mass estimates from strong lensing studies (Halkola et al., 2008; Miranda et al., 2008) and the combined strong and weak lensing analysis by Bradač et al. (2008) are systematically higher[§]. In general strong lensing provides an accurate estimate of the projected mass only within the central few hundred kpc, whereas the weak lensing mass is better constrained at larger radii; therefore caution should be taken when combining strong and weak lensing analysis. See also Halkola et al. (2008) for a summary and more discussion of the comparison among these works.

The good agreement shown in Figures 4.6 and 4.9 suggest that the mass estimated from dynamical, X-ray, and weak lensing studies is generally consistent, while strong lensing gives a slightly higher value.

So far, there has been only one other published redshift survey on this cluster, by Cohen & Kneib (2002). They derived from 47 cluster members in their sample a velocity dispersion of 910±130 km s^{-1}, using the same bi-weight method by Beers et al. (1990) as used in this work. This is lower than the value we derived, and thus leads to a lower mass that is in conflict with that from other methods. However, we believe that the value quoted in their paper is in error. When we reanalyze the 47 redshifts as given in their Table 1, we obtain a velocity dispersion of 1098 ± 157 km s^{-1}. Therefore, there is actually no discrepancy between the dynamical mass estimate and that from X-ray and lensing analysis.

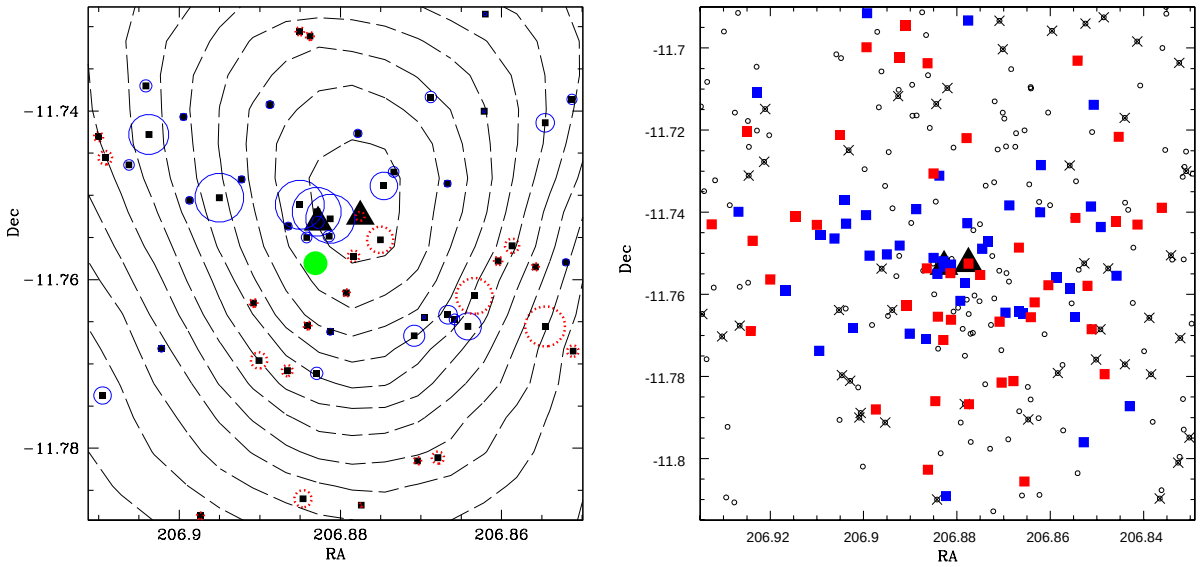

Figure 4.10: Left panel: the spatial distribution of galaxies in the centre of the main cluster (the field of view is ∼1 Mpc × 1 Mpc), with the contours of the weak lensing signal-to-noise mass map overlaid, with an interval of 0.5σ. For clarity, we only plot the confirmed cluster members (the solid squares). The two triangles indicate the two BCGs. The size of the open circles (proportional to δ) around the cluster members show the local deviation from the global mean, with solid open circles indicating negative local deviations ($\bar{z} < 0.4513$) and dashed open circles positive local deviations ($\bar{z} > 0.4513$). The big filled green circle indicates the region ∼ 20 arcsec SE from cluster centre, where the shocked gas is detected. See text for details. Right panel: the spatial distribution of galaxies in the centre of the cluster, with a field of view of ∼2 Mpc × 2 Mpc. The open circles indicate possible potential members (not targeted), the crosses indicate nonmembers, the blue solid squares represent confirmed members with $z < 0.4513$, and the red solid squares represent confirmed members with $z > 0.4513$. Again the two triangles indicate the two BCGs.

Merger in the centre?

One important reason the merger scenario was proposed for this cluster is to explain the large discrepancy between the mass estimated from the velocity dispersion by Cohen & Kneib (2002) and the X-ray and lensing mass estimates discussed in the above section. However, as shown above, our new measurement resolves this discrepancy, and thus removes the original motivation for believing the system is undergoing a major merger.

Nonetheless, there is other evidence suggesting that this cluster might have recently undergone a merger. Although the X-ray morphology is generally relaxed in the centre of the cluster, the existence of a region with shocked gas $\sim 10-20$ arcsec (~ 0.09 Mpc) SE of the cluster centre has been detected as a high-pressure region in X-ray observations (Allen et al., 2002; Gitti & Schindler, 2004; Ota et al., 2008; Bradač et al., 2008; Miranda et al., 2008) and a strong decrement in the Sunyaev-Zel'dovich observations (Komatsu et al., 2001; Mason et al., 2009). Mason et al. (2009) also found discontinuous features in the Chandra map. Further, Miranda et al. (2008) found that their strong lensing data can be much better described by a two component model with comparable mass than the single mass component model. The fact that there are two very bright galaxies in the centre of this cluster $18''$ (~ 0.1 Mpc) apart in the plane of sky is also taken as a possible indication of a merger event (but note their line-of-sight relative velocity is only $\lesssim$100 km/s). Kitayama et al. (2004) suggested that one possible scenario is a collision of equal mass clumps with a collision speed of 4600 km s^{-1}. However, this collision cannot be mostly along the line-of-sight, because as shown in §4.5.1 (and also in the work by Cohen & Kneib 2002), the redshift distribution is better described as a single Gaussian distribution. As discussed in §4.5.1, our velocity data are also consistent (at the 30% significance level), with a model distribution having two Gaussian components. However, even in that case, the radial velocity offset between the two peaks is only about 1000 km s^{-1}, much smaller than 4600 km s^{-1}. Furthermore, if the centre of the cluster is indeed composed of two merging components, each with a much smaller velocity dispersion than what we find for the system as a whole (see §4.5.1), the dynamically–estimated mass profile would be much lower than that shown in Figure 4.6 (the hexagon and the filled points), and that would be inconsistent with the weak lensing and X-ray mass estimates.

To investigate this further, we use the Δ-test proposed by Dressler & Shectman (1988) to examine closely the 3D substructures in the centre of the main cluster. This test measures the deviation of the local velocity and velocity dispersion from the global mean, and is quantified as :

$$\delta^2 = \frac{N_{nb}+1}{\sigma^2}\left[(\bar{v}_{local}-\bar{v})^2 + (\sigma_{local}-\sigma)^2\right], \tag{4.2}$$

[§]We did not include the work by Sahu et al. (1998) because the redshift of the arc they assumed is not correct.

where N_{nb} is the number of neighbour galaxies, $\bar{v}_{local}$ and σ_{local} are local mean velocity and dispersion measured from each galaxy and its N_{nb} nearest neighbours, and $\bar{v}$ and σ are global mean velocity and velocity dispersion, respectively.

In the left panel of Figure 4.10, we show the spatial distribution of the confirmed cluster members (solid squares) with their local deviation from the global mean indicated by the size (proportional to δ) of the circle around them. The solid circles indicate negative local deviations ($\bar{z} < 0.4513$), and dashed open circles positive local deviations ($\bar{z} > 0.4513$). To examine closely the centre of the cluster, in this panel we only plot the region within a radius of ~ 0.5 Mpc from the cluster centre. The two triangles indicate the two BCGs. The region ~ 20 arcsec SE of cluster centre, indicated by the large green filled circle, is where the shocked gas is detected. Around that region, we do not detect significant deviation from the global mean. However, there seems to be a hint of a segregation between the region NE and SW of the cluster centre, in the sense that in the NE region most galaxies have negative local mean velocity relative to the mean redshift of the cluster, while galaxies in the SW region mostly have positive local mean relative velocity. This segregation is along the same direction connecting the main cluster and RXJ1347-SW.

Note the above estimated local mean might be biased by a few galaxies with large deviations due to our sparse data sampling. Therefore, in the right panel of Figure 4.10, we examine directly the spatial distribution of the redshift of individual galaxies, with a field of view of $\sim$2 Mpc $\times$ 2 Mpc. The open circles indicate possible potential members (not targeted), and the crosses represent nonmembers. Cluster members with $z < 0.4513$ are indicated by the blue solid squares, and members with $z > 0.4513$ are indicated by the red solid squares. There is a hint that more galaxies with negative relative velocity reside in the region NE to the cluster centre. To test whether the distribution of the two samples is significantly different, we apply a 2-dimensional Kolmogorov-Smirnov test following the procedure proposed by Peacock (1983). The test suggests that there is a $\sim$60 per cent probability that galaxies with negative and positive relative velocity have different spatial distributions.

The evidence discussed above suggests that this might be a merger more in the plane of the sky than along the line of sight. However, unlike the famous Bullet cluster (e.g. Markevitch et al., 2002; Clowe et al., 2006), also a plane-of-sky merger, the features revealed by X-ray observations of RX J1347-1145 suggest a more complicated picture (e.g. Mason et al., 2009). Thus, further simulations and observations are needed to determine the exact merger scenario.

4.6.2 A possible filamentary connection

As seen in Figure 4.4, cluster RXJ1347-SW is $\sim$ 7 Mpc (projected in the plane of sky) away from the main cluster, and has a rest-frame velocity offset of $\sim$4000 km s^{-1} relative

to the main cluster. This could be a result of two scenarios. One is that RXJ1347-SW is at nearly the same distance as the main cluster, and is falling into the cluster at a speed of ~ 4000 km s^{-1}. The other is that it is ~ 25 Mpc in the background moving with Hubble expansion. We resort to simulations to try distinguishing these two scenarios. Since what we are looking for is how likely it is for two clusters like RX J1347-1145 and RXJ1347-SW to have a relative peculiar velocity as large as observed, we use the Hubble volume simulations (Evrard et al., 2002) because of its large box size ($3000^3 h^{-3}\mathrm{Mpc}^3$).

From the cluster catalogue in the full-sky light cone with ΛCDM cosmology ($\Omega = 0.3, \Lambda = 0.7, \sigma_8 = 0.9$), we search, in a redshift range close to the redshift of RXJ1347, for a pair of clusters that have similar masses ($M_1 \gtrsim 1 \times 10^{15} M_\odot, M_2 \gtrsim 1 \times 10^{14} M_\odot$), projected distance ($\sim 10$ Mpc), and rest-frame velocity offset as RX J1347-1145 and RXJ1347-SW. We do not find any system where they are at the same distance, but with an observed velocity offset of ~ 4000 km s^{-1}. This does not mean definitely that no system could have such a large relative peculiar velocity, because this is based on only one simulation with a large but still limited volume, under the assumption of one particular set of cosmological parameters. Among these parameters, σ_8 is the most uncertain one, and in fact a lower value than used in the simulation is preferred by the latest WMAP measurement (Dunkley et al., 2009). However, in that case, the peculiar velocity between clusters would be even lower due to the lower attracting force from the lower mass density. Even though we cannot reach a definitive conclusion, this does suggest that the probability that RXJ1347-SW is falling into the main cluster with such a high velocity is low; instead, it is more likely to be in the background.

However, just because RXJ1347-SW is far in the background does not necessarily mean that there is no connection between it and the main cluster. The fact that we observed an excess of galaxies between the two in velocity space (Figure 4.4) suggests there might be a physical connection (see Tanaka et al. 2009 for a report of the spectroscopic detection of a large-scale galaxy filament associated with a massive cluster at $z = 0.5$; also Ebeling et al. 2004). We compare our observation with simulations to see if the observed excess of galaxies could represent a real large-scale filamentary structure connecting the main cluster and RXJ1347-SW, rather than foreground and background galaxies *projected* in velocity space. To examine this on the scale of individual galaxies, we make use of the galaxy catalogue from a semi-analytic model by Font et al. (2008)[¶] based on the high resolution Millennium simulation (Springel et al., 2005). Because of the small volume of the simulation, there are only four clusters that have mass greater than $1 \times 10^{15} M_\odot$. We search around these four clusters for a second cluster with lower mass and at a similar distance projected in the plane of sky and along the line-of-sight from the more massive cluster as in the case of our observed RX J1347-1145 and RXJ1347-SW. For the four pairs of systems we found, we calculate the line-of-sight velocity offset of each galaxy relative to

[¶]Note for our purpose here the exact semi-analytic model used is unimportant.

the more massive cluster, and plot it as a function of distance, projected along the direction towards the less massive one. For direct comparison with our observed data, we only plot galaxies in a strip with a width similar to the radius of the FOV as our spectroscopic observation, down to the same magnitude limit as our data. In Figure 4.11 we show one extreme case, where the two clusters ($M_1 \sim 3 \times 10^{15} M_\odot$, $M_2 \sim 2 \times 10^{15} M_\odot$) are connected by a physical, large-scale filament traced by galaxies, with two other clusters in between. This structure is clearly visible in velocity space. The triangles indicate galaxies that are spatially within a cylinder with a radius of 3 Mpc (comparable to the virial radius of the more massive cluster) connecting the two clusters. This is an extreme case where the galaxy filament is very impressive due to the presence of two other massive systems in between the two clusters. However, even in other cases in the simulation where the excess of galaxies between two clusters is smaller ($\sim 5-10$) than this one, the excess is still due to galaxies that *physically reside* in the region between two clusters, instead of being purely due to a *projection* effect. Although this is not definitive, it does support the possibility that the excess of galaxies we observe in velocity space between the two clusters reflects a real physical structure.

4.7 Summary

In this work, we presented photometric and spectroscopic analysis on the dynamics and large-scale structure around the most X-ray luminous cluster RX J1347-1145, and found the following results:

• We identified an elongated large-scale structure around the main cluster, photometrically using red-sequence galaxies, and discovered a rich cluster (RXJ1347-SW) $\sim$ 7 Mpc (projected) away from the main cluster.

• The velocity dispersion of the main cluster is 1163$\pm$97 km s^{-1}, corresponding to $M_{200} = 1.16^{+0.32}_{-0.27} \times 10^{15} M_\odot$, with $r_{200} = 1.85$ Mpc.

• Our dynamical mass estimates based on both the velocity dispersion and velocity caustics are consistent with our weak lensing analysis, and the X-ray studies in the literature. We also find excellent agreement between these mass estimates and that estimated photometrically from the abundance of red-sequence galaxies (the richness).

• Our new measurement resolves a previous claimed discrepancy between the dynamical mass estimate and other methods Cohen & Kneib (2002).

• Our spectroscopic analysis confirmed that the photometrically identified structure RXJ1347-SW is indeed a massive cluster, with a velocity dispersion of 780 ± 100 km s^{-1}.

• Our weak lensing analysis shows good correspondence between the mass concentration and the overdensity of red-sequence galaxies in the main cluster and RXJ1347-SW.

• Comparing with simulations, the observed excess of galaxies between the main cluster and RXJ1347-SW relative to other regions around the main cluster in velocity space sug-

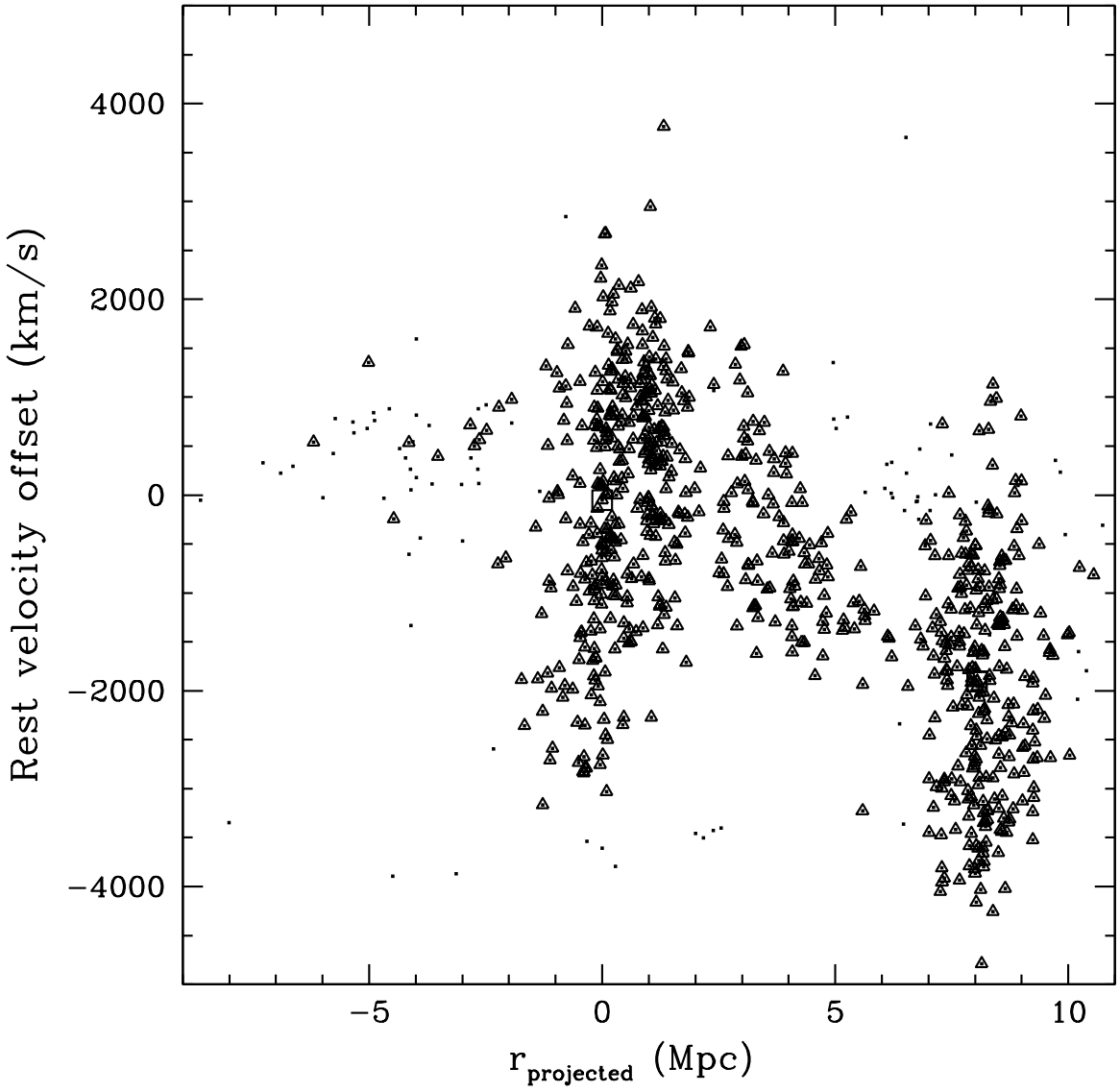

Figure 4.11: This figure shows the rest-frame velocity offset of galaxies around two simulated clusters, as a function of distance projected in the direction connecting the two. The two clusters ($M_1 = 2.7 \times 10^{15} M_\odot$, $M_2 = 1.8 \times 10^{15} M_\odot$) are connected by a real physical filament traced by galaxies, with two other clusters in between. The excess of galaxies between them in velocity space is clearly visible. The two squares indicate the centres of the two clusters, and the triangles indicate galaxies that are spatially within a cylinder with a radius of 3 Mpc connecting the two clusters.

gests a possible filamentary structure connecting these two clusters. This structure has a large population of blue galaxies associated with the overdensity of red-sequence galaxies, suggesting that targeting overdensities of red-sequence galaxies for spectroscopic follow-up allows the efficient selection of cluster members, while still tracing interesting structures with active star formation.

Now that we have closely examined this interesting large-scale structure in RX J1347-1145, in a future project, we will focus on examining the properties of groups residing in and outside the structure. In the next section, we briefly describe this future project.

4.8 Future

Since there is an obvious large scale structure in RX J1347-1145, it would be good to also study a contrasting cluster that has more uniformly distributed substructure. Cl0024 ($z = 0.39$) (Moran et al., 2007) is a cluster at a similar redshift as RX J1347-1145, but is X-ray underluminous, and as we will see below, it does not have obvious large-scale structures in any preferred direction.

We started an extensive spectroscopic campaign on these two clusters, focusing on groups in the outskirt regions out to $\sim$ 8Mpc. The ultimate goal is to put constraints on the effect of the environment by comparing properties of groups in the infall regions, such as their colour and star formation rate distributions, with those of isolated groups and with galaxy formation models.

In Figure 4.8, we show the spatial distribution of galaxies around RX J1347-1145 and Cl0024 in the left and right panels respectively. Again, the black dots represent all galaxies in the field of view, and small open red circles represent red-sequent galaxies. For Cl0024 the blue squares and solid red circles are confirmed blue and red clusters members from Moran et al. (2007). The contrast between the structures around the two clusters is quite obvious, with galaxies around Cl0024 being more uniformly distributed. The large cyan circles show the regions that were observed with the Magellan Telescope described above. The large solid and dashed (for different terms) boxes indicate the target positions we proposed with Gemini.

So far, only a tiny fraction of the data on Cl0024 have been obtained, and the data collection on RX J1347-1145 is finishing up at the moment. When all data are in hand, we will compare the properties of groups, such as their colour distribution and star formation rate in these two clusters, and with isolated groups, to put constraints on the effect of the large-scale structures.

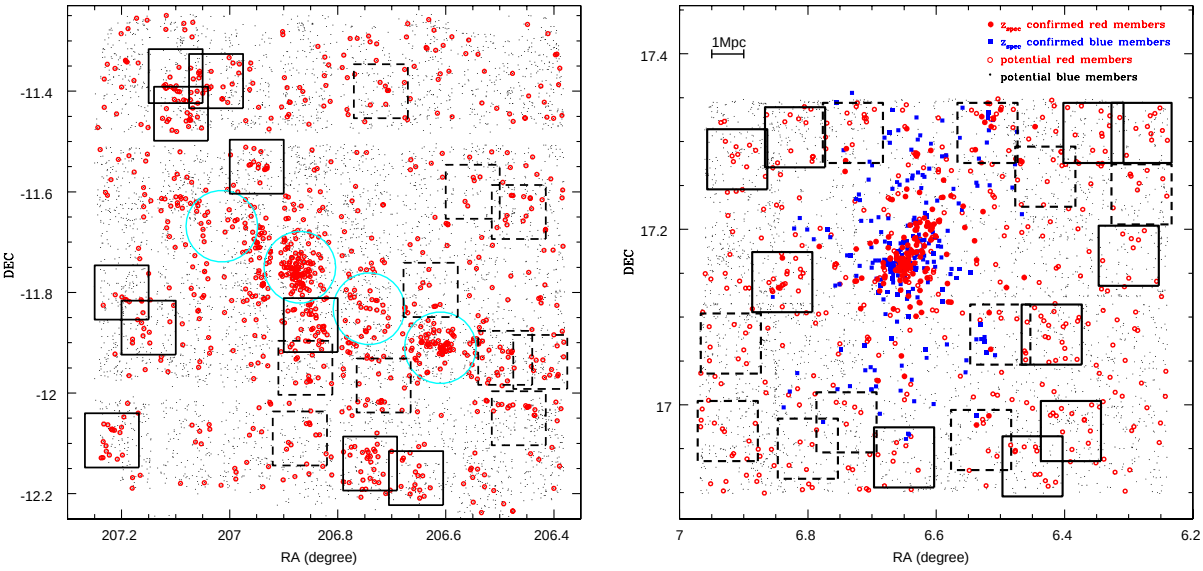

Figure 4.12: Spatial distribution of galaxies around RX J1347-1145 and Cl0024 in the left and right panels respectively. The black dots represent all galaxies (with obvious higher redshift galaxies excluded) in the field of view, and small open red circles represent red-sequence galaxies. For Cl0024 the blue squares and solid red circles are confirmed blue and red clusters members from Moran et al. (2007). The large cyan circles show the regions that were observed with the Magellan Telescope, and the large solid and dashed (for different terms) boxes indicate the target positions proposed with Gemini.

Chapter 5

Conclusions and Future Work

In this thesis, we examined the effect environment has on transforming properties of galaxies. The main sample used here is a cluster sample at $0.15 < z < 0.36$ we detected from the CFHTLS optical survey, covering 171 square degrees of the sky. The detection method is based on the fact that in the core of every rich cluster, there is an overdensity of galaxies that forms a tight red-sequence in colour-magnitude space. We examined the properties of both passive galaxies and star-forming galaxies (using GALEX UV data) in this sample, from cluster cores out to the outskirts, and compared them with that of local clusters and field galaxies.

To examine the passive population, we constructed the $r'-$band luminosity function (LF) of red-sequence galaxies (a population that has had their star formation shut off) in the core regions of clusters. The resulting LF cannot be described by a single Schechter function, due to the presence of a significant inflexion at $M_{r'} \sim -18.5$, suggesting a mixture of two populations.

By comparing the red-sequence LFs of our sample with that of low redshift samples constructed from the SDSS, calculated in a consistent way, we showed that there is a steepening of the faint end with decreasing redshift since $z \sim 0.2$, but no strong evolution between $z \sim 0.2$ and $z \sim 0.4$. To quantify this steepening, we calculated the number of faint galaxies relative to that of bright ones — the dwarf-to-giant ratio (DGR) — and found an increase of a factor of ~ 3 from $z \sim 0.2$ to $z \sim 0$ (over the last 2.5 Gyr).

The fact that we found no evolution of the red-sequence DGR over $0.2 \lesssim z \lesssim 0.4$, but an increase since $z \sim 0.2$, suggests a recent, rapid build-up of the faint end of the cluster red-sequence.

To examine the star formation properties of the clusters, we used the UV luminosity (from GALEX UV data) as an indicator of current star formation. The average SSFR (SFR/stellar mass) of galaxies with SFR above 0.7 $M_\odot$ yr^{-1} shows no dependence on the

distance from the cluster centre, for all three stellar mass ranges ($9.0 < \log_{10}(M_*/\ \mathrm{M}_\odot) < 11.5$) examined here. The distribution of the SSFR shows no difference from that in the field, with the exception of the highest stellar mass galaxies at $z \sim 0.2$. A further examination of the distribution of the SSFR at this stellar mass showed that the number of galaxies with higher SSFR relative to those with lower SSFR is lower in clusters than in the field.

We did not detect any change in the fraction of galaxies with SFR$> 0.7\ \mathrm{M}_\odot\ \mathrm{yr}^{-1}$ (our detection limit) at $z \sim 0.3$, at all clustercentric distances. However, at $z \sim 0.2$, we can probe a lower SFR limit ($0.3\ \ \mathrm{M}_\odot\mathrm{yr}^{-1}$), and we found that the fraction of galaxies with SFR higher than this limit is constant between 3 Mpc $\lesssim r \lesssim$ 7 Mpc, but shows a clear decrease from $1 < r < 3$ Mpc to $0 < r < 1$ Mpc. Correspondingly, the fraction of galaxies with red colour shows no dependence on the clustercentric radius from $\sim$ 3 Mpc out to $\sim$ 7 Mpc, but an abrupt increase within the central 3 Mpc towards the core. For the lowest stellar mass galaxies, their red fraction has increased by a factor of 2 from $z \sim 0.3$ to $z \sim 0.2$ (over 1 Gyr).

Our results suggest that rapid star formation quenching (where ram pressure stripping is a good candidate in the core) might be happening to at least some of the galaxies, especially those with the lowest stellar mass. This is based on the observation that there is an increase of a factor of two in the red fraction over the time of 1 Gyr (from $z \sim 0.3$ to $z \sim 0.2$), and yet no difference in the SSFR distribution as a function of clustercentric radius is detected. However, a more gradual process may also be possible, if only a small fraction of the star-forming galaxies is affected. Further, note that our SFR detection limit is $0.3\ \mathrm{M}_\odot\ \mathrm{yr}^{-1}$; therefore the change in the SSFR could be happening below this limit. One could put a limit on what fraction of the galaxies could be in the process of slowly shutting off their star formation without distorting the observed SSFR distribution, and then check if this could also produce the observed increase in the red fraction over the time scale of 1 Gyr. This needs detailed modelling, and would be useful future work. Note, for higher stellar mass galaxies, the redshift evolution of their red fraction is not significant, suggesting that either their transformation happens on a longer time scale, or they are less affected by the environment. The latter case may occur if their star formation ended a long time ago due to internal feedback processes.

Furthermore, the fact that we found that, even in the outskirts of clusters, the red fraction is still higher than that in the field, suggests that those galaxies have had their star formation quenched relative to the field population. At distance that far from cluster centres, ram pressure stripping and tidal force are not likely to be effecient; therefore other mechanisms such as interactions between galaxies might be more likely to be responsible. Also, AGN feedback might be another good candidate, but some studies showed that the fraction of AGNs in clusters is not higher than that in the general field (e.g. Miller et al., 2003).

With our statistical study, it is not clear whether those galaxies in the outskirts are mostly in groups or relatively isolated, or whether they reside in the proximity of any large-scale filamentary structures. To examine that, we need to look at individual groups in the outskirts, instead of the overall excess of galaxies. This is a future project that we have described in the end of Chapter 4. Another possibility is that galaxies or groups of galaxies in the outskirts assembled earlier than those in the field, and thus modelling the formation time of groups in the outskirts would shed more light on this matter.

More insight could be gained on all the above mentioned issues by a survey of HI gas from the cluster cores to the outskirts, which would tell us whether and where the cold disk are stripped. The large collection area and high resolution of Square Kilometre Array would be suitable for this.

APPENDICES

Appendix A

A.1 Redshift Completeness, Success Rate and Efficiency

In Figure A.1 and A.2, we show the sampling completeness (number of galaxies targeted / number of all targets), and overall completeness, i.e. the success rate (number of galaxies with secure redshift obtained / number targeted) multiplied by the sampling completeness, for the red and blue population in the 4 pointings, respectively. Our overall completeness is about 50 per cent.

For red galaxies, in pointings "Centre" and "SW", about 90 per cent of galaxies with secure redshifts obtained turned out to be members; and in the rest of the two less densed pontings, the efficiency is ∼60 per cent and ∼70 per cent. For blue galaxies, the typical efficiency is about 30 per cent. (The relatively low efficiency of obtaining blue members is not surprising.)

A.2 Redshift Uncertainty

We possess duplicate observations for some of the objects that appear on both masks at each pointing. To determine the uncertainty on the redshift, we compare the difference in the redshifts of the same object from two observations in Figure A.3. The histogram is the distribution of the difference in redshift (top axis) or rest-frame velocity (bottom axis) from repeated observations. The vertical solid line is the mean of the distribution, and vertical dashed lines indicate 1σ. It shows that the uncertainty on our redshift is ∼113 km s^{-1} in the rest frame.

We also compare the redshifts determined from our observation with that from Cohen & Kneib (2002) for the matched objects. The distribution of the difference is shown in

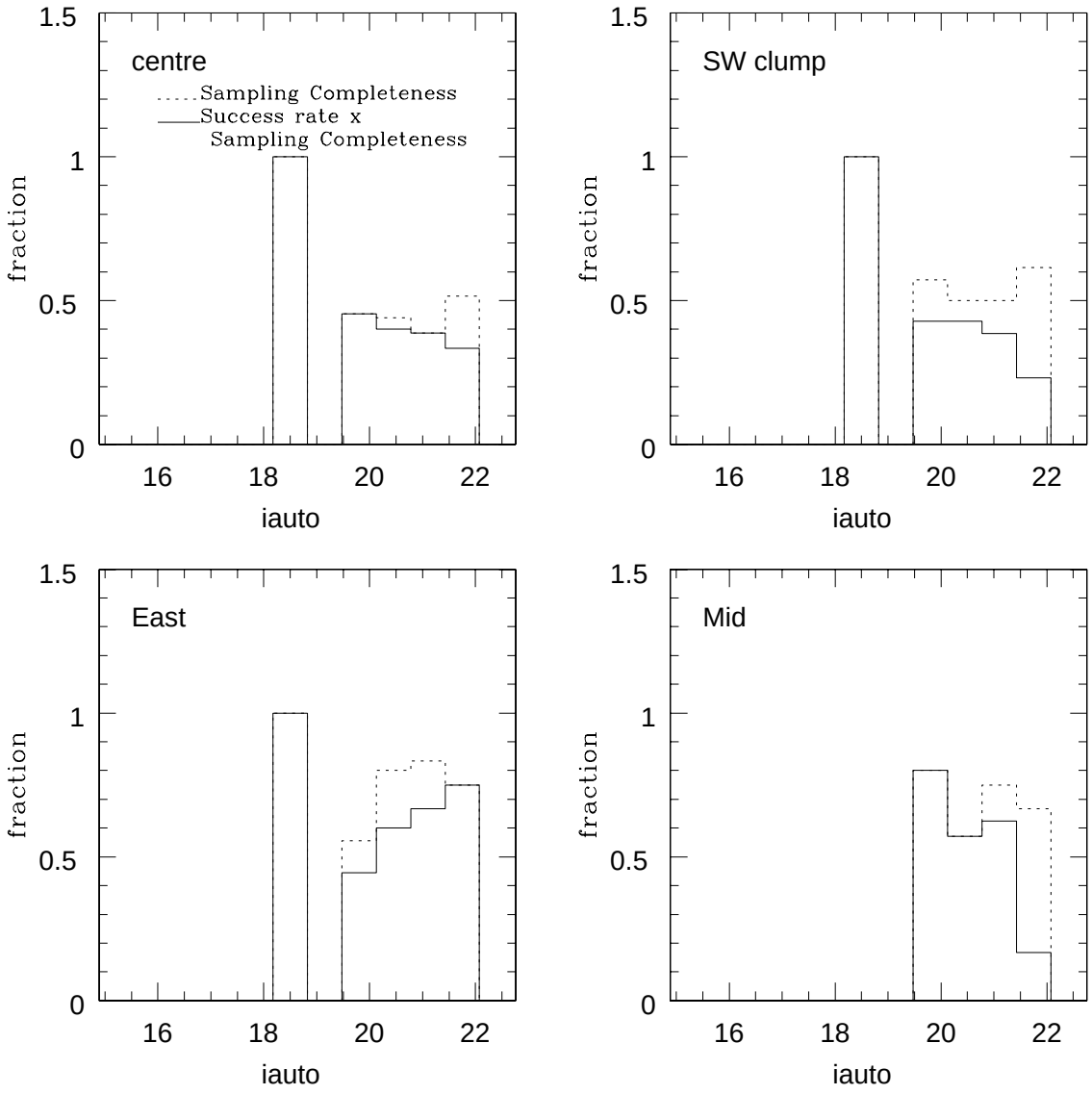

Figure A.1: The completeness of spectroscopic follow-up and success rate for red galaxies in the 4 pointings. The dashed lines show the sampling completeness (number of galaxies targeted / number of all targets), and the solid lines show the overall completeness, i.e. the success rate (number of galaxies with secure redshift obtained / number targeted) multiplied by the sampling completeness.

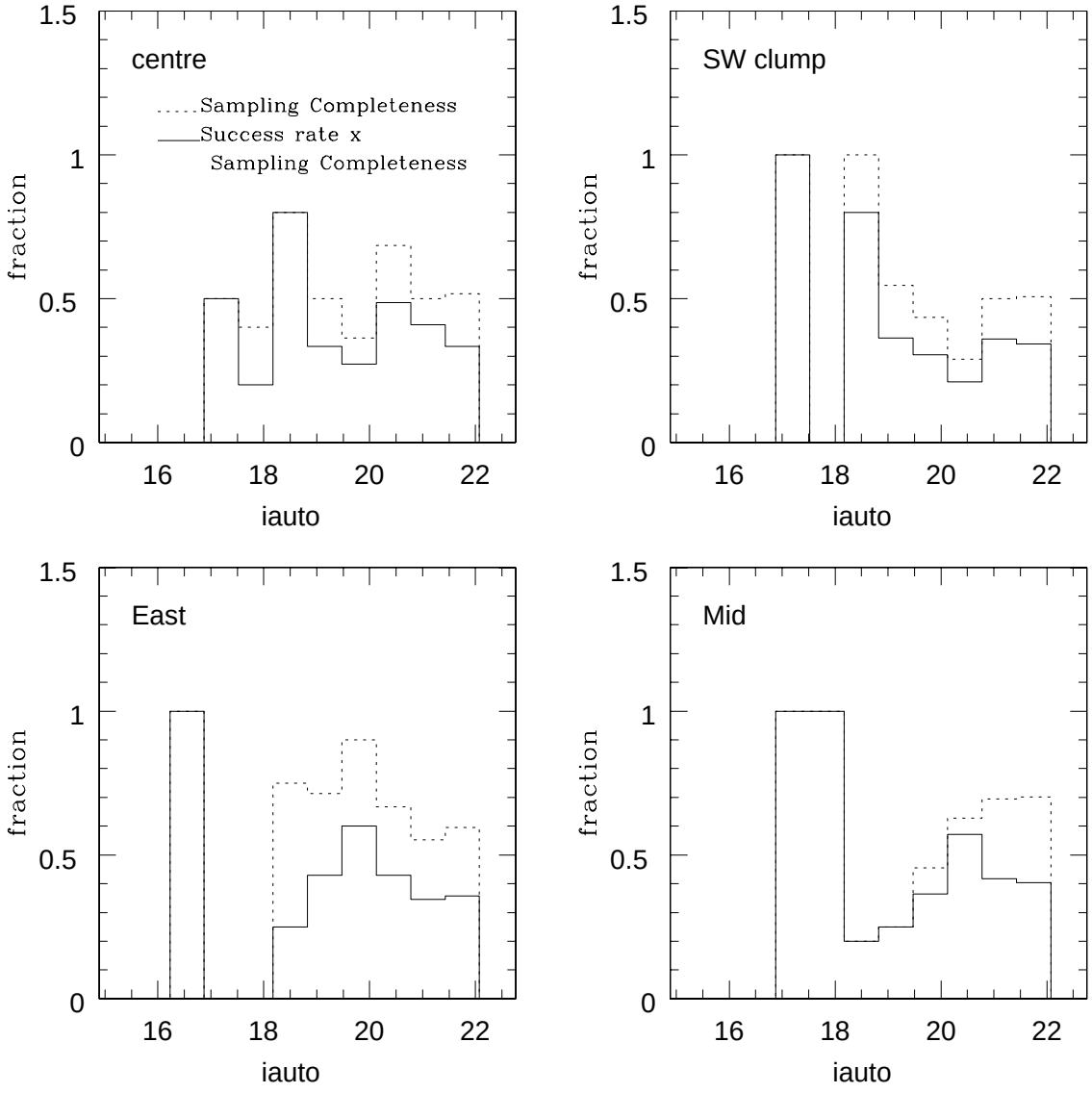

Figure A.2: The same as Figure A.1, but for the blue population.

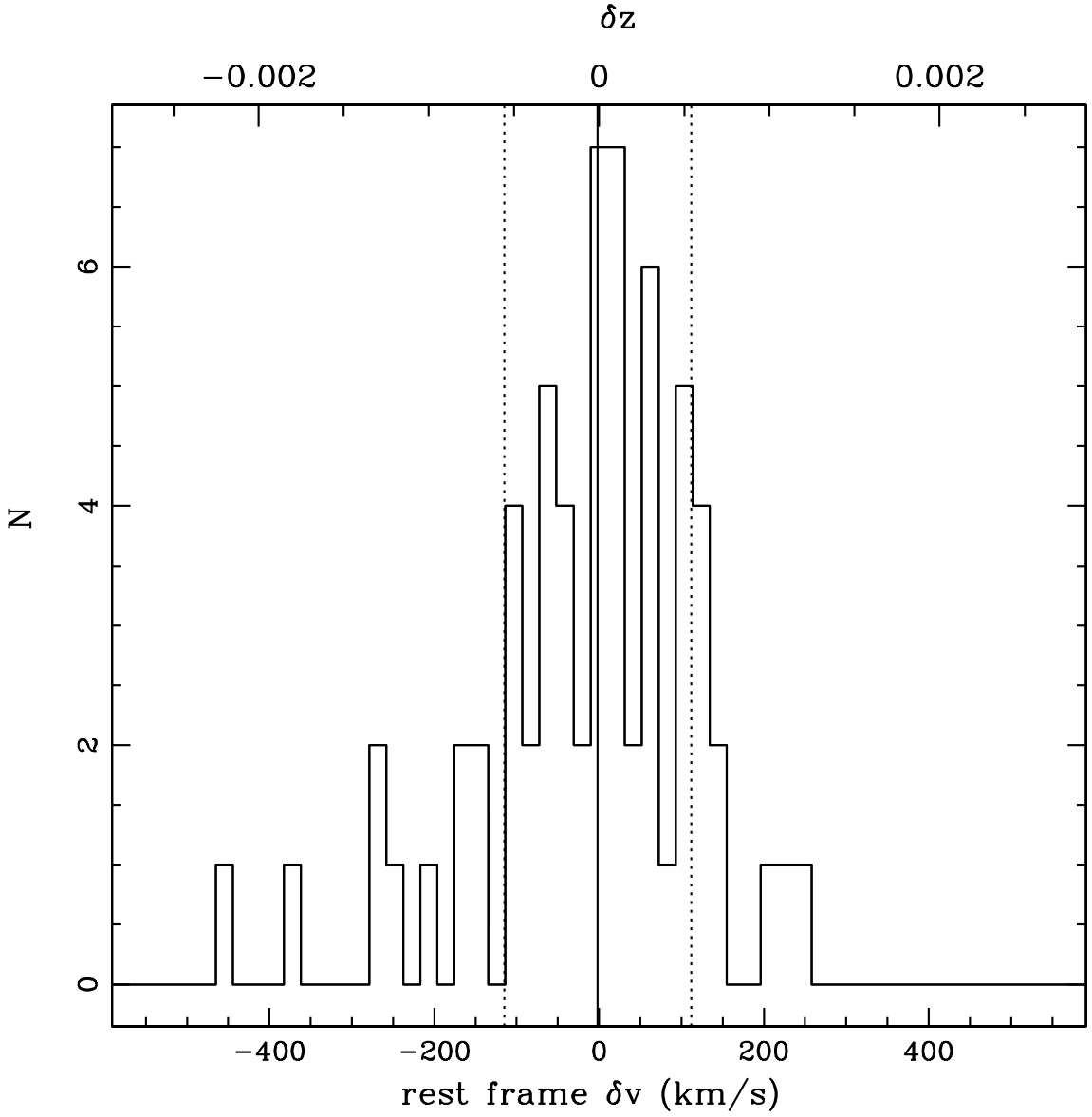

Figure A.3: The distribution of the difference in redshift (top axis) or rest-frame velocity (bottom axis) for galaxies with repeated observations in our sample. The vertical solid line is the mean of the distribution, and the vertical dashed lines indicate 1σ dispersion of the distribution.

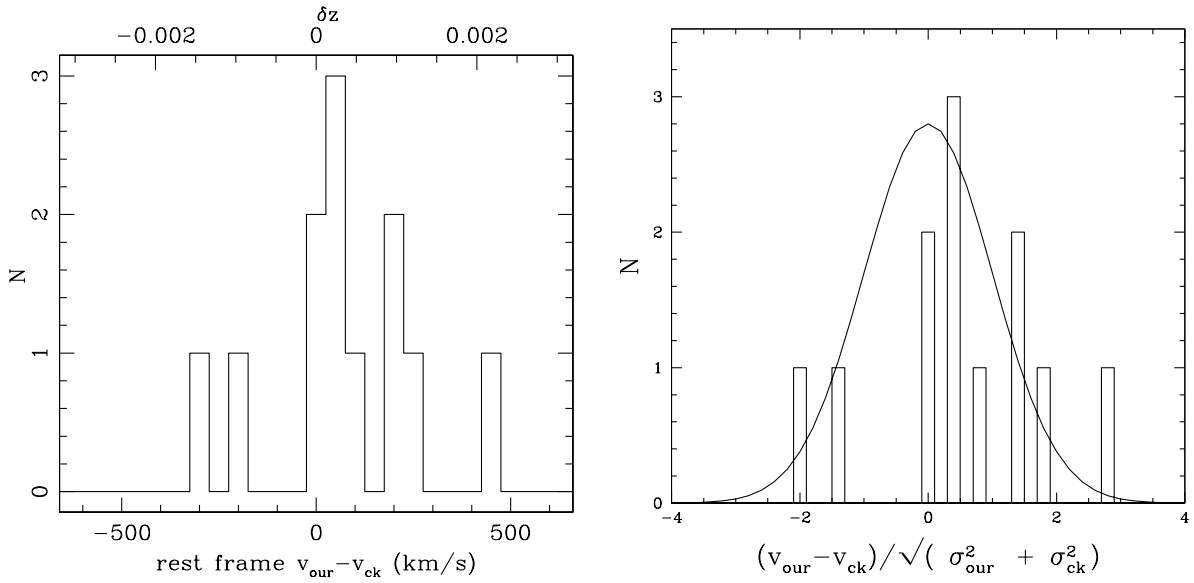

Figure A.4: Left panel: the distribution of the difference in redshift (top axis) and rest-frame velocity (bottom axis) for common objects between our sample and the sample of Cohen & Kneib (2002). Right panel: the distribution of the difference in the rest-frame velocity for the common objects normalized by the quadratically added uncertainties on our redshifts and those of Cohen & Kneib (2002). The curve is a standard normal distribution.

the left panel of Figure A.4, with top axis in unit of redshift and bottom axis rest-frame velocity. In the right panel of Figure A.4, the distribution of the difference in terms of the rest-frame velocity is normalized by the quadratically added uncertainties on our redshift (113 km s^{-1}) and that of Cohen & Kneib (2002) (which they assumed to be 100 km s^{-1}). This distribution is not significantly different from a standard normal distribution shown as the curve, although it is a small number statistics. This suggests that there is no systematic offset between the redshifts measured by Cohen & Kneib (2002) and us; therefore, we add the extra 34 redshift from Cohen & Kneib (2002) to our sample when applicable.

A.3 Sample Spectra

Figure A.5 shows example spectra of two typical absorption-line galaxies with i'=21.4 mag and i'=21.8 mag, close to the magnitude limit of our sample. Multiple absorption features are visible, including prominent CaK, CaH, Hδ, Hβ lines. See figure caption for description of different lines.

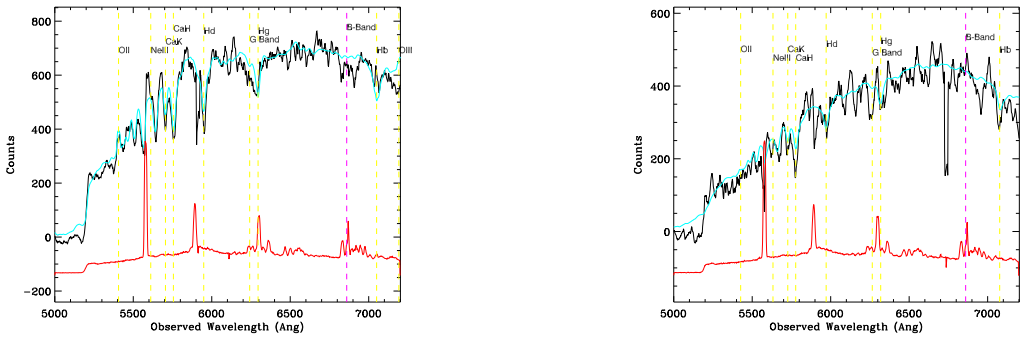

Figure A.5: Example spectra (the black line) of two typical galaxies with i'=21.4 mag and i'=21.8 mag, close to the magnitude limit of our sample. The cyan line shows the template spectrum. The red line shows the sky spectrum, arbitrarily shifted and renormalized, to indicate where bright sky lines give rise to residuals. The positions of different spectral features are indicated with vertical lines, and in both spectra there are multiple absorption features identified, ensuring a secure redshift.

Bibliography

Abell, G. O. 1958, ApJS, 3, 211 7

Allanson, S. P., Hudson, M. J., Smith, R. J., & Lucey, J. R. 2009, ApJ, 702, 1275 3, 15

Allen, S. W., Rapetti, D. A., Schmidt, R. W., Ebeling, H., Morris, R. G., & Fabian, A. C. 2008, MNRAS, 383, 879 90

Allen, S. W., Schmidt, R. W., & Fabian, A. C. 2002, MNRAS, 335, 256 90, 109, 112

Andreon, S. 2006, MNRAS, 369, 969 29

—. 2008, MNRAS, 386, 1045 10, 16, 52, 54, 60

Arimoto, N. & Yoshii, Y. 1986, AAP, 164, 260 6

Baldry, I. K., Balogh, M. L., Bower, R. G., Glazebrook, K., Nichol, R. C., Bamford, S. P., & Budavari, T. 2006, MNRAS, 373, 469 10, 11, 16

Baldry, I. K., Glazebrook, K., Brinkmann, J., Ivezić, Ž., Lupton, R. H., Nichol, R. C., & Szalay, A. S. 2004, ApJ, 600, 681 15

Balogh, M., Eke, V., Miller, C., Lewis, I., Bower, R., Couch, W., Nichol, R., Bland-Hawthorn, J., Baldry, I. K., Baugh, C., Bridges, T., Cannon, R., Cole, S., Colless, M., Collins, C., Cross, N., Dalton, G., de Propris, R., Driver, S. P., Efstathiou, G., Ellis, R. S., Frenk, C. S., Glazebrook, K., Gomez, P., Gray, A., Hawkins, E., Jackson, C., Lahav, O., Lumsden, S., Maddox, S., Madgwick, D., Norberg, P., Peacock, J. A., Percival, W., Peterson, B. A., Sutherland, W., & Taylor, K. 2004a, MNRAS, 348, 1355 9, 15, 62, 89

Balogh, M. L., Baldry, I. K., Nichol, R., Miller, C., Bower, R., & Glazebrook, K. 2004b, ApJL, 615, L101 15

Balogh, M. L. & McGee, S. L. 2010, MNRAS, 402, L59 12, 63, 85, 89

Balogh, M. L., McGee, S. L., Wilman, D., Bower, R. G., Hau, G., Morris, S. L., Mulchaey, J. S., Oemler, Jr., A., Parker, L., & Gwyn, S. 2009, MNRAS, 398, 754 11

Balogh, M. L., Morris, S. L., Yee, H. K. C., Carlberg, R. G., & Ellingson, E. 1997, ApJL, 488, L75+ 11, 62

—. 1999, ApJ, 527, 54 11, 89

Balogh, M. L., Navarro, J. F., & Morris, S. L. 2000, ApJ, 540, 113 12, 85, 89

Balogh, M. L., Schade, D., Morris, S. L., Yee, H. K. C., Carlberg, R. G., & Ellingson, E. 1998, ApJL, 504, L75+ 11, 62

Barger, A. J., Aragon-Salamanca, A., Ellis, R. S., Couch, W. J., Smail, I., & Sharples, R. M. 1996, MNRAS, 279, 1 11

Barkhouse, W. A., Yee, H. K. C., & López-Cruz, O. 2007, ApJ, 671, 1471 41, 45, 50, 51, 53, 55, 56

Barnes, J. E. & Hernquist, L. 1992, nat, 360, 715 2

Baugh, C. M., Lacey, C. G., Frenk, C. S., Granato, G. L., Silva, L., Bressan, A., Benson, A. J., & Cole, S. 2005, MNRAS, 356, 1191 4

Beers, T. C., Flynn, K., & Gebhardt, K. 1990, AJ, 100, 32 96, 110

Bell, E. F. 2002, ApJ, 577, 150 75

Bell, E. F., McIntosh, D. H., Katz, N., & Weinberg, M. D. 2003, ApJS, 149, 289 76

Bell, E. F., Wolf, C., Meisenheimer, K., Rix, H.-W., Borch, A., Dye, S., Kleinheinrich, M., Wisotzki, L., & McIntosh, D. H. 2004, ApJ, 608, 752 6, 15

Bell, E. F., Zheng, X. Z., Papovich, C., Borch, A., Wolf, C., & Meisenheimer, K. 2007, ApJ, 663, 834 6, 62

Bennett, C. L., Hill, R. S., Hinshaw, G., Nolta, M. R., Odegard, N., Page, L., Spergel, D. N., Weiland, J. L., Wright, E. L., Halpern, M., Jarosik, N., Kogut, A., Limon, M., Meyer, S. S., Tucker, G. S., & Wollack, E. 2003, ApJS, 148, 97 1

Bennett, C. L., Smoot, G. F., Hinshaw, G., Wright, E. L., Kogut, A., de Amici, G., Meyer, S. S., Weiss, R., Wilkinson, D. T., Gulkis, S., Janssen, M., Boggess, N. W., Cheng, E. S., Hauser, M. G., Kelsall, T., Mather, J. C., Moseley, Jr., S. H., Murdock, T. L., & Silverberg, R. F. 1992, ApJL, 396, L7 1

Benson, A. J. & Bower, R. 2010, MNRAS, 600 4

Benson, A. J., Bower, R. G., Frenk, C. S., Lacey, C. G., Baugh, C. M., & Cole, S. 2003, ApJ, 599, 38 4, 5

Bernardi, M., Nichol, R. C., Sheth, R. K., Miller, C. J., & Brinkmann, J. 2006, AJ, 131, 1288 2

Berrier, J. C., Stewart, K. R., Bullock, J. S., Purcell, C. W., Barton, E. J., & Wechsler, R. H. 2009, ApJ, 690, 1292 12, 85, 89

Bertin, E. & Arnouts, S. 1996, A&AS, 117, 393 17, 64, 91

Bertin, E., Mellier, Y., Radovich, M., Missonnier, G., Didelon, P., & Morin, B. 2002, in Astronomical Society of the Pacific Conference Series, Vol. 281, Astronomical Data Analysis Software and Systems XI, ed. D. A. Bohlender, D. Durand, & T. H. Handley, 228–+ 91

Binggeli, B., Sandage, A., & Tammann, G. A. 1988, ARA&A, 26, 509 45

Blanton, M. R., Dalcanton, J., Eisenstein, D., Loveday, J., Strauss, M. A., SubbaRao, M., Weinberg, D. H., Anderson, Jr., J. E., Annis, J., Bahcall, N. A., Bernardi, M., Brinkmann, J., Brunner, R. J., Burles, S., Carey, L., Castander, F. J., Connolly, A. J., Csabai, I., Doi, M., Finkbeiner, D., Friedman, S., Frieman, J. A., Fukugita, M., Gunn, J. E., Hennessy, G. S., Hindsley, R. B., Hogg, D. W., Ichikawa, T., Ivezić, Ž., Kent, S., Knapp, G. R., Lamb, D. Q., Leger, R. F., Long, D. C., Lupton, R. H., McKay, T. A., Meiksin, A., Merelli, A., Munn, J. A., Narayanan, V., Newcomb, M., Nichol, R. C., Okamura, S., Owen, R., Pier, J. R., Pope, A., Postman, M., Quinn, T., Rockosi, C. M., Schlegel, D. J., Schneider, D. P., Shimasaku, K., Siegmund, W. A., Smee, S., Snir, Y., Stoughton, C., Stubbs, C., Szalay, A. S., Szokoly, G. P., Thakar, A. R., Tremonti, C., Tucker, D. L., Uomoto, A., Vanden Berk, D., Vogeley, M. S., Waddell, P., Yanny, B., Yasuda, N., & York, D. G. 2001, AJ, 121, 2358 22

Blanton, M. R. & Roweis, S. 2007, AJ, 133, 734 72, 75, 76

Böhringer, H., Voges, W., Huchra, J. P., McLean, B., Giacconi, R., Rosati, P., Burg, R., Mader, J., Schuecker, P., Simiç, D., Komossa, S., Reiprich, T. H., Retzlaff, J., & Trümper, J. 2000, ApJS, 129, 435 8

Bond, J. R., Kofman, L., & Pogosyan, D. 1996, Nature, 380, 603 12, 63, 89

Bower, R. G., Benson, A. J., Malbon, R., Helly, J. C., Frenk, C. S., Baugh, C. M., Cole, S., & Lacey, C. G. 2006, MNRAS, 370, 645 4, 11, 16

Bower, R. G., Lucey, J. R., & Ellis, R. S. 1992, MNRAS, 254, 601 3, 22, 25, 59

Bradač, M., Erben, T., Schneider, P., Hildebrandt, H., Lombardi, M., Schirmer, M., Miralles, J.-M., Clowe, D., & Schindler, S. 2005, A&A, 437, 49 90

Bradač, M., Schrabback, T., Erben, T., McCourt, M., Million, E., Mantz, A., Allen, S., Blandford, R., Halkola, A., Hildebrandt, H., Lombardi, M., Marshall, P., Schneider, P., Treu, T., & Kneib, J.-P. 2008, ApJ, 681, 187 90, 110, 112

Broadhurst, T., Umetsu, K., Medezinski, E., Oguri, M., & Rephaeli, Y. 2008, ApJL, 685, L9 90

Bruzual, G. & Charlot, S. 2003, MNRAS, 344, 1000 6, 22, 26, 27, 40, 51, 86

Bruzual A., G. 1983, ApJ, 273, 105 6

Bruzual A., G. & Charlot, S. 1993, ApJ, 405, 538 6

Buat, V. 1992, A&A, 264, 444 75

Butcher, H. & Oemler, Jr., A. 1978, ApJ, 219, 18 9

—. 1984, ApJ, 285, 426 9, 100

Buzzoni, A. 1989, ApJS, 71, 817 6

Calzetti, D., Kinney, A. L., & Storchi-Bergmann, T. 1994, ApJ, 429, 582 75

Charlot, S. & Longhetti, M. 2001, MNRAS, 323, 887 6

Christlein, D. & Zabludoff, A. I. 2003, ApJ, 591, 764 54

Cimatti, A., Daddi, E., & Renzini, A. 2006, A&A, 453, L29 15

Clemens, D. P. 1985, ApJ, 295, 422 1

Clowe, D., Bradač, M., Gonzalez, A. H., Markevitch, M., Randall, S. W., Jones, C., & Zaritsky, D. 2006, ApJL, 648, L109 113

Clowe, D., Luppino, G. A., Kaiser, N., Henry, J. P., & Gioia, I. M. 1998, ApJL, 497, L61+ 105

Cohen, J. G. & Kneib, J.-P. 2002, ApJ, 573, 524 xii, 90, 91, 96, 110, 112, 115, 123, 127

Colberg, J. M., White, S. D. M., Jenkins, A., & Pearce, F. R. 1999, MNRAS, 308, 593 12, 63, 89

Colberg, J. M., White, S. D. M., Yoshida, N., MacFarland, T. J., Jenkins, A., Frenk, C. S., Pearce, F. R., Evrard, A. E., Couchman, H. M. P., Efstathiou, G., Peacock, J. A., Thomas, P. A., & The Virgo Consortium. 2000, MNRAS, 319, 209 33

Cole, S., Aragon-Salamanca, A., Frenk, C. S., Navarro, J. F., & Zepf, S. E. 1994, MNRAS, 271, 781 4

Cole, S., Lacey, C. G., Baugh, C. M., & Frenk, C. S. 2000, MNRAS, 319, 168 4

Cole, S., Percival, W. J., Peacock, J. A., Norberg, P., Baugh, C. M., Frenk, C. S., Baldry, I., Bland-Hawthorn, J., Bridges, T., Cannon, R., Colless, M., Collins, C., Couch, W., Cross, N. J. G., Dalton, G., Eke, V. R., De Propris, R., Driver, S. P., Efstathiou, G., Ellis, R. S., Glazebrook, K., Jackson, C., Jenkins, A., Lahav, O., Lewis, I., Lumsden, S., Maddox, S., Madgwick, D., Peterson, B. A., Sutherland, W., & Taylor, K. 2005, MNRAS, 362, 505 1

Colless, M., Dalton, G., Maddox, S., Sutherland, W., Norberg, P., Cole, S., Bland-Hawthorn, J., Bridges, T., Cannon, R., Collins, C., Couch, W., Cross, N., Deeley, K., De Propris, R., Driver, S. P., Efstathiou, G., Ellis, R. S., Frenk, C. S., Glazebrook, K., Jackson, C., Lahav, O., Lewis, I., Lumsden, S., Madgwick, D., Peacock, J. A., Peterson, B. A., Price, I., Seaborne, M., & Taylor, K. 2001, MNRAS, 328, 1039 9

Contaldi, C. R., Hoekstra, H., & Lewis, A. 2003, Physical Review Letters, 90, 221303 1

Cooper, M. C., Gallazzi, A., Newman, J. A., & Yan, R. 2009, MNRAS, 1868 94

Cortese, L., Boselli, A., Buat, V., Gavazzi, G., Boissier, S., Gil de Paz, A., Seibert, M., Madore, B. F., & Martin, D. C. 2006, ApJ, 637, 242 75

Cortese, L., Boselli, A., Franzetti, P., Decarli, R., Gavazzi, G., Boissier, S., & Buat, V. 2008, MNRAS, 386, 1157 75

Couch, W. J., Barger, A. J., Smail, I., Ellis, R. S., & Sharples, R. M. 1998, ApJ, 497, 188 10

Couch, W. J., Ellis, R. S., Sharples, R. M., & Smail, I. 1994, ApJ, 430, 121 9

Couch, W. J. & Sharples, R. M. 1987, MNRAS, 229, 423 9

Coupon, J., Ilbert, O., Kilbinger, M., McCracken, H. J., Mellier, Y., Arnouts, S., Bertin, E., Hudelot, P., Schultheis, M., Le Fèvre, O., Le Brun, V., Guzzo, L., Bardelli, S., Zucca, E., Bolzonella, M., Garilli, B., Zamorani, G., Zanichelli, A., Tresse, L., & Aussel, H. 2009, aap, 500, 981 71

Cowie, L. L. & Barger, A. J. 2008, ApJ, 686, 72 6

Cowie, L. L., Songaila, A., Hu, E. M., & Cohen, J. G. 1996, AJ, 112, 839 6

Crawford, S. M., Bershady, M. A., & Hoessel, J. G. 2009, ApJ, 690, 1158 10, 16

Cretton, N., Naab, T., Rix, H., & Burkert, A. 2001, ApJ, 554, 291 2

Croton, D. J., Springel, V., White, S. D. M., De Lucia, G., Frenk, C. S., Gao, L., Jenkins, A., Kauffmann, G., Navarro, J. F., & Yoshida, N. 2006, MNRAS, 365, 11 4

Cruddace, R., Voges, W., Böhringer, H., Collins, C. A., Romer, A. K., MacGillivray, H., Yentis, D., Schuecker, P., Ebeling, H., & De Grandi, S. 2002, ApJS, 140, 239 30, 32

Dalcanton, J. J. 1996, ApJ, 466, 92 8

Damen, M., Labbé, I., Franx, M., van Dokkum, P. G., Taylor, E. N., & Gawiser, E. J. 2009, ApJ, 690, 937 6

De Lucia, G., Poggianti, B. M., Aragón-Salamanca, A., White, S. D. M., Zaritsky, D., Clowe, D., Halliday, C., Jablonka, P., von der Linden, A., Milvang-Jensen, B., Pelló, R., Rudnick, G., Saglia, R. P., & Simard, L. 2007, MNRAS, 374, 809 10, 16, 46, 47, 48, 49, 52, 53, 54, 58, 59, 60

Diaferio, A. 1999, MNRAS, 309, 610 98, 102, 103

Diaferio, A. & Geller, M. J. 1997, ApJ, 481, 633 102

Dressler, A. 1980, ApJ, 236, 351 9

Dressler, A., Oemler, Jr., A., Couch, W. J., Smail, I., Ellis, R. S., Barger, A., Butcher, H., Poggianti, B. M., & Sharples, R. M. 1997, ApJ, 490, 577 9

Dressler, A. & Shectman, S. A. 1988, AJ, 95, 985 112

Duffy, A. R., Schaye, J., Kay, S. T., & Dalla Vecchia, C. 2008, MNRAS, 390, L64 105

Dunkley, J., Komatsu, E., Nolta, M. R., Spergel, D. N., Larson, D., Hinshaw, G., Page, L., Bennett, C. L., Gold, B., Jarosik, N., Weiland, J. L., Halpern, M., Hill, R. S., Kogut, A., Limon, M., Meyer, S. S., Tucker, G. S., Wollack, E., & Wright, E. L. 2009, ApJS, 180, 306 33, 114

Ebeling, H., Barrett, E., & Donovan, D. 2004, ApJL, 609, L49 114

Ebeling, H., Edge, A. C., & Henry, J. P. 2001, ApJ, 553, 668 8

Efstathiou, G. 1992, MNRAS, 256, 43P 4

Eggen, O. J., Lynden-Bell, D., & Sandage, A. R. 1962, ApJ, 136, 748 2

Ellingson, E., Lin, H., Yee, H. K. C., & Carlberg, R. G. 2001, ApJ, 547, 609 100

Ettori, S., Tozzi, P., Borgani, S., & Rosati, P. 2004, A&A, 417, 13 90, 109

Evrard, A. E., MacFarland, T. J., Couchman, H. M. P., Colberg, J. M., Yoshida, N., White, S. D. M., Jenkins, A., Frenk, C. S., Pearce, F. R., Peacock, J. A., & Thomas, P. A. 2002, ApJ, 573, 7 33, 35, 114

Evrard, A. E., Metzler, C. A., & Navarro, J. F. 1996, ApJ, 469, 494 35

Evrard, A. E., Summers, F. J., & Davis, M. 1994, ApJ, 422, 11 3

Faber, S. M., Willmer, C. N. A., Wolf, C., Koo, D. C., Weiner, B. J., Newman, J. A., Im, M., Coil, A. L., Conroy, C., Cooper, M. C., Davis, M., Finkbeiner, D. P., Gerke, B. F., Gebhardt, K., Groth, E. J., Guhathakurta, P., Harker, J., Kaiser, N., Kassin, S., Kleinheinrich, M., Konidaris, N. P., Kron, R. G., Lin, L., Luppino, G., Madgwick, D. S., Meisenheimer, K., Noeske, K. G., Phillips, A. C., Sarajedini, V. L., Schiavon, R. P., Simard, L., Szalay, A. S., Vogt, N. P., & Yan, R. 2007, ApJ, 665, 265 15

Fahlman, G., Kaiser, N., Squires, G., & Woods, D. 1994, ApJ, 437, 56 105

Fischer, P. & Tyson, J. A. 1997, AJ, 114, 14 90, 110

Font, A. S., Bower, R. G., McCarthy, I. G., Benson, A. J., Frenk, C. S., Helly, J. C., Lacey, C. G., Baugh, C. M., & Cole, S. 2008, MNRAS, 389, 1619 11, 114

Fujita, Y. 1998, ApJ, 509, 587 11

—. 2004, PASJ, 56, 29 89

Fukugita, M., Shimasaku, K., & Ichikawa, T. 1995, PASP, 107, 945 52, 100

Gavazzi, R. & Soucail, G. 2007, aap, 462, 459 9

Gehrels, N. 1986, ApJ, 303, 336 100

Gilbank, D. G. & Balogh, M. L. 2008, MNRAS, 385, L116 52

Gilbank, D. G., Balogh, M. L., Glazebrook, K., Bower, R. G., Baldry, I. K., Davies, G. T., Hau, G. K. T., Li, I. H., & McCarthy, P. 2010, MNRAS, 704 6

Gilbank, D. G., Bower, R. G., Castander, F. J., & Ziegler, B. L. 2004, MNRAS, 348, 551 8

Gilbank, D. G., Yee, H. K. C., Ellingson, E., Gladders, M. D., Loh, Y.-S., Barrientos, L. F., & Barkhouse, W. A. 2008, ApJ, 673, 742 9, 10, 16, 41, 58

Gitti, M., Piffaretti, R., & Schindler, S. 2007, A&A, 472, 383 90, 109, 110

Gitti, M. & Schindler, S. 2004, A&A, 427, L9 90, 112

Gladders, M. D. & Yee, H. K. C. 2000, AJ, 120, 2148 8, 22, 24, 35, 41, 60, 91

—. 2005, ApJS, 157, 1 58

Gnedin, O. Y. 2003, ApJ, 582, 141 89

Godwin, J. G. & Peach, J. V. 1977, MNRAS, 181, 323 54

Gómez, P. L., Nichol, R. C., Miller, C. J., Balogh, M. L., Goto, T., Zabludoff, A. I., Romer, A. K., Bernardi, M., Sheth, R., Hopkins, A. M., Castander, F. J., Connolly, A. J., Schneider, D. P., Brinkmann, J., Lamb, D. Q., SubbaRao, M., & York, D. G. 2003, ApJ, 584, 210 9, 62

Gonzalez, A. H., Tran, K., Conbere, M. N., & Zaritsky, D. 2005, ApJL, 624, L73 12

Gonzalez, A. H., Zaritsky, D., Dalcanton, J. J., & Nelson, A. 2001, ApJS, 137, 117 8

Gonzalez, A. H., Zaritsky, D., & Wechsler, R. H. 2002, ApJ, 571, 129 33

Green, P. J., Silverman, J. D., Cameron, R. A., Kim, D., Wilkes, B. J., Barkhouse, W. A., LaCluyzé, A., Morris, D., Mossman, A., Ghosh, H., Grimes, J. P., Jannuzi, B. T., Tananbaum, H., Aldcroft, T. L., Baldwin, J. A., Chaffee, F. H., Dey, A., Dosaj, A., Evans, N. R., Fan, X., Foltz, C., Gaetz, T., Hooper, E. J., Kashyap, V. L., Mathur, S., McGarry, M. B., Romero-Colmenero, E., Smith, M. G., Smith, P. S., Smith, R. C., Torres, G., Vikhlinin, A., & Wik, D. R. 2004, ApJS, 150, 43 8

Grove, L. F., Benoist, C., & Martel, F. 2009, aap, 494, 845 8

Gunn, J. E. & Gott, J. R. I. 1972, ApJ, 176, 1 11

Haines, C. P., La Barbera, F., Mercurio, A., Merluzzi, P., & Busarello, G. 2006, ApJL, 647, L21 9, 62

Halkola, A., Hildebrandt, H., Schrabback, T., Lombardi, M., Bradač, M., Erben, T., Schneider, P., & Wuttke, D. 2008, A&A, 481, 65 90, 110

Hansen, S. M., Sheldon, E. S., Wechsler, R. H., & Koester, B. P. 2009, ApJ, 699, 1333 30, 51, 92

Hoekstra, H. 2001, A&A, 370, 743 104

—. 2003, MNRAS, 339, 1155 104

—. 2007, MNRAS, 379, 317 104

Hoekstra, H., Franx, M., & Kuijken, K. 2000, ApJ, 532, 88 107

Hoekstra, H., Franx, M., Kuijken, K., & Squires, G. 1998, ApJ, 504, 636 104

Hogg, D. W., Blanton, M., Strateva, I., Bahcall, N. A., Brinkmann, J., Csabai, I., Doi, M., Fukugita, M., Hennessy, G., Ivezić, Ž., Knapp, G. R., Lamb, D. Q., Lupton, R., Munn, J. A., Nichol, R., Schlegel, D. J., Schneider, D. P., & York, D. G. 2002, AJ, 124, 646 55

Hubble, E. P. 1936, Realm of the Nebulae, ed. Hubble, E. P. 2

Ilbert, O., Arnouts, S., McCracken, H. J., Bolzonella, M., Bertin, E., Le Fèvre, O., Mellier, Y., Zamorani, G., Pellò, R., Iovino, A., Tresse, L., Le Brun, V., Bottini, D., Garilli, B., & Maccagni, D. 2006, A&A, 457, 841 71, 104

Iye, M., Karoji, H., Ando, H., Kaifu, N., Kodaira, K., Aoki, K., Aoki, W., Chikada, Y., Doi, Y., Ebizuka, N., Elms, B., Fujihara, G., Furusawa, H., Fuse, T., Gaessler, W., Harasawa, S., Hayano, Y., Hayashi, M., Hayashi, S., Ichikawa, S., Imanishi, M., Ishida, C., Kamata, Y., Kanzawa, T., Kashikawa, N., Kawabata, K., Kobayashi, N., Komiyama, Y., Kosugi, G., Kurakami, T., Letawsky, M., Mikami, Y., Miyashita, A., Miyazaki, S., Mizumoto, Y., Morino, J., Motohara, K., Murakawa, K., Nakagiri, M., Nakamura, K., Nakaya, H., Nariai, K., Nishimura, T., Noguchi, K., Noguchi, T., Noumaru, T., Ogasawara, R., Ohshima, N., Ohyama, Y., Okita, K., Omata, K., Otsubo, M., Oya, S., Potter, R., Saito, Y., Sasaki, T., Sato, S., Scarla, D., Schubert, K., Sekiguchi, K., Sekiguchi, M., Shelton, I., Simpson, C., Suto, H., Tajitsu, A., Takami, H., Takata, T., Takato, N., Tamae, R., Tamura, M., Tanaka, W., Terada, H., Torii, Y., Uraguchi, F., Usuda, T., Weber, M., Winegar, T., Yagi, M., Yamada, T., Yamashita, T., Yamashita, Y., Yasuda, N., Yoshida, M., & Yutani, M. 2004, pasj, 56, 381 12

Jeltema, T. E., Mulchaey, J. S., Lubin, L. M., & Fassnacht, C. D. 2007, ApJ, 658, 865 11

Johnston, D. E., Sheldon, E. S., Wechsler, R. H., Rozo, E., Koester, B. P., Frieman, J. A., McKay, T. A., Evrard, A. E., Becker, M. R., & Annis, J. 2007, ArXiv e-prints 30, 92

Jones, C. & Forman, W. 1999, ApJ, 511, 65 51

Kaiser, N. & Squires, G. 1993, ApJ, 404, 441 104

Kaiser, N., Squires, G., & Broadhurst, T. 1995, ApJ, 449, 460 104

Katz, N., Hernquist, L., & Weinberg, D. H. 1992, ApJL, 399, L109 3

Kauffmann, G., Heckman, T. M., White, S. D. M., Charlot, S., Tremonti, C., Peng, E. W., Seibert, M., Brinkmann, J., Nichol, R. C., SubbaRao, M., & York, D. 2003, MNRAS, 341, 54 10, 63, 76

Kauffmann, G., White, S. D. M., & Guiderdoni, B. 1993, MNRAS, 264, 201 4

Kaviraj, S., Schawinski, K., Devriendt, J. E. G., Ferreras, I., Khochfar, S., Yoon, S.-J., Yi, S. K., Deharveng, J.-M., Boselli, A., Barlow, T., Conrow, T., Forster, K., Friedman, P. G., Martin, D. C., Morrissey, P., Neff, S., Schiminovich, D., Seibert, M., Small, T., Wyder, T., Bianchi, L., Donas, J., Heckman, T., Lee, Y.-W., Madore, B., Milliard, B., Rich, R. M., & Szalay, A. 2007, ApJS, 173, 619 54

Kenney, J. D. P., van Gorkom, J. H., & Vollmer, B. 2004, AJ, 127, 3361 11

Kennicutt, Jr., R. C. 1998, ARA&A, 36, 189 76

Kimm, T., Somerville, R. S., Yi, S. K., van den Bosch, F. C., Salim, S., Fontanot, F., Monaco, P., Mo, H., Pasquali, A., Rich, R. M., & Yang, X. 2009, MNRAS, 394, 1131 10, 62

Kitayama, T., Komatsu, E., Ota, N., Kuwabara, T., Suto, Y., Yoshikawa, K., Hattori, M., & Matsuo, H. 2004, PASJ, 56, 17 90, 112

Kling, T. P., Dell'Antonio, I., Wittman, D., & Tyson, J. A. 2005, ApJ, 625, 643 90, 110

Knop, R. A., Aldering, G., Amanullah, R., Astier, P., Blanc, G., Burns, M. S., Conley, A., Deustua, S. E., Doi, M., Ellis, R., Fabbro, S., Folatelli, G., Fruchter, A. S., Garavini, G., Garmond, S., Garton, K., Gibbons, R., Goldhaber, G., Goobar, A., Groom, D. E., Hardin, D., Hook, I., Howell, D. A., Kim, A. G., Lee, B. C., Lidman, C., Mendez, J., Nobili, S., Nugent, P. E., Pain, R., Panagia, N., Pennypacker, C. R., Perlmutter, S., Quimby, R., Raux, J., Regnault, N., Ruiz-Lapuente, P., Sainton, G., Schaefer, B., Schahmaneche, K., Smith, E., Spadafora, A. L., Stanishev, V., Sullivan, M., Walton, N. A., Wang, L., Wood-Vasey, W. M., & Yasuda, N. 2003, ApJ, 598, 102 1

Kodama, T. & Arimoto, N. 1997, A&A, 320, 41 3, 15, 22

Kodama, T., Balogh, M. L., Smail, I., Bower, R. G., & Nakata, F. 2004, MNRAS, 354, 1103 54

Kodama, T. & Bower, R. G. 2001, MNRAS, 321, 18 9, 10

Kodama, T., Smail, I., Nakata, F., Okamura, S., & Bower, R. G. 2001, ApJL, 562, L9 12

Kodama, T., Tanaka, M., Tamura, T., Yahagi, H., Nagashima, M., Tanaka, I., Arimoto, N., Futamase, T., Iye, M., Karasawa, Y., Kashikawa, N., Kawasaki, W., Kitayama, T., Matsuhara, H., Nakata, F., Ohashi, T., Ohta, K., Okamoto, T., Okamura, S., Shimasaku, K., Suto, Y., Tamura, N., Umetsu, K., & Yamada, T. 2005, pasj, 57, 309 12

Koester, B. P., McKay, T. A., Annis, J., Wechsler, R. H., Evrard, A., Bleem, L., Becker, M., Johnston, D., Sheldon, E., Nichol, R., Miller, C., Scranton, R., Bahcall, N., Barentine, J., Brewington, H., Brinkmann, J., Harvanek, M., Kleinman, S., Krzesinski, J., Long, D., Nitta, A., Schneider, D. P., Sneddin, S., Voges, W., & York, D. 2007, ApJ, 660, 239 8, 30, 31, 35, 38

Komatsu, E., Dunkley, J., Nolta, M. R., Bennett, C. L., Gold, B., Hinshaw, G., Jarosik, N., Larson, D., Limon, M., Page, L., Spergel, D. N., Halpern, M., Hill, R. S., Kogut, A., Meyer, S. S., Tucker, G. S., Weiland, J. L., Wollack, E., & Wright, E. L. 2009, ApJS, 180, 330 1

Komatsu, E., Kogut, A., Nolta, M. R., Bennett, C. L., Halpern, M., Hinshaw, G., Jarosik, N., Limon, M., Meyer, S. S., Page, L., Spergel, D. N., Tucker, G. S., Verde, L., Wollack, E., & Wright, E. L. 2003, ApJS, 148, 119 1

Komatsu, E., Matsuo, H., Kitayama, T., Hattori, M., Kawabe, R., Kohno, K., Kuno, N., Schindler, S., Suto, Y., & Yoshikawa, K. 2001, PASJ, 53, 57 90, 112

Kong, X., Charlot, S., Brinchmann, J., & Fall, S. M. 2004, MNRAS, 349, 769 75

Lacey, C. & Cole, S. 1993, MNRAS, 262, 627 7, 10

Landy, S. D. & Szalay, A. S. 1993, ApJ, 412, 64 33

Larson, D., Dunkley, J., Hinshaw, G., Komatsu, E., Nolta, M. R., Bennett, C. L., Gold, B., Halpern, M., Hill, R. S., Jarosik, N., Kogut, A., Limon, M., Meyer, S. S., Odegard, N., Page, L., Smith, K. M., Spergel, D. N., Tucker, G. S., Weiland, J. L., Wollack, E., & Wright, E. L. 2010, ArXiv e-prints 1

Larson, R. B., Tinsley, B. M., & Caldwell, C. N. 1980, ApJ, 237, 692 11

Lewis, I., Balogh, M., De Propris, R., Couch, W., Bower, R., Offer, A., Bland-Hawthorn, J., Baldry, I. K., Baugh, C., Bridges, T., Cannon, R., Cole, S., Colless, M., Collins, C., Cross, N., Dalton, G., Driver, S. P., Efstathiou, G., Ellis, R. S., Frenk, C. S., Glazebrook, K., Hawkins, E., Jackson, C., Lahav, O., Lumsden, S., Maddox, S., Madgwick, D.,

Norberg, P., Peacock, J. A., Percival, W., Peterson, B. A., Sutherland, W., & Taylor, K. 2002, MNRAS, 334, 673 11, 62

Li, I. H., Yee, H. K. C., & Ellingson, E. 2009, ApJ, 698, 83 89

Lilly, S. J., Le Fevre, O., Hammer, F., & Crampton, D. 1996, ApJL, 460, L1+ 6, 62

Łokas, E. L. & Mamon, G. A. 2001, MNRAS, 321, 155 102

Lu, T., Gilbank, D. G., Balogh, M. L., & Bognat, A. 2009, MNRAS, 399, 1858 91, 92, 94

Madau, P., Ferguson, H. C., Dickinson, M. E., Giavalisco, M., Steidel, C. C., & Fruchter, A. 1996, MNRAS, 283, 1388 6, 62

Mahdavi, A., Hoekstra, H., Babul, A., & Henry, J. P. 2008, MNRAS, 384, 1567 109

Maraston, C. 2005, MNRAS, 362, 799 6

Markevitch, M., Gonzalez, A. H., David, L., Vikhlinin, A., Murray, S., Forman, W., Jones, C., & Tucker, W. 2002, ApJL, 567, L27 113

Martini, P., Kelson, D. D., Mulchaey, J. S., & Trager, S. C. 2002, ApJL, 576, L109 76

Mason, B. S., Dicker, S. R., Korngut, P. M., Devlin, M. J., Cotton, W. D., Koch, P. M., Molnar, S. M., Sievers, J. L., Aguirre, J. E., Benford, D., Staguhn, J. G., Moseley, H., Irwin, K. D., & Ade, P. A. R. 2009, ArXiv e-prints 90, 112, 113

Mather, J. C., Cheng, E. S., Eplee, Jr., R. E., Isaacman, R. B., Meyer, S. S., Shafer, R. A., Weiss, R., Wright, E. L., Bennett, C. L., Boggess, N. W., Dwek, E., Gulkis, S., Hauser, M. G., Janssen, M., Kelsall, T., Lubin, P. M., Moseley, Jr., S. H., Murdock, T. L., Silverberg, R. F., Smoot, G. F., & Wilkinson, D. T. 1990, ApJL, 354, L37 1

Maulbetsch, C., Avila-Reese, V., Colín, P., Gottlöber, S., Khalatyan, A., & Steinmetz, M. 2007, ApJ, 654, 53 89

McGee, S. L., Balogh, M. L., Bower, R. G., Font, A. S., & McCarthy, I. G. 2009, MNRAS, 400, 937 12, 85, 89

McGee, S. L., Balogh, M. L., Henderson, R. D. E., Wilman, D. J., Bower, R. G., Mulchaey, J. S., & Oemler, A. J. 2008, MNRAS, 387, 1605 11, 89

Mercurio, A., Merluzzi, P., Haines, C. P., Gargiulo, A., Krusanova, N., Busarello, G., Barbera, F. L., Capaccioli, M., & Covone, G. 2006, MNRAS, 368, 109 45

Meurer, G. R., Heckman, T. M., & Calzetti, D. 1999, ApJ, 521, 64 75

Mihos, J. C. & Hernquist, L. 1996, ApJ, 464, 641 2

Miley, G. & De Breuck, C. 2008, aapr, 15, 67 9

Milkeraitis, M., van Waerbeke, L., Heymans, C., Hildebrandt, H., Dietrich, J. P., & Erben, T. 2010, MNRAS, 701 8

Miller, C. J., Nichol, R. C., Gómez, P. L., Hopkins, A. M., & Bernardi, M. 2003, ApJ, 597, 142 76, 120

Miller, C. J., Nichol, R. C., Reichart, D., Wechsler, R. H., Evrard, A. E., Annis, J., McKay, T. A., Bahcall, N. A., Bernardi, M., Boehringer, H., Connolly, A. J., Goto, T., Kniazev, A., Lamb, D., Postman, M., Schneider, D. P., Sheth, R. K., & Voges, W. 2005, AJ, 130, 968 8

Miranda, M., Sereno, M., de Filippis, E., & Paolillo, M. 2008, MNRAS, 385, 511 90, 110, 112

Mitchell, R. J., Culhane, J. L., Davison, P. J. N., & Ives, J. C. 1976, MNRAS, 175, 29P 7

Moore, B., Katz, N., Lake, G., Dressler, A., & Oemler, A. 1996, Nature, 379, 613 11

Moran, S. M., Ellis, R. S., Treu, T., Smith, G. P., Rich, R. M., & Smail, I. 2007, ApJ, 671, 1503 117, 118

Morris, S. L., Hutchings, J. B., Carlberg, R. G., Yee, H. K. C., Ellingson, E., Balogh, M. L., Abraham, R. G., & Smecker-Hane, T. A. 1998, ApJ, 507, 84 11

Morrissey, P., Conrow, T., Barlow, T. A., Small, T., Seibert, M., Wyder, T. K., Budavári, T., Arnouts, S., Friedman, P. G., Forster, K., Martin, D. C., Neff, S. G., Schiminovich, D., Bianchi, L., Donas, J., Heckman, T. M., Lee, Y., Madore, B. F., Milliard, B., Rich, R. M., Szalay, A. S., Welsh, B. Y., & Yi, S. K. 2007, ApJS, 173, 682 64

Navarro, J. F., Frenk, C. S., & White, S. D. M. 1997, ApJ, 490, 493 98, 104, 105, 109

Navarro, J. F. & Steinmetz, M. 1997, ApJ, 478, 13 3

Nelan, J. E., Smith, R. J., Hudson, M. J., Wegner, G. A., Lucey, J. R., Moore, S. A. W., Quinney, S. J., & Suntzeff, N. B. 2005, ApJ, 632, 137 15

Noeske, K. G., Weiner, B. J., Faber, S. M., Papovich, C., Koo, D. C., Somerville, R. S., Bundy, K., Conselice, C. J., Newman, J. A., Schiminovich, D., Le Floc'h, E., Coil, A. L., Rieke, G. H., Lotz, J. M., Primack, J. R., Barmby, P., Cooper, M. C., Davis, M., Ellis, R. S., Fazio, G. G., Guhathakurta, P., Huang, J., Kassin, S. A., Martin, D. C., Phillips, A. C., Rich, R. M., Small, T. A., Willmer, C. N. A., & Wilson, G. 2007, ApJL, 660, L43 6, 62, 78

Olsen, L. F., Benoist, C., Cappi, A., Maurogordato, S., Mazure, A., Slezak, E., Adami, C., Ferrari, C., & Martel, F. 2007, aap, 461, 81 8

Ota, N., Murase, K., Kitayama, T., Komatsu, E., Hattori, M., Matsuo, H., Oshima, T., Suto, Y., & Yoshikawa, K. 2008, A&A, 491, 363 90, 112

Pacaud, F., Pierre, M., Adami, C., Altieri, B., Andreon, S., Chiappetti, L., Detal, A., Duc, P., Galaz, G., Gueguen, A., Le Fèvre, J., Hertling, G., Libbrecht, C., Melin, J., Ponman, T. J., Quintana, H., Refregier, A., Sprimont, P., Surdej, J., Valtchanov, I., Willis, J. P., Alloin, D., Birkinshaw, M., Bremer, M. N., Garcet, O., Jean, C., Jones, L. R., Le Fèvre, O., Maccagni, D., Mazure, A., Proust, D., Röttgering, H. J. A., & Trinchieri, G. 2007, MNRAS, 382, 1289 8, 35, 38

Peacock, J. A. 1983, MNRAS, 202, 615 113

Peng, Y., Lilly, S. J., Kovac, K., Bolzonella, M., Pozzetti, L., Renzini, A., Zamorani, G., Ilbert, O., Knobel, C., Iovino, A., Maier, C., Cucciati, O., Tasca, L., Carollo, C. M., Silverman, J., Kampczyk, P., de Ravel, L., Sanders, D., Contini, T., Mainieri, V., Scodeggio, M., Kneib, J., Le Fevre, O., Bardelli, S., Bongiorno, A., Caputi, K., Coppa, G., de la Torre, S., Franzetti, P., Garilli, B., Lamareille, F., Le Borgne, J., Le Brun, V., Mignoli, M., Perez Montero, E., Pello, R., Ricciardelli, E., Tanaka, M., Tresse, L., Vergani, D., Welikala, N., Zucca, E., Oesch, P., Abbas, U., Barnes, L., Bordoloi, R., Bottini, D., Cappi, A., Cassata, P., Cimatti, A., Fumana, M., Hasinger, G., Koekemoer, A. M., Leauthaud, A., Maccagni, D., Marinoni, C., McCracken, H. J., Memeo, P., Meneux, B., Nair, P., Porciani, C., Presotto, V., & Scaramella, R. 2010, ArXiv e-prints 12, 62, 78

Pimbblet, K. A., Smail, I., Edge, A. C., Couch, W. J., O'Hely, E., & Zabludoff, A. I. 2001, MNRAS, 327, 588 51

Pimbblet, K. A., Smail, I., Edge, A. C., O'Hely, E., Couch, W. J., & Zabludoff, A. I. 2006, VizieR Online Data Catalog, 736, 60645 51

Poggianti, B. M., Smail, I., Dressler, A., Couch, W. J., Barger, A. J., Butcher, H., Ellis, R. S., & Oemler, Jr., A. 1999, ApJ, 518, 576 11

Pointecouteau, E., Giard, M., Benoit, A., Désert, F. X., Bernard, J. P., Coron, N., & Lamarre, J. M. 2001, ApJ, 552, 42 90

Popesso, P., Biviano, A., Böhringer, H., & Romaniello, M. 2006, A&A, 445, 29 45

Postman, M., Lubin, L. M., Gunn, J. E., Oke, J. B., Hoessel, J. G., Schneider, D. P., & Christensen, J. A. 1996, AJ, 111, 615 7

Pozzetti, L., Bolzonella, M., Zucca, E., Zamorani, G., Lilly, S., Renzini, A., Moresco, M., Mignoli, M., Cassata, P., Tasca, L., Lamareille, F., Maier, C., Meneux, B., Halliday, C., Oesch, P., Vergani, D., Caputi, K., Kovac, K., Cimatti, A., Cucciati, O., Iovino, A., Peng, Y., Carollo, M., Contini, T., Kneib, J. P., Le F'evre, O., Mainieri, V., Scodeggio, M., Bardelli, S., Bongiorno, A., Coppa, G., de la Torre, S., de Ravel, L., Franzetti, P., Garilli, B., Kampczyk, P., Knobel, C., Le Borgne, J. F., Le Brun, V., Pell'o, R., Perez Montero, E., Ricciardelli, E., Silverman, J. D., Tanaka, M., Tresse, L., Abbas, U., Bottini, D., Cappi, A., Guzzo, L., Koekemoer, A. M., Leauthaud, A., Maccagni, D., Marinoni, C., McCracken, H. J., Memeo, P., Porciani, C., Scaramella, R., Scarlata, C., & Scoville, N. 2009, ArXiv e-prints 6, 62

Romer, A. K., Viana, P. T. P., Liddle, A. R., & Mann, R. G. 2001, ApJ, 547, 594 8

Rubin, V. C. & Ford, Jr., W. K. 1970, ApJ, 159, 379 1

Rubin, V. C., Thonnard, N., & Ford, Jr., W. K. 1978, ApJL, 225, L107 1

Sahu, K. C., Shaw, R. A., Kaiser, M. E., Baum, S. A., Ferguson, H. C., Hayes, J. J. E., Gull, T. R., Hill, R. J., Hutchings, J. B., Kimble, R. A., Plait, P., & Woodgate, B. E. 1998, ApJL, 492, L125+ 90, 112

Salim, S., Rich, R. M., Charlot, S., Brinchmann, J., Johnson, B. D., Schiminovich, D., Seibert, M., Mallery, R., Heckman, T. M., Forster, K., Friedman, P. G., Martin, D. C., Morrissey, P., Neff, S. G., Small, T., Wyder, T. K., Bianchi, L., Donas, J., Lee, Y., Madore, B. F., Milliard, B., Szalay, A. S., Welsh, B. Y., & Yi, S. K. 2007, ApJS, 173, 267 78

Sandage, A. & Visvanathan, N. 1978a, ApJ, 225, 742 3

—. 1978b, ApJ, 223, 707 3

Scarlata, C., Carollo, C. M., Lilly, S. J., Feldmann, R., Kampczyk, P., Renzini, A., Cimatti, A., Halliday, C., Daddi, E., Sargent, M. T., Koekemoer, A., Scoville, N., Kneib, J.-P., Leauthaud, A., Massey, R., Rhodes, J., Tasca, L., Capak, P., McCracken, H. J., Mobasher, B., Taniguchi, Y., Thompson, D., Ajiki, M., Aussel, H., Murayama, T., Sanders, D. B., Sasaki, S., Shioya, Y., & Takahashi, M. 2007, ApJS, 172, 494 15

Schindler, S., Guzzo, L., Ebeling, H., Boehringer, H., Chincarini, G., Collins, C. A., de Grandi, S., Neumann, D. M., Briel, U. G., Shaver, P., & Vettolani, G. 1995, A&A, 299, L9+ 90

Schindler, S., Hattori, M., Neumann, D. M., & Boehringer, H. 1997, A&A, 317, 646 90, 109

Schlegel, D. J., Finkbeiner, D. P., & Davis, M. 1998, ApJ, 500, 525 17, 64

Schweizer, F. & Seitzer, P. 1992, AJ, 104, 1039 55

Secker, J. & Harris, W. E. 1996, ApJ, 469, 623 45

Shimizu, M., Kitayama, T., Sasaki, S., & Suto, Y. 2003, ApJ, 590, 197 35

Silverman, B. W. 1986, Density estimation for statistics and data analysis (London: Chapman and Hall) 103

Smail, I., Dressler, A., Couch, W. J., Ellis, R. S., Oemler, Jr., A., Butcher, H., & Sharples, R. M. 1997, ApJS, 110, 213 10

Smail, I., Edge, A. C., Ellis, R. S., & Blandford, R. D. 1998, MNRAS, 293, 124 52, 53

Smith, G. P., Treu, T., Ellis, R. S., Moran, S. M., & Dressler, A. 2005, ApJ, 620, 78 10

Smith, R. J., Hudson, M. J., Lucey, J. R., Nelan, J. E., & Wegner, G. A. 2006, MNRAS, 369, 1419 3, 15

Smith, R. J., Lucey, J. R., Hudson, M. J., Allanson, S. P., Bridges, T. J., Hornschemeier, A. E., Marzke, R. O., & Miller, N. A. 2009, MNRAS, 392, 1265 49, 60

Smoot, G. F., Bennett, C. L., Kogut, A., Aymon, J., Backus, C., de Amici, G., Galuk, K., Jackson, P. D., Keegstra, P., Rokke, L., Tenorio, L., Torres, S., Gulkis, S., Hauser, M. G., Janssen, M. A., Mather, J. C., Weiss, R., Wilkinson, D. T., Wright, E. L., Boggess, N. W., Cheng, E. S., Kelsall, T., Lubin, P., Meyer, S., Moseley, S. H., Murdock, T. L., Shafer, R. A., & Silverberg, R. F. 1991, ApJL, 371, L1 1

Springel, V. 2005, MNRAS, 364, 1105 3

Springel, V., White, S. D. M., Jenkins, A., Frenk, C. S., Yoshida, N., Gao, L., Navarro, J., Thacker, R., Croton, D., Helly, J., Peacock, J. A., Cole, S., Thomas, P., Couchman, H., Evrard, A., Colberg, J., & Pearce, F. 2005, Nature, 435, 629 33, 114

Stott, J. P., Smail, I., Edge, A. C., Ebeling, H., Smith, G. P., Kneib, J.-P., & Pimbblet, K. A. 2007, ApJ, 661, 95 10, 16, 50, 51, 52, 53, 54, 60

Strateva, I., Ivezić, Ž., Knapp, G. R., Narayanan, V. K., Strauss, M. A., Gunn, J. E., Lupton, R. H., Schlegel, D., Bahcall, N. A., Brinkmann, J., Brunner, R. J., Budavári, T., Csabai, I., Castander, F. J., Doi, M., Fukugita, M., Győry, Z., Hamabe, M., Hennessy, G., Ichikawa, T., Kunszt, P. Z., Lamb, D. Q., McKay, T. A., Okamura, S., Racusin, J., Sekiguchi, M., Schneider, D. P., Shimasaku, K., & York, D. 2001, AJ, 122, 1861 55

Sunyaev, R. A. & Zeldovich, Y. B. 1972, Comments on Astrophysics and Space Physics, 4, 173 8

Tanaka, M., Finoguenov, A., Kodama, T., Koyama, Y., Maughan, B., & Nakata, F. 2009, A&A, 505, L9 114

Tanaka, M., Kodama, T., Arimoto, N., Okamura, S., Umetsu, K., Shimasaku, K., Tanaka, I., & Yamada, T. 2005, MNRAS, 362, 268 51

Tanaka, M., Kodama, T., Arimoto, N., & Tanaka, I. 2006, MNRAS, 365, 1392 12, 89

Tinsley, B. M. & Gunn, J. E. 1976, ApJ, 203, 52 4

Trager, S. C., Faber, S. M., Worthey, G., & González, J. J. 2000, AJ, 120, 165 3, 15

Tran, K., Saintonge, A., Moustakas, J., Bai, L., Gonzalez, A. H., Holden, B. P., Zaritsky, D., & Kautsch, S. J. 2009, ApJ, 705, 809 11

Urquhart, S. A., Willis, J. P., Hoekstra, H., & Pierre, M. 2010, MNRAS, 406, 368 100

van Haarlem, M. & van de Weygaert, R. 1993, ApJ, 418, 544 98

Vanderlinde, K., Crawford, T. M., de Haan, T., Dudley, J. P., Shaw, L., Ade, P. A. R., Aird, K. A., Benson, B. A., Bleem, L. E., Brodwin, M., Carlstrom, J. E., Chang, C. L., Crites, A. T., Desai, S., Dobbs, M. A., Foley, R. J., George, E. M., Gladders, M. D., Hall, N. R., Halverson, N. W., High, F. W., Holder, G. P., Holzapfel, W. L., Hrubes, J. D., Joy, M., Keisler, R., Knox, L., Lee, A. T., Leitch, E. M., Loehr, A., Lueker, M., Marrone, D. P., McMahon, J. J., Mehl, J., Meyer, S. S., Mohr, J. J., Montroy, T. E., Ngeow, C., Padin, S., Plagge, T., Pryke, C., Reichardt, C. L., Rest, A., Ruel, J., Ruhl, J. E., Schaffer, K. K., Shirokoff, E., Song, J., Spieler, H. G., Stalder, B., Staniszewski, Z., Stark, A. A., Stubbs, C. W., van Engelen, A., Vieira, J. D., Williamson, R., Yang, Y., Zahn, O., & Zenteno, A. 2010, ArXiv e-prints 8

Vazdekis, A., Sánchez-Blázquez, P., Falcón-Barroso, J., Cenarro, A. J., Beasley, M. A., Cardiel, N., Gorgas, J., & Peletier, R. F. 2010, MNRAS, 404, 1639 6

Visvanathan, N. & Sandage, A. 1977, ApJ, 216, 214 3

Voges, W., Aschenbach, B., Boller, T., Bräuninger, H., Briel, U., Burkert, W., Dennerl, K., Englhauser, J., Gruber, R., Haberl, F., Hartner, G., Hasinger, G., Kürster, M., Pfeffermann, E., Pietsch, W., Predehl, P., Rosso, C., Schmitt, J. H. M. M., Trümper, J., & Zimmermann, H. U. 1999, aap, 349, 389 8

Wake, D. A., Collins, C. A., Nichol, R. C., Jones, L. R., & Burke, D. J. 2005, ApJ, 627, 186 100

Wall, J. & Jenkins, C. R. 2003, Practical Statistics for Astronomers (Cambridge University Press) 96, 103

Weinmann, S. M., van den Bosch, F. C., Yang, X., & Mo, H. J. 2006a, MNRAS, 366, 2 8, 9, 11, 16, 62

Weinmann, S. M., van den Bosch, F. C., Yang, X., Mo, H. J., Croton, D. J., & Moore, B. 2006b, MNRAS, 372, 1161 16, 89

White, S. D. M. & Frenk, C. S. 1991, ApJ, 379, 52 4

White, S. D. M. & Rees, M. J. 1978, MNRAS, 183, 341 2

Wilman, D. J., Pierini, D., Tyler, K., McGee, S. L., Oemler, Jr., A., Morris, S. L., Balogh, M. L., Bower, R. G., & Mulchaey, J. S. 2008, in Astronomical Society of the Pacific Conference Series, Vol. 399, Astronomical Society of the Pacific Conference Series, ed. T. Kodama, T. Yamada, & K. Aoki, 340–+ 11

Wittman, D., Dell'Antonio, I. P., Hughes, J. P., Margoniner, V. E., Tyson, J. A., Cohen, J. G., & Norman, D. 2006, ApJ, 643, 128 9

Wittman, D., Tyson, J. A., Margoniner, V. E., Cohen, J. G., & Dell'Antonio, I. P. 2001, ApJL, 557, L89 8

Wolf, C., Aragón-Salamanca, A., Balogh, M., Barden, M., Bell, E. F., Gray, M. E., Peng, C. Y., Bacon, D., Barazza, F. D., Böhm, A., Caldwell, J. A. R., Gallazzi, A., Häußler, B., Heymans, C., Jahnke, K., Jogee, S., van Kampen, E., Lane, K., McIntosh, D. H., Meisenheimer, K., Papovich, C., Sánchez, S. F., Taylor, A., Wisotzki, L., & Zheng, X. 2009, MNRAS, 393, 1302 54

Wolf, C., Gray, M. E., & Meisenheimer, K. 2005, A&A, 443, 435 16

Worthey, G. 1994, ApJS, 95, 107 3, 15

Wyder, T. K., Martin, D. C., Schiminovich, D., Seibert, M., Budavári, T., Treyer, M. A., Barlow, T. A., Forster, K., Friedman, P. G., Morrissey, P., Neff, S. G., Small, T., Bianchi, L., Donas, J., Heckman, T. M., Lee, Y., Madore, B. F., Milliard, B., Rich, R. M., Szalay, A. S., Welsh, B. Y., & Yi, S. K. 2007, ApJS, 173, 293 64

Yang, X., Mo, H. J., van den Bosch, F. C., Pasquali, A., Li, C., & Barden, M. 2007, ApJ, 671, 153 8

Yee, H. K. C. 1991, PASP, 103, 396 91

Yee, H. K. C., Gladders, M. D., Gilbank, D. G., Majumdar, S., Hoekstra, H., Ellingson, E., & the RCS-2 Collaboration. 2007, ArXiv Astrophysics e-prints 8

Yee, H. K. C. & López-Cruz, O. 1999, AJ, 117, 1985 58

York, D. G., Adelman, J., Anderson, Jr., J. E., Anderson, S. F., Annis, J., Bahcall, N. A., Bakken, J. A., Barkhouser, R., Bastian, S., Berman, E., Boroski, W. N., Bracker, S., Briegel, C., Briggs, J. W., Brinkmann, J., Brunner, R., Burles, S., Carey, L., Carr, M. A., Castander, F. J., Chen, B., Colestock, P. L., Connolly, A. J., Crocker, J. H., Csabai, I., Czarapata, P. C., Davis, J. E., Doi, M., Dombeck, T., Eisenstein, D., Ellman, N., Elms, B. R., Evans, M. L., Fan, X., Federwitz, G. R., Fiscelli, L., Friedman, S., Frieman, J. A., Fukugita, M., Gillespie, B., Gunn, J. E., Gurbani, V. K., de Haas, E., Haldeman, M., Harris, F. H., Hayes, J., Heckman, T. M., Hennessy, G. S., Hindsley, R. B., Holm, S., Holmgren, D. J., Huang, C., Hull, C., Husby, D., Ichikawa, S., Ichikawa, T., Ivezić, Ž., Kent, S., Kim, R. S. J., Kinney, E., Klaene, M., Kleinman, A. N., Kleinman, S., Knapp, G. R., Korienek, J., Kron, R. G., Kunszt, P. Z., Lamb, D. Q., Lee, B., Leger, R. F., Limmongkol, S., Lindenmeyer, C., Long, D. C., Loomis, C., Loveday, J., Lucinio, R., Lupton, R. H., MacKinnon, B., Mannery, E. J., Mantsch, P. M., Margon, B., McGehee, P., McKay, T. A., Meiksin, A., Merelli, A., Monet, D. G., Munn, J. A., Narayanan, V. K., Nash, T., Neilsen, E., Neswold, R., Newberg, H. J., Nichol, R. C., Nicinski, T., Nonino, M., Okada, N., Okamura, S., Ostriker, J. P., Owen, R., Pauls, A. G., Peoples, J., Peterson, R. L., Petravick, D., Pier, J. R., Pope, A., Pordes, R., Prosapio, A., Rechenmacher, R., Quinn, T. R., Richards, G. T., Richmond, M. W., Rivetta, C. H., Rockosi, C. M., Ruthmansdorfer, K., Sandford, D., Schlegel, D. J., Schneider, D. P., Sekiguchi, M., Sergey, G., Shimasaku, K., Siegmund, W. A., Smee, S., Smith, J. A., Snedden, S., Stone, R., Stoughton, C., Strauss, M. A., Stubbs, C., SubbaRao, M., Szalay, A. S., Szapudi, I., Szokoly, G. P., Thakar, A. R., Tremonti, C., Tucker, D. L., Uomoto, A., Vanden Berk, D., Vogeley, M. S., Waddell, P., Wang, S., Watanabe, M., Weinberg, D. H., Yanny, B., & Yasuda, N. 2000, AJ, 120, 1579 8, 17, 37

Zabludoff, A. I. & Mulchaey, J. S. 1998, ApJ, 496, 39 12, 85

Zwicky, F. 1933, Helvetica Physica Acta, 6, 110 1